

UNCLASSIFIED
SECURITY CLASSIFICATION OF THIS PAGE

REPORT DOCUMENTATION PAGE

1a. REPORT SECURITY CLASSIFICATION Unclassified			1b. RESTRICTIVE MARKINGS		
2a. SECURITY CLASSIFICATION AUTHORITY			3. DISTRIBUTION/AVAILABILITY OF REPORT Approved for public release Distribution unlimited		
2b. DECLASSIFICATION/DOWNGRADING SCHEDULE					
4. PERFORMING ORGANIZATION REPORT NUMBER(S) VUB-STR-17			5. MONITORING ORGANIZATION REPORT NUMBER(S)		
6a. NAME OF PERFORMING ORGANIZATION Vrije Universiteit Brussel Dept. of Fluid Mechanics		6b. OFFICE SYMBOL (if applicable) VUB-STRO	7a. NAME OF MONITORING ORGANIZATION European Office for Aerospace Research and Development		
6c. ADDRESS (City, State, and ZIP Code) Pleinlaan 2 B-1050 BRUSSELS BELGIUM			7b. ADDRESS (City, State, and ZIP Code) Marylebone Road LONDON ENGLAND		
8a. NAME OF FUNDING/SPONSORING ORGANIZATION Air Force Office for Scientific Research		8b. OFFICE SYMBOL (if applicable) AFOSR	9. PROCUREMENT INSTRUMENT IDENTIFICATION NUMBER AFOSR-89-0375		
10. ADDRESS (City, State, and ZIP Code) Building 410, Bolling AFB DC 20332-6448 UNITED STATES OF AMERICA			10. SOURCE OF FUNDING NUMBERS		
			PROGRAM ELEMENT NO. 61102F	PROJECT NO. 2307	TASK NO. A3
11. TITLE (Include Security Classification) RADIAL MIXING IN TURBOMACHINES			WORK UNIT ACCESSION NO.		
12. PERSONAL AUTHOR(S) SEGAERT P. HIRSCH Ch. DE RUYCK J.					
13a. TYPE OF REPORT Final		13b. TIME COVERED FROM 89-6-1 TO 90-7-31		14. DATE OF REPORT (Year, Month, Day) 91-3-31	
15. PAGE COUNT 193					
16. SUPPLEMENTARY NOTATION					
17. COSATI CODES			18. SUBJECT TERMS (Continue on reverse if necessary and identify by block number)		
FIELD	GROUP	SUB-GROUP	Radial Mixing		
			Secondary Flows		
			Turbomachinery Flow Computations		
19. ABSTRACT (Continue on reverse if necessary and identify by block number)					
<p>A method for the computation of the effects of radial mixing in a turbomachinery blade row has been developed. The method fits in the framework of a Quasi-3D flow computation and hence is applied in a corrective fashion to the through-flow distributions.</p> <p>The method takes into account both secondary flows and turbulent diffusion as possible sources of mixing : the secondary flow velocities determine the magnitude of the convection terms in the energy redistribution equation, while a turbulent diffusion coefficient determines the magnitude of the diffusion terms.</p> <p>The secondary flows are computed by solving a Poisson equation for a secondary streamfunction on a transversal S3-plane, whereby the right-hand side axial vorticity is composed of different contributions, each associated to a particular flow region : inviscid core flow, end-wall boundary layers, profile boundary layers and wakes.</p> <p>The turbulent mixing coefficient is estimated by means of a semi-empirical correlation. PTO</p>					
20. DISTRIBUTION/AVAILABILITY OF ABSTRACT <input checked="" type="checkbox"/> UNCLASSIFIED/UNLIMITED <input type="checkbox"/> SAME AS RPT. <input type="checkbox"/> DTIC USERS			21. ABSTRACT SECURITY CLASSIFICATION Unclassified		
22a. NAME OF RESPONSIBLE INDIVIDUAL DB EAT, MAJ, USAF			22b. TELEPHONE (Include Area Code) 202-767-0461		22c. OFFICE SYMBOL AFOSR/1A

19. ABSTRACT (continued)

The secondary flow theory is applied to the VUB cascade testcase and comparisons are made between the computational results and the extensive experimental data available for this testcase. This comparison shows that the secondary flow computations yield reliable predictions of the secondary flow pattern, both qualitatively and quantitatively, taking into account the limitations of the model.

However, the computations show that the use of a uniform mixing coefficient has to be replaced by a more sophisticated approach, i.e. using increased mixing levels in the end-wall boundary layers.

RADIAL MIXING IN TURBOMACHINES

P. SEGAERT, Ch. HIRSCH, J. DE RUYCK

**Department of Fluid Mechanics
Vrije Universiteit Brussel
Pleinlaan 2, 1050 Brussels
Belgium**

March 31, 1991

**Final Scientific Report
June 1, 1989 – July 31, 1990**

VUB - STR - 17

Approved for public release; distribution unlimited.

- Prepared for -

**Air Force Office for Scientific Research
Bolling AFB, USA**

and

**European Office for Aerospace Research and Development
London, England**

TABLE OF CONTENTS

INTRODUCTION.....	8
PART 1 : QUASI-3D COMPUTATIONS AND RADIAL MIXING	9
CHAPTER 1 : RADIAL MIXING	10
1.1 Definition and Importance of Radial Mixing.....	10
1.1.1 Classical Quasi-3D computations	10
1.1.2 Limitations of classical Quasi-3D computations	11
1.1.3 Radial mixing.....	12
1.2 Mechanisms of Radial Mixing.....	12
1.2.1 Secondary flows.....	12
1.2.2 Turbulence.....	14
1.3 Radial Mixing in the Framework of a Quasi-3D Method Based on an Averaging Procedure.....	15
1.3.1 Introduction.....	15
1.3.2 Quasi-3D turbomachinery flow computation.....	15
1.3.3 Turbomachinery streamsurfaces	16
1.3.4 Definition of secondary flows.....	17
1.4 Review of Previous Work.....	18
1.4.1 The convective mixing model of Adkins & Smith	18
1.4.2 The diffusive mixing model of Gallimore & Cumpsty.....	18
1.4.3 Convective mixing versus diffusive mixing.....	19
1.4.4 The convective-diffusive mixing model developed at the VUB Dept of Fluid Mechanics.....	20
PART 2 : COMPUTATION OF SECONDARY FLOW, TURBULENT.....	21
DIFFUSION AND MIXING	
CHAPTER 2 : GENERAL PRINCIPLES.....	22
2.1 Decomposition of the Flow Field.....	22
2.2 Turbomachinery Flow Regions.....	24
2.3 Fundamental Equations.....	24
2.3.1 Streamfunction ψ	24
2.3.2 Poisson equation.....	25
2.4 General Computation Strategy.....	26
2.4.1 Axial vorticity contributions	26
2.4.2 Computational domain.....	27
CHAPTER 3 : INVISCID FLOW REGION.....	28
3.1 Introduction.....	28
3.2 Governing Equation	28
3.3 Supplementary Equations.....	30
3.3.1 Introduction.....	30

3.3.2 Tangential vorticity	30
3.3.3 Radial vorticity.....	31
3.3.4 Axial velocity jump.....	31
3.3.5 Radial velocity jump	32
3.4 Numerical Solution	33
CHAPTER 4 : END-WALL BOUNDARY LAYERS REGION	35
4.1 Introduction.....	35
4.2 Theoretical Equations.....	35
4.2.1 Fundamental equations.....	36
4.2.2 Supplementary equations	37
4.2.3 Velocity profile models.....	38
4.3 Axial Vorticity Contribution.....	41
4.4 Numerical Solution	41
CHAPTER 5 : PROFILE BOUNDARY LAYERS REGION.....	43
5.1 Introduction.....	43
5.2 Theoretical Equations.....	43
5.2.1 Fundamental equations.....	43
5.2.2 Supplementary equations	45
5.2.3 Velocity profile models.....	45
5.3 Axial Vorticity Contribution.....	48
5.4 Numerical Solution	48
5.4.1 Initialisation and required input	48
5.4.2 Vorticity computation	49
CHAPTER 6 : WAKE REGION.....	50
6.1 Introduction.....	50
6.2 Theoretical Equations.....	50
6.2.1 Velocity profile models.....	51
6.2.2 Basic equations.....	52
6.3 Axial Vorticity Contribution.....	54
6.4 Numerical Solution	55
6.4.1 Initialisation and required input	55
6.4.2 Vorticity computation	55
CHAPTER 7 : TURBULENT DIFFUSION.....	56
7.1 Introduction.....	56
7.2 Turbulent Diffusion Coefficient.....	56
7.3 Turbulent Mixing Model.....	58
CHAPTER 8 : ENERGY REDISTRIBUTION.....	59
8.1 General Energy Transport Equation.....	59
8.2 General Mixing Equation.....	60
8.3 Explicit Mixing Equation and Numerical Solution.....	61
8.4 Boundary Conditions.....	61bis
PART 3 : NUMERICAL TECHNIQUES.....	62
CHAPTER 9 : MESH GENERATION.....	63
9.1 Introduction.....	63

9.2 Finite Element Discretization.....	64
9.2.1 Motivation.....	64
9.2.2 Basic principles.....	64
9.2.3 Serendipity elements.....	65
9.2.4 Finite element subdivision of computational surface.....	65
9.3 Finite Element Shape Functions.....	66
9.4 Isoparametric Mapping	66
CHAPTER 10 : NUMERICAL SOLVING TECHNIQUES.....	69
10.1 Introduction.....	69
10.2 Finite Element Solution of the Secondary Flow	69
10.2.1 Galerkin weighted residual formulation.....	69
10.2.2 Some remarks on numerical techniques.....	72
10.3 Numerical Solution of Radial Mixing Equation	73
10.3.1 Numerical integration technique.....	73
10.3.2 Numerical treatment of boundary conditions.....	74
10.4 Numerical Computation of Partial Derivatives.....	75
10.4.1 Introduction.....	75
10.4.2 Second-order finite difference formula for a first-order derivative	75
10.4.3 Second-order finite difference formula for a second-order derivative.....	76
PART 4 : RESULTS AND CONCLUSIONS	78
CHAPTER 11 : RESULTS.....	79
11.1 Introduction.....	79
11.2 Experimental Set-up.....	79
11.2.1 General features of testcase.....	79
11.2.2 Available experimental data.....	80
11.3 Overview of Computational Program.....	80
11.4 Discussion of Results.....	81
11.4.1 Results at 44% chord.....	82
11.4.2 Results at 66% chord.....	83
11.4.3 Results at 99% chord (Trailing edge).....	83
11.4.4 Results at 104% chord (Near wake).....	85
11.4.5 Results at 112% chord (Near wake).....	86
11.4.6 Results at 125% chord (Far wake).....	86
11.5 Velocity Vector Plots.....	88
11.6 Wake Radial Velocity Profiles.....	88
11.6.1 Radial velocity profiles near the end-walls.....	89
11.6.2 Radial velocity profiles near midspan.....	89
11.7 Wake Axial Velocity Profiles	89
11.7.1 Axial velocity profiles with standard wake mixing	89bis
11.7.2 Axial velocity profiles with increased wake mixing.....	89bis
11.8 Wake Radial Velocity Profiles with Increased Wake Mixing	89bis
11.9 Conclusions.....	89ter
CONCLUSIONS AND RECOMMENDATIONS FOR FUTURE WORK.....	90
PRESENTATION OF RESULTS.....	91
REFERENCES.....	180

APPENDIX A : MERIDIONAL COORDINATE SYSTEM.....	182
APPENDIX B : CONSTANT BLOCKAGE ASSUMPTION.....	184
APPENDIX C : INVISCID FLOW RELATIONS.....	186
C.1 Velocity Jump Relations.....	186
C.1.1 Tangential velocity jump.....	186
C.1.2 Radial velocity jump.....	186
C.2 Tangential Vorticity.....	187
C.3 Radial Vorticity	188

NOMENCLATURE

b	mechanical blockage factor, boundary layer velocity defect parameter
c	chord
f	wake profile model function (Pohlhausen polynomial)
F	defect force
g	wake profile model function (bridging function)
h	static enthalpy
H	total enthalpy
H_r	relative total enthalpy
I	rothalpy
L	axial stage length
n	boundary layer power law exponent
N	number of blades
\vec{N}	vector normal to material wall
r	radius
s	pitch
T	static temperature
T_t	total temperature
T_t^r	relative total temperature
T_t^*	rotary total temperature
δT_t^*	correction on Quasi-3D rotary total temperature distribution from radial mixing
U	wheel speed
\vec{W}	3D velocity vector in the blade row reference system
y	normal or tangential distance from the wall (in velocity profile models)
α	absolute flow angle between streamline direction and meridional direction
α_r	radial flow angle (induced by inviscid and end-wall boundary layer secondary flows)
β	relative flow angle between streamline direction and meridional direction
β'	blade angle
δ	physical boundary layer thickness
δ^*	boundary layer displacement thickness
Δ	parameter indicating relative motion between blades and end-wall
ϵ	boundary layer skewing angle
ϵ_t	turbulent diffusion mixing coefficient
ϵ_w	wall skewing angle
$\vec{\zeta}$	3D vorticity vector in the blade row reference system
$\vec{\zeta}_{abs}$	3D vorticity vector in the absolute frame of reference
θ	boundary layer momentum thickness
η	blade lean angle, non-dimensional distance from the wall

η_0	wake asymmetry parameter
μ	dynamic viscosity
ν	kinematic viscosity
ρ	density
σ	angle between meridional and normal directions
σ_w	end-wall inclination angle
τ	shear stress
ψ	streamfunction for the secondary flows
Ω	angular velocity of steadily rotating blade row

Subscripts

abs	absolute
p	pressure side
s	suction side
Q3D	component from Quasi-3D computation
S3	component from S3 computation
z, r, θ	cylindrical coordinates (axial, radial, tangential)
m, n, u	meridional coordinates (meridional, normal, tangential)
s, n, t	streamline coordinates (streamwise, normal, transversal)
inv	inviscid contribution
visc	viscous contribution
ewbl	end-wall boundary layer region
pbl	profile boundary layer region
wake	wake region

Superscripts

-	geometrical pitch-average,
	arithmetical average between pressure and suction side (wake model)
~	density weighted pitch-average
'	deviation from geometrical pitch-average
"	deviation from density-weighted pitch-average
^	inviscid or 'free-stream' reference value

Notations

$\vec{\nabla}$	3D Nabla operator
\otimes	tensorial product (dyad)
$[]_p^s$	difference between suction and pressure side

INTRODUCTION

The present report describes the approach followed by the program RADMIX in computing the radial redistribution of flow quantities between the axisymmetric blade-to-blade streamsurfaces of a finite element Quasi-3D computation code for turbomachinery flows. For the moment, the program is confined to simulations of the radial mixing process in single axial blade rows, but extension to multi-stage axial-flow turbomachines is envisaged.

The basic approach of the method is to take into account the effects of radial mixing by introducing corrections due to the radial transfer of momentum, energy and losses to a previously obtained through-flow computation or full Quasi-3D computation. This radial transfer is attributed to two different physical mechanisms : convective transport due to secondary flows and diffusive transport due to turbulence. The program RADMIX provides options, which allow to select numerical simulation of the mixing process by either of these mechanisms or by the combination of both.

The first part of this report describes the general approach to the radial mixing problem. The term 'radial mixing' is defined and the two mixing mechanisms are considered from the physical point of view. Next, the general Quasi-3D framework in which the present theory is formulated is briefly described. Finally, a review of previous work on radial mixing is presented.

The second part of this report details the theoretical foundations of the computation of secondary flows, turbulent diffusion and radial mixing effects.

For the secondary flow computation, a rigorous decomposition of the real flow into a Quasi-3D flow component and a secondary flow component is introduced. For computational purposes, the turbomachinery flow region is divided into four different subregions : the inviscid mainflow region, the end-wall boundary layers region, the profile boundary layers region and the region of the wakes. The specific theoretical principles and numerical techniques used are detailed in separate chapters for each individual type of flow region.

The numerical computation of the turbulent diffusion mechanism, based on a semi-empirical turbulent mixing coefficient, is described in a separate chapter.

Finally, the overall mixing process and its implementation with respect to the mainflow computation is discussed, including a derivation of the mixing equation from the energy conservation law.

The third part of the report contains a brief description of the numerical aspects of the radial mixing simulation : mesh generation and numerical solving techniques.

The fourth part of the report is mainly devoted to the validation of the proposed secondary flow model for the convective mixing : results of secondary flow computations for a linear compressor cascade are presented and compared with the extensive experimental data available for this testcase.

Finally, the major points of this report are summarized in the conclusions section and recommendations for future work are made.

PART 1

QUASI-3D COMPUTATIONS

AND

RADIAL MIXING

CHAPTER 1

RADIAL MIXING

1.1 DEFINITION AND IMPORTANCE OF RADIAL MIXING

1.1.1 CLASSICAL QUASI-3D COMPUTATIONS

Today, nearly all the computational codes for turbomachinery flow analysis used by industry are of the quasi-three-dimensional type (Quasi-3D). All these computation methods are basically variations of the streamsurface theory of Wu (1952), in which a steady three-dimensional turbomachinery flow is rigorously decomposed into two families of interacting two-dimensional flows on intersecting streamsurfaces.

These two families of 2D-flows are (Figure 1.1) :

- 1) The through-flow on hub-to-shroud surfaces or S2-streamsurfaces, obtained by expressing radial equilibrium.
- 2) The blade-to-blade flow on blade-to-blade surfaces or S1-streamsurfaces, obtained by a cascade potential flow analysis.

For reasons of simplicity, the S1-streamsurfaces are almost always assumed to be surfaces of revolution (with the machine shaft as rotation axis), intersecting the blading of the machine.

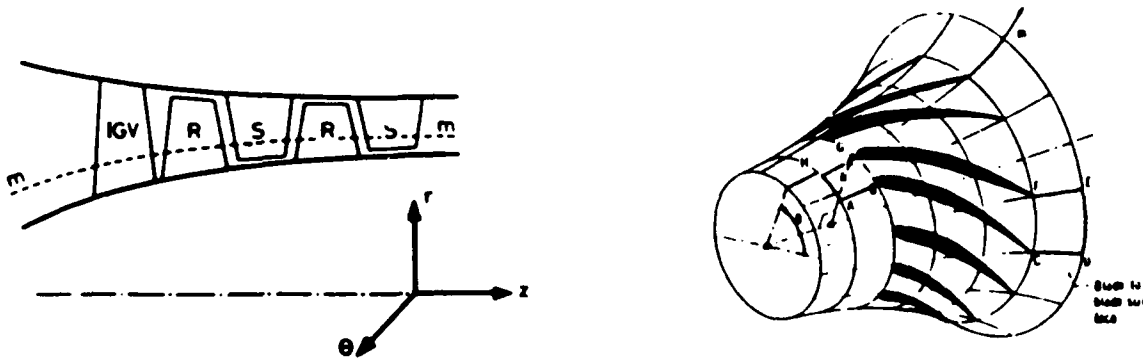


Figure 1.1 : Streamsurfaces for a turbomachinery flow (left = S2 , right = S1)

Although it is theoretically possible to represent a steady three-dimensional flow completely through two families of two-dimensional flows, Yih (1979), all computational methods solve the flow in an approximative way by reducing the number of streamsurfaces.

Generally, only one S2-surface is defined, which is assumed to be representative for all S2-streamsurfaces, i.e. a kind of 'mean through-flow' S2-surface. Similarly, only a small number of blade-to-blade S1-surfaces is defined, in most cases evenly distributed between hub and shroud.

The through-flow computation on the S2-surface yields radial distributions of important design parameters at inlet and exit of each blade row, e.g. axial velocity, swirl angle, mass flow, total pressure and temperature, etc..., while the blade-to-blade computations on the S1-surfaces provide a detailed picture of the flow between two adjacent blades, e.g. deviations and empirical estimations of profile losses through the use of correlations.

The flows on the two types of surfaces are interdependent, i.e. the solution of the flow on the through-flow surface provides the boundary conditions necessary to solve the flow on the blade-to-blade surfaces and vice versa. This clearly leads to an iterative solution procedure. All methods start with a through-flow computation on the S2-surface, using default boundary conditions. This is followed by a set of blade-to-blade computations on the different S1-surfaces, using the results of the previous through-flow solution as boundary conditions. Subsequently, a second through-flow computation is performed, while the previously obtained blade-to-blade solutions provide the necessary boundary conditions. In turn, this computation is again followed by a new set of blade-to-blade computations, etc... Generally, convergence is obtained after a few iterations.

In this way, the computation of a three-dimensional turbomachinery flow is reduced to an assembly of successive solutions of two-dimensional flows, which represents a large simplification with respect to computational procedures. The three-dimensional character of the flow is conserved through the interdependence on the boundary conditions for both flow families, hence the name 'quasi-three-dimensional' computation.

1.1.2 LIMITATIONS OF CLASSICAL QUASI-3D COMPUTATIONS

The Quasi-3D computation of a turbomachinery flow contains two approximations with respect to a real turbomachinery flow :

- 1) The reduction of the number of streamsurfaces to one S2-surface and a finite number of S1-surfaces means that the three-dimensional flowfield cannot anymore be reconstructed rigorously from the two two-dimensional flow families.
In fact, in order to obtain a complete description of the flow, a third kind of stream-surface, intersecting the two previous kinds of streamsurfaces, must be introduced (cf. § 1.3.3).
- 2) The assumption that S1-streamsurfaces are surfaces of revolution represents a severe limitation with respect to physical reality, since it can be shown that S1-surfaces can only have an axisymmetric geometry under very special circumstances, Vavra (1960).
In a real turbomachinery flow, several physical effects generate so-called secondary flows, which distort the geometry of the S1-streamsurfaces with respect to the axisymmetric geometry of a surface of revolution.

In conclusion, the classical quasi-three-dimensional flow description can be regarded as an intermediate level of description between the two-dimensional and fully three-dimensional flow descriptions, suited to configurations that are not "strongly" three-dimensional, in the sense that variations of one velocity component are less important than the other two. For example, in some cases secondary flow effects are small and the limited twisting of blade-to-blade surfaces may be neglected.

1.1.3 RADIAL MIXING

In the previous section, it was shown that the classical Quasi-3D concept, which considers a turbomachinery flow as a series of concentric streamsurfaces of revolution, is not consistent with physical reality. Indeed, the classical concept implies that different S1-streamsurfaces do not interact : each fluid particle is considered to remain on the same axisymmetric surface of revolution during its passage through the machine. However, in a real turbomachinery flow the twisting of S1-streamsurfaces through secondary flows leads to a transfer of fluid particles and their associated mass, momentum and energy with respect to the hypothetical surfaces of revolution, which is not taken into account by the classical Quasi-3D formulation.

Furthermore, like most real-life flows, turbomachinery flows are highly turbulent. The stochastic, chaotic motion associated to turbulence leads to random collisions between the fluid particles of different streamsurfaces, again resulting in a transfer of momentum and energy between different S1-streamsurfaces.

This leads to the conclusion that classical Quasi-3D computations neglect an essential feature of real turbomachinery flows : the radial transfer of mass, energy and momentum between the hypothetically axisymmetric S1-streamsurfaces, leading to a radial redistribution of flow properties. This radial transfer process is called radial mixing.

In the present report, a theoretical method to introduce the effects of radial mixing into classical Quasi-3D computation methods is developed, because radial redistribution of flow properties has become increasingly important in modern axial turbomachinery designs. This is due to the fact that modern design trends towards higher aerodynamic loading and lower aspect-ratio blading increase the three-dimensional character of the flow field, especially in the case of axial compressors.

1.2 MECHANISMS OF RADIAL MIXING

As was already indicated in the previous section, two different physical mechanisms can be distinguished as possible causes for the radial mixing process :

- 1) Convective transport through secondary flows
- 2) Diffusive transport through turbulence

1.2.1 SECONDARY FLOWS

a) Types and physical origin of secondary flows

Secondary flows are a well-known physical phenomenon in turbomachines. However, although the importance of secondary flows is widely recognized, witnessed by the extensive literature on this subject, the computation of secondary flows is a very difficult task and even the definition of secondary flows is the object of considerable debate. Since there is no general rigorous definition for the concept of secondary flows, the different types of secondary flow within turbomachines, their region of occurrence and their physical origin are listed below (Table 1.1).

Type of secondary flow	Occurrence region	Physical origin
1) Passage vortex : a) inviscid b) viscous	Core region Hub region and tip region	Deflection of an inlet flow with transversal vorticity (inviscid : due to non free-vortex behaviour ; viscous : due to end-wall boundary layers)
2) Trailing filament vortex	Blade wake	Stretching of inlet flow transversal vortex filaments (inviscid mechanism)
3) a) Trailing shed vortex (inviscid flow) b) Spanwise fluid migration in the blade wake (viscous flow)	Blade wake Blade wake	Radial pressure gradients, due to spanwise changes of blade circulation Imbalance between imposed radial pressure gradients and centrifugal forces due to streamline curvature
4) Spanwise fluid migration in the blade boundary layer	Blade boundary layer	Imbalance between imposed radial pressure gradients and centrifugal forces due to streamline curvature
5) Tip leakage vortex difference over tip clearance		Tip clearance Pressure (for unshrouded blades)
6) Horseshoe vortex	Hub region and tip region	Roll-up and splitting of end-wall boundary layer before a thick leading edge
7) Scraping vortex	Blade ends	Scraping of part of the end-wall boundary layer by unshrouded blades (relative motion between blade and end-wall)
8) Corner vortex	Endwall / Suction-side corner	Roll-up of end-wall boundary layer fluid that impinges normal to the blade surface

Table 1.1 : Secondary flows in a turbomachine

As this table shows, all of the secondary flow effects are vortical fluid motions, except for the fluid migrations in the blade boundary layer and the blade wake, which are spanwise motions. In general, these secondary flows take place in a surface normal to the main flow direction. All of these motions have radial velocity components associated with them, and these will twist the S1-surfaces with respect to their hypothetical axisymmetric geometry, resulting in radial transfer of flow properties. Figure 1.2 gives a general picture of the different secondary flow effects in a turbomachinery blade row.

For more information on secondary flows in turbomachines, see for instance Horlock & Lakshminarayana (1973), Salvage (1974) and Sieverding (1985).

b) Nature of the mixing process

The secondary flows convect fluid particles with their associated mass, momentum and energy from one streamsurface to another, in a well-defined direction. Therefore, radial mixing by secondary flows is of a deterministic nature, i.e. the radial redistribution of flow properties between two streamsurfaces is completely determined by the magnitude of the radial component of the secondary flow velocity.

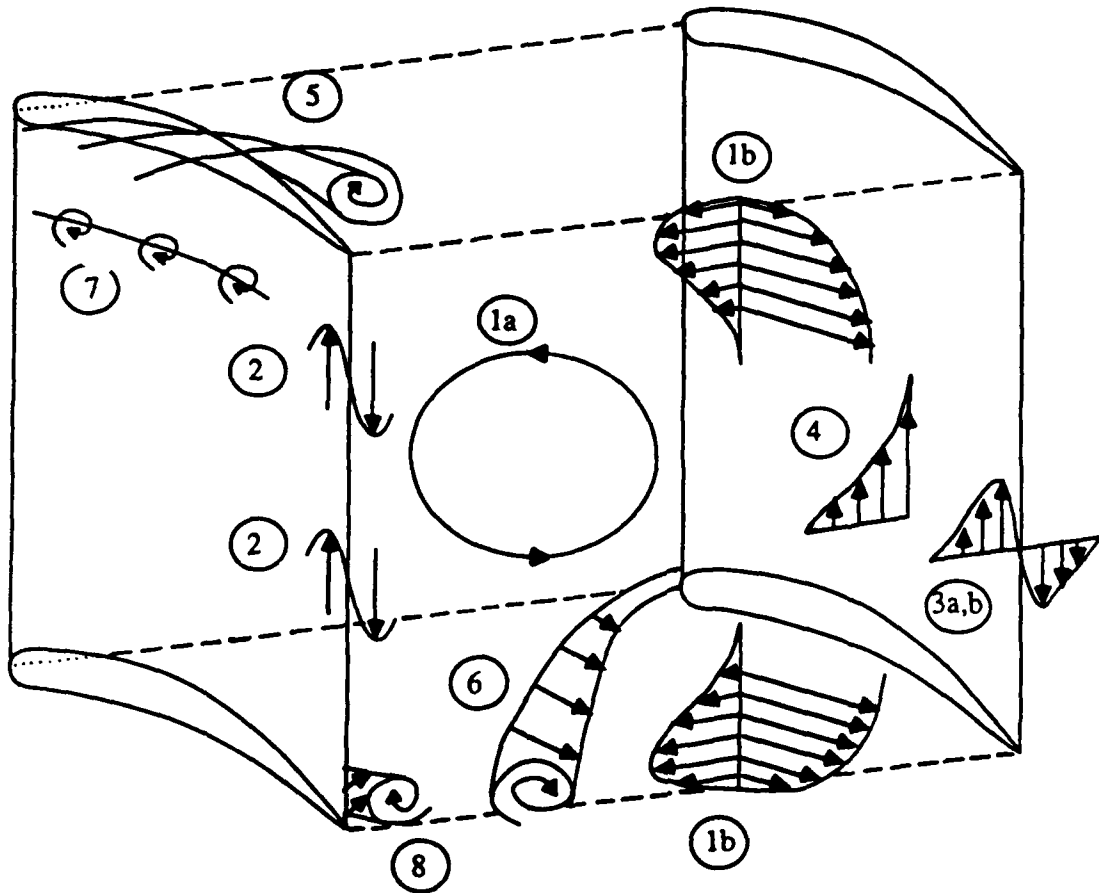


Figure 1.2 : Secondary flows in a turbomachinery blade row

1.2.2 TURBULENCE

a) Nature of the mixing process

In the case of radial mixing by turbulence, the mixing is caused by an exchange of momentum and energy between fluid particles, colliding due to the chaotic motion associated to turbulence, leading to a more uniform distribution of flow properties.

Therefore, radial mixing by turbulence is of a random nature, i.e. the radial redistribution of flow properties is essentially determined by the turbulence intensity, which is irrespective of direction.

This is analogous to the classical molecular diffusion through interacting molecules, but the transport caused by the large-scale chaotic motion of turbulence is some orders of magnitude greater than the transport caused by the small-scale chaotic molecular motion.

In conclusion, radial mixing by turbulence has the features of a diffusion process.

b) Non-isotropic turbulence

It is important to note that a turbomachinery flow can exhibit non-isotropic turbulence, i.e. the turbulence intensity can be dependent upon direction. In this case, radial mixing due to turbulence possesses a less random nature, since the radial redistribution between two streamsurfaces will be determined by the specific turbulence intensity in the radial direction and not by the general level of turbulence only. Therefore, radial mixing due to non-isotropic turbulence possesses some characteristics of a convection process, i.e. the existence of local preferential directions (cf. discussion by Gallimore & Cumpsty of the paper of Wisler, Bauer and Okiishi (1987)).

1.3 RADIAL MIXING IN THE FRAMEWORK OF A QUASI-3D METHOD BASED ON AN AVERAGING PROCEDURE

1.3.1 INTRODUCTION

The theoretical radial mixing model described in this report has been developed to fit in the framework of a Quasi-3D method for turbomachinery flow computations, based on a density-weighted pitch-averaging procedure, Hirsch & Warzée, (1976, 1979). The main purpose of the mixing method is therefore to compute the radial redistributions of flow properties for the averaged flow on the meridional S2-surface.

One of the basic features of the present theoretical model of radial mixing is its afterward application to the classical Quasi-3D turbomachinery flow computation. In other words, the radial redistributions are considered as corrections to the flow property distributions obtained by a classical Quasi-3D computation. This allows the procedure to be adapted more easily to existing Quasi-3D turbomachinery flow computation codes.

1.3.2 QUASI-3D TURBOMACHINERY FLOW COMPUTATION

The current approach is a variant of the original Wu method : it consists in splitting the turbomachinery flow into two families of interacting two-dimensional flows, using a density-weighted pitch-averaging procedure, Hirsch & Warzée (1976, 1979). The through-flow is the circumferentially averaged flow on a meridional plane (S2-plane), i.e. the axisymmetric component of the flow field. The blade-to-blade flows are considered on streamsurfaces of revolution (S1-surfaces), obtained by rotating streamlines in the meridional plane around the machine axis, and contain the circumferential distribution of the non-axisymmetric components of the flow field. Of course, both types of flow influence each other in an iterative way through the boundary conditions.

The method uses only one through-flow plane (since the through-flow is defined as being axisymmetric) and a small number of blade-to-blade surfaces of revolution. Hence, only non-axisymmetries due to flow effects on the non-interacting blade-to-blade surfaces

are taken into account, while non-axisymmetries arising from radial flow interactions between blade-to-blade surfaces are neglected. In other words, radial mixing effects are not considered.

1.3.3 TURBOMACHINERY STREAMSURFACES

a) Meridional coordinates

As axisymmetric geometry is a general feature of turbomachines, an orthogonal meridional coordinate system (m,n,u) is especially suited to represent turbomachinery geometry (Figure 1.3).

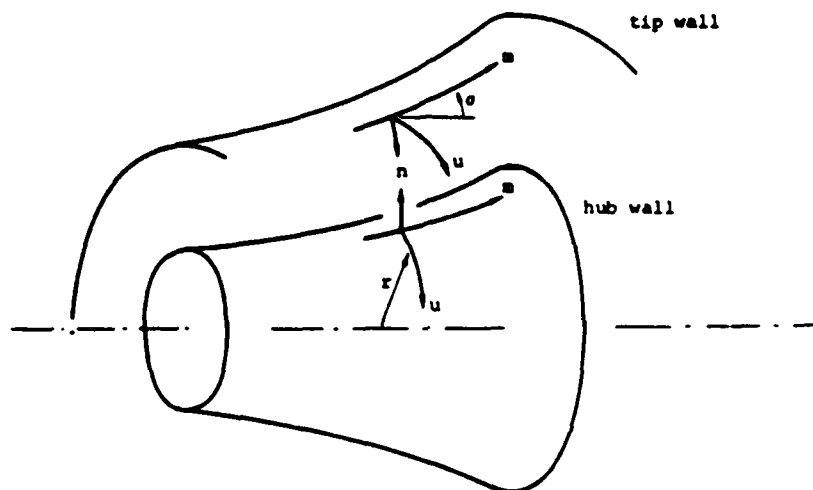


Figure 1.3 : Meridional coordinate system

In the context of a Quasi-3D method based on a pitch-averaging procedure, it is logical to define the streamlines of the averaged axisymmetric flow on the S2-plane as meridional coordinate lines. Consequently, using the curvilinear (m,n,u) -coordinates as intrinsic coordinates, the following three families of orthogonal surfaces can be distinguished :

- (i) Meridional through-flow planes (S2-surfaces) : (m,n) - hub-to-shroud surfaces
- (ii) Blade-to-blade streamsurfaces (S1-surfaces) : (m,u) -surfaces of revolution
- (iii) Transverse surfaces (S3-surfaces) : (n,u) -surfaces of revolution

This clearly shows that transverse S3-surfaces, orthogonal to the meridional direction, appear naturally as a third kind of computational surface for the present Quasi-3D computation method. Flow effects occurring on this surfaces will result in radial interactions between the concentric S1-surfaces, leading to non-axisymmetries. Hence, the radial mixing process may be assumed to originate on these S3-surfaces.

Therefore, the S3-surfaces are designated as surfaces of secondary flow, rather than the classical surfaces normal to the streamwise direction. This is perfectly possible, since the decomposition of a flow into primary and secondary flow components is a purely mathematical operation and no general definition of secondary flows exists.

b) Cylindrical coordinates

The present Quasi-3D computation code has been developed in a cylindrical coordinate system (z, r, θ) , with the z-axis directed along the machine axis. Hence, for ease of integration, the radial mixing theory is also formulated in cylindrical coordinates.

In cylindrical coordinates, the meridional S2-plane becomes an (r, z) -plane, but the cylindrical coordinates form no intrinsic coordinate system for the S1- and S3-surfaces. However, although the S3-surface appears naturally in a mathematical way, this surface is not suitable from the physical and computational point of view. Indeed, most of the experimental data on secondary flows is obtained in measurement planes perpendicular to the machine axis, while the computation stations for through-flow computations are very often defined as stations with constant axial coordinate. Therefore, in the present radial mixing theory the secondary flow field is defined on an (r, θ) -plane, perpendicular to the machine axis, whose intersection with the through-flow plane forms a through-flow computation station. The secondary flow field on this simplified S3-surface can be considered as the projection of the secondary flow field on the original curved S3-surface onto this plane.

1.3.4 DEFINITION OF SECONDARY FLOWS

As the previous sections have already indicated, the term 'secondary flow' in the present theory does not correspond to the classical secondary flow, associated to the development of streamwise vorticity. Rather, in the context of radial mixing, the secondary flow field is defined as a correction with respect to the Quasi-3D flow field and is assumed to be two-dimensional, i.e. confined to a radial-tangential S3-plane.

Thus, the total velocity \vec{W} can be decomposed as follows :

$$\vec{W} = \vec{W}_{Q3D} + \vec{W}_{S3} \quad (1.1)$$

where the Quasi-3D component \vec{W}_{Q3D} represents the velocity component from the through flow and blade-to-blade computations, while \vec{W}_{S3} represents by definition the two-dimensional deviation between the velocity of real flow field and the velocity of the computed Quasi-3D flow field.

The definition of the (r, θ) -plane as S3-streamsurface for the secondary flows implicitly contains the important assumption that the different secondary flow effects, listed in Table 1.1, do not give rise to axial flow components.

Thus, the proposed mixing method is inherently based on an approximative description of the complex turbomachinery flow pattern. Hence, the theoretical mixing model cannot be applied in full generality to an arbitrary turbomachinery flow, but is limited to turbomachinery flows that do not exhibit a strongly three-dimensional secondary flow behaviour. This is the case for axial-flow compressors and axial-flow turbines with moderate deflections. However, axial-flow turbines possessing large deflections show strongly three-dimensional secondary flow patterns and will in general have to be dealt with by fully three-dimensional methods.

1.4 REVIEW OF PREVIOUS WORK

In this paragraph, previous work relating to radial mixing phenomena in axial compressors is briefly reviewed. Different efforts to compute the effects of radial mixing on the distribution of flow quantities as well as attempts to determine the physical nature of the mixing process are covered.

1.4.1 THE CONVECTIVE MIXING MODEL OF ADKINS & SMITH

A convective mixing computation method was proposed by Adkins & Smith (1982), who were the first to recognize the importance of incorporating the effects of radial mixing into computational methods for multi-stage axial compressors. They put forward the concept that radial mixing is caused exclusively by secondary flows and model the mixing of any physical quantity P through the following diffusion equation :

$$\frac{\partial \bar{P}}{\partial z} = \epsilon \frac{\partial^2 \bar{P}}{\partial y^2} \quad (1.2)$$

where \bar{P} is a cross-passage averaged value, z is the streamwise direction, y is the spanwise direction and ϵ is the mixing coefficient.

The mixing coefficient is a function of streamwise and spanwise location and is at any streamwise location taken to be the sum of the contributions of all upstream blade rows. The local value of the mixing coefficient is essentially determined from the computed radial secondary velocities, but is empirically adjusted to take into account viscous dissipation and interaction with end-walls and successive blade rows.

The secondary flows are computed from Smith's inviscid secondary flow theory and include the effects of mainstream non-free vortex flow, end-wall boundary layers, tip clearances, blade end shrouding, and profile boundary layer and wake centrifugation.

The results from the mixing computation are impressive : stagnation temperature profiles obtained from a flow computation including mixing agree much better with experimental data than results from previous computations which neglected mixing.

1.4.2 THE DIFFUSIVE MIXING MODEL OF GALLIMORE & CUMPSTY

A diffusive mixing model was introduced by Gallimore & Cumpsty (1986a, 1986b), who concluded from ethylene tracer experiments that radial mixing is completely due to turbulence, while the influence of convective secondary flows on the mixing is negligible.

They compute the radial mixing effects by introducing transport terms of diffusive nature into an axisymmetric through-flow computation based on the streamline curvature method, the intensity of these terms being determined through semi-empirical turbulence-dependent coefficients. Since in a flow with radial mixing, the traditional assumptions of adiabatic and inviscid flow are no longer valid, the flow equations are modified by adding axial and tangential shear stress terms, due to radial transport of momentum, and radial heat transfer terms, due to radial transport of energy.

Gallimore and Cumpsty also present a simple formula to estimate the turbulent mixing coefficient on the basis of stage geometry, flow coefficient and loss coefficient.

The results from their mixing computations are as impressive as those from Adkins & Smith : stagnation temperature profiles obtained from flow computations including mixing

are in much better agreement with experimental profiles than profiles from computations neglecting mixing.

1.4.3 CONVECTIVE MIXING VERSUS DIFFUSIVE MIXING

The fact that the two discussed radial mixing models, based on totally different physical mechanisms, yielded very similar results aroused much interest and controversy. An attempt to obtain a better understanding of the radial mixing process in axial turbomachines was undertaken by Wisler et al. (1987) : the relative importance of secondary flows and turbulence as sources of mixing was investigated by conducting experiments using hot-wire anemometry and ethylene tracer gas techniques in a large low-speed compressor. The results indicated that both mechanisms of radial mixing are important : diffusive mixing due to turbulence is important everywhere, while the contribution of convective mixing due to secondary flows is mainly of importance in regions of low-momentum flow like boundary layers and wakes. Wisler et al. therefore propose the following physical picture of the mixing process : "In addition to being mixed by turbulent diffusion, the low-momentum fluid in the end-walls is convected radially by secondary flow. The passing rotor then chops, turns and transports this convected fluid and the wake fluid, spreading them circumferentially. The mixing process is then completed by turbulent diffusion. Similarly, low-momentum fluid is convected radially outward in the rotor suction-side wake and is chopped by the next stator."

This physical picture of the mixing process was challenged by Gallimore and Cumpsty, who argued that the experimental results, reported by Wisler et al. to indicate substantial convective mixing due to secondary flows, could also be interpreted as being due to the effects of non-isotropic turbulence (cf. § 1.2.2).

Recently, however, further evidence supporting the physical picture put forward by Wisler et al. has been provided by Leylek and Wisler (1990), who performed fully three-dimensional turbulent Navier-Stokes flow computations on the compressor configuration used in the experiments of Wisler, Bauer and Okiishi (1987). The numerical solutions agreed very well with experimental data and hence support the previous interpretations of experimental data by Wisler et al., because the simulations revealed that local regions with strong secondary flows do exist, even at design point conditions. At off-design conditions, secondary flows with radial velocity components up to 20% of the rotor pitch velocity were predicted, which indicates that at off-design conditions, convective mixing may become as important as the mixing due to turbulence.

It should be stressed that most of the computations and experiments to date have been performed on relatively low-speed multi-stage compressors, where diffusive mixing due to turbulence seems to be dominant. However, for transonic and supersonic compressors, the picture may be very different : while in subsonic compressors operating near peak efficiency, the boundary layers are relatively unseparated, suction surface boundary layers on transonic or supersonic compressor rotor blades frequently separate due to shock impingement, leading to large regions of separated flow and associated large secondary flow velocities, Wennerstrom (1990).

Recently, Kotidis (1989,1990) presented some interesting concepts related to radial fluid transport in transonic compressors. To explain the mass transport to the hub, he introduces the concept of radial transport due to radial variations in the strength of the von Kármán vortices shed from the blades. On the other hand, according to Kotidis, mass transport towards the tip can be attributed to radial secondary flows in regions of separation.

In conclusion, it seems that turbulent diffusion always is an important contributor to the mixing process, whereas convective mixing by secondary flows becomes of equal or

greater importance when the turbomachine operates at off-design conditions or at high Mach numbers.

1.4.4 THE CONVECTIVE-DIFFUSIVE MIXING MODEL DEVELOPED AT THE VUB DEPT OF FLUID MECHANICS

At the Department of Fluid Mechanics of the Vrije Universiteit Brussel, a radial mixing method was developed which can be considered as an amalgamation of the Adkins-Smith and Gallimore-Cumpsty approaches, De Ruyck & Hirsch (1987, 1988a, 1988b) and De Ruyck, Hirsch & Segaut (1989). Rather than attributing radial mixing to one specific mechanism, the method takes into account both secondary flows and turbulence as possible sources of radial mixing. In hindsight to the conclusions of the preceding paragraph, this seems to have been the right decision.

This report actually describes the present state of development of this radial mixing method.

The general principles of this method are as follows. The energy redistribution is computed from a convection-diffusion type transport equation, where the convective terms are related to secondary flows and the diffusive terms are linked to turbulence. The secondary flows are computed using a streamfunction approach coupled to integral methods for boundary layers and wakes, while the effects of turbulence are governed by a semi-empirical turbulence coefficient.

Qualitative computations on a plane compressor cascade and two single-stage axial compressors showed that radial mixing effects result in more uniform radial temperature distributions, De Ruyck, Hirsch & Segaut (1989). The qualitative picture of the computations agreed fairly well with that of computations with the other mixing methods. Turbulent diffusion was identified as the dominant mixing mechanism, but it should be noted that the three test cases operated in the low subsonic flow regime.

PART 2

COMPUTATION OF SECONDARY FLOW, TURBULENT DIFFUSION AND MIXING

CHAPTER 2

GENERAL PRINCIPLES

2.1 DECOMPOSITION OF THE FLOW FIELD

The total velocity \vec{W} is decomposed into two components : a Quasi-3D component \vec{W}_{Q3D} and a secondary flow component on the transverse S3-plane \vec{W}_{S3} :

$$\vec{W} = \vec{W}_{Q3D} + \vec{W}_{S3} \quad (2.1)$$

It is important to observe that the Quasi-3D component does not only contain the traditional contributions from the through-flow computation and the blade-to-blade computation, but also includes the 2D-effects of viscous layers (end-wall boundary layers, profile boundary layers and wakes) in these surfaces. In other words, the blockage effect of the viscous layers on the axial velocity profiles and the subsequent influence on the continuity equation is taken into account in the Quasi-3D approximation (cf. Figure 2.1).

By definition, the transverse secondary flow component \vec{W}_{S3} represents any deviation between the real flow and the Quasi-3D flow. Following the discussion above, this means that the secondary flow field essentially consists of the crossflow components of the viscous layers (circumferential velocity profile for the end-wall boundary layers, radial velocity profile for the profile boundary layers and wakes), i.e. the three-dimensional effects of the viscous layers, occurring in a direction normal to the computation surface considered.

Through the use of a density-weighted, geometrical pitch-average, each of these components can be further subdivided into an averaged, axisymmetric component and a 'fluctuation' component, representing the deviations from axisymmetry, Hirsch & Warzée (1979) :

$$\vec{W}_{Q3D} = \vec{\bar{W}}_{Q3D} + \vec{W}_{Q3D}'' \quad \vec{W}_{S3} = \vec{\bar{W}}_{S3} + \vec{W}_{S3}'' \quad (2.2)$$

with the geometrical pitch-average or 'passage average' defined by

$$\bar{A} = \frac{1}{\theta_s - \theta_p} \int_p^s A \, d\theta \quad \bar{A}' = 0 \quad (2.3)$$

(where the subscripts s and p refer to suction side and pressure side respectively, and the

superscript ' denotes the fluctuations with respect to the geometrical pitch-average), while the density-weighted pitch-average is defined by

$$\tilde{A} = \overline{\rho A} / \bar{\rho} \quad \overline{\rho A''} = 0 \quad (2.4)$$

(where the superscript '' denotes the fluctuations with respect to the density-weighted pitch-average).

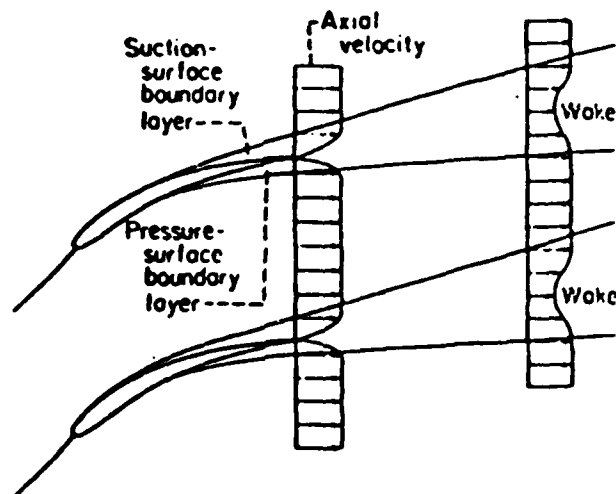
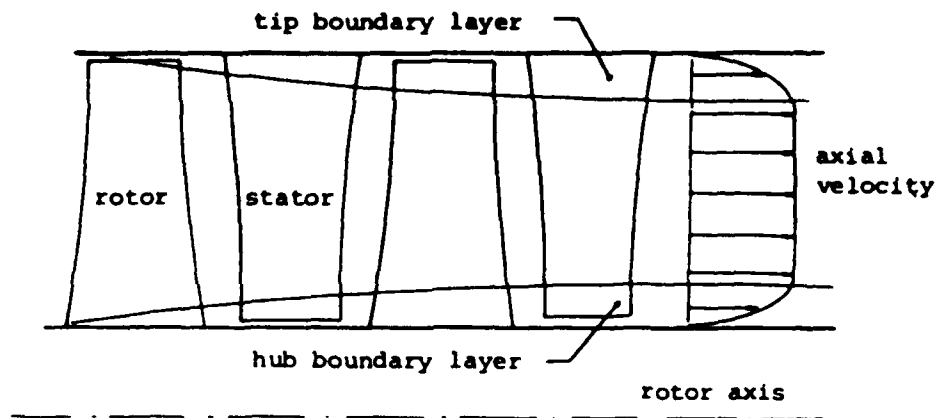


Figure 2.1 : Blockage of axial velocity profile by viscous layers

Through this approach, two types of non-axisymmetric contributions to the velocity field can be distinguished :

- a) Non-axisymmetries due to the flow deflection induced by the blades : \vec{W}_{Q3D}''
 The deflection of a flow by a blade row immediately implies the existence of a circumferential pressure gradient, i.e. a turbomachinery flow is intrinsically non-axisymmetric. These non-axisymmetric components are determined by the blade-to-blade computations on the S1-streamsurfaces and influence the through-flow computation of the axisymmetric flow components through interaction terms.
- b) Non-axisymmetries due to the secondary flows on the transverse S3-plane : \vec{W}_{S3}''
 These non-axisymmetries are hitherto not taken into account in the Quasi-3D computation. In this report, a method to compute explicitly those non-axisymmetric components and their influence on the axisymmetric through-flow computation is developed.

These results are coherent with previous remarks made from a physical point of view (cf § 1.3.2).

2.2 TURBOMACHINERY FLOW REGIONS

A turbomachinery flow is always highly turbulent and viscous, but for fluids with very small viscosity, Prandtl's boundary layer theory shows that viscous effects are only important in the vicinity of material walls. On this basis, the turbomachinery flow can be considered to be composed of four different flow regions :

- (i) Inviscid flow region ('core' region between viscous layers)
- (ii) End-wall boundary layers region (viscous region near hub/shroud wall)
- (iii) Profile boundary layers region (viscous region near blade)
- (iv) Wake region (viscous region, continuation of profile boundary layers)

Each of these regions is a potential source of flow components on the S3-surface, but the underlying physical mechanisms are different in each case (cf. Table 1.1, listing the various secondary flow effects in a turbomachine). In the subsequent chapters, the computation of the separate contributions for each region will be described.

2.3 FUNDAMENTAL EQUATIONS

2.3.1 STREAMFUNCTION Ψ

Assuming the turbomachinery flow compressible and steady relative to the blade row frame of reference, the continuity equation for this flow is

$$\vec{\nabla} \cdot (\rho \vec{W}) = 0 \quad (2.5)$$

Substitution of the decomposition (2.1), taking into account that continuity is already satisfied by the Quasi-3D flow field (including boundary layer axial blockage effects) leads to :

$$\vec{\nabla} \cdot (\rho \vec{W}_{S3}) = 0 \quad (2.6)$$

Since the flow on the S3-plane is by definition two-dimensional, a streamfunction $\psi(r, \theta)$ can be introduced to satisfy the continuity equation (2.6). In cylindrical coordinates, ψ is thus defined by :

$$W_{r,S3} = -\frac{1}{\rho} \frac{1}{r} \frac{\partial \psi}{\partial \theta} \quad (2.7a)$$

$$W_{\theta,S3} = \frac{1}{\rho} \frac{\partial \psi}{\partial r} \quad (2.7b)$$

This reduces the problem of determining a two-dimensional flow field to the determination of the distribution of a scalar function.

2.3.2 POISSON EQUATION

Taking into account that the streamfunction ψ is independent of z and substituting the definitions of equation (2.7), one can write in cylindrical coordinates :

$$\vec{\nabla} \cdot \left(\frac{1}{\rho} \vec{\nabla} \psi \right) = \frac{1}{r} \frac{\partial}{\partial r} (r W_{\theta,S3}) - \frac{1}{r} \frac{\partial}{\partial \theta} (W_{r,S3}) \quad (2.8)$$

The axial component of the relative vorticity due to the Quasi-3D flow field is given by

$$\zeta_{z,Q3D} = \left[\vec{\nabla} \times \vec{W}_{Q3D} \right]_z = \frac{1}{r} \frac{\partial}{\partial r} (r W_{\theta,Q3D}) - \frac{1}{r} \frac{\partial}{\partial \theta} (W_{r,Q3D}) \quad (2.9)$$

and is a priori known from the Quasi-3D computations. Substituting equation (2.9) into equation (2.8), taking into account decomposition (2.1), yields the following final equation :

$$\boxed{\vec{\nabla} \cdot \left(\frac{1}{\rho} \vec{\nabla} \psi \right) = \zeta_z - \zeta_{z,Q3D} = \zeta_{z,S3}} \quad (2.10)$$

where ζ_z represents the axial component of the relative vorticity of the total flow field :

$$\zeta_z = \left[\vec{\nabla} \times \vec{W} \right]_z \quad (2.11)$$

The quasi-harmonic Poisson-type equation (2.10) determines the distribution of the secondary streamfunction in the S3-plane from the knowledge of the axial vorticity components and is the basic equation to be solved.

2.4 GENERAL COMPUTATION STRATEGY

2.4.1 AXIAL VORTICITY CONTRIBUTIONS

For the computation of the secondary flow field, the following **superposition principle** is introduced :

The axial vorticity component $\zeta_{z,S3}$ can be decomposed as follows :

$$\zeta_{z,S3} = \zeta_{z,S3,inv} + \zeta_{z,S3,visc} \quad (2.12)$$

$\zeta_{z,S3,inv}$ is the axial vorticity component associated to the secondary flows induced by the inviscid 'core' flow region and is defined over the entire computational domain except the end-wall boundary layer regions, because the secondary-flow-inducing mechanism in these regions is identical to that in the inviscid central flow region : generation of transverse flow components due to radial gradients of streamwise velocity in the inlet velocity profile.

$\zeta_{z,S3,visc}$ is the axial vorticity component associated to the secondary flows induced by the viscous regions, and consists of separate contributions for each type of viscous region. Each contribution is defined in its corresponding region only, but the induced secondary flows are defined over the entire computational domain as a result of continuity.

All the axial vorticity components relevant to the secondary flow on a given S3-plane are superposed and this yields the axial vorticity $\zeta_{z,S3}$, the unknown right-hand side of the basic Poisson-equation, from which the secondary flow field can be reconstructed.

This leads to the following sequence of computations :

- (i) Through-flow computation or full Quasi-3D computation
- (ii) Computation of end-wall boundary layers and the corresponding pitch-averaged axial vorticity contribution $\bar{\zeta}_{z,ewbl}$
- (iii) Computation of the pitch-averaged vorticity contribution $\bar{\zeta}_{z,inv}$ of the inviscid flow region
- (iv) Computation of the secondary flow field induced by the superposition of vorticity contributions (ii) and (iii), through the solution of the basic equation (2.10)
- (v) Superposition of the secondary flow field on the Quasi-3D flow field
- (vi) Computation of the profile boundary layers or the wake and the associated axial vorticity contribution $\zeta_{z,pbl}$ or $\zeta_{z,wake}$, depending on whether the S3-plane is located inside a blade row or between two successive blade rows
- (vii) Computation of the secondary flow field induced by the vorticity contribution (vi) through the solution of the basic equation (2.10)

- (viii) Superposition of the secondary flow field on the flow field obtained in (v)
- (ix) Computation of the radial mixing effects, including the effects of turbulent diffusion, through a stationary transport equation

2.4.2 COMPUTATIONAL DOMAIN

The computational domain on which the basic equation (2.10) has to be solved is delimited by the intersection of the given S3-plane with the hub and shroud end-walls and the surfaces of two adjacent blades or their imaginary extensions into the wake region (periodicity of turbomachinery flow), see Figure 2.2. For numerical computations, a structured radial-tangential mesh allowing non-uniform spacings (i.e. clustering) is generated (cf. Chapter 9).

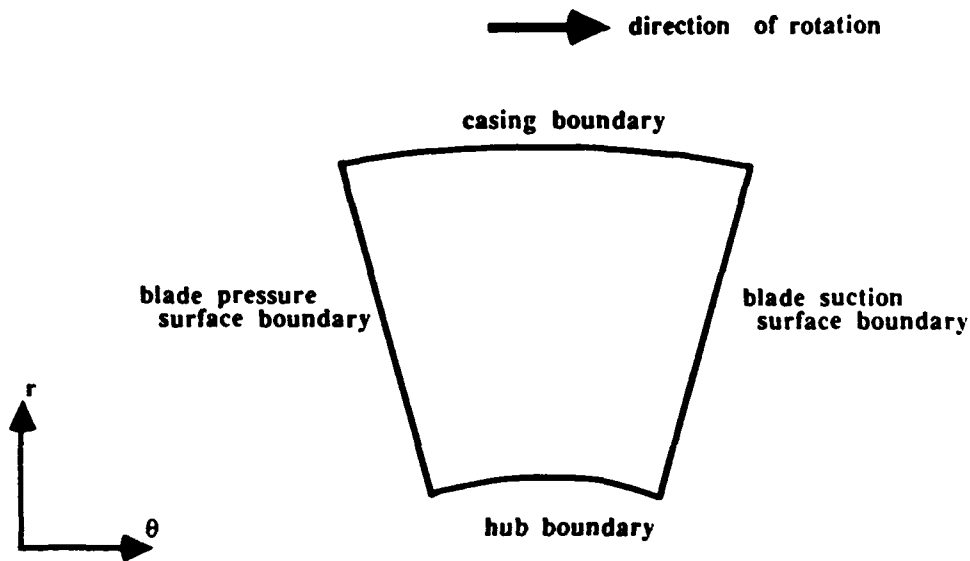


Figure 2.2 : Computational domain on the transversal S3-plane

The boundary conditions for the Poisson equation (2.10) express that the boundaries of the domain are streamlines for the secondary flow :

$$\psi = 0 \quad \text{on the boundaries of the computational domain} \quad (2.13)$$

CHAPTER 3

INVISCID FLOW REGION

3.1 INTRODUCTION

The inviscid flow region contributes to the secondary flow field through the well-known classical secondary flow mechanism : deflection (through the presence of material walls) of a sheared flow generates flows in a surface perpendicular to the main flow direction, the inviscid passage vortex (contribution 1a of Table 1.1).

The trailing filament vortices in the blade wakes, due to vortex stretching (contribution 2 of Table 1.1), are also included in this region because they result from an inviscid mechanism.

3.2 GOVERNING EQUATION

The governing equation of motion for the inviscid flow region is the Helmholtz vorticity equation, written relative to the blade row frame of reference (absolute frame of reference for a stator, steadily rotating frame of reference for a rotor) :

$$\begin{aligned} \frac{\partial \vec{\zeta}}{\partial t} + (\vec{w} \cdot \vec{\nabla}) \vec{\zeta} = & \left[(\vec{\zeta} \cdot \vec{\nabla}) \vec{w} - \vec{\zeta} (\vec{\nabla} \cdot \vec{w}) \right] + \vec{\nabla}_p \times \vec{\nabla} \left(\frac{1}{\rho} \right) + \vec{\nabla} \times \vec{f}_e \\ & + 2 \left[(\vec{\Omega} \cdot \vec{\nabla}) \vec{w} - \vec{\Omega} (\vec{\nabla} \cdot \vec{w}) \right] \end{aligned} \quad (3.1)$$

with

$$\vec{\zeta} = \vec{\nabla} \times \vec{w} \quad \text{relative vorticity} \quad (3.2a)$$

$$\vec{\Omega} = \Omega \cdot \vec{1}_z \quad \text{rotation vector} \quad (3.2b)$$

If the following simplifying assumptions are made :

- volume forces are conservative or may be neglected
- the fluid is a perfect gas with polytropic behaviour

and the tensorial product \otimes is introduced through the relation

$$\vec{\nabla} \cdot (\vec{a} \otimes \vec{b}) = (\vec{a} \cdot \vec{\nabla}) \vec{b} + \vec{b} (\vec{\nabla} \cdot \vec{a}) \quad (3.3)$$

then the Helmholtz equation can be transformed, using the continuity equation, to the following condensed conservative form :

$$\frac{\partial [\vec{\zeta}_{\text{abs}}]}{\partial t} + \vec{\nabla} \cdot [\vec{W} \otimes \vec{\zeta}_{\text{abs}} - \vec{\zeta}_{\text{abs}} \otimes \vec{W}] = 0 \quad (3.4)$$

Note that the vorticity $\vec{\zeta}_{\text{abs}} = \vec{\zeta} + 2\vec{\Omega}$ appearing in the equation is the absolute vorticity of the total flow (Quasi-3D + S3). Furthermore, although the equation takes compressibility effects into account, the density does not appear in the equation !

Since the method is developed in the framework of a Quasi-3D method based on a pitch-averaging procedure, it is assumed that the inviscid axial vorticity contribution $\zeta_{z,S3,\text{inv}}$ can be adequately approximated by its passage-averaged value $\bar{\zeta}_{z,S3,\text{inv}}$. Indeed, in general only spanwise profiles of the passage-averaged Quasi-3D properties are available, and in fact, the passage-averaged axial vorticity represents the 'trace' of the unknown circumferential non-axisymmetric velocity distribution. It is precisely from this trace that the velocity field on the S3-plane will be reconstructed.

Therefore, the axial projection of equation (3.4) is passage-averaged, which yields :

$$\begin{aligned} \bar{W}_m \frac{\partial}{\partial m} \bar{\zeta}_{\text{abs},z} &= \bar{\zeta}_{\text{abs},r} \frac{1}{b} \frac{\partial(b\bar{W}_z)}{\partial r} - \bar{\zeta}_{\text{abs},z} \frac{1}{br} \frac{\partial}{\partial r} (rb\bar{W}_r) + \frac{1}{2\pi b/N} [(\bar{\zeta}_{\text{abs}} \cdot \vec{n}) W_z]_p^s \\ &+ \frac{1}{br} \frac{\partial}{\partial r} [rb(\bar{W}_z' \bar{\zeta}_{\text{abs},r}' - \bar{W}_r' \bar{\zeta}_{\text{abs},z}')] + \frac{1}{2\pi b/N} [(\bar{\zeta}'_{\text{abs}} \cdot \vec{n}) W_z']_p^s \end{aligned} \quad (3.5)$$

where $\bar{\zeta}_{\text{abs},z}$ is the passage-averaged axial component of the absolute vorticity of the total flow (Quasi-3D + S3) and the velocities are the total velocities.

The index m refers to the meridional direction in the (r,z) -plane, where the m coordinate lines are defined by the streamlines of the axisymmetric through-flow on the (r,z) -plane, and the following formula is used (cf. Appendix A) :

$$\bar{W}_m \frac{\partial}{\partial m} = \bar{W}_r \frac{\partial}{\partial r} + \bar{W}_z \frac{\partial}{\partial z} \quad (3.6)$$

Finally, b denotes the tangential blockage factor defined by $\theta_s - \theta_p = 2\pi b/N$, where the left-hand side represents the angular distance between pressure and suction side of the passage and N denotes the number of blades.

The vector normal to the blade surface S , \vec{n} , is given by

$$\vec{n} = \vec{\nabla} S = \left(-\frac{1}{r} \tan \eta\right) \cdot \vec{1}_r + \left(\frac{1}{r}\right) \cdot \vec{1}_\theta + \left(-\frac{1}{r} \tan \beta'\right) \cdot \vec{1}_z \quad (3.7)$$

with the blade surface angles defined through

$$\tan \eta = r \frac{\partial \theta^*}{\partial r} \quad \text{lean angle} \quad \tan \beta' = r \frac{\partial \theta^*}{\partial z} \quad \text{blade angle} \quad (3.8)$$

where θ^* represents the angular coordinate of the blade surface.

Simplifying equation (3.5) by neglecting the fluctuation terms and assuming constant blockage which is equivalent to assuming identical blade angles at pressure and suction side (this amounts to an error of second order, cf. Appendix B), and substituting relation (3.6) yields :

$$\boxed{\begin{aligned} \bar{W}_z \frac{\partial}{\partial z} \bar{\zeta}_{\text{abs},z} &= \bar{\zeta}_{\text{abs},r} \frac{\partial \bar{W}_z}{\partial r} - \bar{\zeta}_{\text{abs},z} \frac{1}{r} \frac{\partial}{\partial r} (r \bar{W}_r) - \bar{W}_r \frac{\partial}{\partial r} \bar{\zeta}_{\text{abs},z} \\ &+ \frac{1}{2\pi b/N} (\bar{\zeta}_{\text{abs}} \cdot \vec{n}) [W_z]_p^s \end{aligned}} \quad (3.9)$$

This is the basic equation to be solved, since it describes the evolution in the axial direction of the passage-averaged axial vorticity $\bar{\zeta}_{\text{abs},z}$, associated to the inviscid flow region on the S3-plane.

3.3 SUPPLEMENTARY EQUATIONS

3.3.1 INTRODUCTION

The right-hand side of the basic equation (3.9) still contains unknowns, i.e. the passage-averaged radial and tangential projections of the absolute vorticity of the total flow, $\bar{\zeta}_{\text{abs},r}$ and $\bar{\zeta}_{\text{abs},\theta}$, and the velocity jump $[W_z]_p^s$. Therefore, supplementary equations are necessary, relating these unknown quantities to quantities of the Quasi-3D flow field which may be directly computed.

3.3.2 TANGENTIAL VORTICITY

The tangential vorticity component $\bar{\zeta}_{\text{abs},\theta}$ is computed directly from the Quasi-3D velocity components and the blade geometry as follows.

Starting from the definition :

$$\bar{\zeta}_{\text{abs},\theta} = \bar{\zeta}_\theta = \left[\vec{\nabla} \times \vec{W} \right]_\theta = \frac{\partial \bar{W}_r}{\partial z} - \frac{\partial \bar{W}_z}{\partial r} \quad (3.10)$$

and assuming constant blockage (to be consistent with the basic equation), yields the following equation (see Appendix C for a detailed derivation) :

$$\begin{aligned}\bar{\zeta}_{abs,\theta} &= \frac{\partial \bar{W}_{r,Q3D}}{\partial z} - \frac{\partial \bar{W}_{z,Q3D}}{\partial r} \\ &\quad - \frac{1}{bs} \left\{ \tan\beta' [W_{r,S3}]_p^s + (\tan\beta' \tan\sigma - \tan\eta) [W_{z,Q3D}]_p^s \right\}\end{aligned}\quad (3.11)$$

where s denotes the pitch, β' is the blade flow angle, η is the blade lean angle and σ is the radial flow angle of the axisymmetric Quasi-3D streamsurface, defined through :

$$\tan\sigma = \frac{\bar{W}_{r,Q3D}}{\bar{W}_{z,Q3D}} \quad (3.12)$$

The two 'velocity jumps' $[W_{r,S3}]_p^s$ and $[W_{z,Q3D}]_p^s$ will be discussed in subsequent paragraphs.

3.3.3 RADIAL VORTICITY

The radial vorticity component $\bar{\zeta}_{abs,r}$ is also computed directly from the Quasi-3D velocity components and the blade geometry.

Starting from the definition :

$$\bar{\zeta}_{abs,r} = \bar{\zeta}_r = \left[\vec{\nabla} \times \vec{W} \right]_r = \frac{1}{r} \frac{\partial W_z}{\partial \theta} - \frac{\partial W_\theta}{\partial z} \quad (3.13)$$

again assuming constant blockage to be consistent with the basic equation, and using the condition that the velocity vector is tangent to the blade surface (cf. Appendix C), yields the following equation (see Appendix C for a detailed derivation) :

$$\begin{aligned}\bar{\zeta}_{abs,r} &= -\frac{\partial \bar{W}_\theta}{\partial z} + \frac{1}{bs} \left\{ (1 + \tan^2\beta' + \tan\beta' \tan\eta \tan\sigma) [W_{z,Q3D}]_p^s \right\} \\ &\quad + \frac{1}{bs} \left\{ (\tan\beta' \tan\eta) [W_{r,S3}]_p^s \right\}\end{aligned}\quad (3.14)$$

The two 'velocity jumps' $[W_{r,S3}]_p^s$ and $[W_{z,Q3D}]_p^s$ also appear in this equation, but will be discussed in subsequent paragraphs.

3.3.4 AXIAL VELOCITY JUMP

The basic equation as well as the two supplementary equations for the radial and tangential vorticity components contain the unknown tangential jump in axial velocity $[W_z]_p^s$. Since it is assumed that the secondary flow effects do not give rise to axial velocity components, this jump is equal to the tangential jump in axial velocity for the Quasi-3D flow field $[W_{z,Q3D}]_p^s$.

If a full Quasi-3D computation is performed, $[W_{z,Q3D}]_p^s$ can be obtained directly from the blade-to-blade computations.

If only a through-flow computation is performed, $[W_{z,Q3D}]_p^s$ has to be expressed in function of passage-averaged quantities. This is obtained by expressing that the passage-averaged vorticity normal to the blade-to-blade surfaces is zero, i.e. the blade-to-blade flows are assumed to be potential flows, which is consistent with the present Quasi-3D framework. This condition yields the following equation :

$$[W_z]_p^s = \left\{ \frac{\sin\sigma}{r} \frac{\partial}{\partial r} (r \bar{W}_{\theta,Q3D}) + \cos\sigma \frac{\partial \bar{W}_{\theta,Q3D}}{\partial z} \right\} / \frac{1}{bs} \{ \cos\sigma (1+\tan^2\beta') + \sin\sigma ((1+\tan^2\eta) \tan\sigma + 2 \tan\sigma \tan\beta') \} \quad (3.15)$$

3.3.5 RADIAL VELOCITY JUMP

The only remaining unknown parameter is the tangential jump in radial velocity for the S3 flow component, $[W_{r,S3}]_p^s$. In order to compute this unknown, a supplementary equation is introduced : the continuity equation for the secondary flow components, averaged over a half pitch.

In addition, the following secondary flow velocity profiles are prescribed : a linear velocity profile for the radial secondary flows and a parabolic velocity profile for the tangential secondary flows :

$$W_{r,S3} = \frac{1}{2} [W_{r,S3}]_p^s x \quad (3.16a)$$

$$W_{\theta,S3} = \frac{3}{2} \bar{W}_{\theta,S3} (1-x^2) \quad (3.16b)$$

where x is a dimensionless tangential distance ($x=-1$ at pressure side, $x=0$ at mid-pitch, $x=1$ at suction side).

The definition of a linearly varying radial secondary flow profile has the advantage that the passage-averaged radial secondary flow component $\bar{W}_{r,S3}$ is zero (cf. Appendix C, § C.2).

Combining the averaged secondary flow continuity equation with the prescribed velocity profiles, neglecting density variations in the S3-plane, yields the following ordinary second order differential equation :

$$\frac{b}{12r} \frac{\partial}{\partial r} \left\{ s \frac{\partial}{\partial r} (r [W_{r,S3}]_p^s) \right\} + \frac{1}{3r} \frac{\partial}{\partial r} (\tan\eta (r [W_{r,S3}]_p^s)) - \frac{1}{bsr} (r [W_{r,S3}]_p^s) = \bar{\zeta}_{abs,z} - 2\Omega - \frac{1}{r} \frac{\partial}{\partial r} (r \bar{W}_{\theta,Q3D}) + \frac{1}{bs} \{ (1+\tan^2\eta) \tan\sigma + \tan\sigma \tan\beta' \} [W_{z,Q3D}]_p^s \quad (3.17)$$

At the end-wall boundaries, the axisymmetric geometry of the hub and casing end-walls is imposed upon the streamsurfaces. Hence, the end-wall streamsurfaces will not be distorted with respect to the axisymmetric geometry of a surface of revolution. In other words, at the end-walls the non-axisymmetric S3-component of the radial velocity is zero ! This yields the following end-wall boundary conditions for the unknown radial velocity jump :

$$[W_{r,S3}]_p^s = 0 \quad \text{at hub and casing end-walls} \quad (3.18)$$

The solution of equation (3.17), taking into account the boundary conditions (3.18), yields the jump in radial secondary flow velocity across the blade passage $[W_{r,S3}]_p^s$.

Thus, the jump of the total radial flow component across the blade passage $[W_r]_p^s = [W_{r,Q3D}]_p^s + [W_{r,S3}]_p^s$ may be computed, since $[W_{r,Q3D}]_p^s$ is known from the Quasi-3D computation.

3.4 NUMERICAL SOLUTION

The basic equation to be solved is the passage-averaged axial component of the Helmholtz vorticity equation, equation (3.9), whereby the following parameters are considered to be known :

- 1) Blade and blade row geometrical data
- 2) Passage-averaged velocities : $\bar{W}_{r,Q3D}$, $\bar{W}_{z,Q3D}$
- 3) Passage-averaged vorticity components $\bar{\zeta}_{abs,r}$ and $\bar{\zeta}_{abs,\theta}$, from equations (3.11) and (3.14)
- 4) Velocity jump $[W_z]_p^s$: either directly known from blade-to-blade computations or from equation (3.15).
- 5) The unknown velocity jump $[W_r]_p^s$ is computed from the supplementary equation (3.17)

The basic equation can now be written in the general form :

$$\bar{W}_z \frac{\partial}{\partial z} \bar{\zeta}_{abs,z} = f(z, \bar{\zeta}_{abs,z}) \quad (3.19)$$

and will be solved numerically using a fifth-order Runge-Kutta method.

The equation is thereby integrated in the axial direction from the blade row inlet to the blade row outlet in several intermediate steps, and at each step the right-hand side of equation (3.9) is recomputed. Each time, this recomputation involves solving the supplementary equations (3.11), (3.14), (3.15), (3.17). The values of the Quasi-3D quantities between through-flow computation stations are thereby estimated using linear interpolation.

This finally yields $\bar{\zeta}_{abs,z}$, the passage-averaged axial component of the absolute vorticity of the total flow in the inviscid region on the S3-plane. The passage-averaged axial

vorticity component $\bar{\zeta}_{z,S3,inv}$, associated to the secondary flows induced by the inviscid flow region, can be directly obtained from the total axial vorticity through :

$$\boxed{\bar{\zeta}_{z,S3,inv} = \bar{\zeta}_{abs,z} - \bar{\zeta}_{abs,z,Q3D}} \quad (3.20)$$

where $\bar{\zeta}_{abs,z,Q3D}$ represents the passage-averaged axial component of the absolute vorticity, associated to the Quasi-3D flow field (cf. equations (2.10) and (2.12)).

It is very important to note that the inviscid vorticity contribution $\bar{\zeta}_{z,S3,inv}$ is defined over the entire computational domain including the viscous regions except the end-wall boundary layer regions. This is necessary because the vorticity contributions of the blade boundary layers and the blade wakes are caused by physical effects which are not accounted for in the inviscid secondary flow computation. In contrast, the secondary flow in the end-wall boundary layer regions arises from the same physical effect as the inviscid secondary flow : the deflection of a velocity profile possessing radial gradients in streamwise velocity. These gradients may be imposed on the inviscid flow profile through different inviscid mechanisms, whereas in the end-wall boundary layers they are caused by the frictional effects between the flow and the end-walls, due to viscosity. However, the resulting secondary flow mechanism is the same. Therefore, the vorticity contributions of these regions may not over

CHAPTER 4

END-WALL BOUNDARY LAYERS REGION

4.1 INTRODUCTION

In the end-wall boundary layers at the hub and the casing, crossflows are generated as a consequence of the higher curvature of streamlines inside the EWBL, necessary to maintain equilibrium with the pressure gradient between pressure and suction side of the blade passage as the mainflow velocity decreases from its freestream value at the boundary layer edge to zero at the wall. These crossflows then generate radial flows through the presence of the blade walls (contribution 1b of Table 1.1).

Also included in this region is the influence from the tip clearances, causing leakage flows from the pressure side to the suction side of the blade (contribution 5 of Table 1.1).

However, secondary flow phenomena like the horseshoe vortex, the scraping vortex and the corner vortex (contributions 6, 7 and 8 of Table 1.1) are not considered : the horseshoe vortex is only important in the case of turbines (thick leading edges), for which the present theory has limited applications, while the corner vortex is a very local phenomenon that is difficult to discern.

The overall result is thus a two-dimensional flow pattern on the S3-plane, which has not been taken into account in the Quasi-3D computation, although the blockage effect of the EWBLs on the axial velocity profile has been introduced in the Quasi-3D computation.

4.2 THEORETICAL EQUATIONS

The end-wall boundary layers (EWBL) are predicted by a procedure, developed to include the effects of the presence of EWBLs on axial turbomachinery performance into a Quasi-3D computation code for turbomachinery flows, De Ruyck (1982) and De Ruyck & Hirsch (1981,1983). The procedure is based on an axisymmetric three-dimensional integral method - with the axisymmetry obtained through pitch-averaging - coupled to prescribed velocity profiles adapted to turbomachinery flows.

Although the Quasi-3D method and the radial mixing theory are developed in cylindrical coordinates, the end-wall boundary layer theory has been developed in meridional coordinates to obtain an easier treatment of the curved geometry of the end-walls at hub and casing. However, since both coordinate systems have the circumferential direction as a common coordinate, the only difference between them lies in the coordinate system on the S2 through-flow plane : in cylindrical coordinates this is a cartesian system (r,z), while in meridional coordinates this system is a curvilinear system (m,n). For further details on the relation between the cylindrical and meridional coordinate systems, see Appendix A.

4.2.1 FUNDAMENTAL EQUATIONS

The fundamental equations that are solved are the meridional and tangential projections of the integral form of the passage-averaged momentum equation and the integral form of the passage-averaged continuity equation or entrainment equation. The term 'integral' refers to an integration in the normal direction over the physical boundary layer thickness, removing all local details about the boundary layer flow.

If r , the machine radius, is large with respect to δ , the physical boundary layer thickness, the integral momentum equations can be written in the absolute meridional coordinate system as follows.

The meridional integral momentum equation is of the form

$$\frac{d}{dm} \rho r C_m^2 \theta_{mm} + \rho r C_m \delta_m^* \frac{dC_m}{dm} - \rho C_m^2 \sin \sigma (\delta_u^* \tan \alpha + \theta_{uu}) = r \tau_m + r F_m \quad (4.1)$$

while the tangential integral momentum equation is of the form

$$\frac{d}{dm} \rho r C_m^2 \theta_{um} + \rho r C_m \delta_m^* \frac{dC_u}{dm} + \rho C_m^2 \sin \sigma (\delta_m^* \tan \alpha + \theta_{um}) = r \tau_u + r F_u \quad (4.2)$$

Both equations have been simplified by dropping terms that are negligible with respect to the remaining terms. Remark the use of the absolute velocity \vec{C} , instead of the relative velocity \vec{W} . In addition, all variables in these equations are expressed at the end-wall.

δ is the physical boundary layer thickness, δ_i^* the displacement thickness in the i -direction and θ_{ij} the momentum thickness in the i -direction weighted by the j -direction.

τ_m and τ_u are the meridional and tangential components of the wall shear stress, while F_m and F_u are the meridional and tangential defect force components.

For a detailed derivation of these equations, the reader is referred to previous reports by De Ruyck & Hirsch (1987, 1988a).

The integral continuity equation or entrainment equation, written in absolute meridional coordinates, reads :

$$\frac{1}{r \rho C_m} \frac{d}{dm} \{ r \rho C_m (\delta - \delta_m^*) \} = \frac{E}{\cos \alpha} \quad (4.3)$$

E is the so-called 'entrainment rate', while α is the absolute flow angle (between the direction of the streamline s on a streamsurface of revolution and the meridional direction m).

For a detailed derivation of the equation above, the reader is again referred to De Ruyck & Hirsch (1987, 1988a).

In the three equations above, the velocity components are obtained from the Quasi-3D computation, but the index Q3D has been omitted for ease of notation. The indexes m and u refer to the local meridional and tangential directions respectively.

4.2.2 SUPPLEMENTARY EQUATIONS

a) Entrainment rate

The entrainment rate E is given as an empirical function of Head's shape factor H_k^* through :

$$E = 0.0306 / (H_k^* - 3.)^{0.653} \quad (4.4)$$

H_k^* is defined as :

$$H_k^* = \frac{\delta - \delta_{mk}^*}{\theta_{mmk}} \quad (4.5)$$

where the index k refers to a 'kinematic' definition, i.e. density variations are not taken into account.

b) Skin friction components

The mainstream skin friction is estimated by means of a non-dimensional skin friction coefficient, generally denoted as C_f and defined through

$$\tau_s = C_f \rho \frac{\widehat{W}_s^2}{2} \quad (4.6)$$

where s indicates the streamline direction (projection of Quasi-3D streamline on an S1 surface of revolution) and the overhead carat (^) denotes the inviscid 'free-stream' velocity at the boundary layer edge.

The skin friction coefficient C_f is computed from the empirical Ludwig-Tillmann relation for turbulent boundary layers, which expresses C_f as a function of Reynolds number and shape factor :

$$C_f = 0.246 Re_{\theta_m}^{-0.268} \exp(-1.56 H) \quad (4.7)$$

with the Reynolds number defined as

$$Re_{\theta_m} = \frac{\widehat{W}_s \theta_{ss}}{\nu} \quad (4.8)$$

The streamwise momentum thickness θ_{ss} can be computed from the momentum thicknesses associated to the meridional coordinate system, through the following relation :

$$\theta_{ss} = \{ \theta_{mm} + (\theta_{um} + \theta_{mu}) \tan \alpha + \theta_{uu} \tan^2 \alpha \} \cos^4 \alpha \quad (4.9)$$

The skin friction in the transversal direction (the direction orthogonal to the streamline direction on an S1 streamsurface of revolution), τ_t , can be directly obtained from the knowledge of the mainstream skin friction τ_s and the wall skewing angle ϵ_w :

$$\tau_t = \tau_s \tan \epsilon_w \quad (4.10)$$

The wall skewing angle ϵ_w itself is defined as the limiting value at the wall of the angle between the streamwise and transversal velocity components :

$$\tan \epsilon_w = \lim_{n \rightarrow 0} \tan \epsilon = \lim_{n \rightarrow 0} \frac{W_t}{W_s} = \frac{\tau_t}{\tau_s} \quad (4.11)$$

where n denotes the normal direction to the end-wall.

The skin friction components in the meridional coordinate system, τ_m and τ_u , can easily be obtained from the skin friction components in the streamline coordinate system through the following equations :

$$\tau_m = \tau_s \cos \alpha_w - \tau_t \sin \alpha_w \quad (4.12a)$$

$$\tau_u = \tau_s \sin \alpha_w + \tau_t \cos \alpha_w \quad (4.12b)$$

c) Defect forces

The defect forces, which represent the changes of blade loading inside the end-wall boundary layer, are estimated through empirical correlations, i.e. a transversal blade lift defect force correlation, including the effects of tip clearance on the blade lift, and a streamwise blade drag defect force correlation.

For a detailed account of these defect force correlations, the reader is referred to De Ruyck (1982).

4.2.3 VELOCITY PROFILE MODELS

Closure of the system of equations for the end-wall boundary layers is obtained by the introduction of passage-averaged velocity profile models, adapted to turbomachinery flows.

For the Quasi-3D computation, the meridional velocity distribution inside the EWBL and the corresponding circumferential velocity distribution are given by :

$$\frac{\bar{W}_{m,Q3D,ewbl}}{\hat{W}_{m,Q3D}} = 1 - b \left\{ 1 - \frac{y}{\delta} \right\}^n \quad (4.13a)$$

$$\bar{W}_{\theta,Q3D,ewbl} = \bar{W}_{m,Q3D,ewbl} \tan \beta \quad (4.13b)$$

where y/δ is the non-dimensional normal distance from the wall and β is the relative flow angle of the Quasi-3D flow. The velocity with an overhead carat (\wedge) denotes the 'reference' freestream velocity at the boundary layer edge. Both velocity profiles are clearly determined by two model parameters : the velocity defect parameter b and the power law exponent n .

The circumferential or tangential crossflow velocity profile, associated with the 3D-effects of the EWBL and inducing flows on the S3-surface, is defined as the non-collateral part of the boundary layer flow in the blade frame of reference (cf. Figure 4.1) :

$$\overline{W}_{\theta,S3,ewbl} = \overline{W}_{\theta,ewbl}|_{blade} - \overline{W}_{m,Q3D,ewbl} \tan\beta|_{blade} \quad (4.14)$$

where the subscript 'blade' denotes that the corresponding quantities are defined in the blade frame of reference.

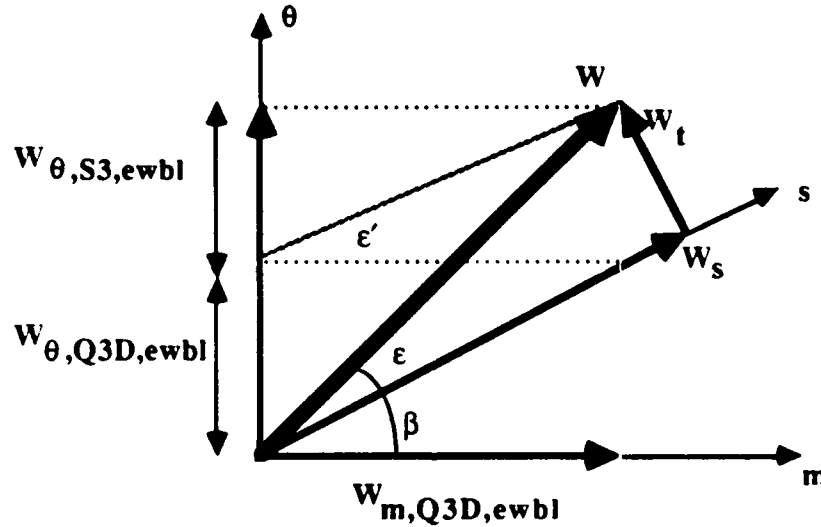


Figure 4.1 : Velocity components in the end-wall boundary layer

The non-collateral part of the boundary layer flow in the wall frame of reference is defined as follows :

$$\frac{\overline{W}_{\theta,S3,ewbl}|_{wall}}{\widehat{W}_{m,Q3D}} = \frac{\overline{W}_{\theta,ewbl}|_{wall} - \overline{W}_{m,Q3D,ewbl} \tan\beta|_{wall}}{\widehat{W}_{m,Q3D}} \quad (4.15)$$

and is described by the following velocity profile model :

$$\frac{\overline{W}_{\theta,S3,ewbl}|_{wall}}{\widehat{W}_{m,Q3D}} = (1-b) \tan \epsilon'_w \left(1 - \frac{y}{\delta}\right)^n \quad (4.16)$$

where the parameters b and n are identical with those of the meridional velocity profile model (4.13a) and the additional parameter ϵ'_w is defined through the relation :

$$\tan \epsilon'_w = \tan (\epsilon_w + \beta) - \tan \beta \quad (4.17)$$

where β denotes the flow angle of the Quasi-3D flow in the wall frame of reference.

The velocity profile model of equation (4.16) can be introduced in the definition of the S3 crossflow velocity, by rewriting equation (4.14) as follows :

$$\begin{aligned} \overline{W}_{\theta,S3,ewbl} = & \left[\overline{W}_{\theta,ewbl}|_{wall} - \overline{W}_{m,Q3D,ewbl} \tan \beta|_{wall} \right] - \Delta U \\ & + \overline{W}_{m,Q3D,ewbl} (\tan \beta|_{wall} - \tan \beta|_{blade}) \end{aligned} \quad (4.18)$$

where U denotes the wheel speed and Δ is a parameter which describes the relation between the blade frame of reference and the end-wall frame of reference :

$\Delta = 0$: No relative motion between blades and end-wall

$\Delta = 1$: Relative motion : rotating blades and stationary end-wall

$\Delta = -1$: Relative motion : stationary blades and rotating end-wall

The first term of equation (4.18) can be directly substituted by the velocity profile model of equation (4.16), while the last term can also be expressed in function of the velocity profile model parameters by rewriting the angles in function of the velocity components and substitution of equation (4.13a).

Finally, the following expression for the tangential velocity profile associated with the 3D-effects of the EWBL is obtained :

$$\overline{W}_{\theta,S3,ewbl} = \left[\widehat{W}_{m,Q3D} (1-b) \tan \epsilon'_w - \Delta b U \right] \left(1 - \frac{y}{\delta}\right)^n \quad (4.19)$$

From equation (4.19), it then follows that the passage-averaged EWBL-crossflow $\overline{W}_{\theta,S3,ewbl}$ will be determined by three model parameters : b , n and $\tan \epsilon'_w$.

The parameters b and n are interconnected through the skin friction coefficient C_f because of the following empirical relation :

$$b = \exp \left\{ -10 n C_f^{0.5} \cos \beta^{-0.134} \right\} \quad (4.20)$$

For more information about the end-wall boundary layer computation procedure, the reader is again referred to De Ruyck (1982).

4.3 AXIAL VORTICITY CONTRIBUTION

The passage-averaged axial vorticity $\bar{\zeta}_{z,S3,ewbl}$, associated to the contribution of the end-wall boundary layers to the secondary flow on the S3-plane, is given by the following equation, obtained by passage-averaging the definition equation of the axial component of vorticity and assuming constant blockage :

$$\bar{\zeta}_{z,S3,ewbl} = \frac{1}{r} \frac{\partial}{\partial r} (r \bar{W}_{\theta,S3,ewbl}) - \frac{1}{bs} \tan \eta [W_{\theta,S3,ewbl}]_p^s - \frac{1}{bs} [W_{r,S3,ewbl}]_p^s \quad (4.21)$$

The second term can be neglected in most cases, due to the small value of the lean angle η . This will not always be the case for the last term, expressing the difference in induced radial flows between pressure and suction side of the passage. However, for the moment, this term is also neglected.

Substituting the model equation (4.19) for $\bar{W}_{\theta,S3,ewbl}$ yields the following expression :

$$\begin{aligned} \bar{\zeta}_{z,S3,ewbl} = & \widehat{W}_{m,Q3D} (1-b) (\tan \epsilon'_w) \left[\frac{1}{r} \left(1 - \frac{y}{\delta}\right)^n - \cos \sigma \frac{n}{\delta} \left(1 - \frac{y}{\delta}\right)^{n-1} \right] \\ & + \Delta b \Omega \left[\cos \sigma \frac{n}{\delta} \left(1 - \frac{y}{\delta}\right)^{n-1} - 2 \left(1 - \frac{y}{\delta}\right)^n \right] \end{aligned} \quad (4.22)$$

where Ω is the angular velocity of the rotor and σ denotes the angle between the meridional and axial directions in the meridional S2-plane (cf. equation (3.12)).

Remark that the second term of the right-hand side contains the end-wall boundary layer axial vorticity contribution due to the relative motion between the blades and the end-wall. This contribution is due to the fact that the S3 crossflow velocity is defined as the non-collateral part of the boundary layer flow in the blade reference frame, while the velocity profile models are defined in the end-wall reference frame.

Observe that the end-wall boundary layer vorticity contribution is completely determined by the following parameters : velocity defect b and power law exponent n (which are connected through equation (4.20)), physical boundary layer thickness δ and skewing angle ϵ'_w .

4.4 NUMERICAL SOLUTION

The three fundamental equations (4.1) to (4.3), supplemented with equations (4.4) to (4.20), can be written in the following general form :

$$\frac{d}{dm} (b, n, \tan \epsilon'_w) = f(m, b, n, \tan \epsilon'_w) \quad (4.23)$$

The system of the three equations can thus be simultaneously integrated in the m-direction. In the present method a fifth-order Runge-Kutta integration is used.

However, because of considerations of numerical stability, the following unknowns are used in practice : $\log (-\log b)$, $\log n$, and $\tan \epsilon'_w$.

Once the parameters $b, n, \tan \epsilon'_w$ are obtained, the axial vorticity contribution inside the end-wall boundary layer can be directly determined from equation (4.22).

Remark that the axial vorticity contribution is zero outside the EWBL, although the associated secondary flows are defined throughout the computational domain as a result of continuity (recirculation of the flow).

CHAPTER 5

PROFILE BOUNDARY LAYERS REGION

5.1 INTRODUCTION

Boundary layers along turbomachine blades are of a three-dimensional nature and contribute to the convective mixing through radial transport of fluid, caused by an imbalance between radial pressure gradients and centrifugal forces (contribution 4 of Table 1.1).

In a rotor blade boundary layer, the fluid has lower streamwise velocity relative to the blades than the inviscid free-stream fluid. Therefore, a velocity triangle argument easily shows that the boundary layer fluid has a larger swirl velocity in the absolute frame of reference than does the free-stream fluid. If it is assumed that radial pressure gradients and centrifugal forces balance each other in the free-stream region, the boundary layer fluid, which is subject to the same radial pressure gradients as the free-stream fluid, thus experiences an excess centrifugal force because of the larger swirl velocity. Therefore, blade boundary layer fluid is centrifuged outward in a rotor.

Conversely, stator blade boundary layer fluid possesses a smaller swirl velocity in the absolute frame of reference than does the free-stream fluid, leading to a centrifugal force defect with respect to the equilibrium free-stream. Therefore, the blade boundary layer fluid in a stator is said to move inward through radial pressure gradients.

5.2 THEORETICAL EQUATIONS

Although it is usual to express profile boundary layer equations in a coordinate system associated to the profile walls, in the present theory they are developed in a meridional coordinate system (cf. Appendix A). Furthermore, although the radial mixing theory is developed in cylindrical coordinates, the meridional coordinate system is used because it will yield a system of equations very similar to that of the end-wall boundary layer theory.

5.2.1 FUNDAMENTAL EQUATIONS

The fundamental equations that are solved are the meridional and normal projections of the integral form of the momentum equation and the integral form of the continuity equation or entrainment equation. The term 'integral' refers to an integration in the tangential direction over the physical boundary layer thickness δ , removing all local details about the boundary layer flow.

The meridional integral momentum equation is of the form

$$\begin{aligned}
& \frac{\partial}{\partial m} \rho W_m^2 \theta_{mm} + \frac{\partial}{\partial n} \rho W_m^2 \theta_{nn} + \rho W_m \delta_m^* \frac{\partial W_m}{\partial m} + \rho W_m \delta_n^* \frac{\partial W_m}{\partial n} \\
& + \frac{1}{R_{mm}} \rho W_m (W_m \theta_{nn} - W_m \theta_{mm} + W_n \delta_n^*) - \frac{1}{R_{nn}} \rho W_m^2 (2\theta_{nn} + \delta_n^*) \\
& + \frac{1}{R_{um}} \rho W_u \{ W_u (\theta_{mm} + \delta_m^*) + 2U \delta_m^* \} = \tau_s \quad (5.1)
\end{aligned}$$

while the normal integral momentum equation is of the form

$$\begin{aligned}
& \frac{\partial}{\partial m} \rho W_m^2 \theta_{mm} + \frac{\partial}{\partial n} \rho W_m^2 \theta_{nn} + \rho W_m \delta_m^* \frac{\partial W_n}{\partial m} + \rho W_m \delta_n^* \frac{\partial W_n}{\partial n} \\
& + \frac{1}{R_{mm}} \rho W_m^2 (\theta_{mm} + \delta_m^* - \theta_{nn}) - \frac{1}{R_{nn}} \rho W_m (2W_m \theta_{nn} + W_n \delta_m^*) \\
& + \frac{1}{R_{un}} \rho W_u \{ W_u (\theta_{mm} + \delta_m^*) + 2U \delta_m^* \} = \tau_n \quad (5.2)
\end{aligned}$$

In both equations, terms which are of small magnitude compared to the other terms have been neglected.

The integral continuity equation or entrainment equation reads :

$$\begin{aligned}
& \frac{\partial}{\partial m} \rho W_m (\delta - \delta_m^*) + \frac{\partial}{\partial n} \rho W_m (\delta - \delta_n^*) - \frac{1}{R_{mm}} \rho W_m (\delta - \delta_m^*) \\
& - \frac{1}{R_{nn}} \rho W_m (\delta - \delta_n^*) + \rho \delta \left(\frac{W_m}{R_{um}} + \frac{W_n}{R_{un}} \right) = \rho \frac{W_s}{\cos \sigma \cos \beta} E \quad (5.3)
\end{aligned}$$

The three equations above are expressed in the blade reference system (absolute frame of reference for stator blades, steadily rotating relative frame of reference for rotor blades).

The velocity components in the three equations above are the superposition of the Quasi-3D velocity components and the S3 secondary flow components induced by the inviscid mainflow and the end-wall boundary layers.(cf. § 2.4). The indexes m,n,u refer to the local meridional, normal and tangential directions respectively.

The quantities R_{ij} are radii of curvature, associated to the meridional coordinate system,

δ is the physical boundary layer thickness, δ_i^* the displacement thickness in the i-direction and θ_{ij} the momentum thickness in the i-direction weighted by the j-direction.

W_s is the Quasi-3D component of the velocity along a streamline, β is the relative flow angle, and E is the so-called 'entrainment rate'.

For further details, see Appendix C of the previous progress report of De Ruyck and Hirsch (1987), which contains a complete derivation of the equations above.

5.2.2 SUPPLEMENTARY EQUATIONS

a) Entrainment equation

The entrainment rate E is given as an empirical function of Head's shape factor H^* through :

$$E = 0.0306 / (H^* - 3.)^{0.653} \quad (5.4)$$

Head's shape factor H^* is defined as :

$$H^* = \frac{\delta - \delta_s^*}{\theta_s} \quad (5.5)$$

where the index s refers to the local streamwise direction.

b) Mainstream skin friction

The mainstream skin friction is estimated by means of a non-dimensional skin friction coefficient generally denoted as C_f and defined through

$$\tau_s = C_f \rho \frac{\widehat{W}_s^2}{2} \quad (5.6)$$

The skin friction coefficient C_f is computed from the empirical Ludwig-Tillmann relation for turbulent boundary layers, which expresses C_f as a function of Reynolds number and shape factor :

$$C_f = 0.246 Re_{\theta_m}^{-0.268} \exp(-1.56 H) \quad (5.7)$$

with the Reynolds number defined as

$$Re_{\theta_m} = \frac{\widehat{W}_s \theta_m}{\nu} \quad (5.8)$$

5.2.3 VELOCITY PROFILE MODELS

Closure of the system of equations for the profile boundary layers is obtained by the introduction of velocity profile models, adapted to turbomachinery flows. Although the equations are expressed in meridional coordinates (m,n,u) , the profile models will be defined in streamline coordinates (s,n,t) , which are associated to the profile walls. Transformation from one coordinate system to another is straightforward, since m and u coordinate lines and s and t coordinate lines are all defined on an $S1$ streamsurface of revolution and their relation is completely determined by the relative flow angle β between the streamline s and the meridional coordinate line m (Figure 5.1).

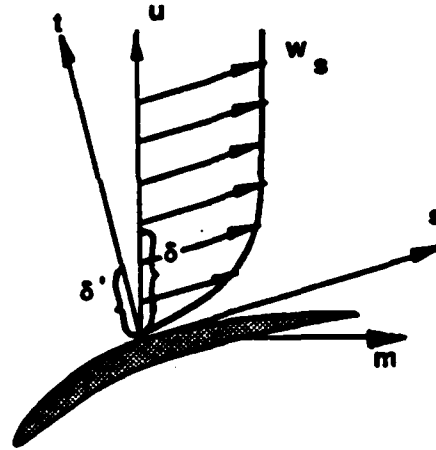


Figure 5.1 : Blade boundary layer velocity profile in meridional and streamline coordinates (both intrinsic coordinates for a streamsurface of revolution)

In analogy with the EWBL profile models, the following model equation for the streamwise velocity profile inside the profile boundary layer is introduced :

$$\frac{W_{s,Q3D,pbl}}{\widehat{W}_{s,Q3D}} = 1 - b \left\{ 1 - \frac{y}{\delta} \right\}^n \quad (5.9)$$

where y/δ represents the non-dimensional tangential distance from the blade wall, while the velocity defect b and the power law exponent n are model parameters.

The overhead carat (^) denotes a 'reference' freestream velocity at the boundary layer edge, e.g. the velocity at the wall obtained from the previous inviscid Quasi-3D computation.

The passage-averaged streamwise velocity component $\widehat{W}_{s,Q3D}$ can be computed from the passage-averaged axial velocity component $\widehat{W}_{z,Q3D}$ through the following relation :

$$\widehat{W}_{s,Q3D} = \frac{\widehat{W}_{m,Q3D}}{\cos \beta} = \frac{\widehat{W}_{z,Q3D}}{\cos \beta \cos \sigma} \quad (5.10)$$

where β denotes the relative flow angle between the meridional direction m and the streamline direction s on the $S1$ streamsurface of revolution, while σ is the flow angle between the axial direction and the meridional direction m (cf. Figure 5.1).

In further analogy to the end-wall boundary layers, the radial velocity induced by the profile boundary layers on the $S3$ -plane is defined as (cf. Figure 5.2) :

$$\frac{W_{r,S3,pbl}}{\widehat{W}_{s,Q3D}} = \frac{W_{r,pbl} - W_{z,Q3D,pbl} \tan(\sigma + \alpha_r)}{\widehat{W}_{s,Q3D}}$$

$$= \frac{W_{r,pbl} - W_{s,Q3D,pbl} \cos \beta \cos \sigma \tan(\sigma + \alpha_r)}{\widehat{W}_{s,Q3D}} \quad (5.11)$$

α_r is the radial flow angle, i.e. the angle between the axial direction and the meridional direction m' , induced by the combination of the Quasi-3D velocity components and the velocity components due to the secondary flow effects in the inviscid and end-wall boundary layers region, while σ is the flow angle between the axial direction and the meridional direction m of the Quasi-3D flow and β is the angle between the streamline direction s and the meridional direction m for the Quasi-3D flow (cf. Figure 5.2).

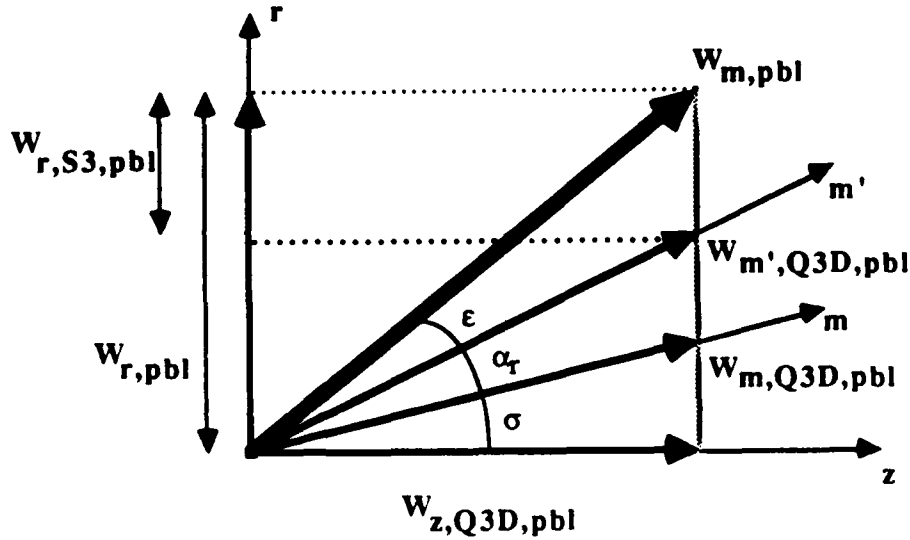


Figure 5.2 : Velocity components in the profile boundary layer

The radial secondary flows induced by the profile boundary layers are described by the following velocity profile model :

$$\frac{W_{r,S3,pbl}}{\widehat{W}_{s,Q3D}} = (1 - b) \cos \beta \cos \sigma \tan \epsilon_w' \left(1 - \frac{y}{\delta}\right)^n \quad (5.12)$$

where the parameters b and n are identical with those of the streamwise velocity profile model (5.9) and the additional parameter ϵ_w' is defined through :

$$\tan \epsilon_w' = \tan (\epsilon_w + \alpha_r + \sigma) - \tan (\alpha_r + \sigma) \quad (5.13)$$

The velocity profile model (5.12) is selected because it yields a value of $W_{r,S3,pbl}$ at the wall, which is identical to the value of $W_{r,S3,pbl}$ at the wall obtained by substituting the velocity profile model (5.9) in the definition (5.11) and setting y to zero.

Observe that the profile boundary layer contribution to the S3 flow field is modeled in such a way, that the radial velocities induced by the inviscid and EWBL flow regions are already taken into account for the PBL computation (through the radial flow angle α_r), i.e. the contribution of the profile boundary layers is an extra radial velocity component, to be superposed on the previous components (cf. § 2.4).

5.3 AXIAL VORTICITY CONTRIBUTION

The contribution of the profile boundary layers to the secondary flow on the S3 plane is represented by an axial vorticity contribution $\zeta_{z,S3,pbl}$ computed by the following formula, obtained through substitution of velocity profile model (5.12) into the axial vorticity definition equation, taking into account relation (5.10) :

$$\zeta_{z,S3,pbl} = \widehat{W}_{z,Q3D} (1 - b) (\tan \epsilon'_w) \left(\frac{n}{\delta} \right) \left(1 - \frac{y}{\delta} \right)^{n-1} \quad (5.14)$$

whereby radial variations were neglected, based on the reasonable assumption that they are an order of magnitude smaller than tangential variations in the case of profile boundary layers.

Observe that this vorticity contribution is local, not passage-averaged, and that it is determined by the following boundary layer parameters : velocity defect b , power law exponent n , skewing angle ϵ'_w and physical boundary layer thickness δ .

5.4 NUMERICAL SOLUTION

5.4.1 INITIALISATION AND REQUIRED INPUT

The profile boundary layer computation is initialised by assuming the following default values for the momentum thickness and shape factor : $\theta=0.001$, $H=1.3$, which are typical values for a 'well-behaving' thin boundary layer.

In addition, the following parameters are considered as being known beforehand and are thus required as input :

- 1) Blade row and blade geometrical data
- 2) Pitch-averaged Quasi-3D velocity components
- 3) Secondary flow field induced by the inviscid flow region and the end-wall boundary layers

5.4.2 VORTICITY COMPUTATION

The three fundamental equations (5.1) to (5.3), supplemented with equations (5.4) to (5.13), can be written in the following general form :

$$\frac{\partial}{\partial m} \{ b, n, \tan \epsilon'_w \} = f(m, b, n, \tan \epsilon'_w) \quad (5.15)$$

This system of three equations can thus be simultaneously integrated in the m -direction. In the present method a fifth-order Runge-Kutta integration is used.

Remark that a set of unknowns $\{ b, n, \tan \epsilon'_w \}$ exists at each spanwise position for either blade side, and hence the system of equations (5.15) is simultaneously integrated in the m -direction for every spanwise position at both the pressure and suction side of the blade. Because of numerical stability considerations, the following unknowns are used in practice: $\log(-\log b)$, $\log n$, and $\tan \epsilon'_w$.

Once the parameters b , n and $\tan \epsilon'_w$ are obtained, the axial vorticity contribution of the profile boundary layers is directly determined from equation (5.14). Remark that this contribution is zero outside the profile boundary layers. However, the associated secondary flow field induced by the profile boundary layers is not zero outside these layers because of continuity (recirculation of radially convected fluid in the circumferential direction).

Also, notice that the axial vorticity contribution of the profile boundary layers is superposed on the axial vorticity contribution of the inviscid flow region, because the secondary flow generation mechanism of the profile boundary layers (centrifugation) is not accounted for in the inviscid secondary flow computation.

CHAPTER 6

WAKE REGION

6.1 INTRODUCTION

Since the blade wakes form the continuation of the profile boundary layers, the convective mixing in the wake region is also due to radial fluid migration, caused by an imbalance between centrifugal forces and radial pressure gradients.

However, two different types of wake fluid migration can be distinguished. In the case of an inviscid flow, the wake does not exist, but a vortex sheet is shed from the trailing edges of the blades : the sheet of trailing shed vortices (contribution 3a of Table 1.1), due to radial pressure gradients resulting from spanwise changes of blade circulation. In the case of a viscous flow, wakes are formed behind the trailing edges of the blades and radial fluid migration occurs in these wakes due to the same mechanism that causes radial flows in the blade boundary layers (cf. § 5.1) : imbalance between imposed radial pressure gradients and centrifugal forces related to swirl velocity (contribution 3b of Table 1.1).

It is important to note that the wake fluid migration in the inviscid case can be considered as a limiting case for zero viscosity of the wake fluid migration in the viscous case. Indeed, the blade wake can be interpreted as a finite vortex layer where vorticity diffuses under influence of the effects of viscosity. For the limiting case of zero viscosity, an infinitely thin vortex sheet at the blade trailing edges is obtained, because the absence of viscous diffusion keeps the vorticity confined to the sheet where it originates.

Finally, the wake can be considered to have an important influence on the overall mixing. In subsonic compressors, peak radial velocities of the order of 20%-25% of the mainflow velocities may be reached in the near wake, due to the very low axial momentum of the fluid. In transonic compressors, radial velocities of the same order of magnitude as the axial or tangential velocities have been observed in the blade wakes just downstream of the blade trailing edges, Kerrebrock (1981).

6.2 THEORETICAL EQUATIONS

In reality, wake velocity profiles can be highly asymmetric ; pressure and suction side radial flows can even have opposite signs. Therefore, pressure and suction side of the wake are treated separately in the present wake approach and the concept of 'peak' radial velocities at the wake center, often employed in wake models, is not used.

Although the radial mixing theory is developed in cylindrical coordinates, curvilinear streamline coordinates are used in the S2 through-flow plane. For the relation between the curvilinear streamline coordinate system, the curvilinear meridional coordinate system and the cylindrical coordinate system, the reader is referred to Chapter 5 and Appendix A.

6.2.1 VELOCITY PROFILE MODELS

The asymmetric wake velocity profile models are determined as follows : the velocity profiles at pressure and suction side of the wake have an identical form, but the model parameters are independent for each wake side ; the velocity profiles of both wake sides are merged smoothly at the wake center by means of a 'bridging function' incorporated in the model profiles.

The streamwise velocity profile inside the wake layer (pressure side or suction side) is thus modeled as :

$$\frac{W_{s,Q3D,wake}^{p/s}}{\widehat{W}_{s,Q3D}} = 1 - b^{p/s} f(\eta) - (\bar{b} - b^{p/s}) g(\eta) \quad (6.1)$$

where the superscripts p/s refer to pressure or suction side respectively, b denotes the velocity defect parameter, \bar{b} denotes the arithmetic average of the velocity defects at pressure and suction side, η is the non-dimensional tangential distance from the wake centerline and the functions f and g are defined by

$$f(\eta) = 1 - 6\eta^2 + 8\eta^3 - 3\eta^4 \quad \text{Pohlhausen polynomial} \quad (6.2a)$$

$$g(\eta) = \exp \{-\eta / \eta_0\} \quad \text{bridging function} \quad (6.2b)$$

The function g corrects the velocity profile in the neighbourhood of the wake center to fit the profile on one side with the profile on the opposite side : it is easily verified that the velocity profile model (6.1) yields an identical value for the streamwise velocity at the wake center for both wake sides :

$$W_{s,Q3D,wake} = (1 - \bar{b}) \widehat{W}_{s,Q3D} \quad \text{at the wake center} \quad (6.3)$$

where the overhead carat (^) denotes a 'reference' streamwise velocity.

The 'bridging function' g affects the profile over a distance determined by η_0 . For small values of η_0 , the influence of the bridging function is small, and pressure and suction side of the wake conserve their identity. At higher values of η_0 , the influence of the bridging function increases, leading to an increased mixing of both wake sides and the wake velocity profile shape becomes more symmetric.

Large second derivatives are present around the wake centerline and thus the asymmetry gives rise to a diffusive mixing between pressure and suction side of the wake. Hence, the non-dimensional mixing length η_0 can be approached by the following formula, based on diffusion theory :

$$\eta_0 = \frac{1}{\delta} \sqrt{\epsilon_t \Delta t} = \frac{1}{\delta} \sqrt{\epsilon_t \Delta z / W_z} \quad (6.4)$$

where Δt is the time it takes a fluid element to travel from the trailing edge of the blade to

the point in the wake where the mixing length η_0 is being evaluated and is approximated as the ratio of the axial distance from trailing edge and the local axial velocity at the wake center. δ denotes the half wake width, while ϵ_t is the turbulent mixing coefficient which will be discussed in Chapter 7.

The radial velocity profile associated to the 3D effects of the wake, inducing flows on the S3-plane, is described by the following velocity profile model for either wake side:

$$\frac{W_{r,S3,wake}}{\widehat{W}_{s,Q3D}} = \frac{W_{r,wake} - W_{s,Q3D,wake} \tan \alpha}{\widehat{W}_{s,Q3D}} \\ = \tan \bar{\epsilon} (1-\bar{b}) f(\eta) + \{ (1-\bar{b}) (\tan \bar{\alpha} - \tan \alpha) + (1-\bar{b}) \tan \bar{\epsilon} - (1-b) \tan \epsilon \} g(\eta) \quad (6.5)$$

whereby η denotes the non-dimensional tangential distance from the wake center and the velocity defect parameter b is identical with that of the streamwise velocity profile model (6.1) for the corresponding wake side. ϵ is the skewing angle model parameter and f and g are the model functions as defined in (6.2a) and (6.2b).

α is the radial flow angle between the axial direction and the streamline direction. The overbars denote arithmetic mean values of pressure and suction side values.

This velocity profile model ensures that both sides of the wake yield the same value for the total radial velocity W_r at the wake centerline. This can be easily verified by substituting the streamwise velocity profile model (6.1) in equation (6.5) and setting η to zero, which yields :

$$\frac{W_{r,wake}}{\widehat{W}_{s,Q3D}} = (1 - \bar{b}) (\tan \bar{\alpha} + \tan \bar{\epsilon}) \quad \text{at the wake center} \quad (6.6)$$

The asymmetric streamwise and radial wake velocity profiles are illustrated on Figure 6.1 for different values of the asymmetry parameter η_0 .

6.2.2 BASIC EQUATIONS

a) Integral momentum equations

Since pressure and suction side of the wake are considered separately, two sets of integral momentum equations are used.

As the wake is the continuation of the profile boundary layers, the meridional and normal projections of the integral momentum equation for the wake are identical to equations (5.1) and (5.2). After introduction of the velocity profile models (cf. § 6.2.1), it can be shown that the pressure and suction side friction force components have identical magnitude but opposite signs, and the friction at the wake centerline becomes zero in the case of a symmetric wake profile only (De Ruyck & Hirsch, 1987).

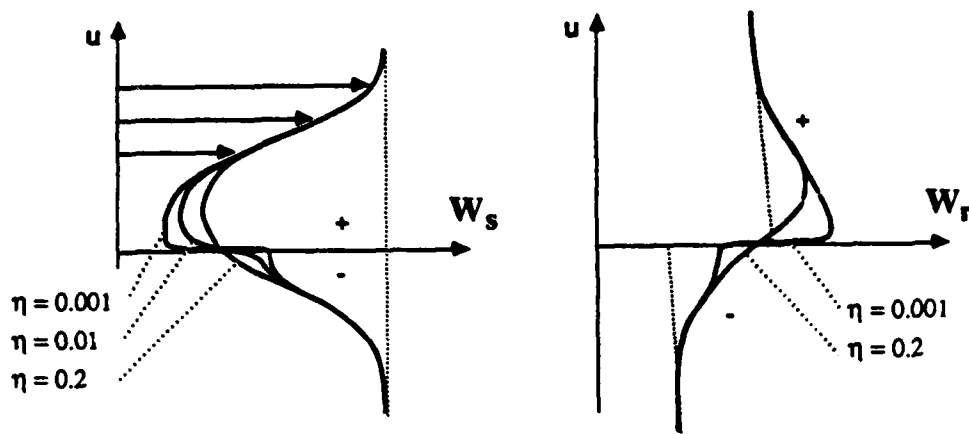


Figure 6.1 : Asymmetric wake velocity profiles

The following three integral momentum equations are used in practice, where the term 'integral' refers to an integration in the tangential direction from the wake centerline to the wake edge, removing all local details from the wake flow :

- 1) Meridional integral momentum equation, respectively at pressure side and at suction side.
- 2) The sum of the normal integral momentum equations at pressure and suction side

The two normal integral momentum equations could be considered at the pressure and suction side separately, but this led to numerical instabilities (De Ruyck & Hirsch, 1987). Therefore, the normal integral momentum equation has been expressed over the full wake width only and an extra relation will be added to account for this.

b) Local wake decay equations

In addition to the integral equations, three local equations are used :

- 1) Meridional momentum equation, expressed locally at the wake center
- 2) Difference between local meridional momentum equations at pressure and suction sides
- 3) Difference between local normal momentum equations at pressure and suction sides

The last of these local equations is the extra relation, needed to close the system of wake equations because only the sum of the normal integral momentum equations is used, instead of the individual equations.

c) Summary

For the wake, a system of six partial differential equations in six independent variables :

δ^p, δ^s : pressure and suction side wake thickness
 b^p, b^s : pressure and suction side wake velocity defect
 ϵ^p, ϵ^s : pressure and suction side skewing angle

has been obtained.

For an explicit form of the equations, the reader is referred to a previous report by De Ruyck & Hirsch (1987), where a detailed analysis of the wake model including the derivation of the equations is presented.

6.3 AXIAL VORTICITY CONTRIBUTION

The contribution of the wakes to the secondary flow on the S3 plane is represented by an axial vorticity contribution $\zeta_{z,S3,wake}$.

Substituting velocity profile model (6.5) into the axial vorticity definition equation

$$\zeta_{z,S3,wake} = -\frac{1}{r} \frac{\partial W_{r,S3,wake}}{\partial \theta} = -\frac{\partial W_{r,S3,wake}}{\partial u} \quad (6.7)$$

whereby radial variations have been neglected, based on the assumption that they are an order of magnitude smaller than tangential variations in the case of a wake, yields the following expression for the axial vorticity contribution of the wake secondary flow :

$$\begin{aligned} \zeta_{z,S3,wake} = & -(1 - b^{p/s}) (\tan \epsilon^{p/s}) (-12\eta + 24\eta^2 - 12\eta^3) \frac{\widehat{W}_{s,Q3D}}{\delta^{p/s}} \\ & + \frac{\widehat{W}_{s,Q3D}}{\delta^{p/s} \eta_0} \exp\{-\eta/\eta_0\} [(1 - \bar{b}) \tan \bar{\epsilon} - (1 - b^{p/s}) \tan \epsilon^{p/s} \\ & + (1 - \bar{b}) (\tan \bar{\alpha} - \tan \alpha^{p/s})] \end{aligned} \quad (6.8)$$

The superscripts p/s indicate wake pressure side and wake suction side respectively, while the overbars indicate the arithmetic mean of pressure and suction side values.

Observe that the wake vorticity contribution is local, not passage-averaged.

Remark also that the vorticity contribution $\zeta_{z,S3,wake}$ is confined to the wake region and vanishes outside the wake layer, while the associated secondary flows are defined on the entire S3-plane due to continuity.

6.4 NUMERICAL SOLUTION

6.4.1 INITIALISATION AND REQUIRED INPUT

The wake computation is initialised by carrying over three parameters from the profile boundary layer computation, which are assumed to be conserved during the transition from the profile boundary layers to the near wake : the physical boundary layer thickness δ , the displacement thickness δ^* and the streamwise momentum thickness θ_{ss} . Using the velocity profile models, all other variables needed to start the wake computation can be calculated from these variables.

The following parameters are again assumed to be known and hence required as input :

- 1) Geometrical parameters : blade and blade row geometry
- 2) Pitch-averaged Quasi-3D velocity components
- 3) Secondary flow field induced in the preceding blade row by the inviscid flow region, the end-wall boundary layers and the profile boundary layers.

6.4.2 VORTICITY COMPUTATION

The system of wake equations assumes a form similar to that of equation (5.15) :

$$\frac{\partial}{\partial m} \{ \delta^p, \delta^s, b^p, b^s, \epsilon^p, \epsilon^s \} = f \{ \delta^p, \delta^s, b^p, b^s, \epsilon^p, \epsilon^s \} \quad (6.8)$$

and is also integrated in the m-direction by a fifth order Runge-Kutta method, starting at the trailing edge and proceeding to a specified axial distance downstream of the blade row.

Once the wake parameters b, ϵ, δ have been obtained for both sides of the asymmetric wake, the axial vorticity contribution associated to the wakes can be immediately determined from equation (6.8).

CHAPTER 7

TURBULENT DIFFUSION

7.1 INTRODUCTION

Due to the high turbulence levels in turbomachinery flows, the random, stochastic fluid motions associated to turbulence represent a substantial contribution to the radial mixing process.

No attempt is made here to make an explicit computation of the turbulence field, since the numerical simulation of the turbulence mechanism is still largely an unresolved problem. Rather, the effects of turbulence on the radial mixing process are introduced in an empirical way by means of a turbulent diffusion coefficient ϵ_t that controls the amount of diffusive mixing.

7.2 TURBULENT DIFFUSION COEFFICIENT

Since it has been mentioned in the introduction to the previous chapter that the wake can have a large impact on the radial mixing process, it seems logical to correlate the overall turbulent mixing coefficient to a parameter describing the magnitude of turbulent diffusion in the wake.

Schlichting (1979) gives the following semi-empirical expression for the eddy viscosity in a two-dimensional turbulent wake behind a circular cylinder :

$$\nu_t = 0.047 \cdot 2 b_{1/2} (U_\infty - U_c) \quad (7.1)$$

where U_∞ is the freestream velocity, U_c is the velocity at the wake center and $b_{1/2}$ denotes the distance from the wake center to the wake edge at 'half depth' (i.e. the location in the wake velocity profile where $U_\infty - U = 0.5 (U_\infty - U_c)$).

Experimental measurements in the wake of circular cylinders have shown that the 'half wake width at half depth' $b_{1/2}$ may be written as (Schlichting, 1979) :

$$b_{1/2} = 0.441 b \quad (7.2)$$

where $2b$ denotes the full width of the wake.

Equation (7.1) can thus be rewritten as :

$$\nu_t = 0.042 b (U_\infty - U_c) \quad (7.3)$$

The semi-empirical formula (7.3) will now be generalized to give an estimation of the turbulent diffusion coefficient as follows.

Based on experimental evidence, the turbulent Schmidt number Sc_t can be reasonably approximated as unity (see, for example, Gallimore & Cumpsty (1986a)) :

$$Sc_t = \nu_t / \epsilon_t = 1 \quad (7.4)$$

where ϵ_t denotes the turbulent diffusion coefficient.

Combining equations (7.3) and (7.4), and taking into account the wake velocity profile models from Chapter 6, the following semi-empirical relation for the turbulent diffusion coefficient is obtained :

$$\epsilon_t = K \delta \bar{b} \widehat{W}_{s,Q3D} \quad (7.5)$$

where δ is the physical wake thickness measured from the wake center to the wake edge, \bar{b} is the mean velocity defect and hence $\bar{b} \widehat{W}_{s,Q3D}$ is the difference between the freestream streamwise velocity and the streamwise velocity at the wake center (cf. equation (6.3)), while the empirical parameter K depends on turbulence intensity.

The order of magnitude of the empirical parameter K can be determined as follows.

In Schlichting's analysis of the two-dimensional wake of a circular cylinder, the following empirical relation for the wake turbulent diffusion coefficient is established :

$$\epsilon_t = 0.0222 C_D U_\infty d \quad (7.6)$$

where C_D denotes the drag coefficient of the cylinder, U_∞ is the free-stream velocity and d is the cylinder diameter.

The value for C_D is typically 1.0. For the other parameters, values are chosen which are typical for the linear compressor cascade testcase which will be used to compare theoretical computations with experimental data (see Chapter 11). The free-stream velocity for the cascade is of the order of 23.7 m/s, while the cylinder diameter d may be taken equal to the blade thickness, which is 0.02 m (NACA 65-1810 blading with 0.2 m chord).

This yields a value of 0.01052 m²/s for the turbulent diffusion coefficient.

If this value is non-dimensionalized through division by the free-stream velocity and the axial stage length L (equal to the axial chord for the linear cascade : 0.196 m), the following value is obtained :

$$\frac{\epsilon_t}{\widehat{W}_{s,Q3D} L} = 0.0022 \quad (7.7)$$

This value compares very well with the corresponding non-dimensional values of the turbulent mixing coefficient for other compressor testcases, obtained from ethylene tracer experiments by Gallimore & Cumpsty (1986a).

Writing equation (7.5) in non-dimensionalized form and solving for K yields the following relation for this empirical parameter :

$$K = \frac{L}{\delta \bar{b}} \left[\frac{\epsilon_t}{\widehat{W}_{a,Q3D} L} \right] \quad (7.8)$$

Replacing the non-dimensional turbulent mixing coefficient between brackets by the typical value of 0.002 found above, L by the axial chord length of 0.196m, and taking the physical wake thickness δ from wake center to wake edge equal to half of the blade thickness, i.e. 0.01 m, while the mean velocity defect parameter \bar{b} is set to 0.5 (mean of the value $\bar{b} = 1$ near the trailing edge (maximum velocity defect) and $\bar{b} = 0$ in the far wake (zero velocity defect)), yields the following value for K :

$$K = 0.08 \quad \text{order of magnitude analysis} \quad (7.9)$$

Remark that this value, although it was found from an order of magnitude analysis for a single test case, may be taken as representative, since the ratio L/δ may be assumed to have a limited variation since L and δ both vary with about the same geometric scaling factor.

In practice however, the value of the empirical parameter K will be calibrated in a data-match fashion. Indeed, since K determines the value of the turbulent diffusion coefficient through equation (7.5), K also determines the value of the parameter η_0 (cf. equation (6.4)), which in turn controls the dispersion of the wake downstream from the trailing edge (see Chapter 6). The empirical parameter K can thus be tuned in such a way that the computed dispersion of the wake exactly matches the experimentally observed wake dispersion. For the linear compressor cascade testcase this yields the following result :

$$K = 0.10 \quad \text{data-match calibration} \quad (7.10)$$

7.3 TURBULENT MIXING MODEL

The influence of turbulence on the radial mixing process is introduced through the energy transport equation : the magnitude of the terms describing energy diffusion is controlled by the turbulent mixing coefficient ϵ_t . Hereby, it is assumed that the effects of molecular diffusion are negligible with respect to the effects due to turbulence.

For a description of the modeling of the influence of turbulence on the energy redistribution, the reader is referred to Chapter 8 of this report.

CHAPTER 8

ENERGY REDISTRIBUTION

8.1 GENERAL ENERGY TRANSPORT EQUATION

The governing equation for the radial mixing process is derived from a basic law, i.e. the first law of thermodynamics formulated for a compressible flow. It may be shown that, neglecting volume forces (e.g. gravity) and external heat sources (e.g. chemical reactions), assuming steady flow relative to the blade row reference system, taking into account only the contribution of the work of the shear stresses related to the diffusion of kinetic energy and assuming a unity Prandtl number $Pr = \mu C_p / k = 1$, the general energy equation in a steadily rotating frame of reference reduces to, cf. Hirsch (1988), p.23 :

$$\vec{\nabla} \cdot (\rho \vec{W} I) = \vec{\nabla} \cdot (\mu \vec{\nabla} H_r) \quad (8.1)$$

with the rothalpy I defined as

$$I = h + \frac{W^2}{2} - \frac{U^2}{2} = H - UV_\theta \quad (8.2)$$

and

$$H = h + \frac{V^2}{2} \quad \text{total enthalpy} \quad (8.3a)$$

$$H_r = h + \frac{W^2}{2} \quad \text{relative total enthalpy} \quad (8.3b)$$

The classical energy equation for the Quasi-3D formulation incorporating the distributed loss model reads:

$$\vec{\nabla} \cdot (\rho \vec{W} I) = \rho \vec{W} \cdot \vec{\nabla} I = 0 \quad (8.4)$$

Physically, it means that the rothalpy I is constant along a streamline in the relative frame of reference (blade frame of reference).

From this, it follows that the non-zero right-hand side of equation (8.1) describes a diffusion of energy between the streamlines, thereby destroying the constancy of the rothalpy.

This is in accordance with theoretical results obtained by Hirsch and Dring (1987) in the context of through-flow computations. These authors showed that the mass-averaged

rothalpy remains constant along a streamline defined by the density-weighted pitch-averaged flow in the case of axisymmetric streamsurfaces, whereas in the case of non-axisymmetric streamsurfaces this constancy of mass-averaged rothalpy is destroyed due to a source term which describes a radial interaction between the streamsurfaces.

In a turbomachine, the energy is most often described in terms of the total temperature, so the mixing should be performed on this flow property. Defining the following total temperatures (assuming constant specific heat C_p) :

$$T_t^r = H_r / C_p \quad \text{relative total temperature} \quad (8.5a)$$

$$T_t^* = I / C_p \quad \text{rotary total temperature} \quad (8.5b)$$

and taking into account the continuity equation for steady relative flow, equation (8.1) is further reduced to :

$$(\vec{w} \cdot \vec{\nabla}) T_t^* = \frac{\mu}{\rho} \Delta T_t^r = \nu \Delta T_t^r \quad (8.6)$$

with the kinematic viscosity ν appearing as a diffusion coefficient. Since a turbomachinery flow is highly turbulent, this coefficient will of course be the eddy viscosity and not the much smaller molecular viscosity. Consequently, this coefficient is identical to the turbulent diffusion mixing coefficient ϵ_t , given by equation (7.5) (cf. Chapter 7).

This yields the following energy equation :

$$(\vec{w} \cdot \vec{\nabla}) T_t^* = \epsilon_t \Delta T_t^r \quad (8.7)$$

For a stator blade row, $T_t^* = T_t^r = H/C_p = T_t$, and a convection-diffusion equation for the total temperature T_t is obtained.

8.2 GENERAL MIXING EQUATION

Inserting the decomposition of the flow into Quasi-3D and S3 components [equation (2.1)] in equation (8.7) yields the following transport equation :

$$(\vec{w}_{Q3D} \cdot \vec{\nabla}) T_t^* = -(\vec{w}_{S3} \cdot \vec{\nabla}) T_t^* + \epsilon_t \Delta T_t^r \quad (8.8)$$

This equation shows very clearly that two sources of energy redistribution with respect to the original Quasi-3D energy distribution can be distinguished (rhs of the equation) :

- 1) Energy redistribution of a convective nature, due to the secondary flow field on the S3-plane (gradient term).
- 2) Energy redistribution of a diffusive nature, due to the effects of turbulence, controlled by the turbulent mixing coefficient ϵ_t (Laplacian term).

If both of the aforementioned redistribution effects are zero, the transport equation reduces to its familiar form for a Quasi-3D flow without mixing :

$$(\vec{w}_{Q3D} \cdot \vec{\nabla}) T_{i,Q3D}^* = 0 \quad (8.9)$$

where $T_{i,Q3D}^*$ represents the rotary total temperature distribution obtained from a Quasi-3D computation without mixing.

Subtracting equation (8.9) from equation (8.8) yields the following equation for the correction on the the Quasi-3D total temperature distribution :

$$(\vec{w}_{Q3D} \cdot \vec{\nabla}) [T_i^* - T_{i,Q3D}^*] = (\vec{w}_{Q3D} \cdot \vec{\nabla}) \delta T_i^* = -(\vec{w}_{S3} \cdot \vec{\nabla}) T_i^* + \epsilon_i \Delta T_i^* \quad (8.10)$$

This is the **fundamental mixing equation** to be solved : it determines the afterward total temperature correction δT_i^* , due to the mixing effects caused by secondary flows and turbulence, which has to be superposed on the original Quasi-3D total temperature distribution in order to obtain a more realistic prediction of the total temperature distribution inside an axial turbomachine.

8.3 EXPLICIT MIXING EQUATION AND NUMERICAL SOLUTION

Expressing equation (8.10) in cylindrical coordinates finally yields the following explicit equation :

$$\begin{aligned} w_{z,Q3D} \frac{\partial \delta T_i^*}{\partial z} = & -w_{r,Q3D} \frac{\partial \delta T_i^*}{\partial r} - w_{\theta,Q3D} \frac{1}{r} \frac{\partial \delta T_i^*}{\partial \theta} \\ & - w_{r,S3} \frac{\partial T_i^*}{\partial r} - w_{\theta,S3} \frac{1}{r} \frac{\partial T_i^*}{\partial \theta} \\ & + \epsilon_i \left(\frac{1}{r} \frac{\partial}{\partial r} \left[r \frac{\partial T_i^*}{\partial r} \right] + \frac{1}{r^2} \frac{\partial^2 T_i^*}{\partial \theta^2} \right) \end{aligned} \quad (8.11)$$

Remark that axial diffusion effects have been neglected.

The numerical solution of this equation is obtained by integration in the axial direction, going from one transversal S3-plane to another : in order to obtain the corrected total temperature on one S3-plane, the right-hand side of equation (8.11) is evaluated on the previous S3-plane and in this way the solution proceeds from inlet to outlet of the blade row.

The computation is started from the specified temperature distributions at inlet, whereby δT_1^* is set to zero.

8.4 BOUNDARY CONDITIONS

The boundary conditions, necessary to obtain a unique solution to equation (8.11) simply express that the turbomachinery flow is adiabatic, i.e. that there is no heat flux through any material wall. These boundary conditions are imposed by stating that the temperature gradient normal to any material wall is zero :

$$\vec{\nabla} T \cdot \vec{N} = 0 \quad (8.12)$$

where T is the static temperature and \vec{N} is the vector normal to the material wall considered (either an end-wall or a blade surface).

PART 3

NUMERICAL TECHNIQUES

CHAPTER 9

MESH GENERATION

9.1 INTRODUCTION

As explained in Chapter 1 (§ 1.3.3 - 1.3.4), the secondary flows causing convective mixing are assumed to be confined to a two-dimensional (r,θ) -plane, the transversal S3-plane. Furthermore, the domain to which the secondary flows are confined is delimited by the intersection of the S3-plane with the hub and casing end-walls and the surfaces of two adjacent blades or their imaginary extensions into the wake region (periodicity of turbomachinery flow), cf. Figure 9.1.

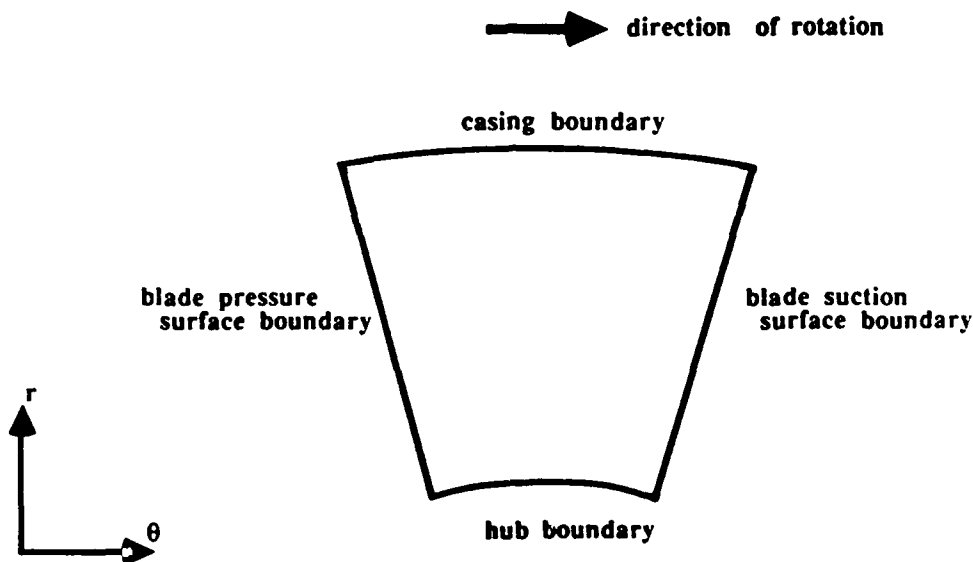


Figure 9.1 : Secondary flow domain on the transversal S3-plane

In principle, the secondary flow computation consists in determining the axial vorticity contributions of the different turbomachinery flow regions on this domain and computing the associated secondary flows in this domain by solving the quasi-harmonic Poisson equation for the secondary streamfunction (cf. Chapter 2, equation (2.10)), taking into account the boundary conditions (equation (2.13)).

In order to execute this computation numerically, a computational mesh must be generated on the secondary flow domain, i.e. the continuum of the surface has to be replaced by a finite number of individual points, distributed on the surface. Afterwards, the

equations can be discretized on this mesh, i.e. the partial differential equations on continuous field functions are approximated by algebraic relations between the values of the functions in the finite set of discrete mesh points. These algebraic relations are ultimately solved by the computer.

9.2 FINITE ELEMENT DISCRETIZATION

9.2.1 MOTIVATION

Three general methods for the discretization of space may be discerned, Hirsch (1988) : Finite Differences, Finite Elements and Finite Volumes. For the secondary flow computation, the Finite Element Method is selected to discretize the computational surface.

This choice is based on the following arguments :

- 1) The radial mixing computation procedure is developed with the purpose of integration into a Quasi-3D turbomachinery flow computation code based on Finite Elements, Hirsch & Warzée (1976, 1979). Thus, selecting Finite Elements for the secondary flow computation means that the implementation of the radial mixing procedure can draw on a number of already existing procedures of the main computation code.
- 2) A routine for solving Poisson equations is already available in the code, which yields the following advantages for the implementation of the numerical solution of the equation for the secondary streamfunction :
 - ease of integration
 - the existing Poisson-solver has been tested and used extensively and may be assumed to be error-free
 - little extra programming effort is required to adapt the existing Poisson solver to the radial mixing computation, thus reducing the likelihood of programming errors

Furthermore, the Poisson equation is an elliptic field problem, i.e. a perturbation in a particular point of a domain will eventually reach all points of the domain. Because of its fundamental principles, the Finite Element Method also has an "elliptical character" : the value of an arbitrary function inside an element is determined by the values of this function in all the nodal points of the element. In conclusion, there exists an equivalence between the physical behaviour of the equation and the numerical behaviour of the solution method, which is mostly an essential condition for a physically correct numerical simulation.

- 3) Finally, the Poisson equation (2.10) is solved on a curvilinear quadrilateral computational domain, taking into account the Dirichlet boundary condition (2.13). One of the specific advantages of the Finite Element Method is the very straightforward, sometimes even trivial, treatment of complicated, curved geometries and the associated boundary conditions.

9.2.2 BASIC PRINCIPLES

In the Finite Element Method, space is discretized by subdivision of the continuum into a number of contiguous elements of arbitrary size and shape, called 'Finite Elements'. In

general, any surface can be regarded as an assembly of triangular or quadrilateral elements (with rectilinear or curvilinear sides), the only restriction being that the elements do not overlap and cover the complete computational domain.

Next, within each element a certain number of points is chosen, which can be positioned along the element sides or inside the elements. These so-called 'nodal points' are the points where the numerical values of the unknown functions are to be determined.

The great advantage of this discretization method is the arbitrary size and shape of the elements, which allows to define unstructured meshes, i.e. the nodal points do not have to be distributed in a regular fashion.

9.2.3 SERENDIPITY ELEMENTS

For the secondary flow computation, the same elements as for the Quasi-3D computation are used, i.e. quadrilateral elements with eight nodes distributed on the element sides - four corner nodes and four mid-side nodes. Such elements, where the nodes are only defined on the element sides, are also called 'serendipity' elements (Zienkiewicz, 1977, Chapter 7), cf. Figure 9.2.

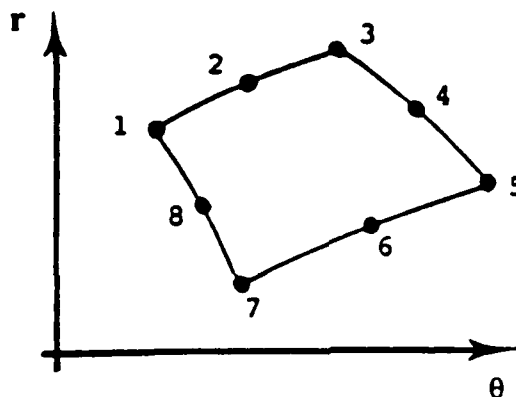


Figure 9.2 : Eight-node quadrilateral 'serendipity' element

9.2.4 FINITE ELEMENT SUBDIVISION OF COMPUTATIONAL SURFACE

Although the Finite Element approach allows the generation of wholly unstructured computational meshes, the computational surface on the S3-plane is subdivided into elements in a regular, structured way as follows.

A number of coordinate lines $r = cst$ is defined from hub to tip of the compressor annulus and a number of coordinate lines $\theta = cst$ is defined from pressure side to suction side of the passage between two adjacent blades. This grid of intersecting orthogonal coordinate lines creates an assembly of curvilinear quadrilaterals on the computational surface. Nodal points are chosen on the corners and the mid-sides of these quadrilaterals, hence forming a subdivision of the computational surface into eight-node 'serendipity' elements.

The mesh generation procedure outlined above produces a very structured mesh. However, the mesh is not necessarily uniform, since one can control the size of the elements. In practice, element size will be small in areas where large gradients of flow

properties occur, e.g. boundary layers and wakes, in order to obtain sufficient numerical accuracy. In other words, the mesh can be 'clustered' towards the material walls. The generation of a non-uniform but highly structured mesh presents the advantage that the formulas of the classical Finite Difference technique may also be applied to this mesh, see Chapter 10.

9.3 FINITE ELEMENT SHAPE FUNCTIONS

The subdivision of the computational domain into elements of arbitrary size and shape is one aspect of the Finite Element Method. The second aspect is the representation of the unknown functions : they are approximated by a linear combination of prescribed functions (called shape, interpolation or trial functions), where the coefficients are the values of the unknown functions in the nodal points to which the shape functions are associated. In classical finite element methods, these shape functions are locally defined polynomials.

So, if \tilde{u} is an approximate solution of the function $u(\vec{x})$, this can be written as :

$$\tilde{u}(\vec{x}) = \sum_i u_i N_i(\vec{x}) \quad (9.1)$$

where the summation extends over all nodes i associated to the element. The N_i are the local element shape functions, \vec{x} is the position vector and u_i is the value of the function $u(\vec{x})$ at node i .

In the case of the secondary flow computation, biquadratic shape functions are used. This choice is linked to the discretization of the computational surface into eight-node elements, cf. Zienkiewicz (1977), Chapter 7. For the secondary streamfunction, this results in the following formula :

$$\psi(r, \theta) = \sum_{i=1}^8 \psi_i N_i(r, \theta) \quad (9.2)$$

Where : ψ_i = value of the secondary streamfunction ψ in nodal point i

$N_i(r, \theta)$ = biquadratic shape function associated to nodal point i

9.4 ISOPARAMETRIC MAPPING

One of the basic aspects connected to the finite element formulation is the mapping between the physical space, where the element is defined in global coordinates, and the computational space, where the element is defined in local coordinates. Indeed, all the individual serendipity elements on the secondary flow domain are considered to be mappings on the physical (r, θ) -space of a single 'parent element' defined in the computational (ξ, η) -space. The mapping thus performs a transformation from local to global coordinates for every element individually and the whole domain is mapped on an element-by-element basis.

This parent element is defined as follows, Figure 9.3 :

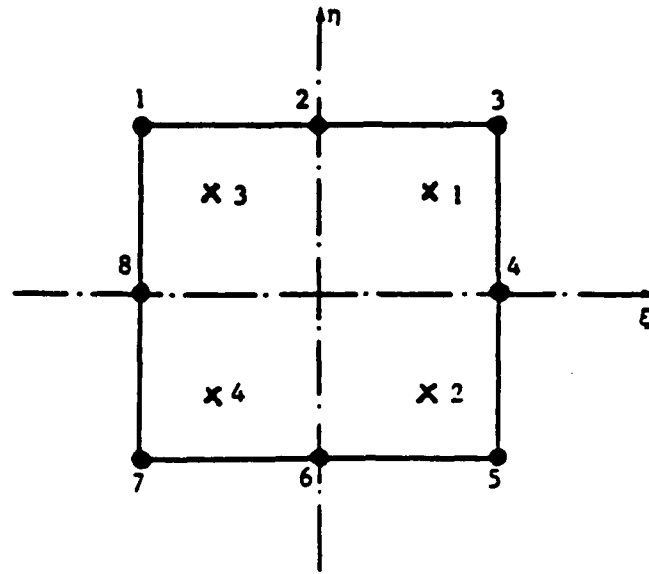


Figure 9.3 : Parent element in the computational space

The isoparametric mapping concept (Zienkiewicz, 1977, Chapter 8) consists in the geometrical mapping of the parent element onto an element in physical space through the following transformation formula, completely identical to the finite element representation of an unknown function :

$$\bar{x} = \sum_i \bar{x}_i N_i(\xi, \eta) \quad (9.3)$$

where \bar{x}_i is the position vector of a nodal point and \bar{x} is the position vector of a point inside the element, while the $N_i(\xi, \eta)$ are the parent element shape functions. In other words, the nodal points of the parent element in the computational space are mapped onto the nodal points of the element in the physical space (r, θ) , while any other point (ξ, η) inside the parent element is mapped onto a corresponding point in the physical element using a linear combination of the element shape functions.

Thus, isoparametric mapping consists in a complete analogy between the geometrical mapping and the representation of unknown functions : the same shape functions and nodal points are used. The mapping is conceptually sketched in Figure 9.4 .

The geometrical mapping of the parent element onto the physical surface is subject to certain requirements.

The first requirement is the condition for a one-to-one mapping : the determinant of the Jacobian matrix of the transformation must have the same sign at all points of the domain mapped. Otherwise, the parent element may have a violently distorted shape on the physical surface, leading to a non-uniqueness in the mapping (Zienkiewicz, 1977, Chapter 8). For 'serendipity' elements with biquadratic shape functions, the necessary conditions for this are that no internal angle within the physical element be greater than 180° and that the mid-side nodes are in the 'middle third' of the distance between adjacent corners.

The second requirement is that of 'geometrical conformability': the subdivision of a surface into curvilinear elements using the parent element should leave no gaps, i.e. the surface should be completely covered by the elements. This condition is satisfied if two adjacent elements are generated from 'parents' in which the shape functions satisfy continuity requirements (Zienkiewicz, 1977, Chapter 8).

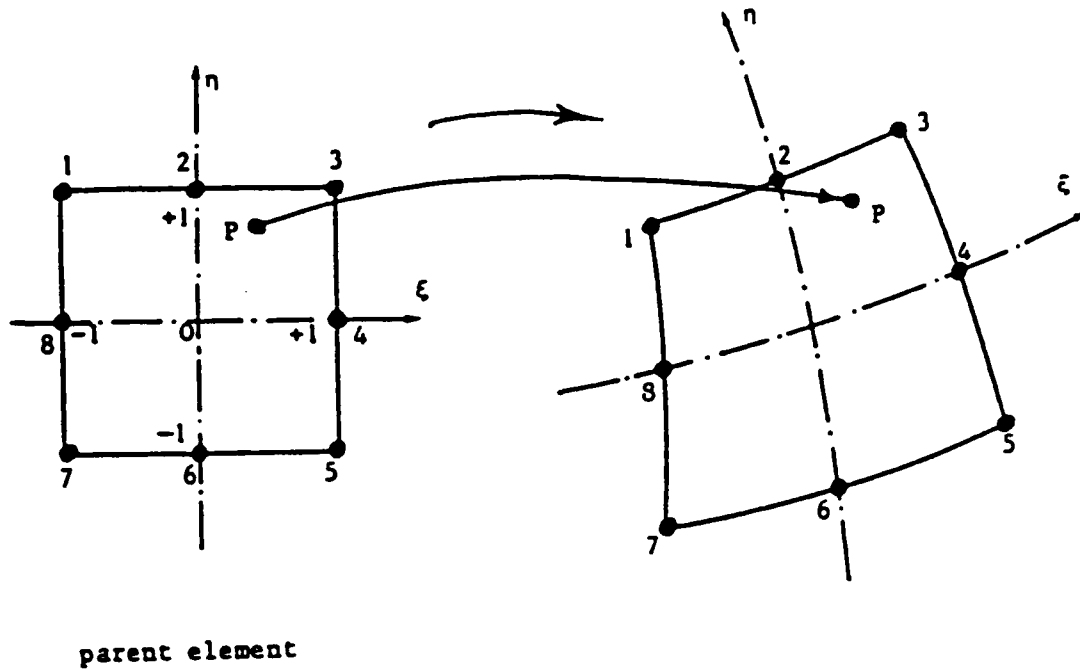


Figure 9.4 : Isoparametric mapping

CHAPTER 10

NUMERICAL SOLVING TECHNIQUES

10.1 INTRODUCTION

This chapter describes the most important techniques applied in the program to solve the equations derived in the previous chapters :

- 1) The Finite Element solution of the Poisson equation for the secondary flows, based on the Galerkin weighted residuals technique.
- 2) The numerical solution of the radial mixing equation, using a first-order integration.
- 3) The numerical computation of partial derivatives on a non-uniform structured mesh, using Finite Differences.

10.2 FINITE ELEMENT SOLUTION OF THE SECONDARY FLOW EQUATION

10.2.1 GALERKIN WEIGHTED RESIDUAL FORMULATION

The principal equation of the secondary flow computation is a quasi-harmonic Poisson equation (equation (2.10)) :

$$\vec{\nabla} \cdot \left(\frac{1}{\rho} \vec{\nabla} \psi \right) = \zeta_z - \zeta_{z,Q3D} = \zeta_{z,S3} \quad (10.1)$$

which determines the secondary flow field associated to the axial vorticity $\zeta_{z,S3}$ on a transversal S3-plane.

In the blade-to-blade part of the Quasi-3D turbomachinery flow computation program Q3DFLO, the blade-to-blade potential flow is computed from the following principal equation :

$$\frac{1}{r} \left\{ \frac{\partial}{\partial m} \left[k_1 \frac{\partial \phi}{\partial m} \right] + \frac{\partial}{\partial \theta} \left[k_2 \frac{\partial \phi}{\partial \theta} \right] + f(m, \phi) \right\} = 0 \quad (10.2)$$

where ϕ denotes the potential function, $k_1 = \rho B r$ and $k_2 = \rho B / r$ (where B denotes the blade-to-blade streamtube thickness).

The quasi-harmonic Poisson equation for the secondary streamfunction, cast in the same form as equation (10.2), reads explicitly (in cylindrical coordinates) :

$$\frac{1}{r} \left\{ \frac{\partial}{\partial r} \left[r \frac{1}{\rho} \frac{\partial \psi}{\partial r} \right] + \frac{\partial}{\partial \theta} \left[\frac{1}{\rho} \frac{1}{r} \frac{\partial \psi}{\partial \theta} \right] - r \zeta_{z,s3} \right\} = 0 \quad (10.3)$$

It is very clear that equations (10.2) and (10.3) possess an identical structure, and hence the quasi-harmonic Poisson equation can be solved by an adapted version of the numerical solution procedure for equation (10.2), obtained by putting $k_1 = r/\rho$, $k_2 = 1/\rho r$ and

$f(m, \theta) = -r \zeta_{z,s3}(r, \theta)$, while (m, θ) -coordinates have been substituted by (r, θ) -coordinates as follows :

$$\frac{\partial}{\partial m} \equiv \frac{\partial}{\partial r} \quad \text{and} \quad \frac{\partial}{\partial \theta} \equiv \frac{\partial}{\partial \theta} \quad (10.4)$$

The Dirichlet type boundary conditions for equation (10.3) (cf. § 2.4.2) can be considered as a special case of a generalized formulation for mixed boundary conditions :

$$k_1 \frac{\partial \psi}{\partial n} + \alpha (\psi - \psi_0) = 0 \quad (10.5)$$

where $\alpha = 0$ on the part of the boundary where Neumann boundary conditions are imposed while $\alpha = \infty$ on the remaining part of the boundary where Dirichlet boundary conditions are imposed (ψ_0 being the prescribed boundary value).

An approximative solution to equation (10.3) can be found, by postulating that the associated "weighted residual" of this solution is zero. In other words, the solution does not have to satisfy the equation locally, it should satisfy the equation only in a global way : the residual of the equation (the non-zero value of the left-hand side of the equation, obtained by substituting the approximate solution in the equation), multiplied by a weighting function and integrated over the entire solution domain must be zero :

$$\int_S W(r, \theta) R_S(r, \theta) dS + \int_C W(r, \theta) R_C(r, \theta) dC = 0 \quad (10.6)$$

With : $W(r, \theta)$ = weighting function

$R_S(r, \theta)$ = surface residual (in internal points of the computational domain)

$R_C(r, \theta)$ = boundary residual (in boundary points of the computational domain)

S = surface of computational domain

C = closed boundary of computational domain (material walls)

If the opposite of the left-hand side of equation (10.3) is selected as surface residual and the left-hand side of equation (10.5) multiplied by $1/r$ is selected as boundary residual,

integrating the first term of equation (10.6) by parts and applying vector analysis relations (formulae of Gauss and Green), substituting the unknown function ψ by its finite element approximation (9.2) and introducing the Galerkin procedure, which consists in taking as weighting functions W_j the shape functions N_j :

$$W_j(r, \theta) = N_j(r, \theta) \quad (10.7)$$

the following equation is obtained for each j (j runs from 1 to n, the total number of nodal points) :

$$\sum_{i=1}^n \left\{ \int_{\Omega} \left[\frac{r}{\rho} \frac{\partial N_i}{\partial r} \frac{\partial N_j}{\partial r} + \frac{1}{\rho r} \frac{\partial N_i}{\partial \theta} \frac{\partial N_j}{\partial \theta} \right] dr d\theta \right\} \psi_i = - \int_{\Omega} [N_j r \zeta_{z,S3}] dr d\theta \quad (10.8)$$

where it was implicitly assumed that the choice of shape functions is such that the Dirichlet boundary conditions are automatically satisfied and the weighting functions are zero on the boundary. It may be easily shown that these requirements are fulfilled by the biquadratic shape functions.

For a detailed explanation of the Finite Element formulation of a 2D Poisson-problem, consult Zienkiewicz (1977), Chapter 3.

Remark that the summation is extended to n, the total number of nodal points : although the streamfunction is interpolated locally within an element from its value in the eight nodal points of the element, the integral is expressed over the entire computational domain, i.e. over all elements.

Furthermore, for the nodal points on the boundary of the transversal S3-plane, equation (10.8) may be directly replaced by the Dirichlet boundary condition :

$$\psi_j = 0 \quad \text{if nodal point } j \text{ is located on the boundary } C \quad (10.9)$$

Finally, the following linear system of n algebraic equations in n unknowns ψ_i is obtained :

$$[K] \{\psi\} = \{\Omega\} \quad \text{or} \quad K_{ji} \psi_i = \Omega_j \quad (10.10)$$

where $\{\psi\}$ is the vector which contains the values of the unknown streamfunction in the n nodal points :

$$\{\psi\}_i = \psi_i \quad (10.11)$$

while

$$\{\Omega\}_j = - \int_{\Omega} [N_j r \zeta_{z,S3}] dr d\theta \quad \text{source vector} \quad (10.12)$$

and

$$[K]_{ji} = \int_{\Omega} \left[\frac{r}{\rho} \frac{\partial N_j}{\partial r} \frac{\partial N_i}{\partial r} + \frac{1}{\rho r} \frac{\partial N_j}{\partial \theta} \frac{\partial N_i}{\partial \theta} \right] dr d\theta \quad \text{stiffness matrix} \quad (10.13)$$

Remark that the system of equations is linear because the source vector is assumed to be independent of the solution $\{\psi\}$. Indeed, the secondary flows are reconstructed from the axial vorticity contribution $\zeta_{z,s3}$ to compute the radial redistribution of flow quantities, but this is applied in a corrective fashion, i.e. a second through-flow or Quasi-3D computation, taking into account the secondary flows, resulting in altered velocities and thermodynamic parameters and hence also influencing the axial vorticity distribution, is not executed.

In practice, the linear system is resolved by the frontal method, a variant of the classical Gauss elimination procedure for linear systems, which is especially adapted to the finite element method, Zienkiewicz (1977), Chapter 24. The frontal scheme works element by element, forming only that part of the stiffness matrix belonging to the 'front' (consisting of the nodes of the elements currently being assembled). After an element is introduced, an equation of the system which is completed, is eliminated by Gauss elimination and the associated node is removed from the front. In this way, the solution front proceeds through the computational domain, continuously eliminating equations from the assembled elements until the whole domain has been covered and finally, the solution to the system of equations is obtained.

10.2.2 SOME REMARKS ON NUMERICAL TECHNIQUES

It is important to note that an element $[K]_{ji}$ of the stiffness matrix will be zero when the nodes i and j do not belong to the same element, because the associated shape functions are only defined in the element to which the node belongs and are zero everywhere else :

$$[K]_{ji} = 0 \quad \text{if node } i \text{ and node } j \text{ belong to different elements} \quad (10.14)$$

This means that the coefficient matrix of the linear system will have a sparse structure, which is advantageous for its numerical solution.

In practice, the coefficients of the stiffness matrix K will be evaluated in the coordinates (ξ, η) of the computational space of the parent element through the isoparametric mapping from the computational space to the physical space (equation (9.3)). It may be shown, see for instance Hirsch (1988), that these elements assume the following form in computational space :

$$[K]_{ji} = \int_{\Omega_e} k [\bar{\nabla}_x N_j \cdot \bar{\nabla}_x N_i] dr d\theta = \int_{\Omega_e} k [\bar{\nabla}_{\xi} N_j (\bar{J}^T \otimes \bar{J}) \cdot \bar{\nabla}_{\xi} N_i] \frac{1}{J} d\xi d\eta \quad (10.15)$$

The first integral is the vector formulation of equation (10.13) (with $k = r/\rho$), the subscript x referring to the physical (r,θ) -coordinates, while the second integral is taken over the parent element, the subscript ξ referring to the computational (ξ,η) -coordinates. J is the determinant of the Jacobian matrix \bar{J} of the isoparametric mapping (derivatives of (ξ,η) -coordinates with respect to (r,θ) -coordinates) and \bar{J}^T is the transposed Jacobian matrix.

Expression (10.15) for the stiffness matrix coefficients in the computational space is evaluated numerically by an approximative integration technique, two-dimensional Gauss-integration, which reads in general form

$$\iint_{\xi,\eta=-1}^{\xi,\eta=+1} \phi(\xi,\eta) d\xi d\eta = \sum_1^{ngauss} \sum_1^{ngauss} H_i H_j \phi(a_i, a_j) \quad (10.16)$$

for the integration of an arbitrary function $\phi(\xi,\eta)$ over the parent element.

Thus, the integral is evaluated as a sum of the weighted values of the integrand in a finite number of so-called Gauss points, distributed within the parent element (usually 2x2 or 3x3). The a_i are the local coordinates of the Gauss points and the H_i are the corresponding weighting values.

10.3 NUMERICAL SOLUTION OF RADIAL MIXING EQUATION

10.3.1 NUMERICAL INTEGRATION TECHNIQUE

The basic radial mixing equation (8.11) can be expressed in the following general form :

$$\frac{\partial}{\partial z} \delta T_i^* = f(r, \theta, z, \bar{W}_{Q3D}, \bar{W}_{S3}, \epsilon_i, \delta T_i^*, T_i^*, T_i^r) \quad (10.17)$$

From this, a first-order integration formula can be derived as follows :

$$\delta T_i^*(z+\Delta z) = \delta T_i^*(z) + \Delta z f(r, \theta, z, \bar{W}_{Q3D}, \bar{W}_{S3}, \epsilon_i, \delta T_i^*, T_i^*, T_i^r) \quad (10.18)$$

where Δz represents the axial distance between two consecutive transversal S3-planes, while all the quantities on the right-hand side are expressed on the first S3-plane (the 'upstream' S3-plane) at axial location z .

Hence, if all the quantities on the 'upstream' S3-plane are known, this formula allows to calculate the correction to be applied to the Quasi-3D total temperature distribution on a 'downstream' S3-plane at axial location $z+\Delta z$.

The partial derivatives occurring in the right-hand side of equation (10.18) (cf. equation (8.11)) are numerically computed from the second-order accurate finite difference formulas for partial derivatives on a non-uniform structured mesh, which are derived in § 10.4.

10.3.2 NUMERICAL TREATMENT OF BOUNDARY CONDITIONS

Equation (8.11) is expressed on the internal points of the computational domain (cf. Chapter 2, Figure 2.2). As the adiabatic boundary condition is imposed, i.e. zero heat flux across any domain boundary (material wall), the temperature gradient normal to any material wall is zero (cf. equation (8.12)). This can be expressed as :

$$\frac{\partial T}{\partial n} = 0 \quad (10.19)$$

where n refers to the direction normal to the boundary.

This boundary condition is discretized as follows.

Figure 10.1 represents three points of the non-uniform structured mesh, in a direction normal to the domain boundary :

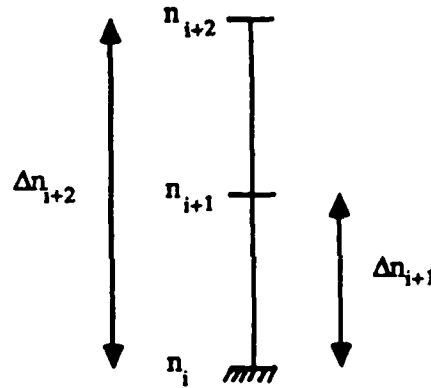


Figure 10.1 : Three mesh points of a non-uniform mesh, normal to a domain boundary

The distribution of the static temperature T in the vicinity of a boundary may be written as a function of the static temperature at the boundary and the derivatives of the static temperature in the direction normal to the boundary through the use of Taylor expansions :

$$T(n_{i+1}) = T(n_i) + \left(\frac{\partial T}{\partial n}\right)_{n_i} \Delta n_{i+1} + \frac{1}{2} \left(\frac{\partial^2 T}{\partial n^2}\right)_{n_i} (\Delta n_{i+1})^2 + \dots \quad (10.20a)$$

$$T(n_{i+2}) = T(n_i) + \left(\frac{\partial T}{\partial n}\right)_{n_i} \Delta n_{i+2} + \frac{1}{2} \left(\frac{\partial^2 T}{\partial n^2}\right)_{n_i} (\Delta n_{i+2})^2 + \dots \quad (10.20b)$$

The second-order terms are eliminated between these equations by multiplying the first equation by $(\Delta n_{i+2})^2$, multiplying the second equation by $(\Delta n_{i+1})^2$, and subtracting the second equation from the first equation. Next, the equation obtained is divided by

$\Delta n_{i+1} \Delta n_{i+2}$, and the first derivative $(\partial T / \partial n)_{n_i}$ is isolated in the left-hand side and is put equal to zero, which finally yields the following numerical expression for the adiabatic boundary condition :

$$T(n_i) = \frac{(\Delta n_{i+2})^2 T(n_{i+1}) - (\Delta n_{i+1})^2 T(n_{i+2})}{(\Delta n_{i+2})^2 - (\Delta n_{i+1})^2} \quad (10.21)$$

From this equation, it follows that the static temperature at the domain boundaries is completely determined by the values of the static temperature in the internal points of the domain.

10.4 NUMERICAL COMPUTATION OF PARTIAL DERIVATIVES

10.4.1 INTRODUCTION

The theoretical formulation of all computational modules is based on partial differential equations. Therefore, it is necessary to develop numerical formulas for partial derivatives in order to be able to compute the different terms of the equations.

Although the radial mixing method is developed as an extension to a turbomachinery flow computation code based on the Finite Element Method, the numerical computation of partial derivatives will be based on finite difference formulas for a non-uniform two-dimensional structured mesh, because the mesh on the computational domain is highly structured. Although the Finite Element Method puts no restrictions on the irregularity of the mesh, this approach is chosen because the finite difference formulas can be directly computed, whereas estimating the partial derivatives using finite element shape functions involves extra computations because the derivatives of the shape functions have to be recomputed for every element.

In this section, the general second-order accurate finite difference formulas for any first-order and second-order partial derivative on a non-uniform, structured, two-dimensional mesh will be derived.

10.4.2 SECOND-ORDER FINITE DIFFERENCE FORMULA FOR A FIRST DERIVATIVE

Consider Figure 10.2, which represents three points of a non-uniform mesh in any coordinate direction.

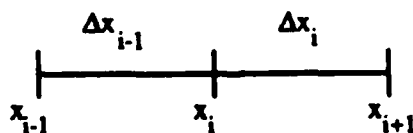


Figure 10.2 : Three mesh points of a non-uniform mesh

The value of an arbitrary function f in the points x_{i+1} and x_{i-1} can be expressed as a function of the values of f and the derivatives of f with respect to x in the point x_i by the use of Taylor expansions :

$$f(x_{i+1}) = f(x_i) + \left(\frac{\partial f}{\partial x}\right)_{x_i} \Delta x_i + \frac{1}{2} \left(\frac{\partial^2 f}{\partial x^2}\right)_{x_i} (\Delta x_i)^2 + \dots \quad (10.22a)$$

$$f(x_{i-1}) = f(x_i) - \left(\frac{\partial f}{\partial x}\right)_{x_i} \Delta x_{i-1} + \frac{1}{2} \left(\frac{\partial^2 f}{\partial x^2}\right)_{x_i} (\Delta x_{i-1})^2 + \dots \quad (10.22b)$$

Subsequently, the second order terms are eliminated between these two equations by multiplying the first equation by $(\Delta x_{i-1})^2$, multiplying the second equation by $(\Delta x_i)^2$ and subtracting the second from the first. Next, the equation obtained is divided by $\Delta x_i \cdot \Delta x_{i-1}$ and the partial derivative is isolated in the left-hand side, yielding :

$$\left(\frac{\partial f}{\partial x}\right)_i = \frac{\Delta x_{i-1}}{\Delta x_i} \frac{1}{[\Delta x_{i-1} + \Delta x_i]} f(x_{i+1}) - \frac{\Delta x_i}{\Delta x_{i-1}} \frac{1}{[\Delta x_{i-1} + \Delta x_i]} f(x_{i-1}) + \left[\frac{\Delta x_i - \Delta x_{i-1}}{\Delta x_{i-1} \Delta x_i} \right] f(x_i) \quad (10.23)$$

This is the general centered finite difference formula for the partial derivative of the first order on a non-uniform structured mesh. For a uniform mesh this formula reduces to the classical centered formula.

The formula is second-order accurate since the largest term of the truncation error is given by :

$$\text{Error} = - \frac{\Delta x_{i-1} \Delta x_i}{6} \left(\frac{\partial^3 f}{\partial x^3}\right)_i \quad (10.24)$$

10.4.3 SECOND-ORDER FINITE DIFFERENCE FORMULA FOR A SECOND DERIVATIVE

The value of an arbitrary function f in the points x_{i+1} and x_{i-1} can be expressed as a function of the values of f and the derivatives of f with respect to x in the point x_i by the use of Taylor expansions :

$$f(x_{i+1}) = f(x_i) + \left(\frac{\partial f}{\partial x}\right)_{x_i} \Delta x_i + \frac{1}{2} \left(\frac{\partial^2 f}{\partial x^2}\right)_{x_i} (\Delta x_i)^2 + \frac{1}{6} \left(\frac{\partial^3 f}{\partial x^3}\right)_{x_i} (\Delta x_i)^3 + \dots \quad (10.25a)$$

$$f(x_{i-1}) = f(x_i) - \left(\frac{\partial f}{\partial x}\right)_{x_i} \Delta x_{i-1} + \frac{1}{2} \left(\frac{\partial^2 f}{\partial x^2}\right)_{x_i} (\Delta x_{i-1})^2 - \frac{1}{6} \left(\frac{\partial^3 f}{\partial x^3}\right)_{x_i} (\Delta x_{i-1})^3 + \dots (10.25b)$$

Subsequently, the third order terms are eliminated between these two equations by multiplying the first equation by $(\Delta x_{i-1})^3$, multiplying the second equation by $(\Delta x_i)^3$ and adding both equations. Next, the equation obtained is divided by $(\Delta x_{i-1})^2 (\Delta x_i)^2$ and the second derivative is isolated in the left-hand side, yielding :

$$\begin{aligned} \left(\frac{\partial^2 f}{\partial x^2}\right)_i = \frac{2}{[\Delta x_{i-1} + \Delta x_i]} \left\{ \frac{\Delta x_{i-1}}{(\Delta x_i)^2} [f(x_{i+1}) - f(x_i) - \left(\frac{\partial f}{\partial x}\right)_i \Delta x_i] \right. \\ \left. + \frac{\Delta x_i}{(\Delta x_{i-1})^2} [f(x_{i-1}) - f(x_i) + \left(\frac{\partial f}{\partial x}\right)_i \Delta x_i] \right\} \quad (10.26) \end{aligned}$$

Substitution of the first-order partial derivatives by the centered finite difference formula (10.23) finally results in the following equation :

$$\boxed{\left(\frac{\partial^2 f}{\partial x^2}\right)_i = \frac{2}{[\Delta x_{i-1} + \Delta x_i]} \left\{ \left[\frac{1}{\Delta x_i}\right] f(x_{i+1}) + \left[\frac{1}{\Delta x_{i-1}}\right] f(x_{i-1}) - \left[\frac{\Delta x_i + \Delta x_{i-1}}{\Delta x_i \Delta x_{i-1}}\right] f(x_i) \right\}} \quad (10.27)$$

This is the general centered finite difference formula for the partial derivative of the second order on a non-uniform structured mesh. For a uniform mesh this formula reduces to the classical centered formula.

If only the first two terms of the truncation error associated to formula (10.27) are retained, this error may be approximated as :

$$\text{Error} = \frac{1}{3} (\Delta x_i - \Delta x_{i-1}) \left(\frac{\partial^3 f}{\partial x^3}\right)_i - \frac{(\Delta x_i)^3 + (\Delta x_{i-1})^3}{12 (\Delta x_i + \Delta x_{i-1})} \left(\frac{\partial^4 f}{\partial x^4}\right)_i \quad (10.28)$$

It is important to observe the presence of a truncation error term proportional to the difference of two consecutive mesh spacings Δx_i and Δx_{i-1} . If the mesh size varies abruptly, this will lead to first-order accuracy only. However, if the mesh size varies smoothly, then the first term of equation (10.28) will be near to zero, and the truncation error will be dominated by the second term, which is second-order accurate.

PART 4

RESULTS AND CONCLUSIONS

CHAPTER 11

RESULTS

11.1 INTRODUCTION

In this chapter, the results of secondary flow computations based on the method developed in the previous chapters are compared with experimental flow data. From these comparisons, conclusions with respect to the validity of the present secondary flow computation method will be drawn.

11.2 EXPERIMENTAL SET-UP

11.2.1 GENERAL FEATURES OF TESTCASE

The testcase selected for comparisons between theory and experiment is the VUB cascade, a linear compressor cascade designed and built at the Department of Fluid Mechanics of the VUB and used for the experimental investigation of the three-dimensional structure of the flow field in compressor blade rows.

The cascade is positioned between two horizontal flat plates in the test section at the end of a small low-speed windtunnel (Mach number = 0.1), designed and built at the Department.

The most important geometrical parameters of the cascade are listed below :

Number of blades	7
Aspect ratio	1.0
Solidity	1.111
Span	0.2 m
Stagger	10°
Chord	0.2 m
Metal inlet angle	32.5° (absolute)
Metal outlet angle	-12.5° (absolute)
Turning angle	45°
Blading	NACA 65-18(A10)10
Design inlet flow angle	30°
Design outlet flow angle	-4°
Design flow turning angle	34°
Design incidence	-2.5°
Design deviation	8.5°

The use of low aspect ratio NACA 65-series blading with a 45° blade turning angle is typical for current compressor designs.

For a more detailed description of the experimental set-up, the reader is referred to the paper by Kang and Hirsch (1991) which describes the experimental research performed on the cascade.

11.2.2 AVAILABLE EXPERIMENTAL DATA

The three-dimensional flow pattern in the VUB cascade has been thoroughly investigated by means of hot-wire anemometry, Kang and Hirsch (1991) : at different transversal planes upstream of the cascade, inside the cascade and downstream of the cascade, spanwise traverses were made at a number of pitchwise locations, yielding local spanwise profiles of axial, radial and tangential velocities and of outlet flow angles. Hence, extensive experimental data is available for comparison with numerical computations.

All measurements were made for an identical inlet velocity profile with the following general characteristics :

Mean axial inlet velocity (mainstream)	23.7 m/s
Reynolds number	316000 (based on span)
Hub/tip inlet boundary layer thickness	approx. 10% of span

The mass-averaged experimental inlet and outlet flow angles differ slightly from the design values mentioned above :

Experimental inlet flow angle	29.3°
Experimental outlet flow angle	-2.5°
Experimental flow turning angle	31.8°

Velocities were measured with an accuracy of 1% of the inlet flow velocity at midspan, i.e. with an accuracy of about 0.25 m/s, while the uncertainty of the measured flow angles is better than 1°. Thus, taking into account the measurement uncertainty, the experimental flow angles correspond to the design values.

For detailed information about the experimental research program on the VUB cascade, consult Kang and Hirsch (1991).

11.3 OVERVIEW OF COMPUTATIONAL PROGRAM

In order to assess the validity of the proposed secondary flow computation method, the following computations were performed and compared with the corresponding experimental data (cf. § 11.4) :

- 1) Computations inside the blade row, including viscous profile boundary layer computations
 - a) Fully inviscid computation across the entire span (classical secondary flow theory : no end-wall boundary layers)
 - b) Inviscid computation in the core flow region coupled to a viscous integral end-wall boundary layer computation

Results are presented for transversal S3-planes located at 44% chord, 66% chord and 99% chord axial distance downstream of the blade row leading edge.

2) Computations in the wake region downstream of the blade row trailing edge, including viscous wake layer computations

a) Fully inviscid computation across the entire span (classical secondary flow theory : no end-wall boundary layers)

b) Inviscid computation in the core flow region coupled to a viscous integral end-wall boundary layer computation

Results are presented for two transversal S3-planes in the 'near' wake (104% chord and 112% chord axial distance downstream of the blade row leading edge or 4% chord and 12% chord downstream of the blade row trailing edge) and one transversal S3-plane in the 'far' wake which coincides with the last experimental traversing plane (125% chord axial distance downstream of the leading edge or 25% downstream of the trailing edge) .

All computational testcases were run with an inlet velocity profile identical to the experimental situation : identical flow velocities, identical inlet flow angles and identical inlet boundary layer thicknesses (cf. Figure 11.1).

The computational mesh on the transversal S3-plane contained 29x31 gridpoints, with radial clustering towards the end-walls to obtain accurate EWBL computations (at least five radial points in each EWBL) and tangential clustering towards the blades or the wake center to obtain accurate profile boundary layer or wake computations (at least five tangential points in the viscous layers at either side of the blade or the wake center).

11.4 DISCUSSION OF RESULTS

All of the computational results are presented in the same format :

The axial location of the transversal S3-plane is expressed in % chord, measured in the downstream direction from the blade row leading edge, while the pitchwise location in the S3-plane is expressed in % pitch, measured from the pressure side of the passage (0% pitch) towards the suction side of the passage (100% pitch).

At each pitchwise location, the spanwise distributions of three physical quantities – tangential velocity component, radial velocity component and tangential outlet flow angle – are compared for three different cases : a 'fully inviscid' computation (represented by square symbols), an inviscid computation coupled to a viscous integral EWBL computation (represented by circular symbols), and experiment (represented by triangular symbols).

In addition, at each transversal S3-plane the pitch-averaged spanwise profiles of the tangential velocity component, the radial velocity component and the tangential outlet flow angle are compared for the three different cases.

Please note that the experimental results were obtained from a spanwise traverse from one of the end-walls to midspan, because due to the symmetrical geometry and the symmetrical inlet velocity profile (with respect to the midspan position), it was assumed that the flow field is also symmetrical with respect to the midspan position.

The computational results are presented for the entire span however, and therefore the experimental results have also been presented in this format by extending the results from the experimental half-span traverse to the other half of the span through mirror symmetry (with respect to the midspan position).

11.4.1 RESULTS AT 44% CHORD

The results for the transversal S3-plane at 44% chord are presented on Figure 11.3a to Figure 11.3l (pages 93-104).

11.4.1.1 Spanwise profiles of tangential velocity at different pitchwise locations

The profiles of total tangential velocity for the fully inviscid computation and the inviscid + EWBL computation agree very well with the experimental profiles, except for a slight overestimation in the midspan region towards the pressure side. There is excellent agreement between theory and experiment in the end-wall boundary layers across the entire pitch, except near the suction side (from about 82% pitch onwards), where the experimental profile is steeper than the theoretically predicted profile.

Remark that the fully inviscid and the inviscid + EWBL approach yield identical results, because the boundary layer growth is yet too small to give rise to differences between the inviscid approach, which cannot simulate boundary layer growth, and the end-wall boundary layer computation which does incorporate this effect.

11.4.1.2 Spanwise profiles of radial velocity at different pitchwise locations

The radial velocity profiles of the inviscid + EWBL approach agree well with the experimental profiles near the pressure side (except very close to the profile wall, at 1% pitch), but they underestimate the magnitude of the radial flow at mid-pitch and near the suction side substantially, although qualitative agreement is good.

Identical conclusions hold for the results of the fully inviscid approach, although the results from the inviscid + EWBL approach are slightly better.

The discrepancy in the mid-pitch region can be attributed to a high relative measurement error : radial velocities are of the order of 0.50 m/s in this region, while the measurement accuracy is about 0.25 m/s, which amounts to a possible measurement error of 50%.

The lesser agreement near the suction side is probably due to the inability of the method to simulate separated flows : the recent experimental investigations of the flow in the cascade (Kang and Hirsch, 1990) have revealed the presence of a large separation bubble on the suction surface of the blade, which may induce strong radial flows (cf. Figure 11.2). This region of separated flow originates at approximately 50% chord from the leading edge. Hence, the accuracy of the computational results close to the suction side must be treated with some reservation.

In all the experimental local profiles, large 'peaks' of radial velocity are observed very close to the end-walls. These results are suspected to be erroneous as a result of large measurement errors induced by the proximity of the end-walls.

11.4.1.3 Spanwise profiles of outlet flow angle at different pitchwise locations

The spanwise variation of the outlet flow angle is predicted remarkably well for both computational approaches (fully inviscid and inviscid + EWBL), including the end-wall boundary layer regions, except near the suction side (from about 82% pitch onwards), where the experimental profile is steeper than the theoretically predicted profile.

11.4.1.4 Pitch-averaged spanwise profiles

The theoretical and experimental pitch-averaged spanwise profiles of tangential velocity and of tangential outlet flow angle agree extremely well : they are identical over almost the

entire pitch, except near the suction side end-walls (from 82% pitch onwards), where the experimental profile is steeper than the theoretically predicted profile.

Agreement between the theoretical and experimental pitch-averaged radial velocity profiles is also very satisfactory, except near the end-walls, where the experimental profile exhibits the large 'peaks' which were also observed in the local profiles and which are suspected to be the result of wall proximity effects on the measurement probe.

Remark that there is no difference between the results from the inviscid + EWBL approach and the fully inviscid approach, because the end-wall boundary layer growth is yet too limited to have noticeable effects.

11.4.2 RESULTS AT 66% CHORD

The results for the transversal S3-plane at 66% chord are presented on Figure 11.4a to Figure 11.4l (pages 105-116). The conclusions are essentially identical with those for the results at 44% chord.

However, there is one exception : near the suction side, there is a discrepancy between the computed and the experimental tangential velocities and outlet flow angles which extends over the full span of the passage and which increases from about 1.5 m/s, respectively 5° at 75% pitch to about 2.5 m/s, respectively about 10° at 91% pitch. This discrepancy is also found in the pitch-averaged tangential velocity profile, but not in the pitch-averaged outlet flow angle profile where the alternating signs of the discrepancies at pressure and suction side have compensated each other.

It is believed that this discrepancy is due to the existence of the large separation bubble on the suction side of the blade, mentioned in the preceding paragraph. This is a region of strongly three-dimensional flow effects which may give rise to flow deflections that deviate considerably from the mainstream flow deflection. Hence, the prediction of these flow deflections is not accurate, even with the inclusion of profile boundary layer effects in the computations.

The observed difference between the theoretical and experimental pitch-averaged radial velocity profiles can be adequately explained by the relative measurement error of 50% to 100%.

Finally, remark that the difference between the fully inviscid and the inviscid + EWBL approach is becoming more apparent due to the increased boundary layer growth. In general, the approach which includes end-wall boundary layer computations is superior because of the accurate simulation of boundary layer growth and the associated accurate prediction of boundary layer thickness.

11.4.3 RESULTS AT 99% CHORD (TRAILING EDGE)

The results for the transversal S3-plane at 99% chord are presented on Figure 11.5a to Figure 11.5n (pages 117-130).

11.4.3.1 Spanwise profiles of tangential velocity at different pitchwise locations

The profiles of total tangential velocity for the inviscid + EWBL computation agree well with the experimental profiles, except for the midspan regions near pressure side (up to 7% pitch) and near suction side (from 85% pitch onwards), where the computation over-estimates the tangential velocity with respect to the experimental values.

The 'peaks' which appear at 15% span and 85% span in the experimental spanwise profile very close to the suction side (from 95% pitch onwards) point to the existence of horseshoe vortices near the hub and the tip of the cascade. Indeed, it can be inferred from the experimentally determined structure of the cascade flow field (Figure 11.2), that the flow near the suction side of the trailing edge may be heavily disturbed by one of the legs of the horseshoe vortices of the adjacent blade. Since the effect of horseshoe vortices is not included in the proposed theoretical secondary flow model (cf. Chapter 2), this explains the discrepancy between the computational results and the experimental results observed near the suction side of the passage.

The results of the fully inviscid computation are obviously identical to those of the inviscid + EWBL computation in the midspan region, but in the end-wall region the agreement between the profile of the fully inviscid computation and the experimental profile is less satisfactory: the velocity at the wall is severely overestimated by the inviscid computation, due to the absence of the velocity-decreasing wall friction in the model.

11.4.3.2 Spanwise profiles of radial velocity at different pitchwise locations

The radial velocity profiles of the inviscid + EWBL approach agree well with the experimental profiles near the pressure side, while they underestimate the magnitude of the radial flow near the suction side substantially, although qualitative agreement is good. Identical conclusions hold for the results of the fully inviscid approach, although the results from the inviscid + EWBL approach are slightly better.

The lesser agreement near the suction side is probably again due to the presence of the large separation bubble on the suction surface of the blade, which may induce strong radial flows which are not accounted for in the theoretical model. Also, the presence of horseshoe vortices may induce extra radial flows which are not accounted for in the proposed theoretical secondary flow model.

Hence, the accuracy of the computational results close to the suction side must be treated with some reservation.

The 'peaks' near the hub (at about 8% span) and the tip (at about 88% span) in the experimental spanwise profiles near the suction side clearly point to the existence of horseshoe vortices at hub and tip.

11.4.3.3 Spanwise profiles of outlet flow angle at different pitchwise locations

The spanwise variation of the outlet flow angle is remarkably well predicted in the midpitch region for both computational approaches (fully inviscid and inviscid + EWBL), including the end-wall boundary layer regions. Although it was found that the fully inviscid computation overestimated the tangential velocity component near the end-walls, this effect is compensated by an identical result for the axial velocity component, thus yielding a correct outlet flow angle over the entire span.

However, very close to the pressure side (5% pitch or less) the agreement is less satisfactory, while close to the suction side (from 90% pitch onwards) the 'peaks' in the experimental profile (around 15% span and 85% span) again point to the existence of horseshoe vortices near hub and tip, which are not accounted for in the theoretical flow model.

11.4.3.4 Pitch-averaged spanwise profiles

The theoretical and experimental pitch-averaged spanwise profiles of tangential velocity agree very well in the case of the inviscid + EWBL computation. The pitch-averaged profile of the fully inviscid computation deviates considerably from the experimental pitch-averaged profile in the vicinity of the end-walls, due to the reason cited in § 11.4.3.1.

The theoretical and experimental pitch-averaged spanwise profiles of radial velocity do not seem to agree very well, but it must be stressed that the averaged values have an order of magnitude of 0.25 m/s, equal to the measurement error, amounting to a possible relative measurement error of 100% !!

The theoretical and experimental pitch-averaged spanwise profiles of tangential outlet flow angle agree very well for both computational approaches.

Remark that for each of the three physical quantities, the 'peaks' in the local spanwise profiles near the suction side (due to the presence of horseshoe vortices) have been smoothed out in the averaging process because they are a very local phenomenon.

11.4.4 RESULTS AT 104% CHORD (NEAR WAKE)

The results for the transversal S3-plane at 104% chord are presented on Figure 11.6a to Figure 11.6l (pages 131-142).

11.4.4.1 Spanwise profiles of tangential velocity at different pitchwise locations

The profile of total tangential velocity for the inviscid + EWBL approach agrees very well with the experimental profile, except near the pressure side of the wake (up to about 15% pitch), where the tangential velocity is overestimated near the end-walls and slightly underestimated in the midspan region.

Close to the suction side (from about 90% pitch onwards), the horseshoe vortices again create 'peaks' in the experimental profile at 15% span and 85% span and also affect the velocity profile in the midspan region, leading to unsatisfactory agreement between theory and experiment.

The profile of the fully inviscid approach differs considerably from the experimental profile in the vicinity of the end-walls, again due to the absence of wall friction effects in the inviscid model. Remark also that the fully inviscid computation underestimates the thickness of the end-wall boundary layers with respect to the inviscid + EWBL computation, since the inviscid model does not include the effect of boundary layer growth.

11.4.4.2 Spanwise profiles of radial velocity at different pitchwise locations

The radial velocity profiles of the inviscid + EWBL approach agree reasonably well with the experimental profiles over the entire pitch. The results of the fully inviscid approach are less satisfactory, although qualitative agreement is good.

The difference between the theoretical and the experimental profiles in the mid-pitch region (20% pitch - 60% pitch) may again be attributed to measurement inaccuracies, since the observed velocities and the measurement accuracy are of the same order of magnitude.

The better agreement near the suction side in the wake than near the suction side inside the blade row (from about 75% pitch onwards) is probably due to the fact that the mixing of pressure and suction sides of the wake significantly reduces the suction side separation bubble in a fashion comparable to reattachment. Hence, the accuracy of the computational results close to the suction side is better in the wake region.

11.4.4.3 Spanwise profiles of outlet flow angle at different pitchwise locations

The spanwise variation of the outlet flow angle is remarkably well predicted for the inviscid + EWBL computation, except near the pressure side (up to 20% pitch). Near the hub and the tip, the flow angle is overestimated, which may be explained by the fact that in the real cascade flow an extra deflection from the pressure side of the wake towards the suction side

of the wake is induced, since pressure and suction side are no longer divided by a material wall, thus leading to a 'less negative' experimental flow angle. In the midspan region, the flow angle is marginally underestimated by the computation.

Also, close to the suction side (from 90% pitch onwards) the agreement is less satisfactory : in the midspan region, the computations overestimate the outlet flow angle, while the 'peaks' in the experimental profile again indicate the continuation of the horseshoe vortices near hub and tip into the wake region, although the intensity of the peaks has reduced.

Near the end-walls, the fully inviscid computation overestimates the flow angle considerably with respect to both the experimental data (up to 20°) and the computational data from the inviscid + EWBL computation (typically 10°). This discrepancy may be attributed to the absence of the velocity-decreasing wall friction effect in the fully inviscid model.

11.4.4.4 Pitch-averaged spanwise profiles

The theoretical and experimental pitch-averaged spanwise profiles of tangential velocity agree very well in the case of the inviscid + EWBL computation. The pitch-averaged profile of the fully inviscid computation deviates considerably from the experimental pitch-averaged profile in the vicinity of the end-walls, for reasons explained in § 11.4.4.1.

The theoretical and experimental pitch-averaged spanwise profiles of radial velocity do not seem to agree very well, but again it must be stressed that the averaged values have an order of magnitude equal to the measurement error, amounting to a possible relative measurement error of 100% !!

The theoretical and experimental pitch-averaged spanwise profiles of the tangential outlet flow angle agree very well for both computational approaches. Again, the very localized 'peaks' in the local profiles near the suction side, due to the presence of horseshoe vortices, have been smoothed out in the averaging process.

11.4.5 RESULTS AT 112% CHORD (NEAR WAKE)

The results for the transversal S3-plane at 112% chord are presented on Figure 11.7a to Figure 11.7l (pages 143-154). The conclusions are essentially identical with those for the results at 104% chord.

However, notice that the 'peaks' in the experimental local tangential velocity and local outlet flow angle profiles near the suction side of the wake have diminished with respect to the 104% chord experimental results, due to the gradual dissipation of the horseshoe vortices through mixing with the main flow. This results in a better agreement between theoretical and experimental results for the 112% chord transversal S3-plane than for the 104% chord transversal S3-plane.

11.4.6 RESULTS AT 125% CHORD (FAR WAKE)

The results for the transversal S3-plane at 125% chord are presented on Figure 11.8a to Figure 11.8l (pages 155-166).

11.4.6.1 Spanwise profiles of tangential velocity at different pitchwise locations

The profile of total tangential velocity for the inviscid + EWBL computation agrees very well with the experimental profile, except near the pressure side of the wake (up to about 15% pitch), where the tangential velocity is somewhat overestimated near the end-walls and very slightly underestimated in the midspan region.

Close to the suction side (from about 85% pitch onwards) the effects of the horseshoe vortices can again be noticed in the experimental profiles : tangential velocity 'peaks' at 15% span and 85% span, and an altered profile in the midspan region, leading to unsatisfactory agreement between theory and experiment. However, with respect to the upstream transverse planes (at 104% and 112% chord), the difference between theory and experiment has been reduced, due to the gradual dissipation of the horseshoe vortices in the wake.

Once again, the profile of the fully inviscid computation differs considerably from the experimental profile in the vicinity of the end-walls, due to the absence of wall friction effects in the inviscid model.

11.4.6.2 Spanwise profiles of radial velocity at different pitchwise locations

The radial velocity profiles of the inviscid + EWBL approach agree reasonably well with the experimental profiles over the entire pitch. The results of the fully inviscid approach are less satisfactory, although qualitative agreement is good.

The difference between the theoretical and the experimental profiles in the mid-pitch region (25% pitch - 50% pitch) may again be attributed to measurement inaccuracies, since the observed velocities and the measurement accuracy are of the same order of magnitude.

11.4.6.3 Spanwise profiles of outlet flow angle at different pitchwise locations

The spanwise variation of the outlet flow angle is remarkably well predicted for the inviscid + EWBL computation, except very near the pressure side (up to 10% pitch). Near the hub and the tip, the flow angle is overestimated, which may again be explained by the induction of an extra deflection from the pressure side of the wake towards the suction side of the wake in the real cascade flow. In the midspan region, the flow angle is marginally underestimated by the computation.

Also, close to the suction side (from 90% pitch onwards) the agreement is less satisfactory : in the midspan region, the computations overestimate the outlet flow angle, while the 'peaks' in the experimental profile again indicate the continuation of the horseshoe vortices near hub and tip into the wake region. However, the intensity of the peaks has been reduced with respect to the intensity at the upstream transverse planes, leading to a better agreement between theory and experiment for the 125% chord transverse plane.

Near the end-walls, the fully inviscid computation overestimates the flow angle considerably with respect to both the experimental data (up to 20°) and the computational data from the inviscid + EWBL computation (typically 10°).

11.4.6.4 Pitch-averaged spanwise profiles

The theoretical and experimental pitch-averaged spanwise profiles of tangential velocity agree quite well in the case of the inviscid + EWBL computation, although the computation overestimates the velocities very close to the end-walls. As expected, the pitch-averaged profile of the fully inviscid computation deviates considerably from the experimental pitch-averaged profile in the vicinity of the end-walls.

The theoretical and experimental pitch-averaged spanwise profiles of radial velocity do not seem to agree very well, but this observation may be explained by the small magnitude of the pitch-averaged radial velocities, amounting to a possible relative measurement error of 100% !!

The theoretical and experimental pitch-averaged spanwise profiles of the tangential outlet flow angle agree very well for both computational approaches, although the result from the

inviscid + EWBL approach is superior to the result from the fully inviscid approach near the end-walls. Again, the very localized 'peaks' in the local spanwise profiles near the suction side (due to the presence of horseshoe vortices) have been smoothed out in the averaging process.

11.5 VELOCITY VECTOR PLOTS

In order to have a global picture of the flow in a transversal S3-plane, two velocity vector plots are presented.

In Figure 11.9a, a qualitative plot of the computed velocity vectors of the total flow field on the transversal S3-plane at the cascade outlet is presented, i.e. the superposition of the Quasi-3D velocities and the secondary velocities computed with the present secondary flow model. This velocity vector plot is in fact the global representation in a single picture of the information contained in the many local spanwise profiles for a particular S3-plane, discussed in § 11.4.

The tangential flow from right to left corresponds to the direction of the main flow at the outlet of the cascade.

The radial flows, associated to secondary flow effects, are easily distinguished near the trailing edges of the blades.

In Figure 11.9b, a qualitative plot of the velocity vectors of the computed secondary flow field on the transversal S3-plane at the cascade outlet is presented.

The classical double vortex structure is easily distinguished : along both end-walls, the pressure gradient generates tangential secondary flows from the pressure side towards the suction side of the flow passage, which deflect into radial secondary flows due to the presence of the blade surfaces and then recirculate in the opposite tangential direction in the midspan region.

Also, the global picture of the secondary flow shows that the largest radial velocities occur near the blade surfaces, due to a combination of the radial recirculation effects mentioned above and the radial flow effects in the profile boundary layers and the wakes.

11.6 WAKE RADIAL VELOCITY PROFILES

In order to make a further assessment of the present secondary flow computation method, the downstream evolutions of the computed and the measured radial velocity distributions in the wake are compared with each other.

Results are presented for five different spanwise positions (5%, 10%, 15%, 25% and 35% span, taking into account the symmetry with respect to the midspan position) and the wake evolution is tracked at three consecutive locations downstream of the cascade trailing edge (104%, 112% and 125% chord transversal S3-plane)

All results are presented in the same format of a pitchwise radial velocity profile at a certain spanwise position and axial location (Figures 11.10a to 11.10c, pages 168-170). The zero position of the pitchwise distance coincides with the trailing edge position, while the positive direction of the pitch is from the pressure side of the passage towards the suction side of the passage. Hence, the suction side of the wake is located left of the trailing edge zero position while the pressure side of the wake is located right of the trailing edge zero position.

The value of the semi-empirical turbulence parameter K , which influences the value of the wake mixing coefficient η_0 , was set to 0.10 (cf. Chapter 7 and § 11.7.1).

11.6.1 RADIAL VELOCITY PROFILES NEAR THE END-WALLS

Near the end-wall (results at 5%, 10% and 15% span), the experimental profile is characterized by a large radial velocity peak in the suction side of the wake and a constant radial velocity profile in the pressure side of the wake. The computation predicts the suction side wake velocity profile quite well and the pressure side wake velocity profile is also predicted quite accurately from 20% pitch onwards, taking into account that the error on the experimental velocities is of the order of 0.25 m/s.

However, the computation predicts a large radial velocity peak near the pressure side, which does not correspond to the observed constant velocity profile.

Also, in proceeding downstream from the trailing edge, the suction side peak velocity in the experimental profile is damped faster than the corresponding peak velocity in the computed profile. The dispersion of the wake downstream of the trailing edge is also underestimated by the computation : the experimental wake profile evolves from a sharp-crested velocity distribution at trailing edge to a more flattened velocity distribution at 125% chord, which is not the case for the computed wake velocity distribution.

These observations point to the fact that the value of the wake diffusion coefficient η_0 used in the theoretical wake model to control the wake dissipation may be too low near the end-walls (cf. § 11.8).

11.6.2 RADIAL VELOCITY PROFILES NEAR MIDSPAN

Near midspan (results at 25% and 35% span), the experimental profile is characterized by a large radial velocity peak in both the suction side and the pressure side of the wake and the constant radial velocity profile in the pressure side of the wake has disappeared. The computed velocity profiles are in satisfactory agreement with the experimental velocity profiles, taking into account that the error on the experimental velocities is of the order of 0.25 m/s. Agreement is better at the suction side than at the pressure side, where the computation tends to underestimate the magnitude of the radial velocities.

The damping of the experimental velocity peaks when proceeding downstream from the trailing edge is smaller than near the the end-walls, possibly due to a smaller turbulence intensity in the freestream than near the end-walls. Consequently, the computational damping corresponds better with the experimental damping than was the case near the end-walls. Also, there is good agreement between the broadening of the experimental wake velocity profiles and the computed wake velocity profiles as the wake proceeds downstream from the trailing edge : they both evolve from a sharp-crested distribution into a more flattened distribution.

11.7 WAKE AXIAL VELOCITY PROFILES

In addition to the wake radial velocity profiles, the wake axial velocity profiles are presented for five different spanwise positions (5%, 10%, 15%, 25% and 35% span, taking into account the symmetry with respect to the midspan position) and the wake evolution is again tracked at three different consecutive locations downstream of the cascade trailing edge (104%, 112% and 125% chord transversal S3-plane).

Again, all results are presented in the form of pitchwise axial velocity profiles at a certain spanwise position and axial location. The zero position of the pitchwise distance coincides

with the trailing edge position, while the suction side is located to the left of the trailing edge and the pressure side is located to the right of the trailing edge.

11.7.1 AXIAL VELOCITY PROFILES WITH STANDARD WAKE MIXING

This set of computations was performed with the value of the semi-empirical turbulence parameter K set to a value of 0.10. This value was selected on the basis of a combination of an order of magnitude analysis (cf. Chapter 7) with data-match computations : the value of K was chosen in such a way that a satisfactory agreement between the computed and measured dispersion of the wake axial velocity distributions was obtained, while the value should be of the same order of magnitude as the value $K = 0.08$, derived in Chapter 7.

The results are presented on Figures 11.11a to 11.11c (pages 171-173).

The theoretical results agree reasonably well with the experimental data near midspan (25% and 35% span), although the broadening of the wake is slightly underestimated by the computation and the computed minimum velocities at the wake center are higher than in reality.

Near the end-walls (5%, 10% and 15% span) the agreement between theory and experiment is less satisfactory : although the general shape of the wake velocity profiles is predicted, quite well, the downstream dispersion of the wake is underestimated by the computations, while the minimum velocities at the wake center are overestimated. This is probably due to an increased turbulent diffusion intensity in the end-wall boundary layers, while the computations assumed a uniform level of turbulent diffusion.

11.7.2 AXIAL VELOCITY PROFILES WITH INCREASED WAKE MIXING

As mentioned in the previous paragraphs, the computation near the end-walls underestimates the damping of the wake velocity peaks and yields an insufficient dispersion of the wake, when a uniform value for the semi-empirical turbulence coefficient K is assumed throughout the machine. Therefore, the computations of § 11.7.1 are repeated with a non-uniform level of wake mixing : the value of the wake mixing coefficient η_0 is artificially increased by a factor 3.33 in the end-wall boundary layers, which is equivalent to increasing the turbulent mixing coefficient ϵ_t by a factor 10 (cf. equation (6.4)).

The results are presented on Figures 11.12a to 11.12c (pages 174-176).

The results near midspan (25% and 35% span) are identical with those of the previous computation, since the wake mixing coefficient has remained the same outside the end-wall boundary layers.

Near the end-walls (5%, 10% and 15% span) the increase by a factor of 3.33 of the wake mixing coefficient has a marked effect on the computed axial velocity profiles. The minimum wake velocities at the wake center remain about the same, but the wake dispersion is dramatically increased : the computed wake thicknesses agree quite well with the measured wake thicknesses, which is only logical since the increase of the wake mixing coefficient was determined in a data-match mode for the axial velocity profiles.

11.8 WAKE RADIAL VELOCITY PROFILES WITH INCREASED WAKE MIXING

Since artificially increasing the value of the wake mixing coefficient η_0 in the end-wall

boundary layers by a factor of 3.33 resulted in improved agreement between theory and experiment for the axial velocity profiles, the computations for the radial velocity profiles were also repeated with an increased wake mixing coefficient near the end-walls.

The results are presented on Figures 11.13a to 11.13c (pages 177-179).

The velocity profiles near midspan (25% and 35% span) are almost unaffected, since they have the same wake mixing coefficient as before. The small variations with respect to the previous computations are due to the influence of the end-wall region, where the wake mixing was increased.

By contrast, the velocity profiles near the end-walls (5% and 10% span) are clearly affected by the increased wake mixing. Indeed, the sharp velocity peaks at the pressure side are reduced to a more flattened velocity distribution. This much improved correspondence between computation and experiment is most significant near the trailing edge (104% chord).

Finally, increasing the wake mixing coefficient does not affect the dispersion of the wake in a significant way, as can be seen from a comparison between the corresponding wake thicknesses of Figures 11.10a-c and 11.13a-c.

11.9 CONCLUSIONS

For the linear compressor cascade testcase, the results of the secondary flow computations are generally in good agreement with the experimental data, both locally and on an averaged basis.

However, the occurrence of certain secondary flow phenomena which are not incorporated in the theoretical secondary flow model can lead to discrepancies between the computed and the experimental secondary flow field. This refers to the phenomena of horseshoe vortices and the presence of large regions of separated flow (predominantly at the suction side of the blades).

The evolution of the wake profiles indicate that employing a uniform turbulent mixing coefficient ϵ_t may not be appropriate, but that this coefficient should be increased by an order of magnitude in end-wall boundary layer regions, thus giving rise to enhanced wake dispersion and wake mixing. The need for an increased mixing coefficient in the end-wall boundary layers may stem from the fact that in reality, the end-wall boundary layer vorticity is dissipated by viscosity, whereas the theoretical model only describes a convection of the end-wall boundary layer vorticity.

It should be stressed however, that the present secondary flow computation method was developed with the objective to compute the convective mixing of physical flow properties (e.g. total temperature) in axial-flow compressors, in order to account in a simple and efficient way for the effects of S1-streamsurfaces with non-axisymmetric geometry in classical Quasi-3D computation methods. In this respect, the present secondary flow computation method is adequate provided the influence of horseshoe vortices or separated flow regions is confined to small areas. Indeed, as was briefly mentioned in Chapter 1, it is not the objective to develop a detailed 3D turbomachinery flow computation method which catches all the details of the flow physics, but to improve the existing Quasi-3D computational models for certain three-dimensional effects, without having to take recourse to detailed, fully three-dimensional Navier-Stokes computations which are very expensive, both in computation time and computation cost.

Finally, it should be mentioned that the 'inviscid+EWBL' approach is superior to the

'fully inviscid' approach, mostly because the former is able to predict the effects of boundary layer growth, whereas the latter is not. In conclusion, the computational approach of an inviscid computation of the core flow region, coupled to an explicit integral end-wall boundary layer computation and including profile boundary layer or wake effects yields the best results.

CONCLUSIONS

RECOMMENDATIONS FOR FUTURE WORK

A method for the computation of the effects of radial mixing on the distribution of total temperature in a turbomachinery blade row has been developed. The method is developed in the framework of a through-flow or Quasi-3D turbomachinery flow computation and hence is applied in a corrective fashion to previously obtained total temperature distributions.

The method takes into account both secondary flows and turbulent diffusion as possible sources of mixing : the secondary flow velocities determine the magnitude of the convection terms in the energy equation, whereas a turbulent diffusion coefficient determines the strength of the diffusion terms in the energy equation.

The secondary flows are assumed to be confined to a transversal S3-plane and are computed by solving a Poisson equation for the secondary streamfunction, where the right-hand side of the equation is the axial vorticity associated to the secondary flows. The axial vorticity is composed of different contributions, each associated to a particular flow region : inviscid core flow region, end-wall boundary layers region, profile boundary layers region and wake region. The axial vorticity of each region is determined by solving the corresponding flow equations, coupled to velocity profile models. The streamfunction-vorticity approach guarantees that the secondary flows do not violate the continuity law. The turbulent mixing coefficient is estimated by means of a semi-empirical correlation based on turbulent wake theory.

Comparison of computational results with experimental results for the VUB cascade show that the secondary flow computation yields reliable predictions of the secondary flow pattern, both qualitatively and quantitatively, with the exception of regions of separated flow. Also, the wake computations indicate that the turbulent mixing coefficient needs to be (artificially) increased by an order of magnitude in the end-wall boundary layers in order to obtain correct results. In other words, the mixing level is not to be taken uniform throughout the machine. In order to obtain further validation of the secondary flow computation and the proposed radial mixing simulation method, computations for other single-stage turbomachines are in progress.

Qualitative computations with the present convective-diffusive mixing model have already been presented for earlier versions of the secondary flow computation method (De Ruyck and Hirsch, 1987, 1988a, 1988b ; De Ruyck, Hirsch and Segaut, 1989) and showed that mixing was dominated by turbulent diffusion in the core flow region while convective mixing by secondary flows becomes of equal importance in the low momentum flow regions (e.g. end-wall boundary layers, wakes), at least for low-speed machines. The present improved secondary flow computation does not result in significant differences with the earlier mixing computations, so these are not repeated here.

In the future, the mixing simulation with the improved secondary flow computation method shall be applied to high-speed single-stage machines since recent discussions have

shown that for these cases the picture may be different, i.e. convection-dominated mixing instead of turbulence-dominated mixing.

The main task for the future then lies in extending the present method to multi-stage turbomachinery applications by introducing and developing correct concepts for the transfer of information from the mixing computation in one blade row to the mixing computation in the next blade row.

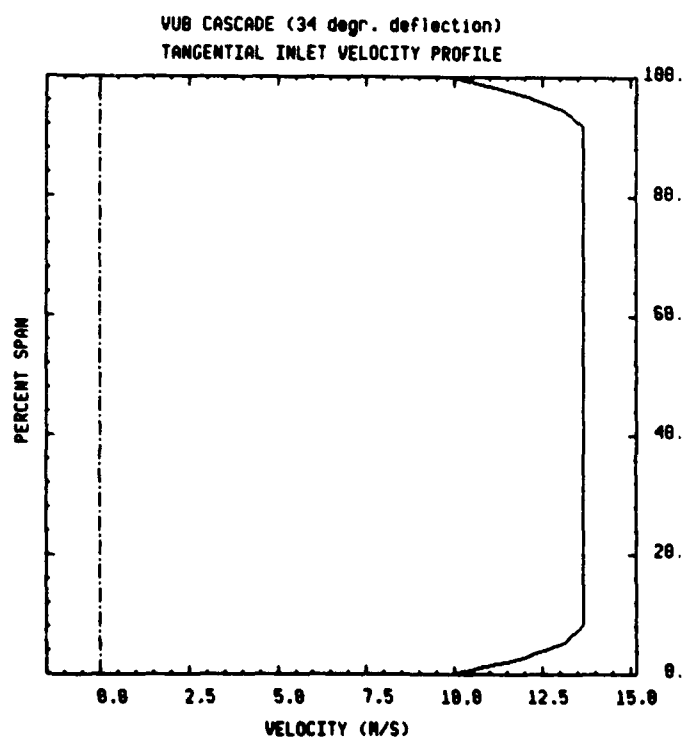
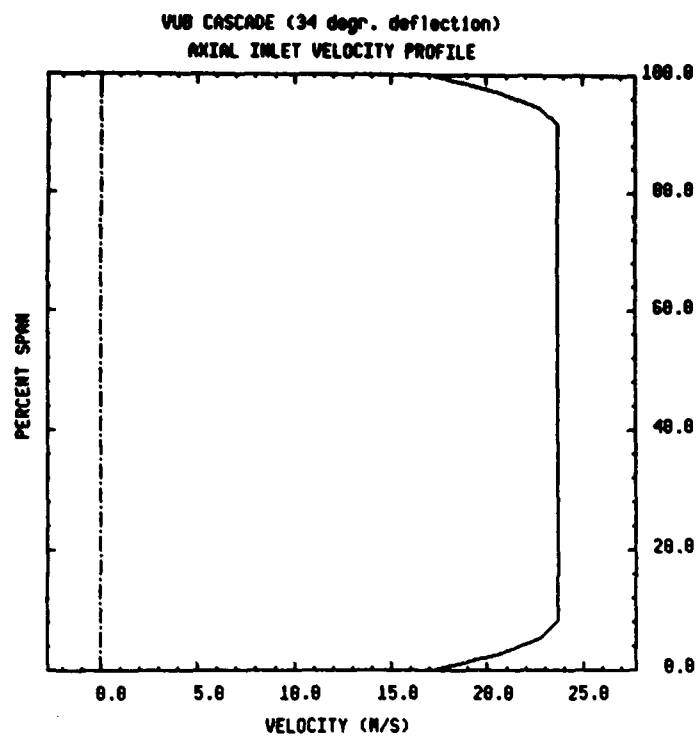


Figure 11.1 : Cascade inlet velocity profiles

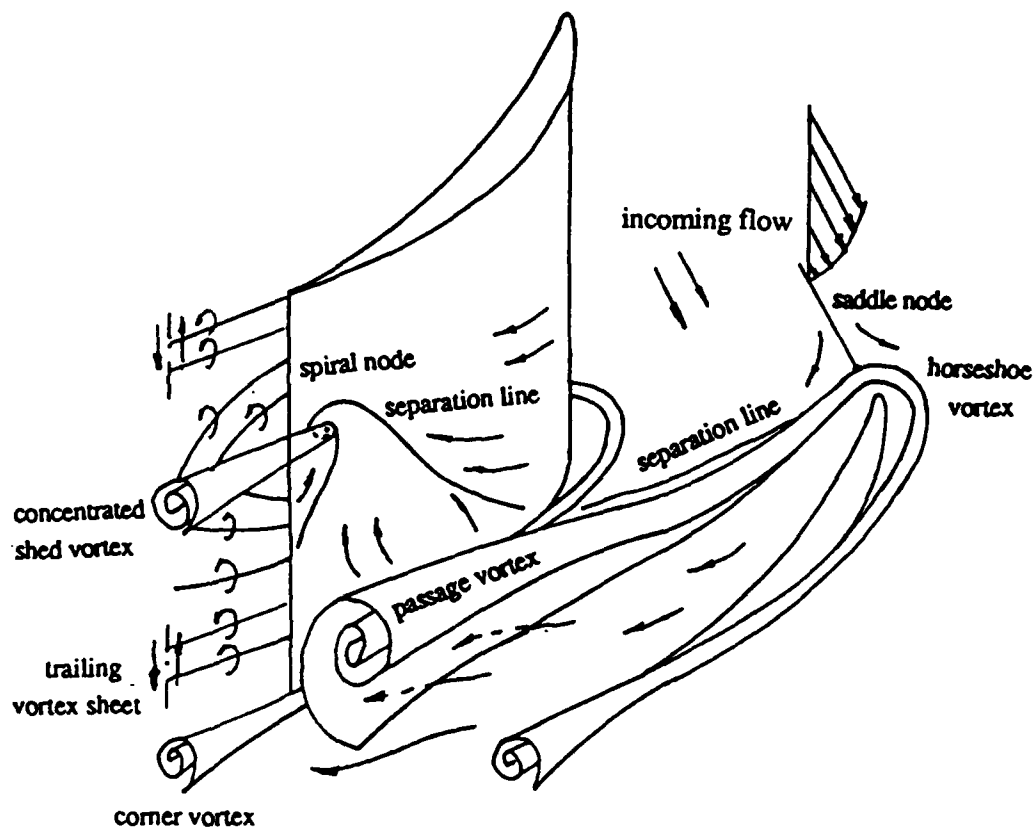


Figure 11.2 : Experimentally determined three-dimensional flow structure inside the VUB cascade (from Kang and Hirsch, 1991)

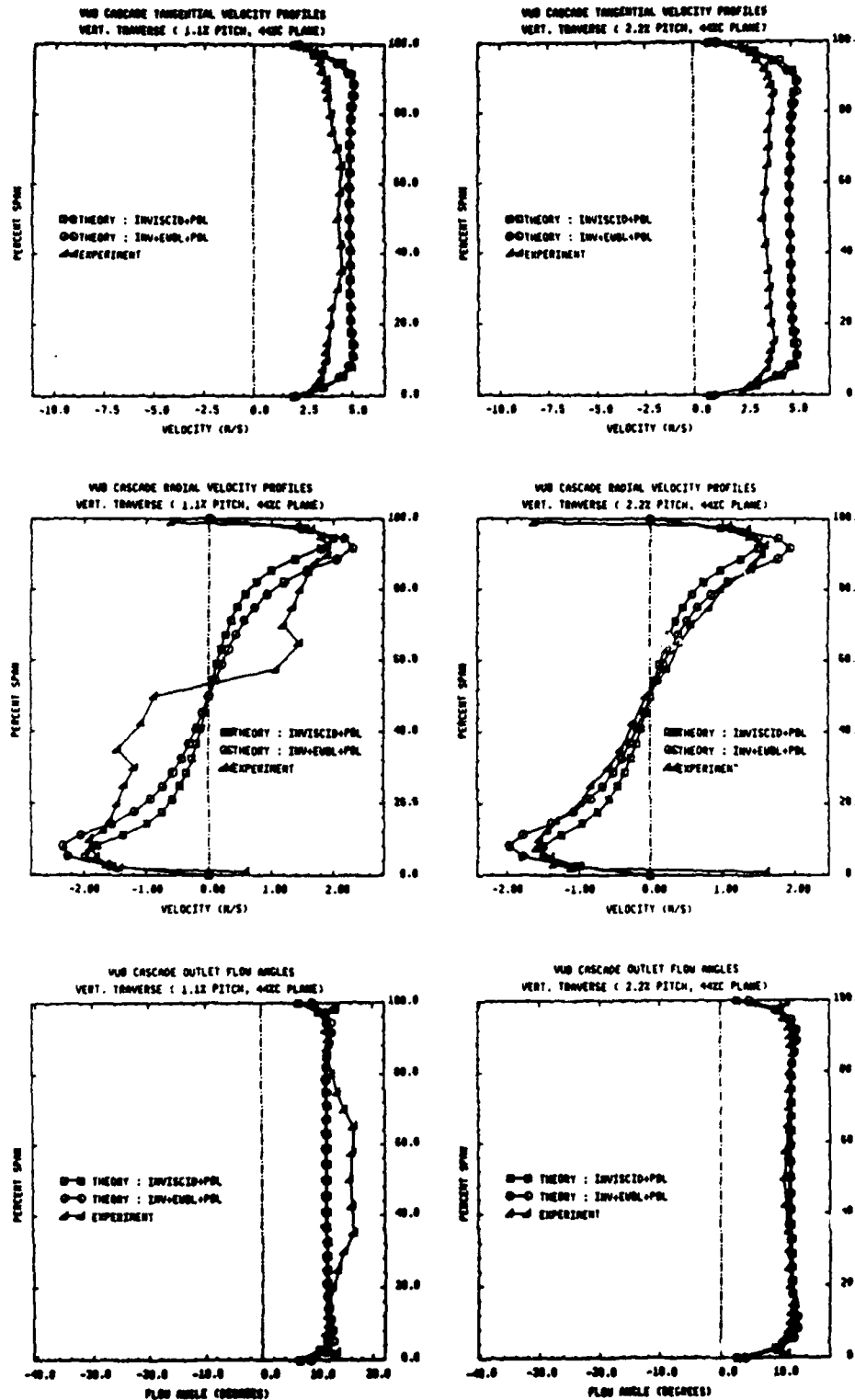


Figure 11.3a : Local spanwise profiles at 1.1% and 2.2% pitch (44% chord plane)

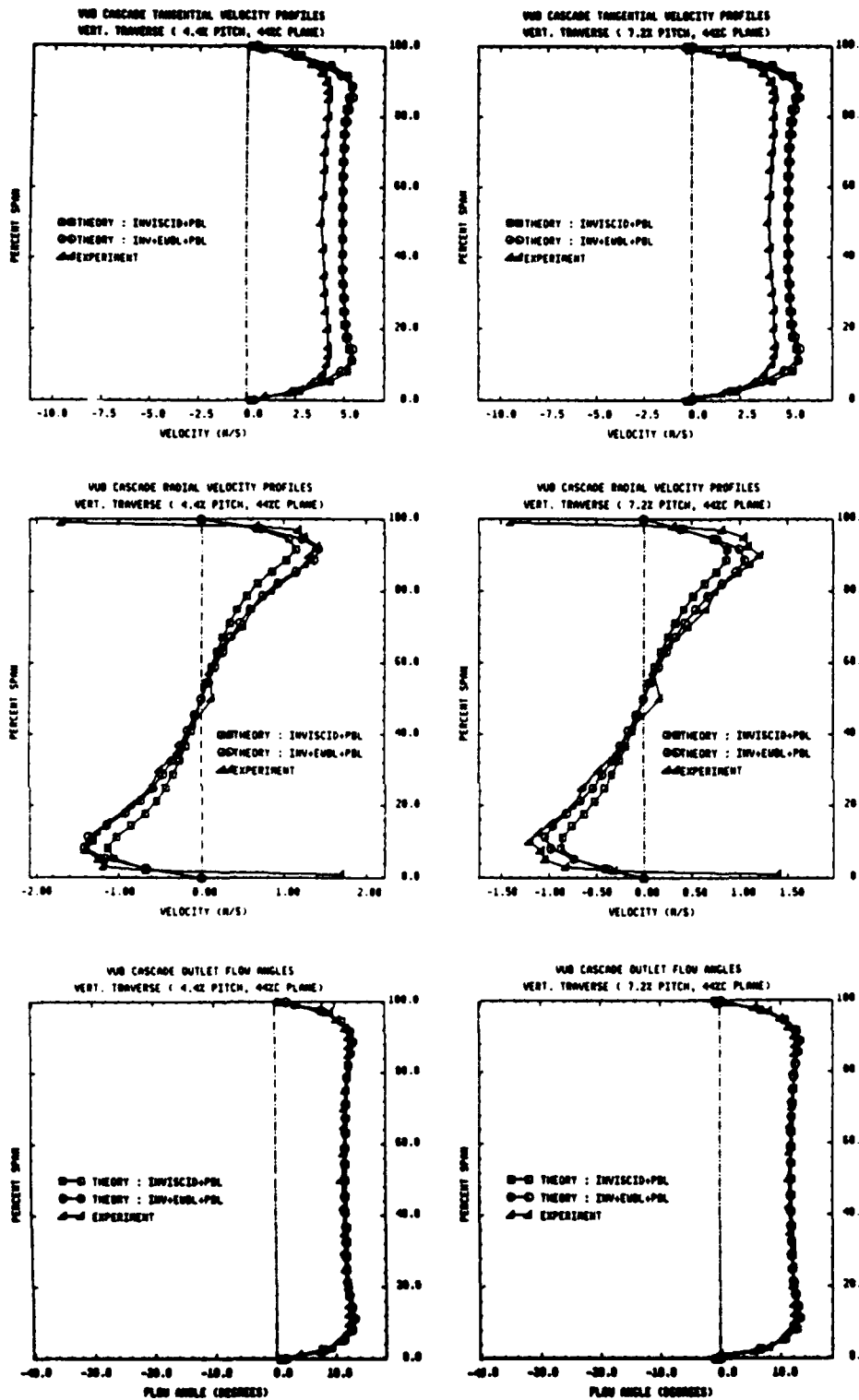


Figure 11.3b : Local spanwise profiles at 4.4% and 7.2% pitch (44% chord plane)

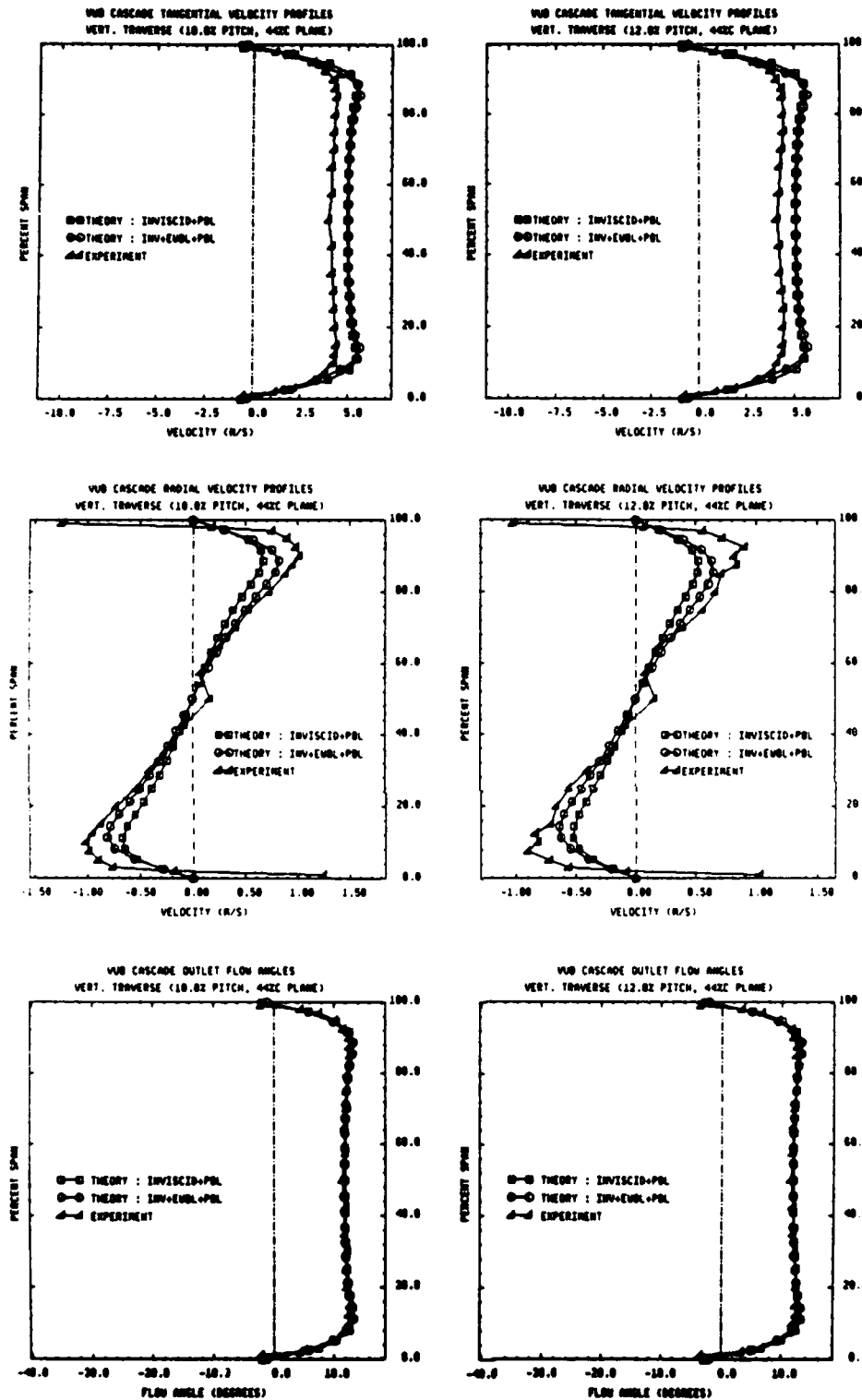


Figure 11.3c : Local spanwise profiles at 10.0% and 12.8% pitch (44% chord plane)

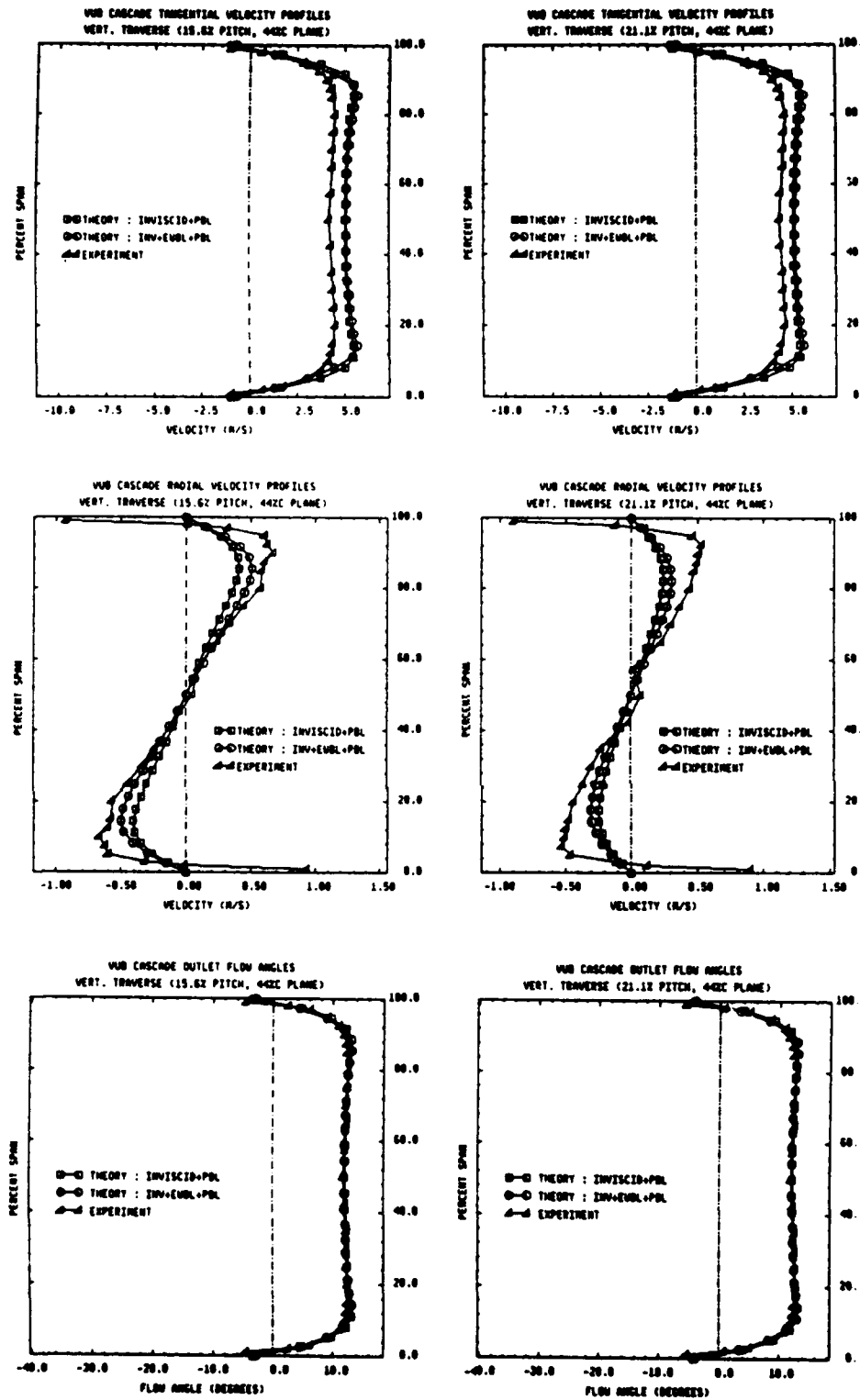


Figure 11.3d : Local spanwise profiles at 15.6% and 21.1% pitch (44% chord plane)

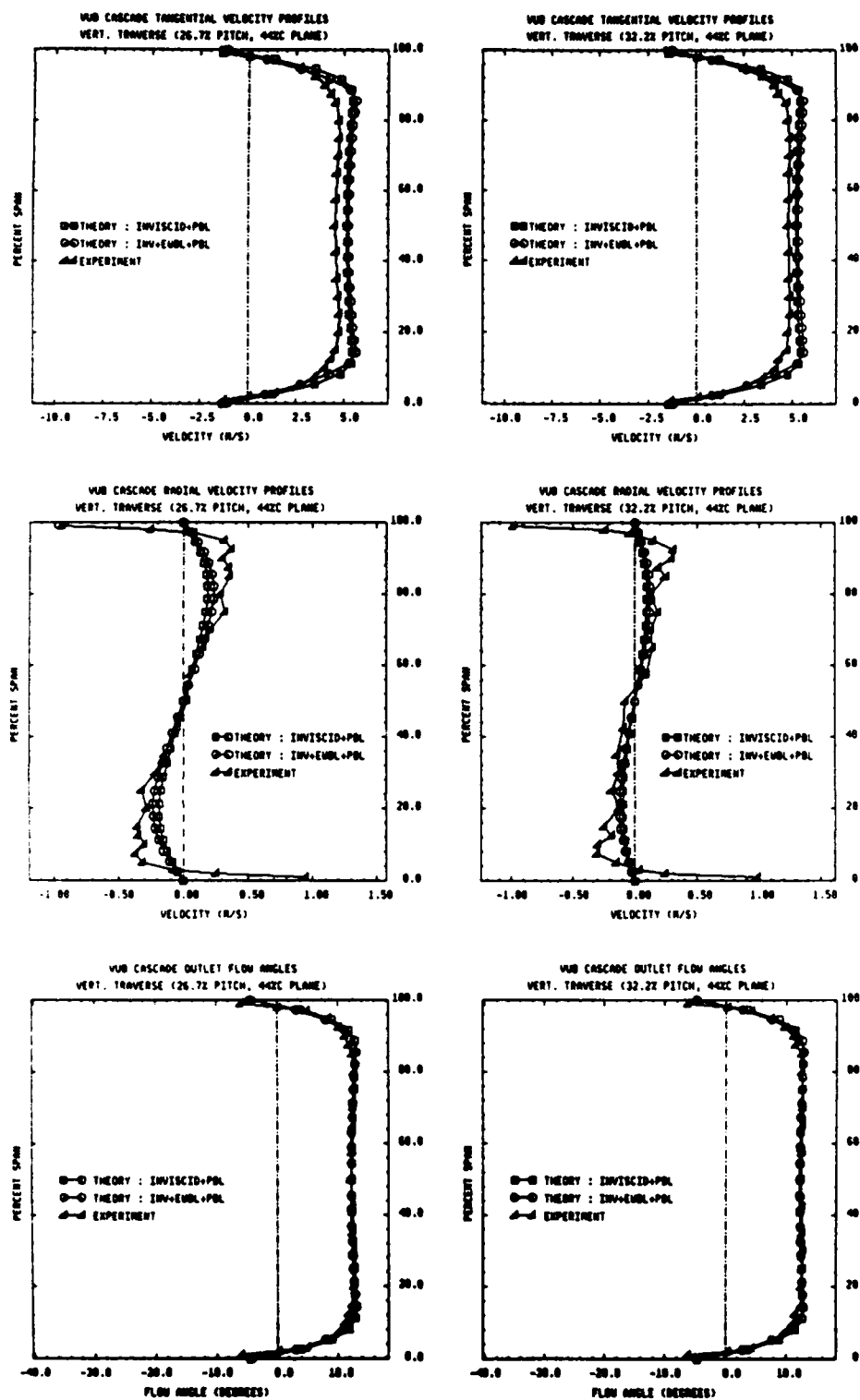


Figure 11.3e : Local spanwise profiles at 26.7% and 32.2% pitch (44% chord plane)

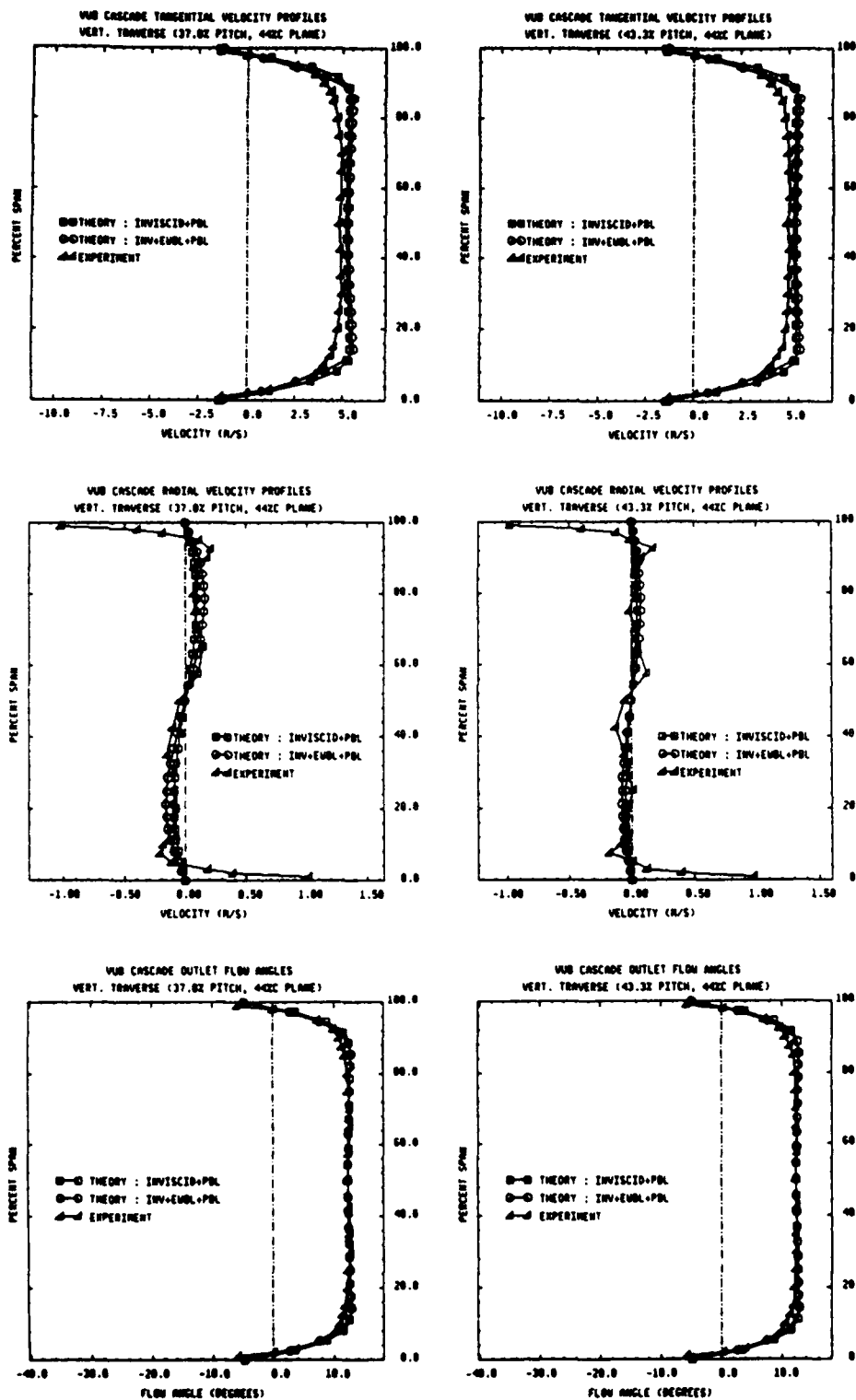


Figure 11.3f: Local spanwise profiles at 37.8% and 43.3% pitch (44% chord plane)

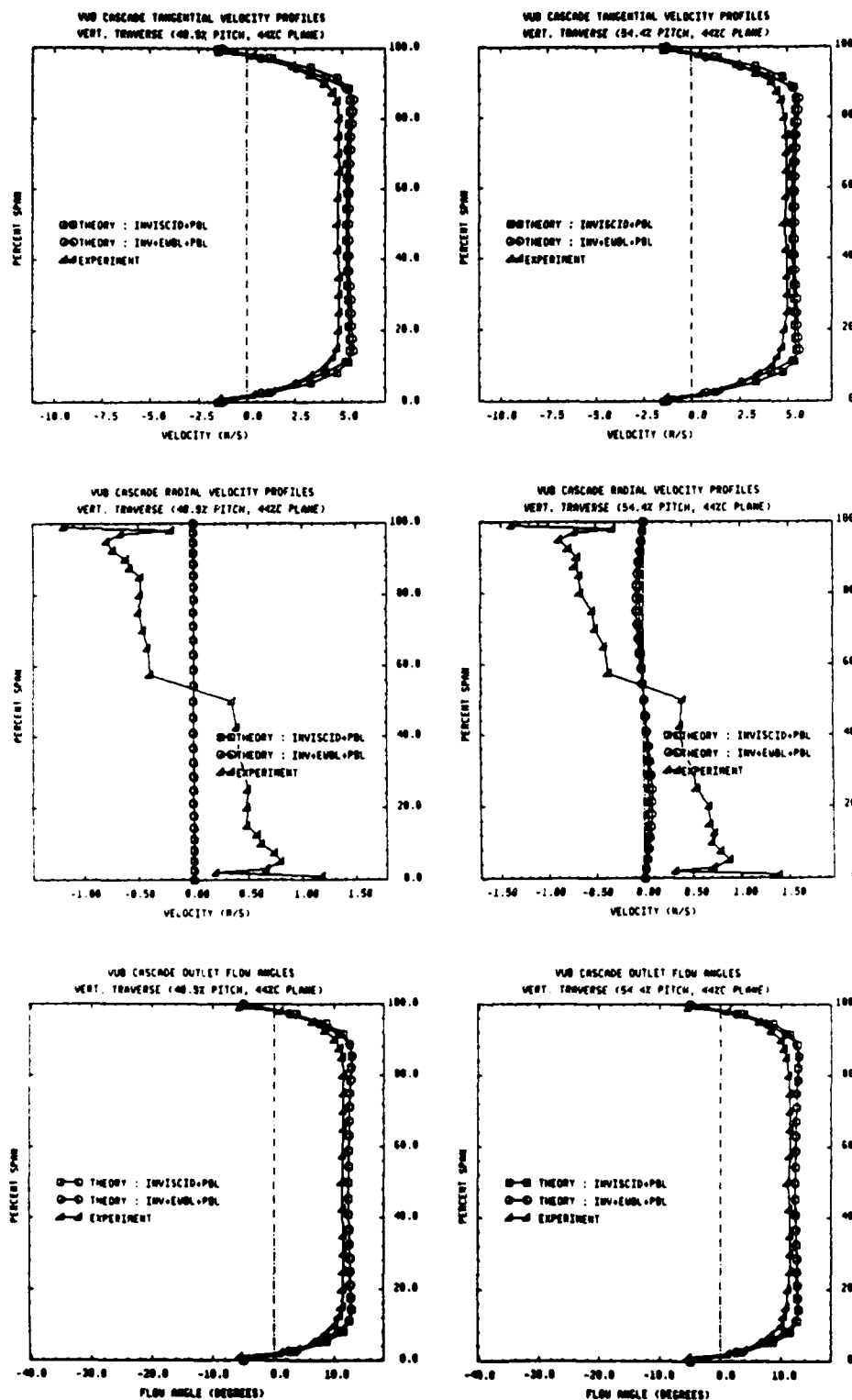


Figure 11.3g : Local spanwise profiles at 48.9% and 54.4% pitch (44% chord plane)

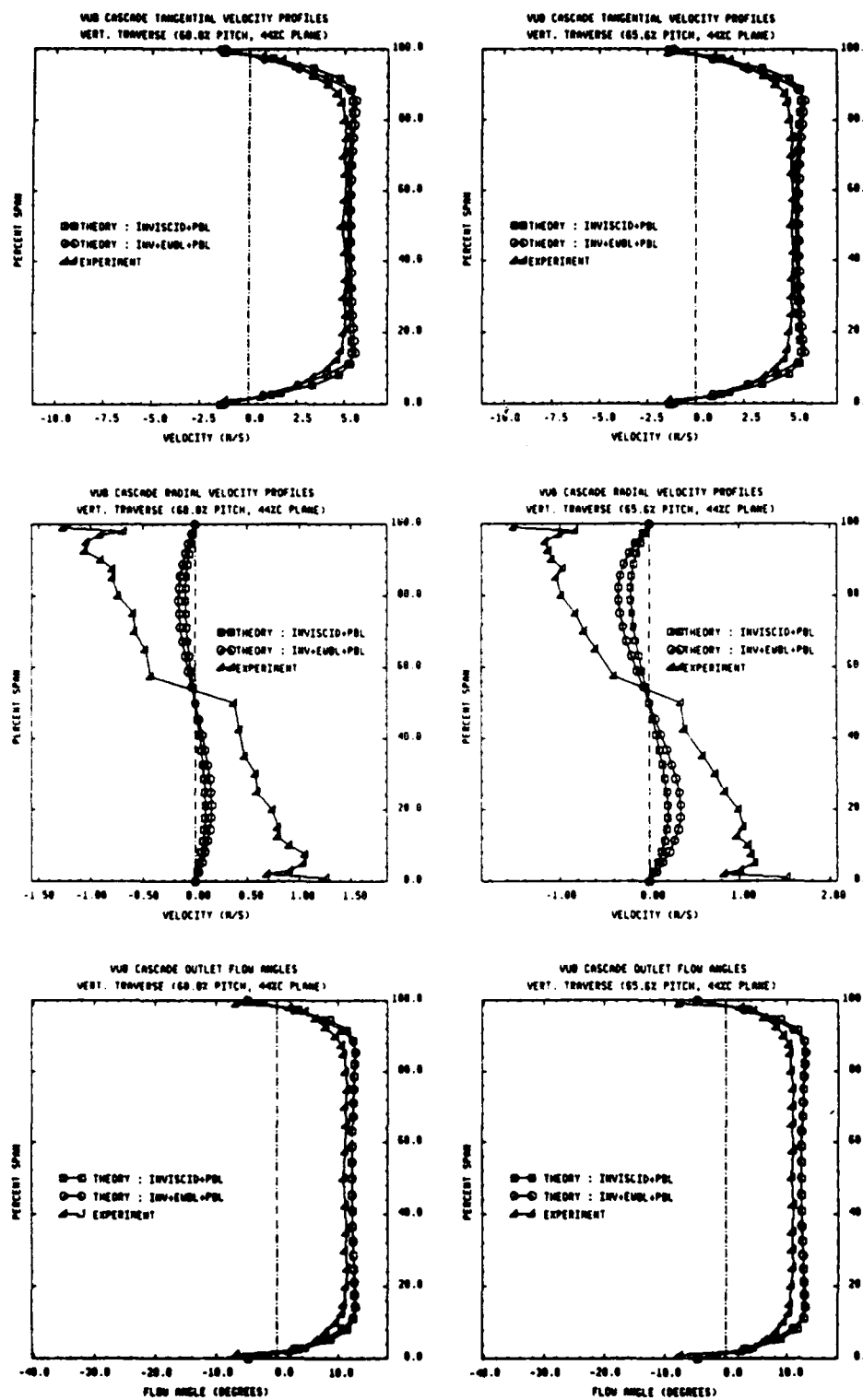


Figure 11.3h : Local spanwise profiles at 60.0% and 65.6% pitch (44% chord plane)

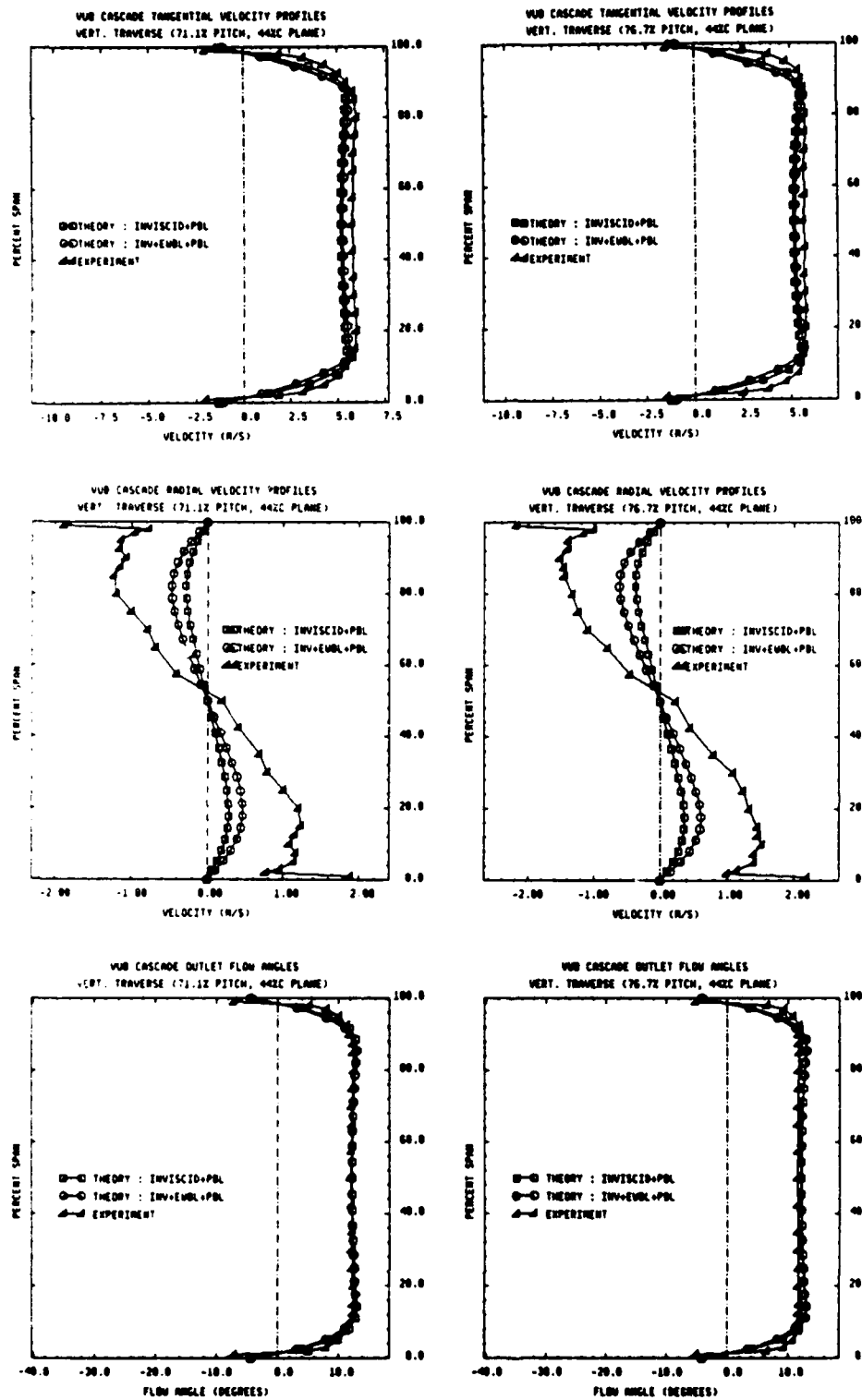


Figure 11.3i : Local spanwise profiles at 71.1% and 76.7% pitch (44% chord plane)

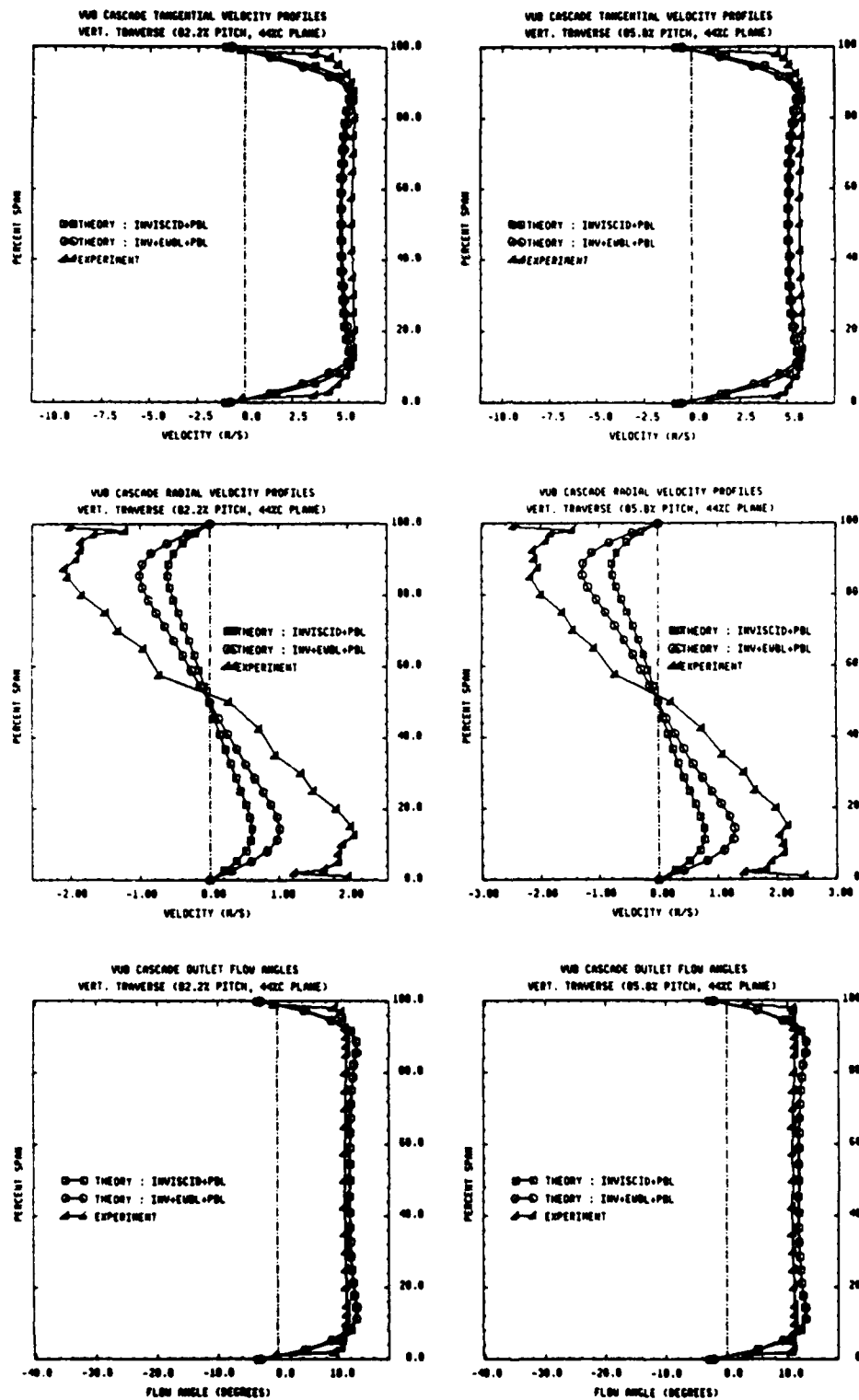


Figure 11.3j: Local spanwise profiles at 82.2% and 85.0% pitch (44% chord plane)

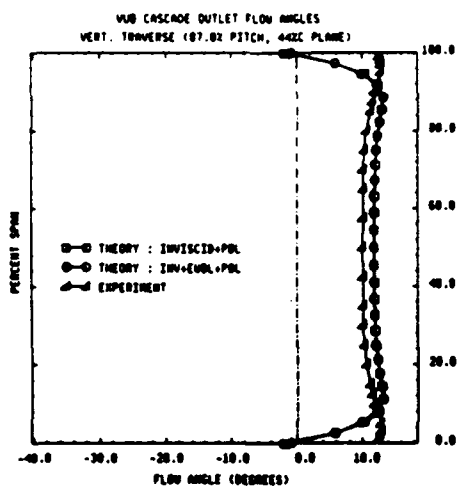
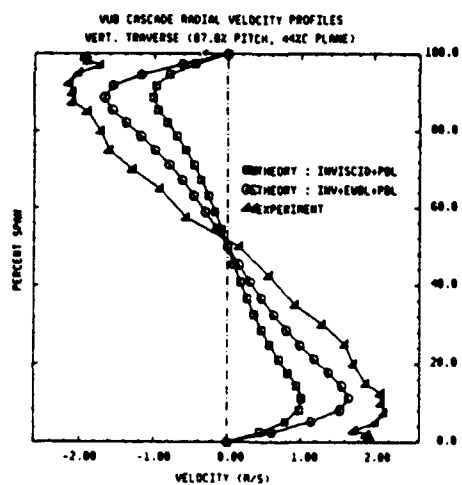
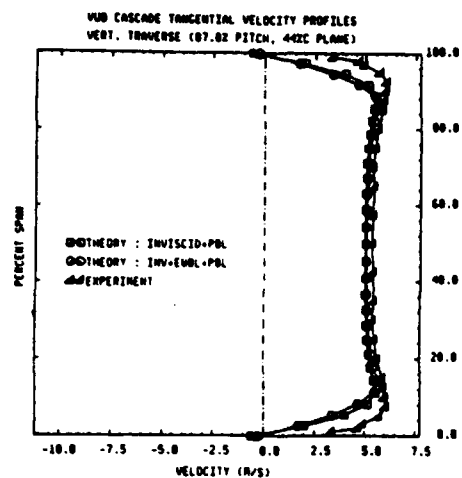


Figure 11.3k : Local spanwise profiles at 87.8% pitch (44% chord plane)

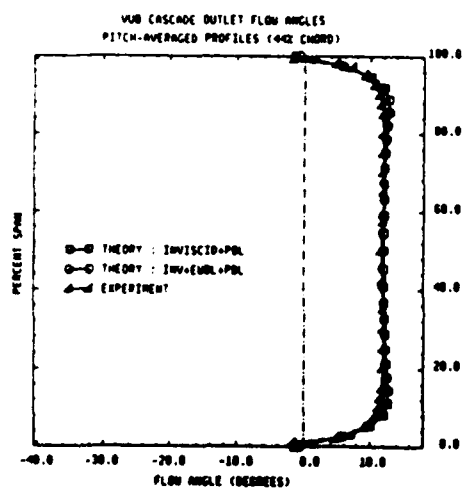
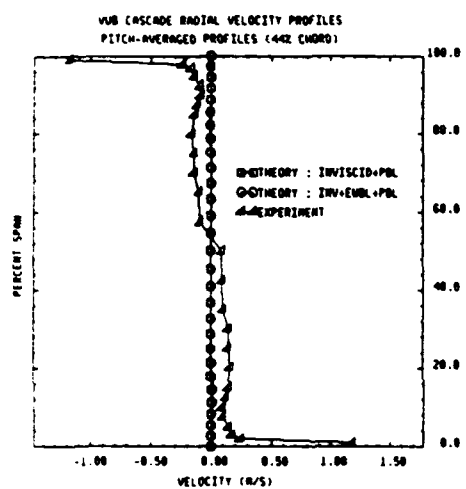
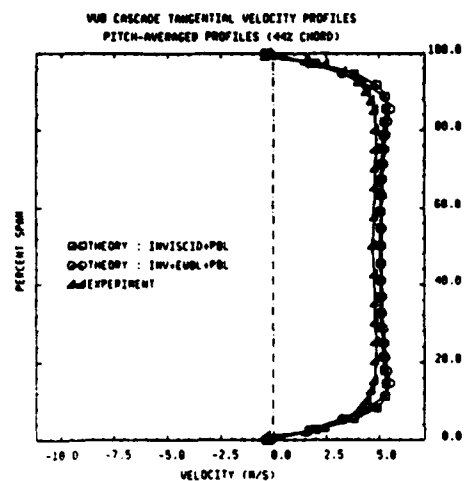


Figure 11.31 : Pitch-averaged spanwise profiles (44% chord plane)

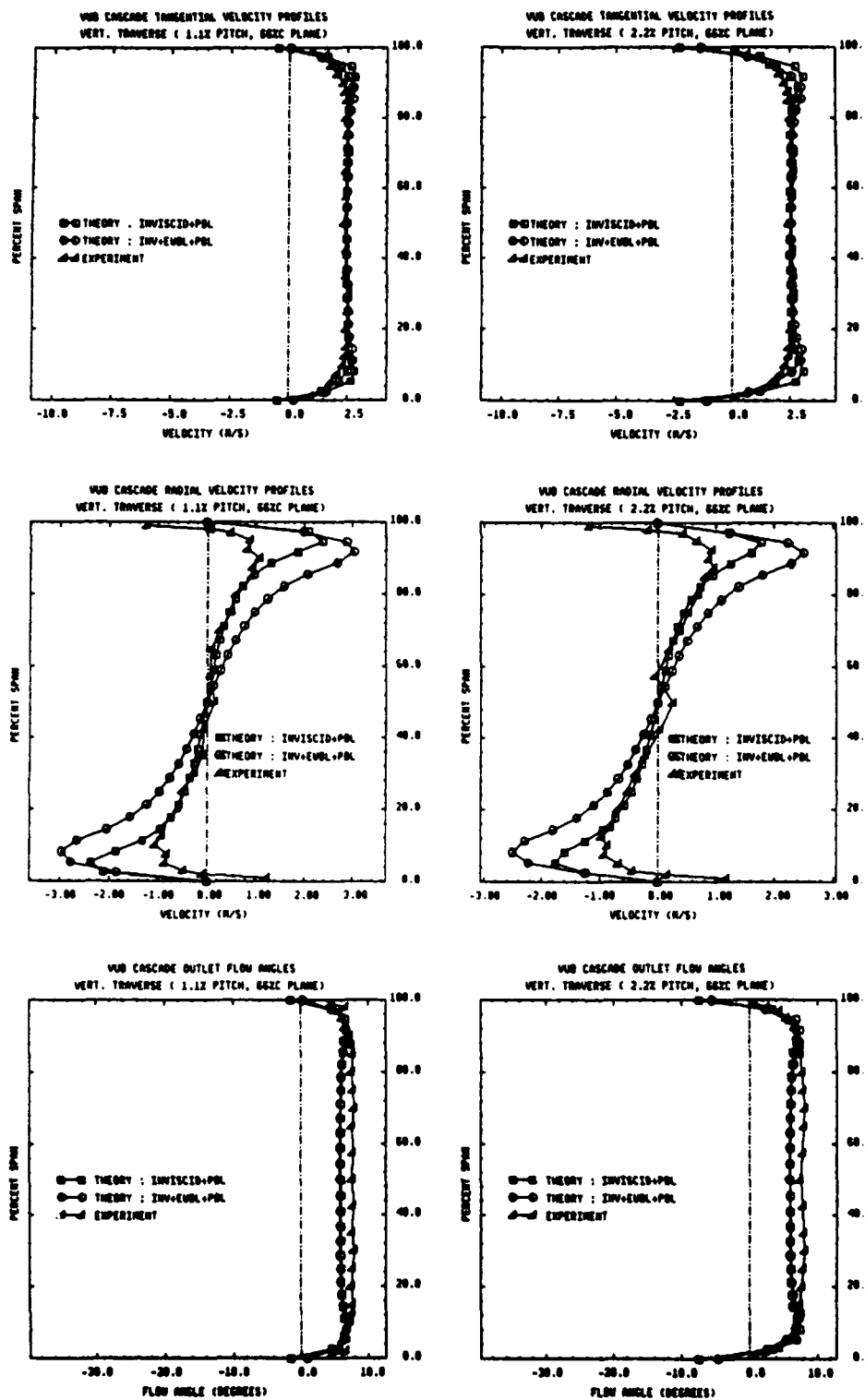


Figure 11.4a : Local spanwise profiles at 1.1% and 2.2% pitch (66% chord plane)

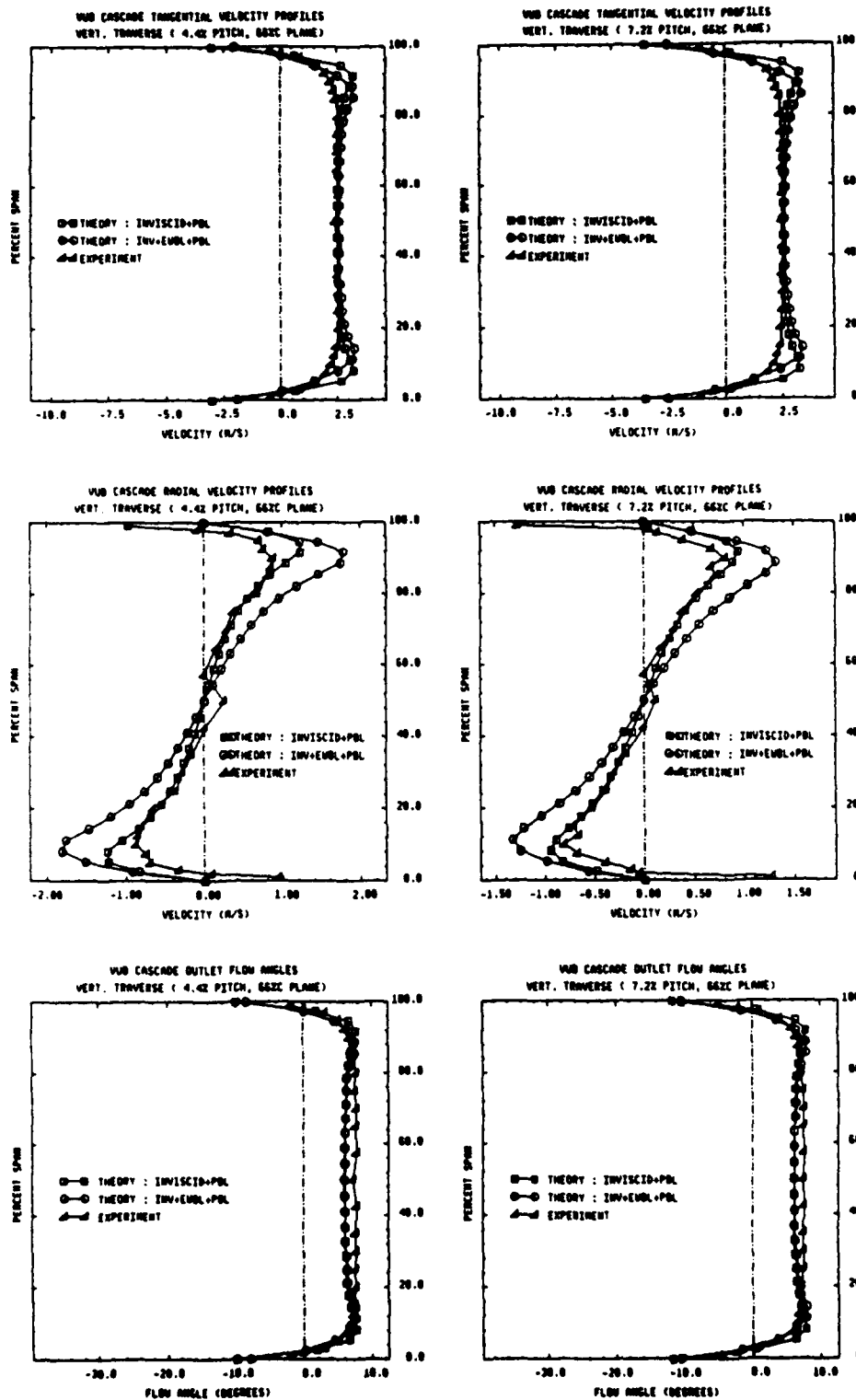


Figure 11.4b : Local spanwise profiles at 4.4% and 7.2% pitch (66% chord plane)

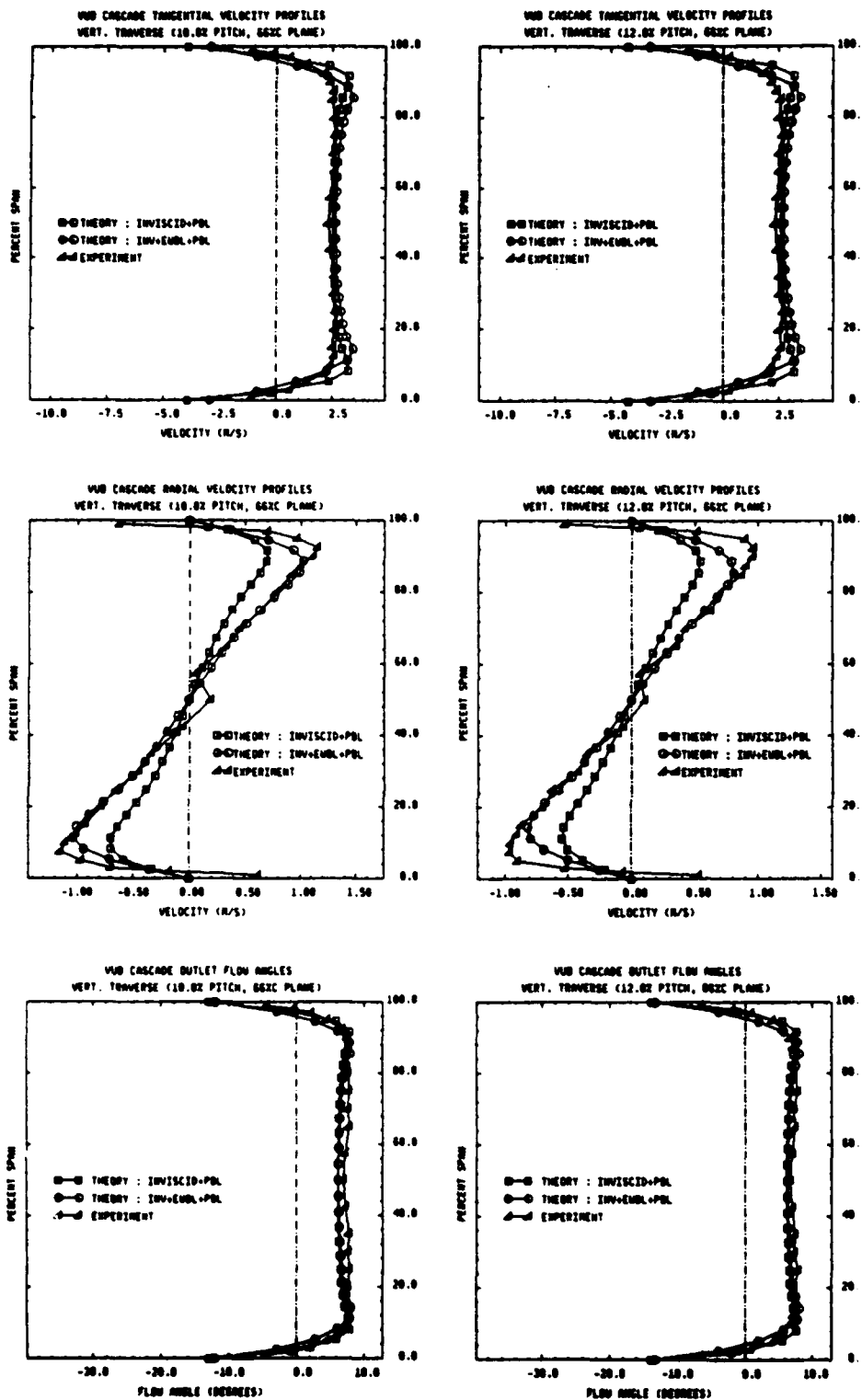


Figure 11.4c : Local spanwise profiles at 10.0% and 12.8% pitch (66% chord plane)

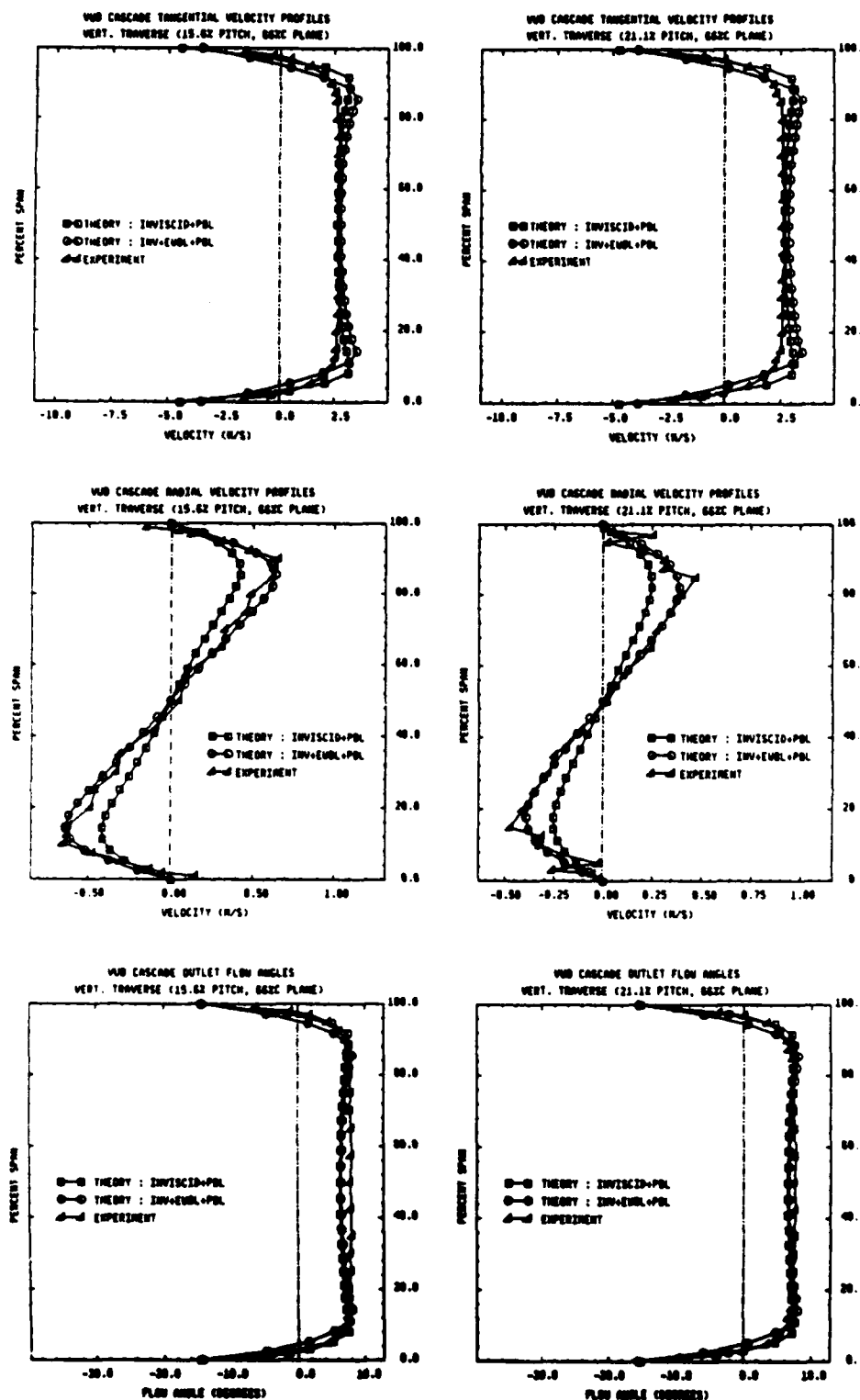


Figure 11.4d : Local spanwise profiles at 15.6% and 21.1% pitch (66% chord plane)

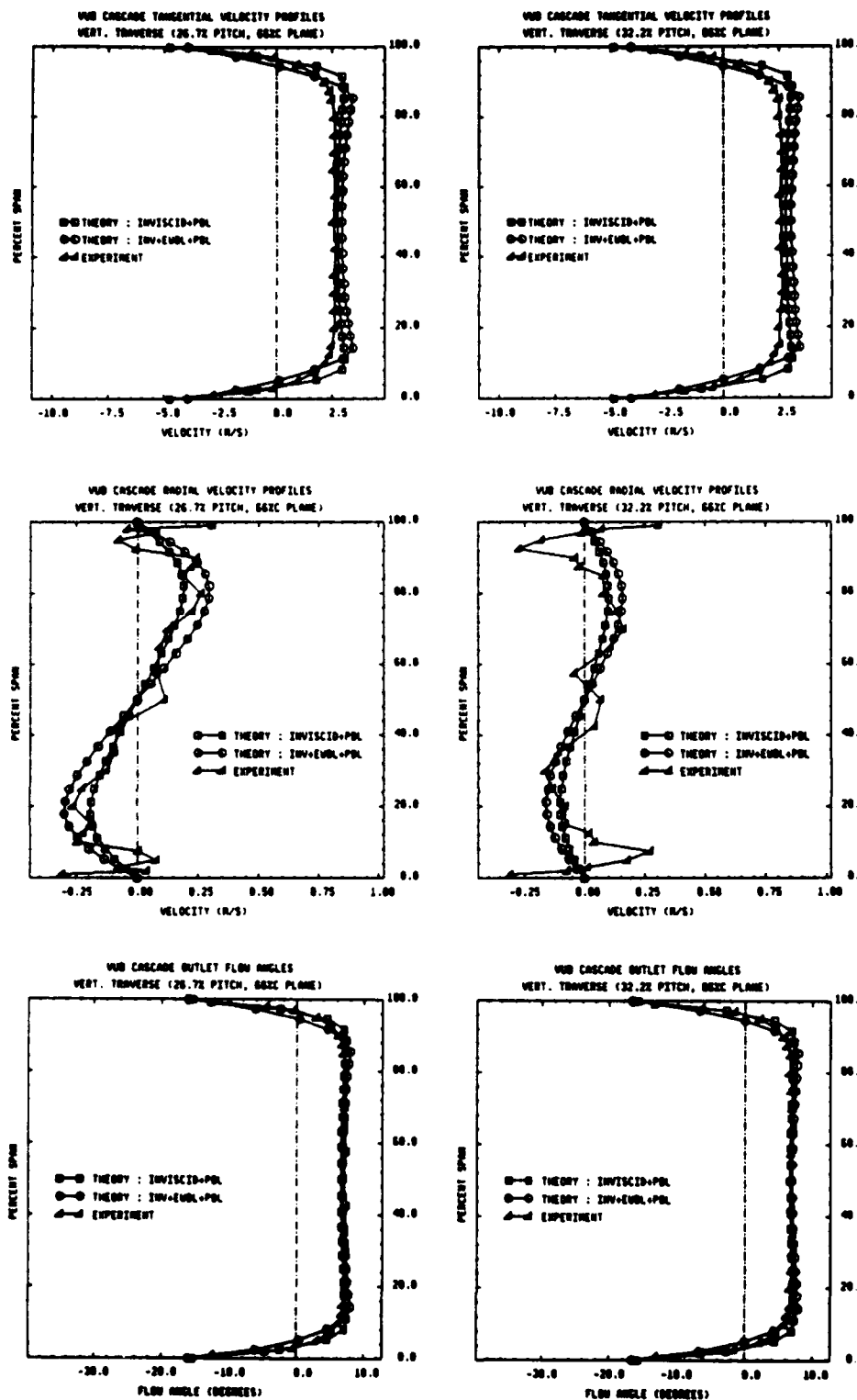


Figure 11.4e : Local spanwise profiles at 26.7% and 32.2% pitch (66% chord plane)

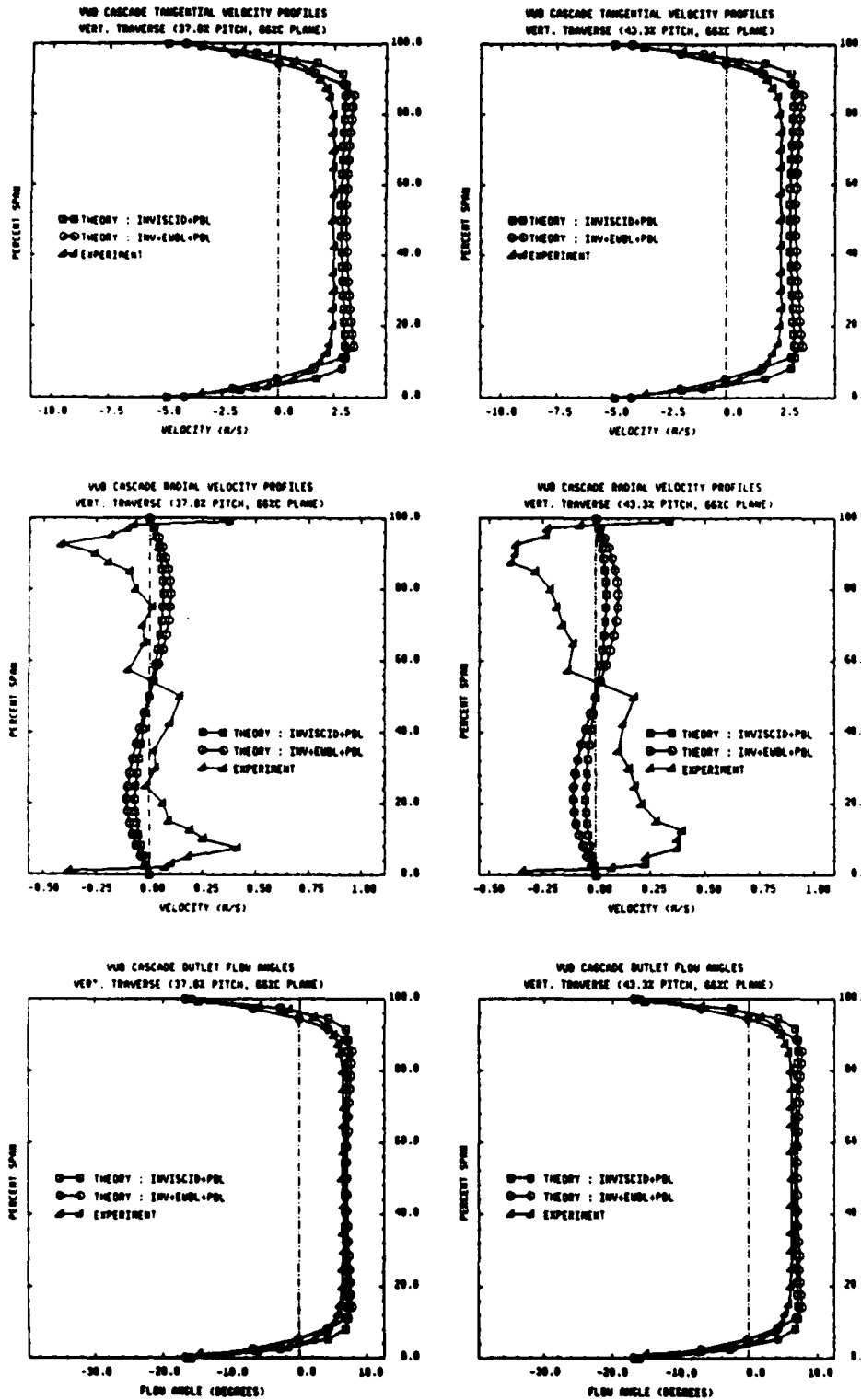


Figure 11.4f: Local spanwise profiles at 37.8% and 43.3% pitch (66% chord plane)

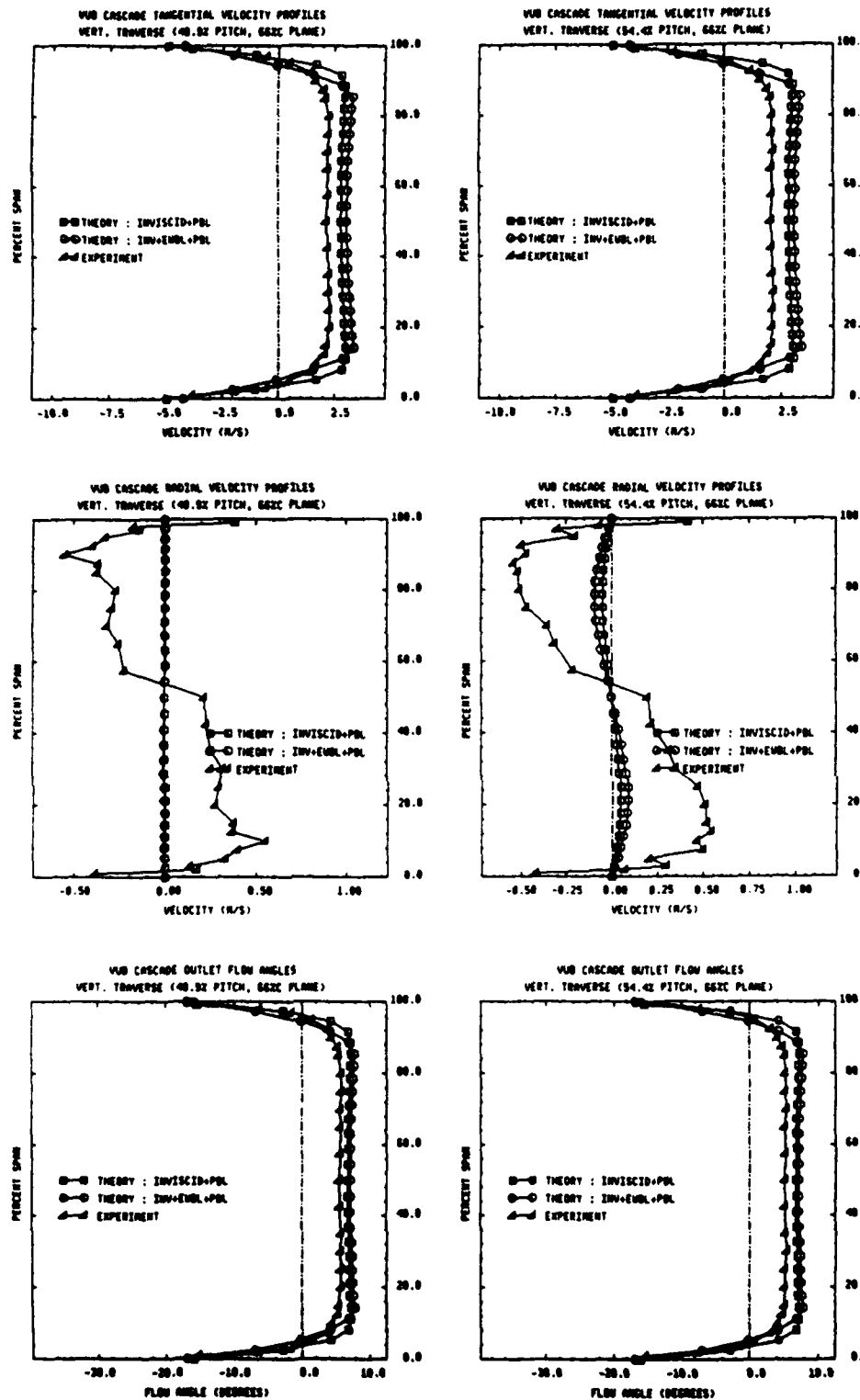


Figure 11.4g : Local spanwise profiles at 48.9% and 54.4% pitch (66% chord plane)

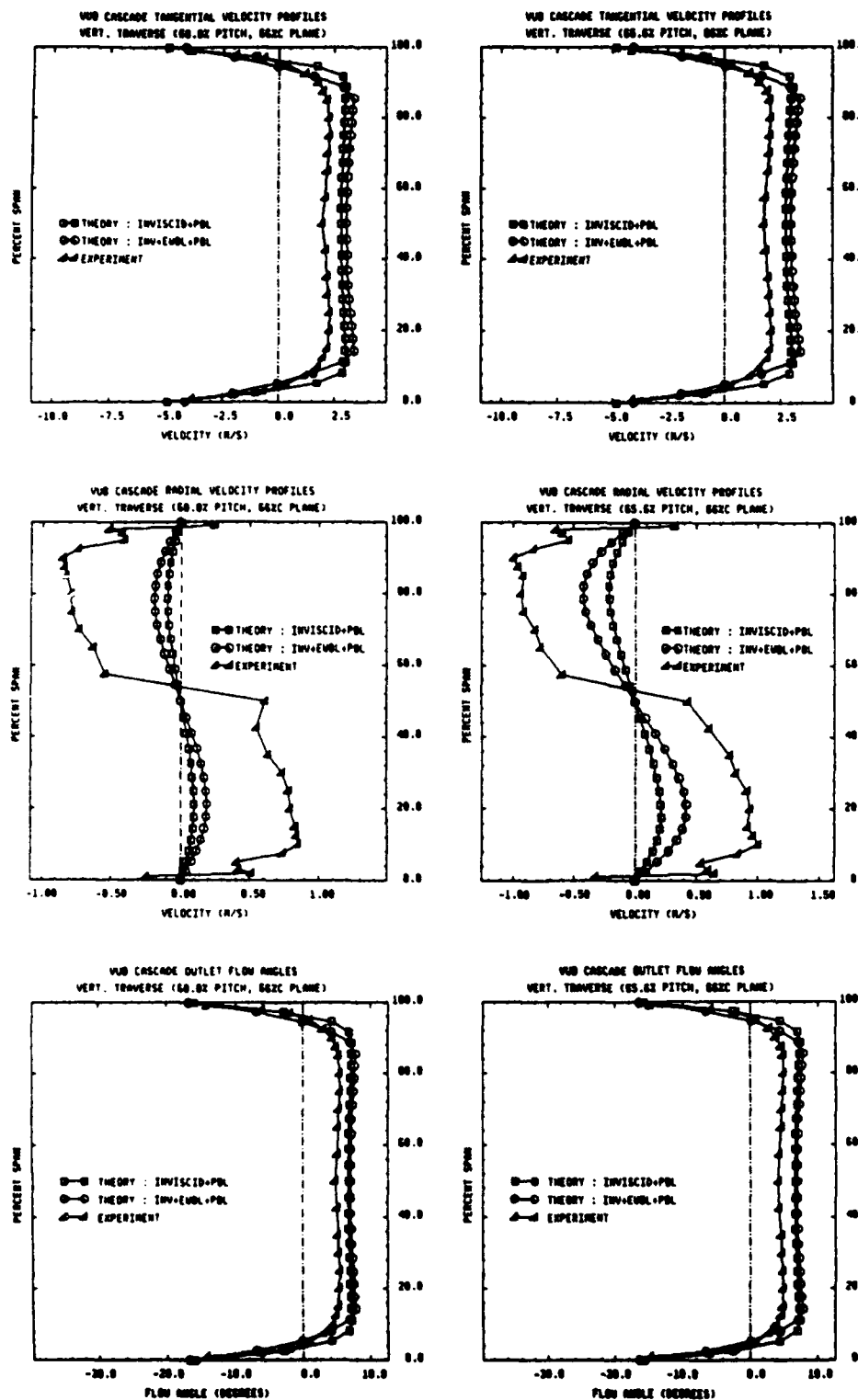


Figure 11.4h : Local spanwise profiles at 60.0% and 65.6% pitch (66% chord plane)

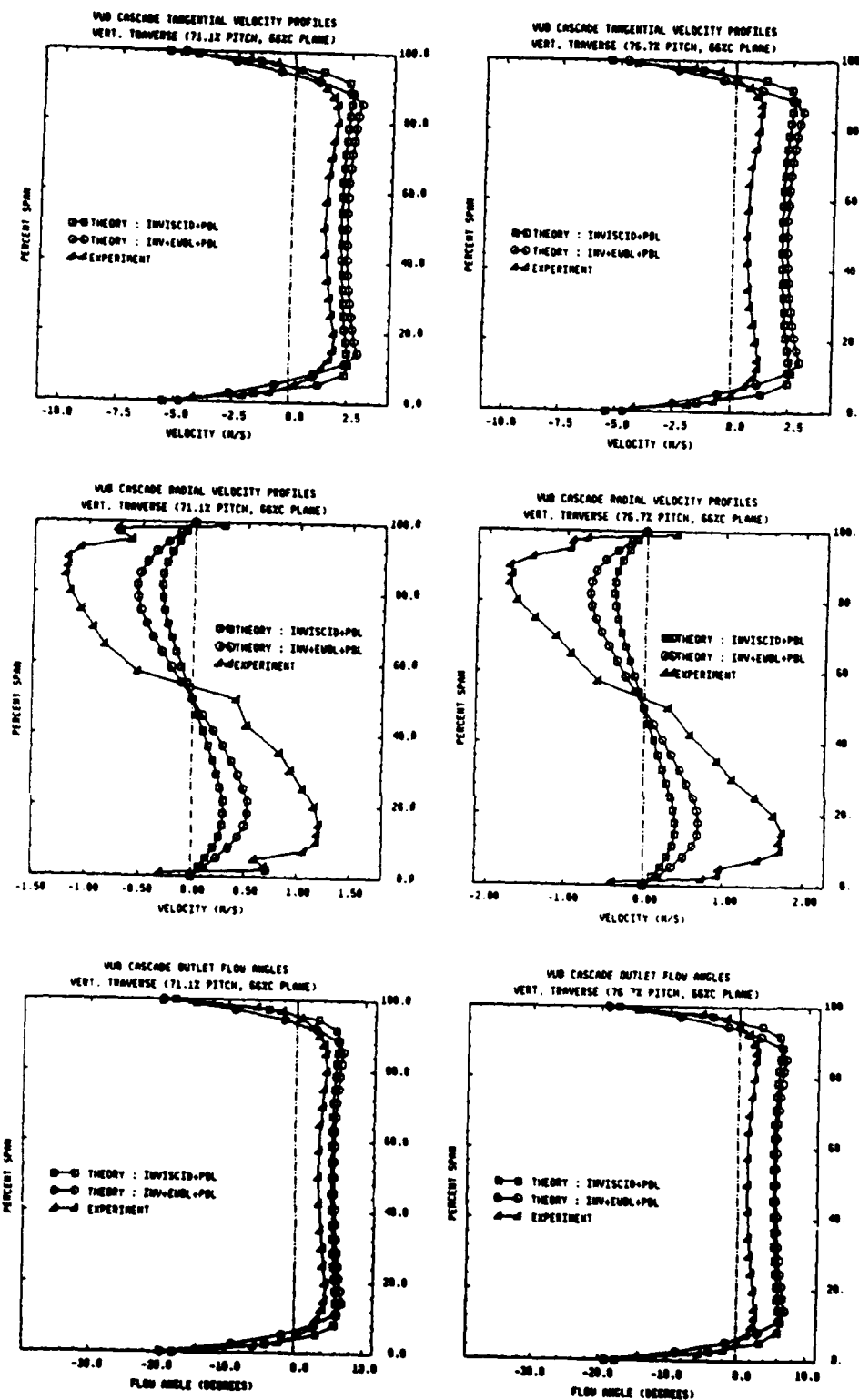


Figure 11.4i: Local spanwise profiles at 71.1% and 76.7% pitch (66% chord plane)

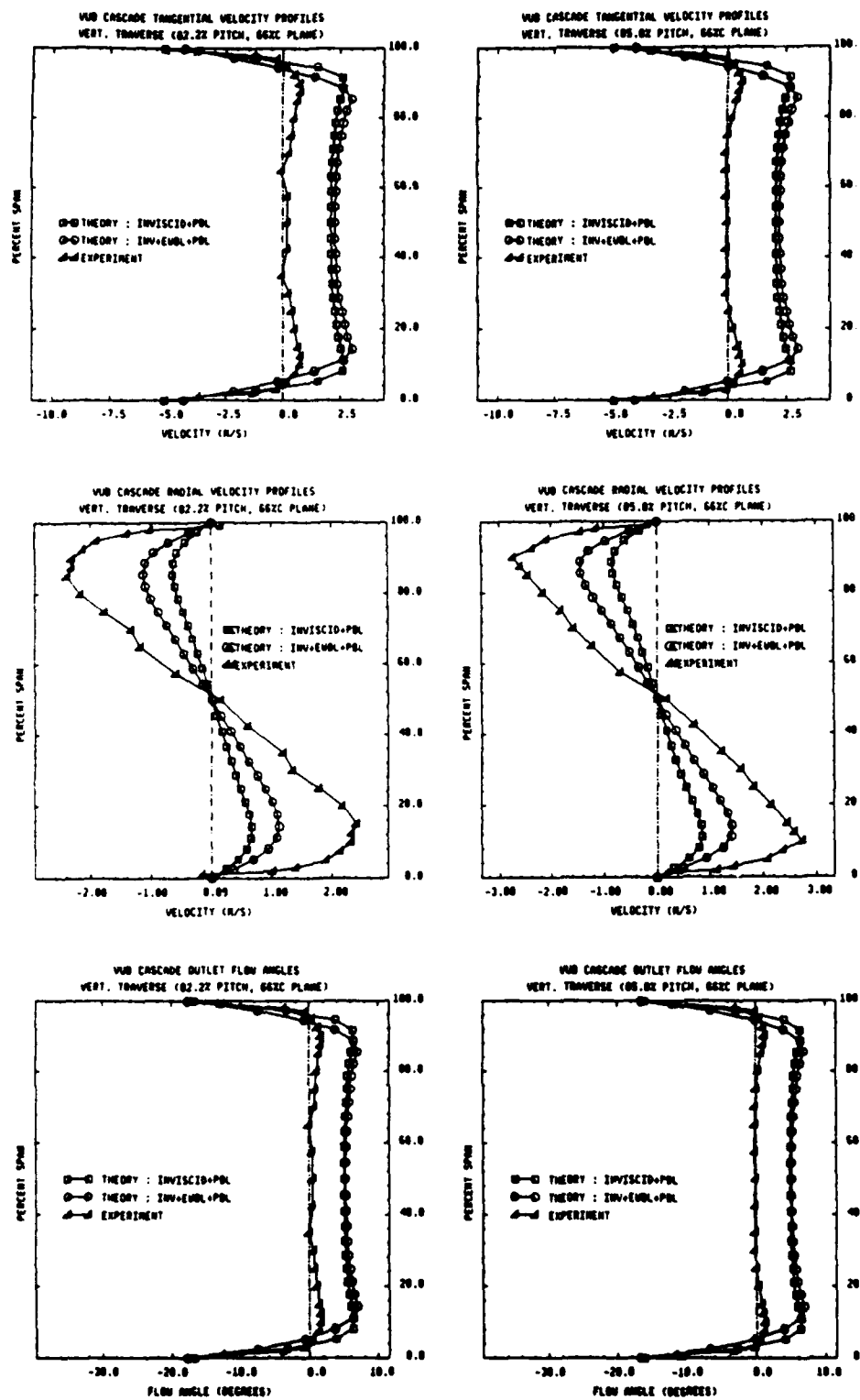


Figure 11.4j : Local spanwise profiles at 82.2% and 85.0% pitch (66% chord plane)

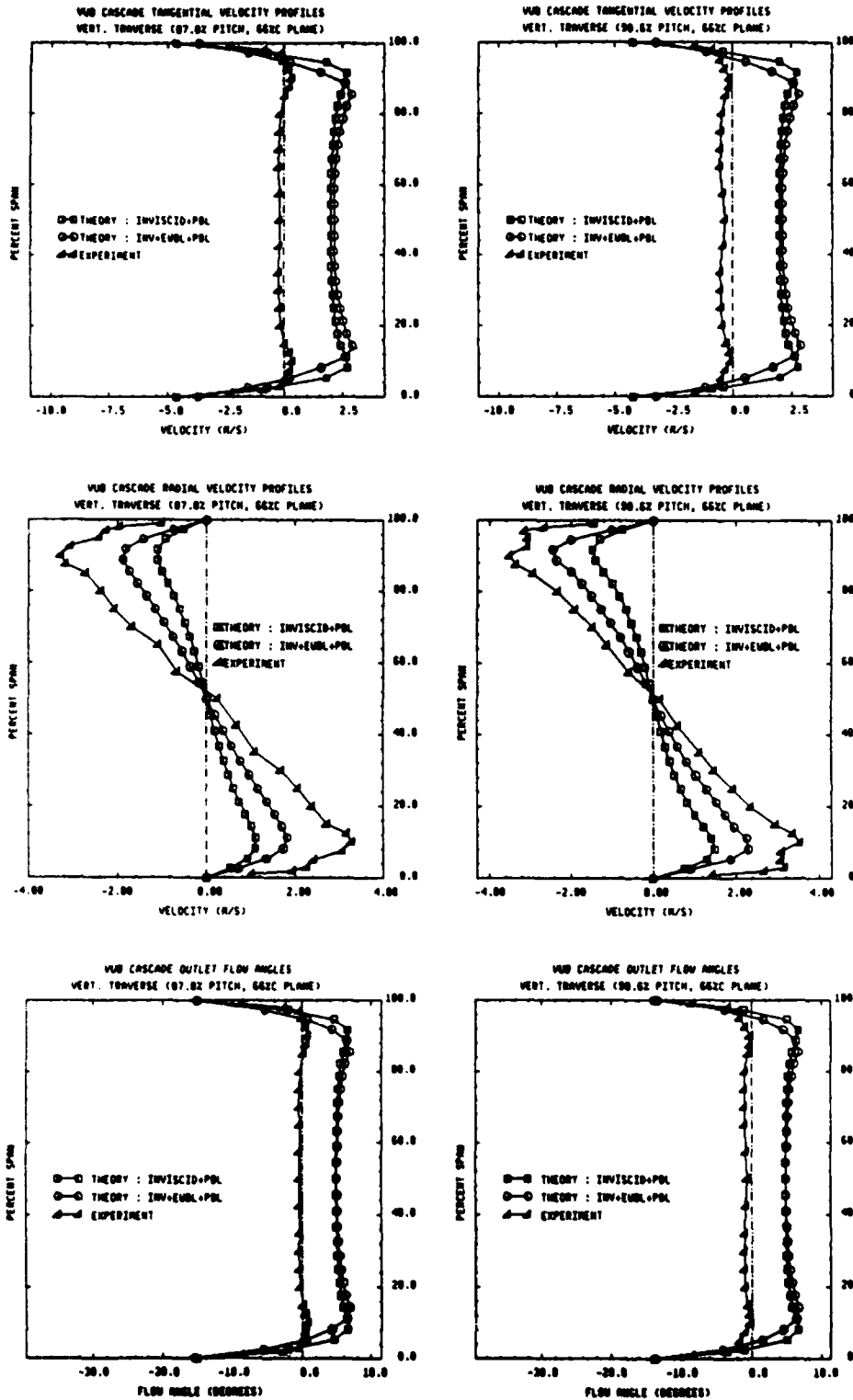


Figure 11.4k : Local spanwise profiles at 87.8% pitch and 90.6% pitch (66% chord plane)

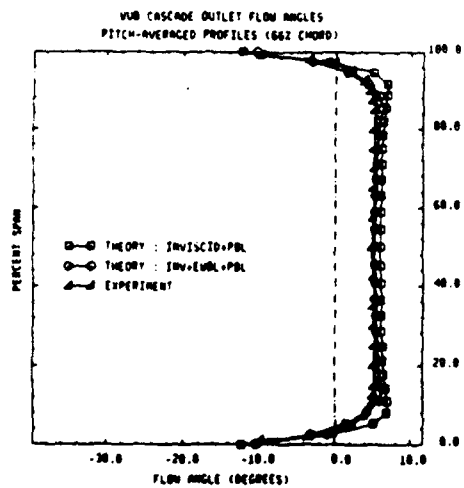
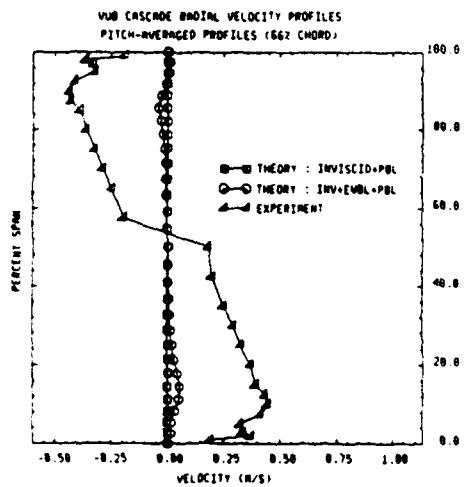
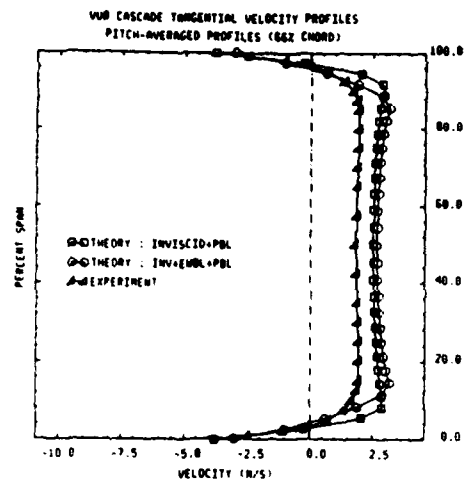


Figure 11.41: Pitch-averaged spanwise profiles (66% chord plane)

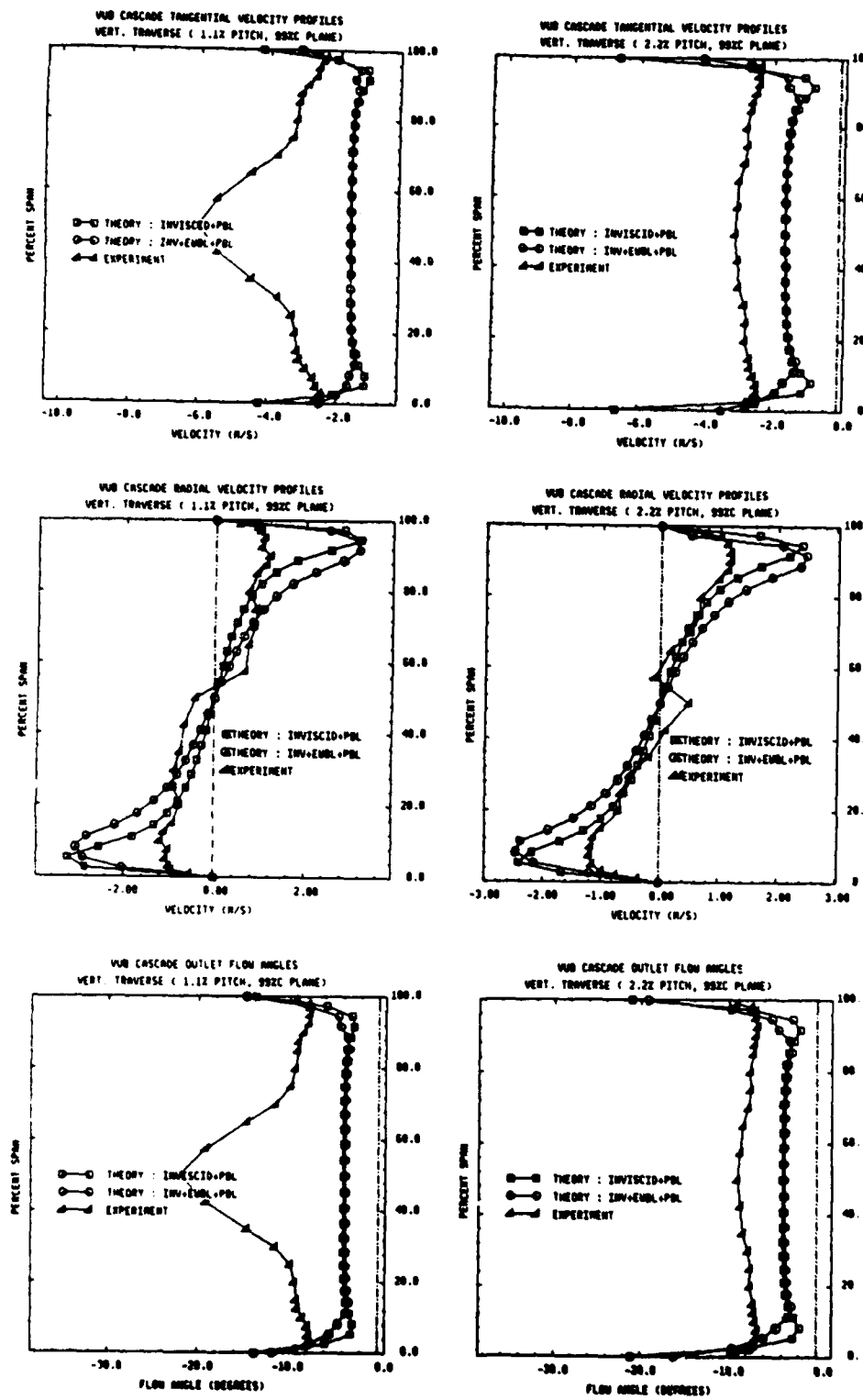


Figure 11.5a : Local spanwise profiles at 1.1% and 2.2% pitch (99% chord plane)

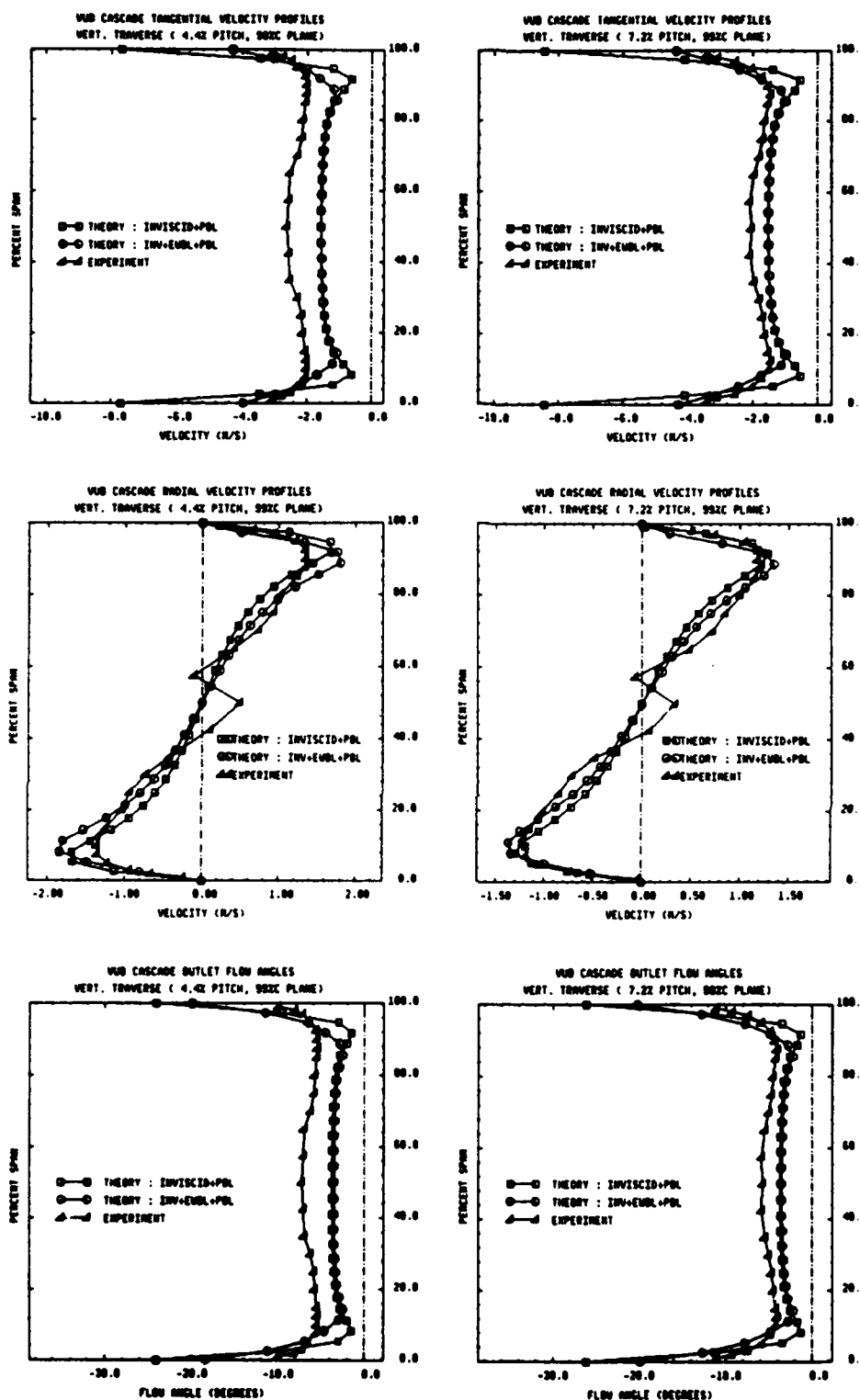


Figure 11.5b : Local spanwise profiles at 4.4% and 7.2% pitch (99% chord plane)

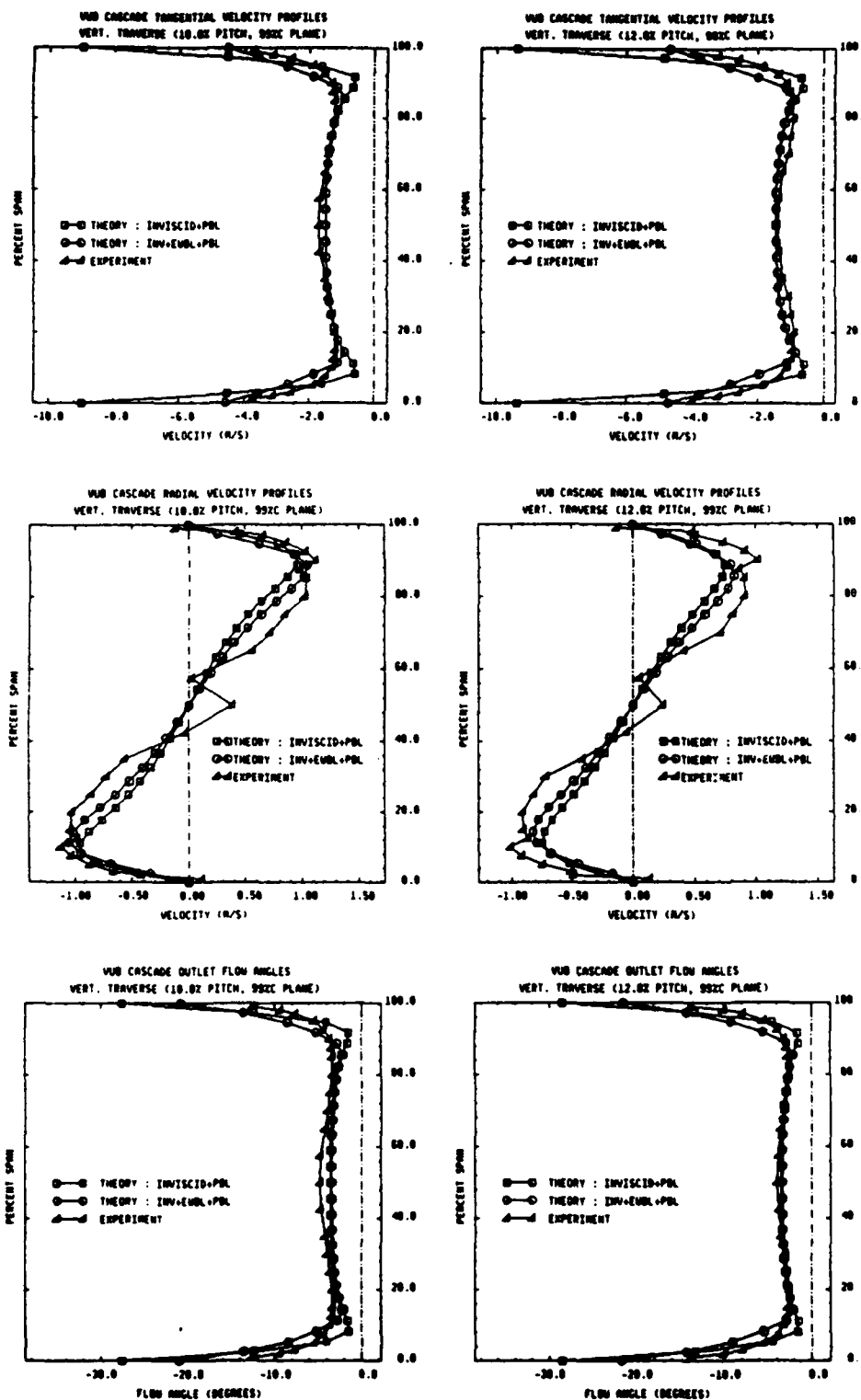


Figure 11.5c : Local spanwise profiles at 10.0% and 12.8% pitch (99% chord plane)

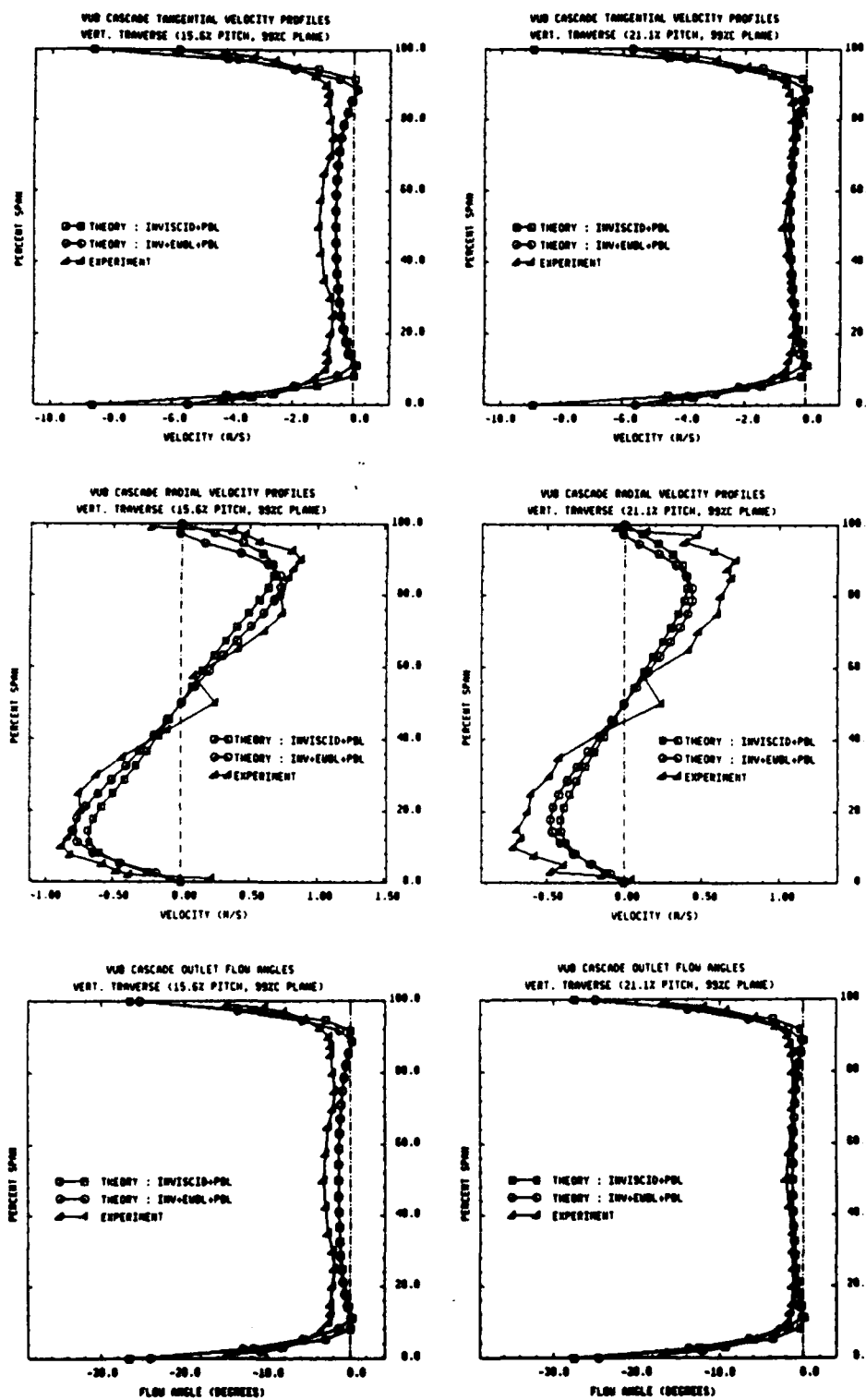


Figure 11.5d : Local spanwise profiles at 15.6% and 21.1% pitch (99% chord plane)

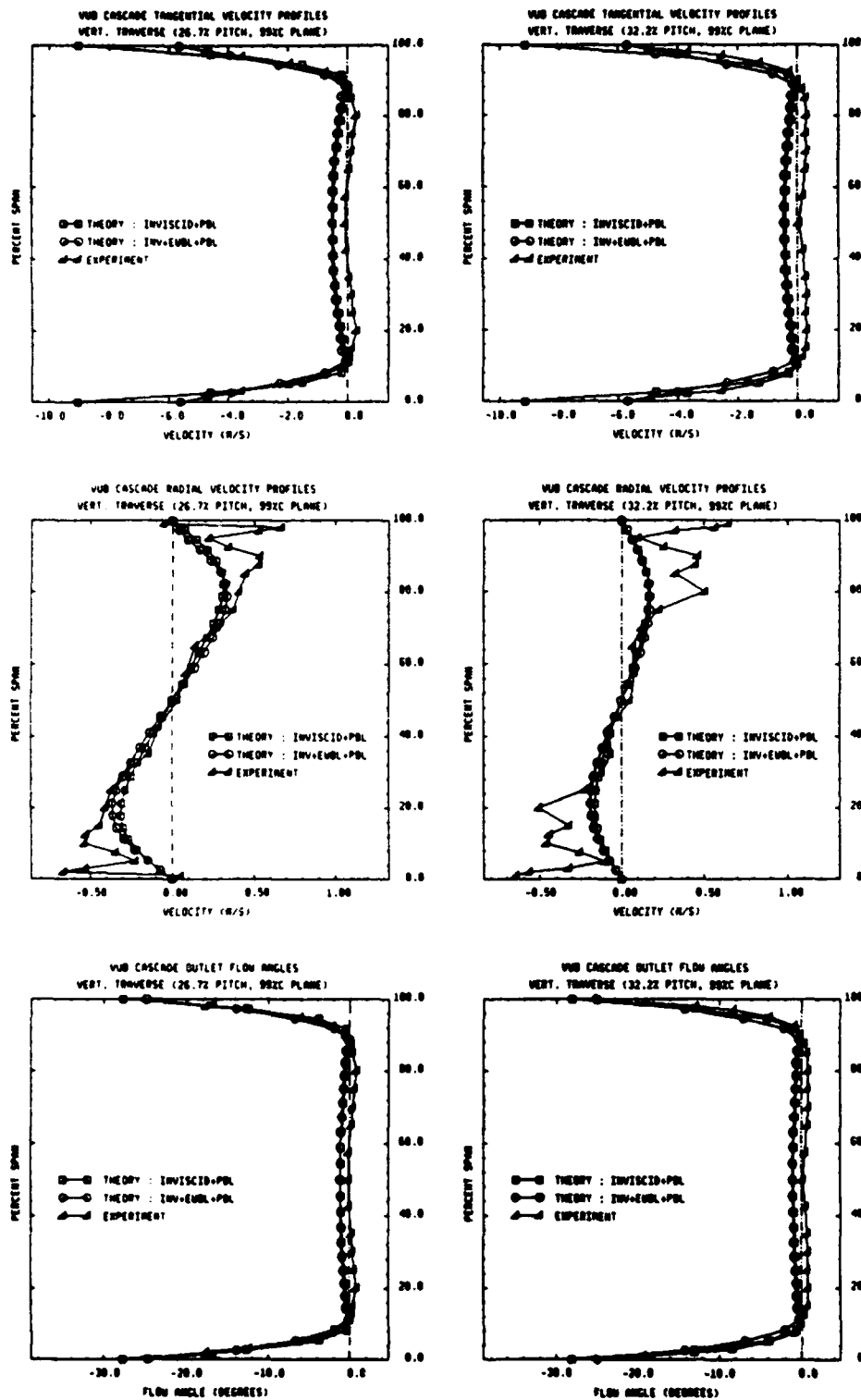


Figure 11.5e : Local spanwise profiles at 26.7% and 32.2% pitch (99% chord plane)

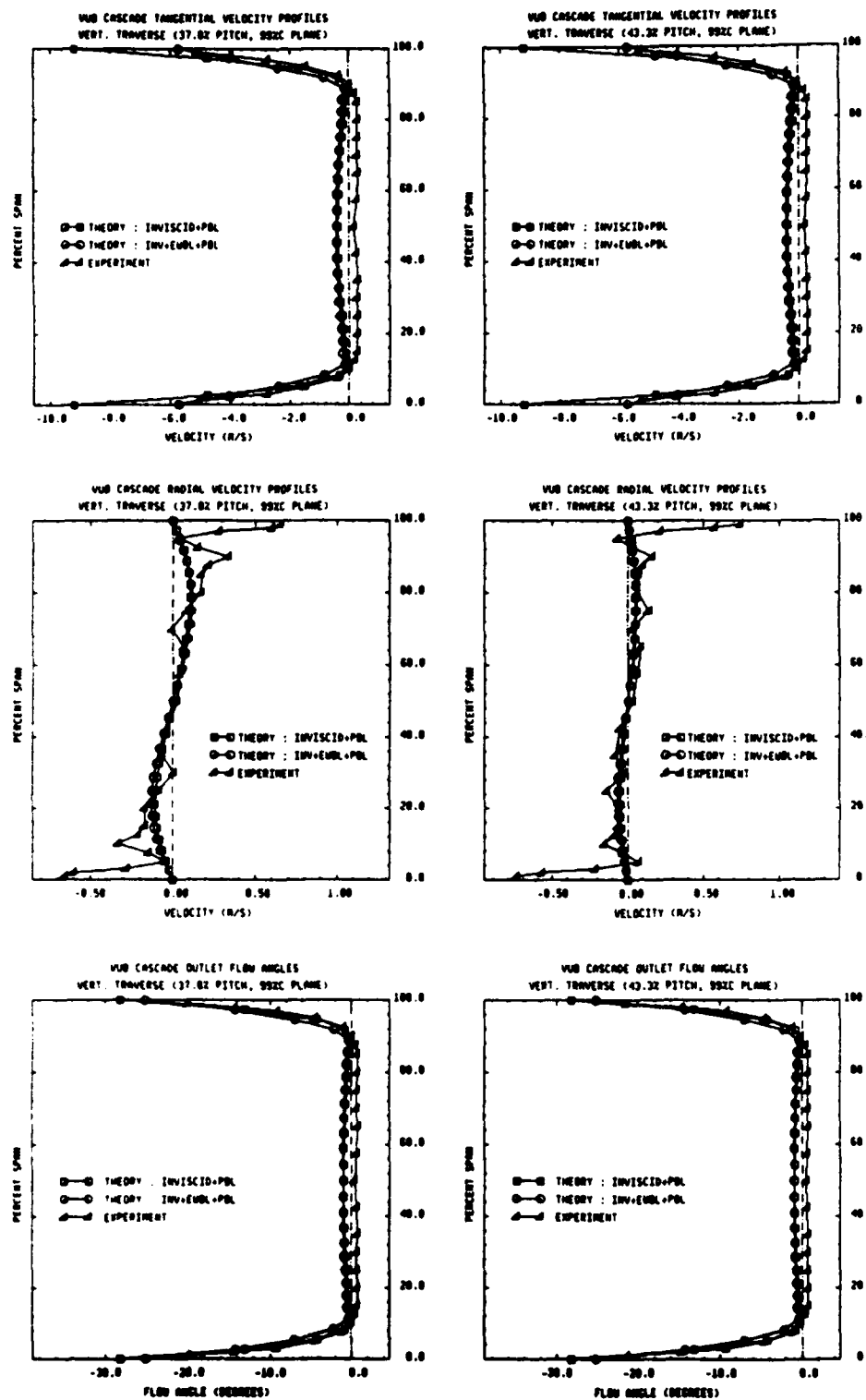


Figure 11.5f : Local spanwise profiles at 37.8% and 43.3% pitch (99% chord plane)

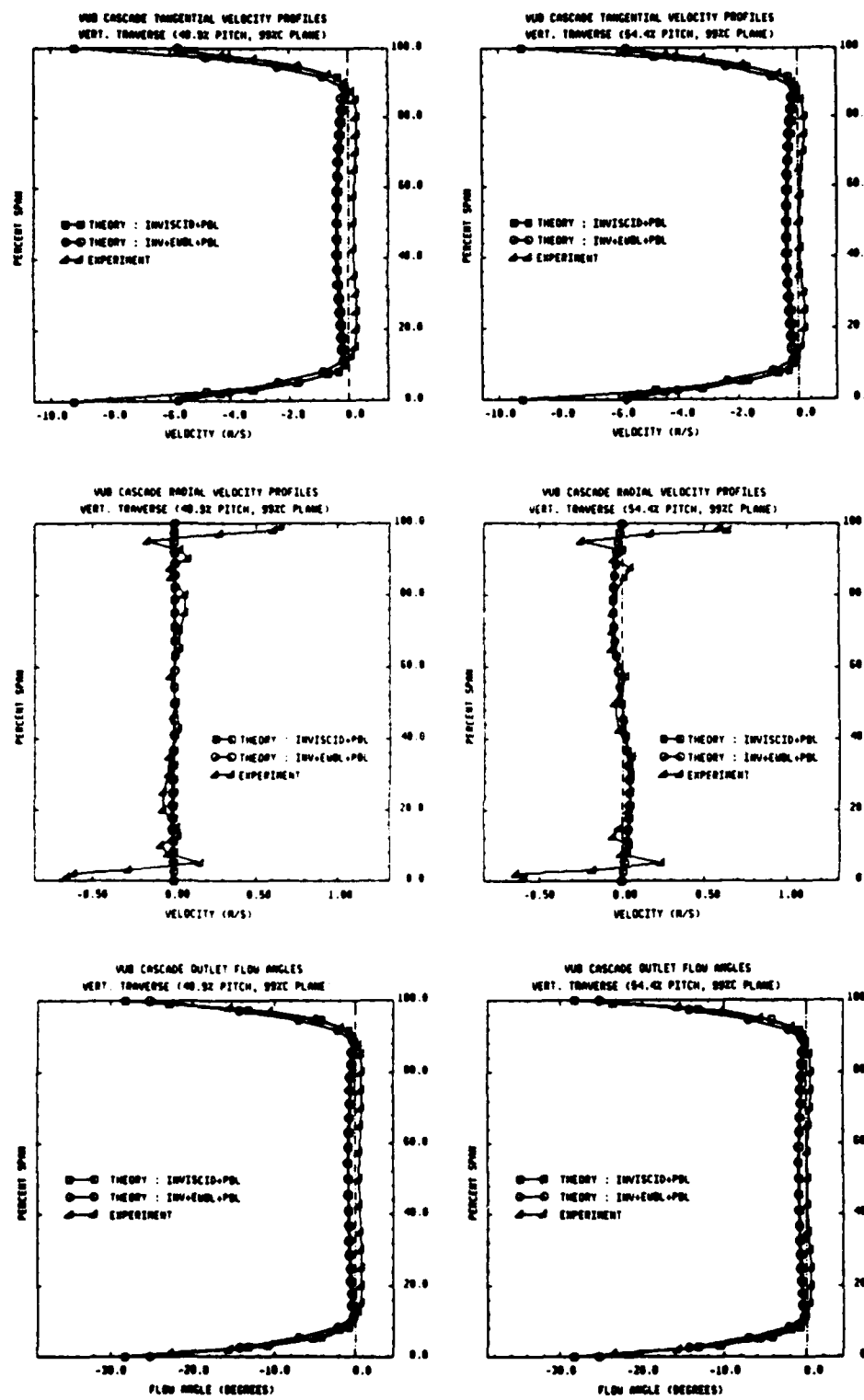


Figure 11.5g : Local spanwise profiles at 48.9% and 54.4% pitch (99% chord plane)

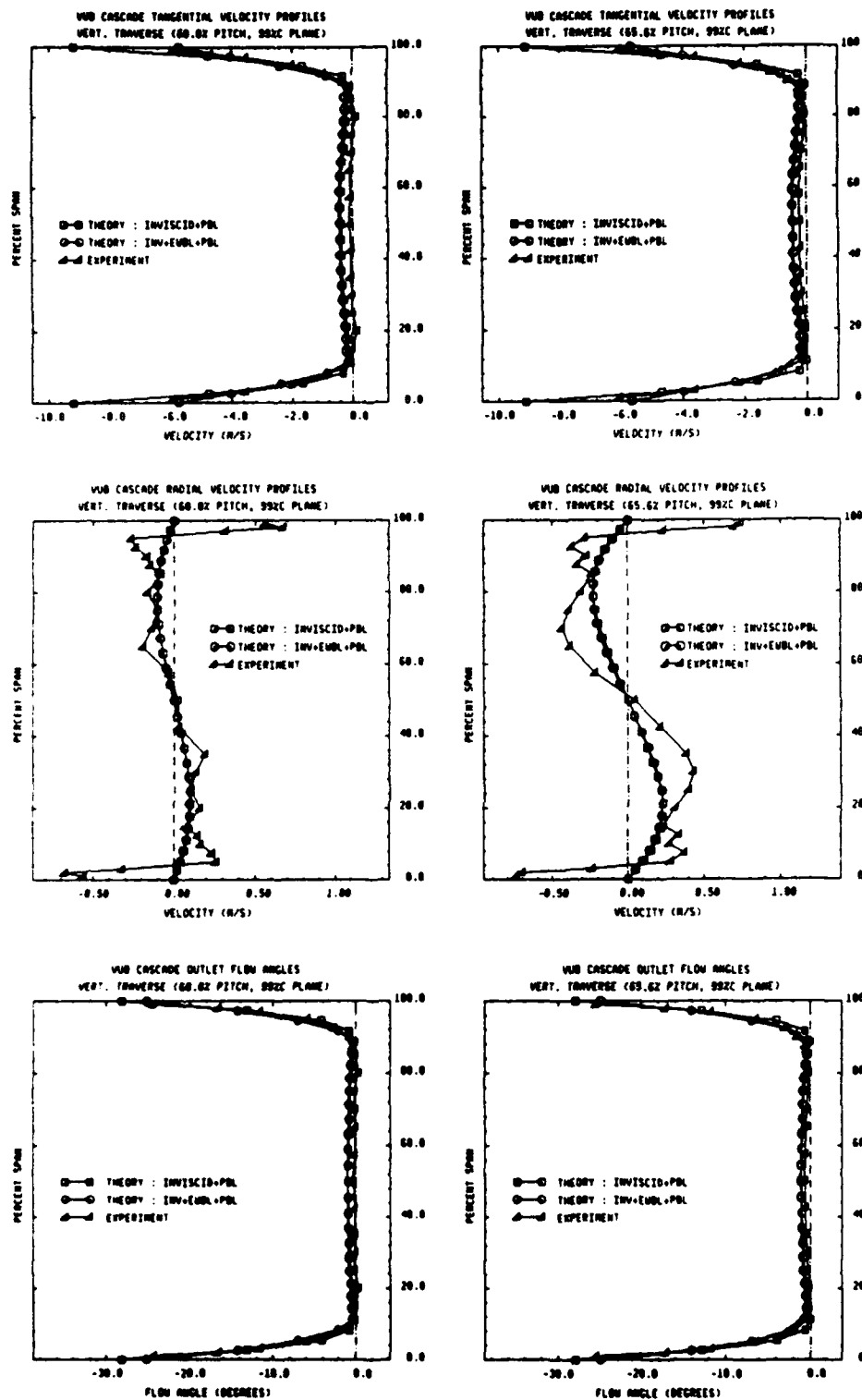


Figure 11.5h : Local spanwise profiles at 60.0% and 65.6% pitch (99% chord plane)

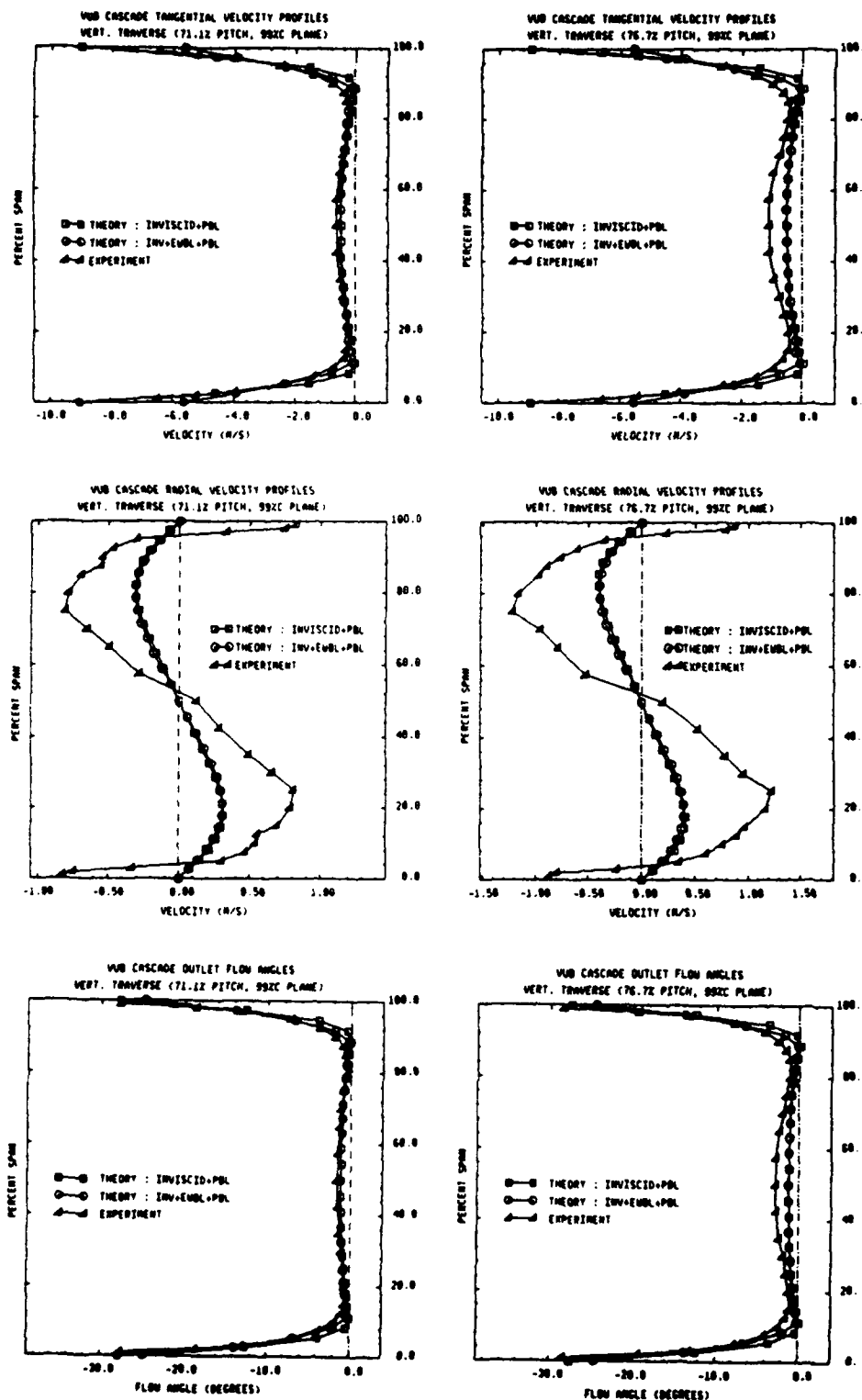


Figure 11.5i : Local spanwise profiles at 71.1% and 76.7% pitch (99% chord plane)

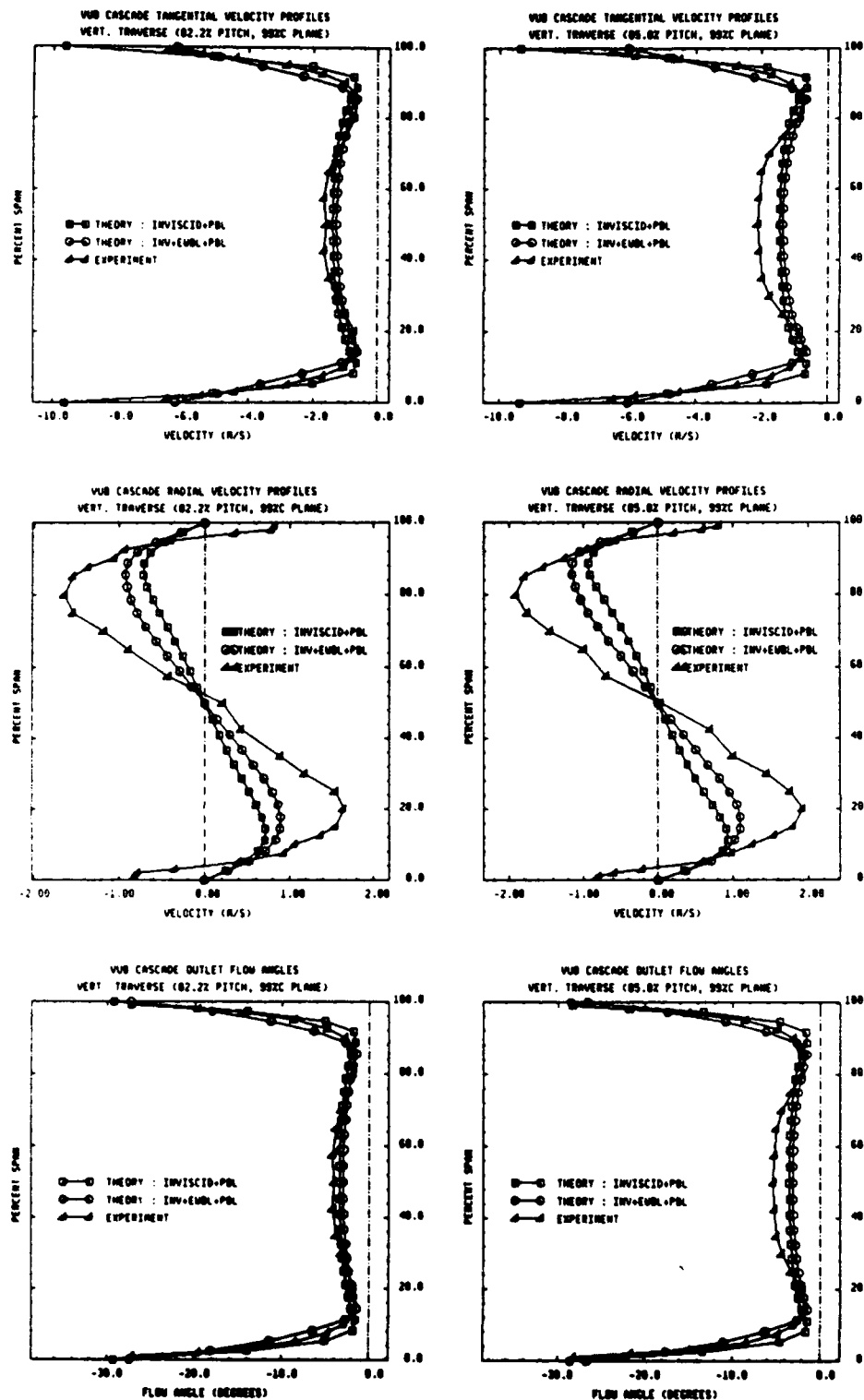


Figure 11.5j: Local spanwise profiles at 82.2% and 85.0% pitch (99% chord plane)

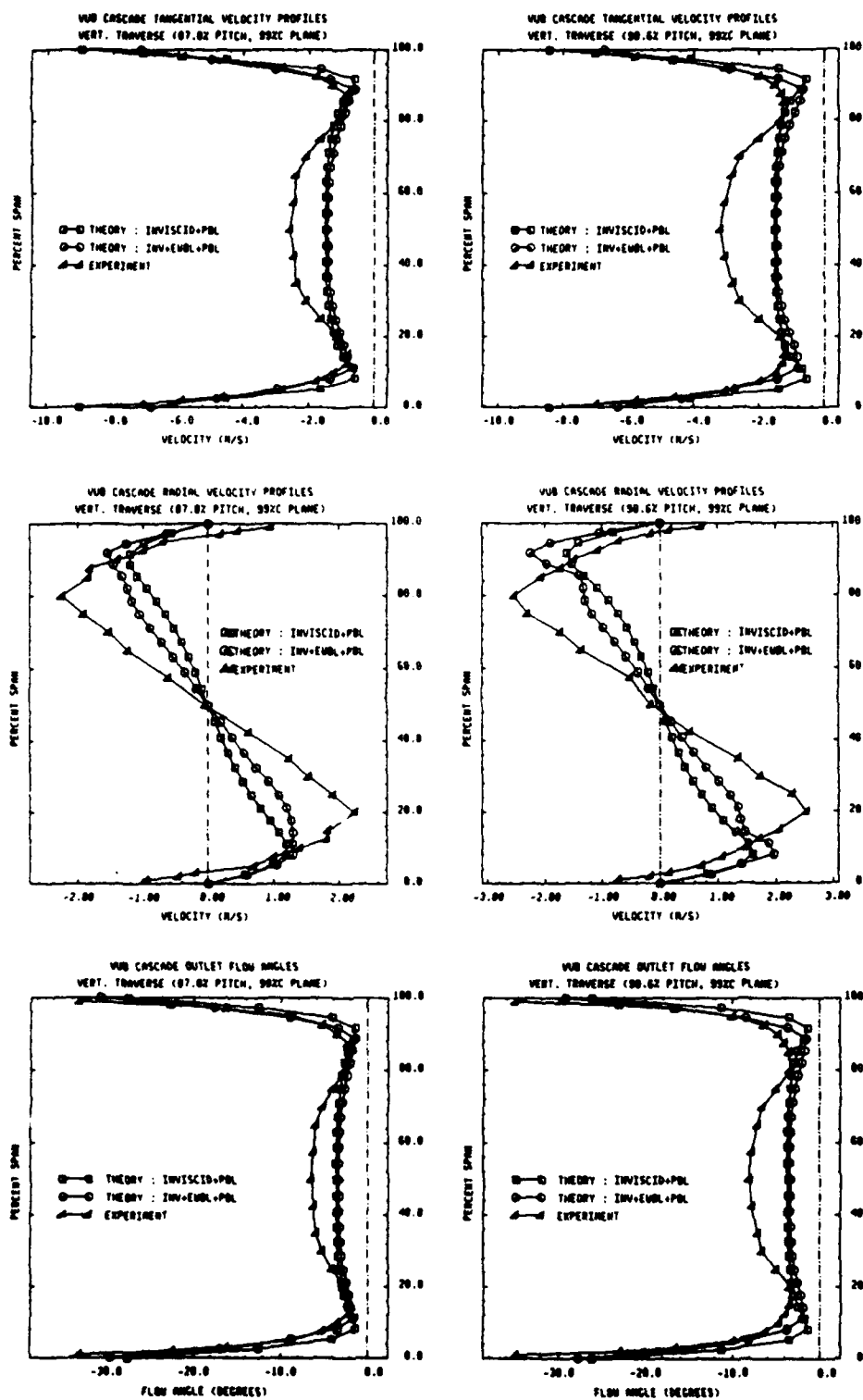


Figure 11.5k : Local spanwise profiles at 87.8% pitch and 90.6% pitch (99% chord plane)

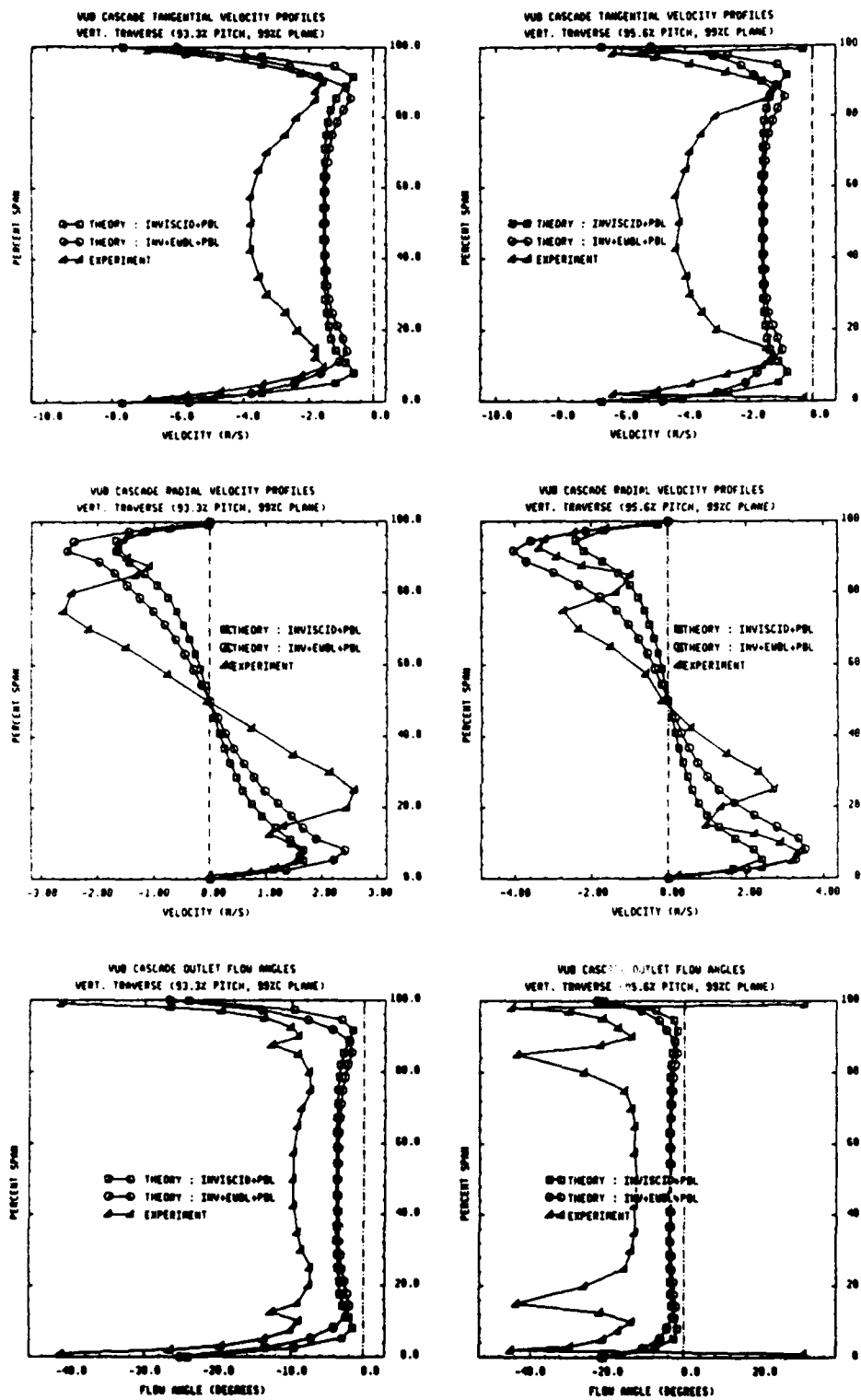


Figure 11.51 : Local spanwise profiles at 93.3% pitch and 95.6% pitch (99% chord plane)

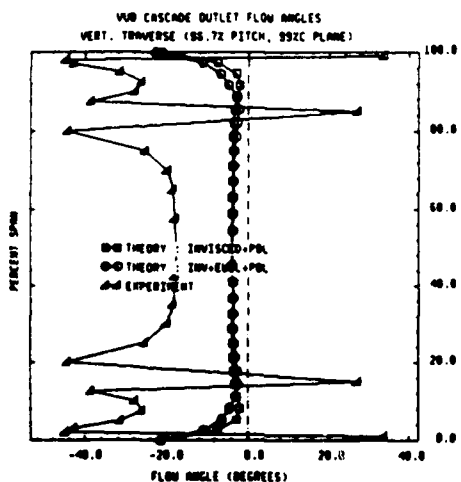
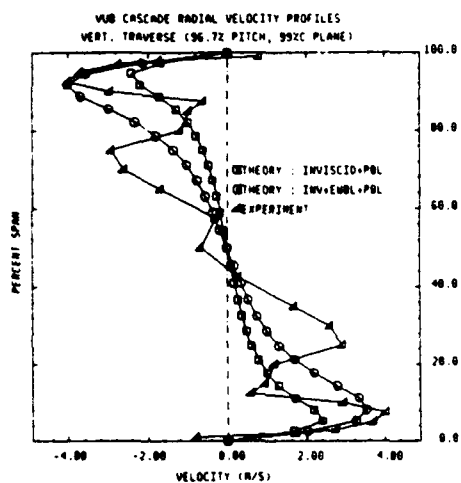
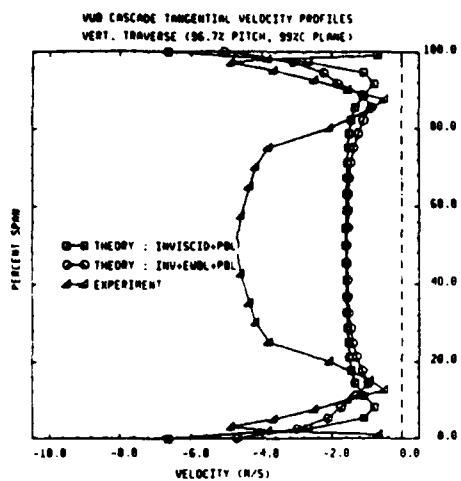


Figure 11.5m : Local spanwise profiles at 96.7% pitch (99% chord plane)

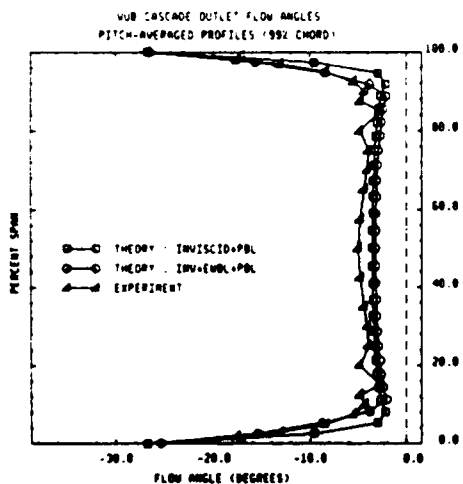
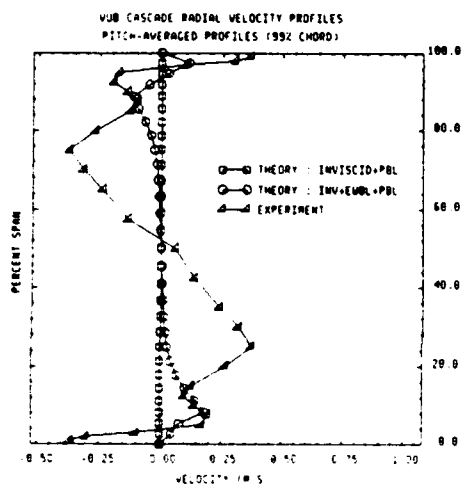
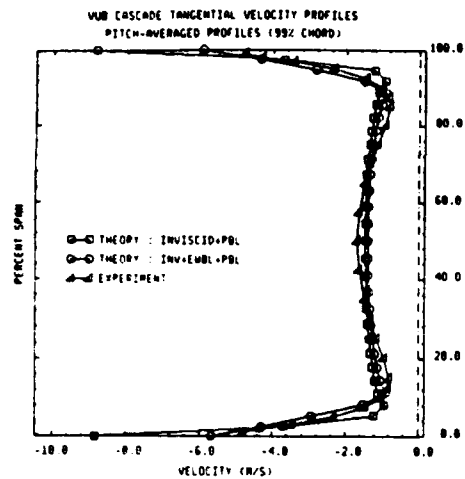


Figure 11.5n : Pitch-averaged spanwise profiles (99% chord plane)

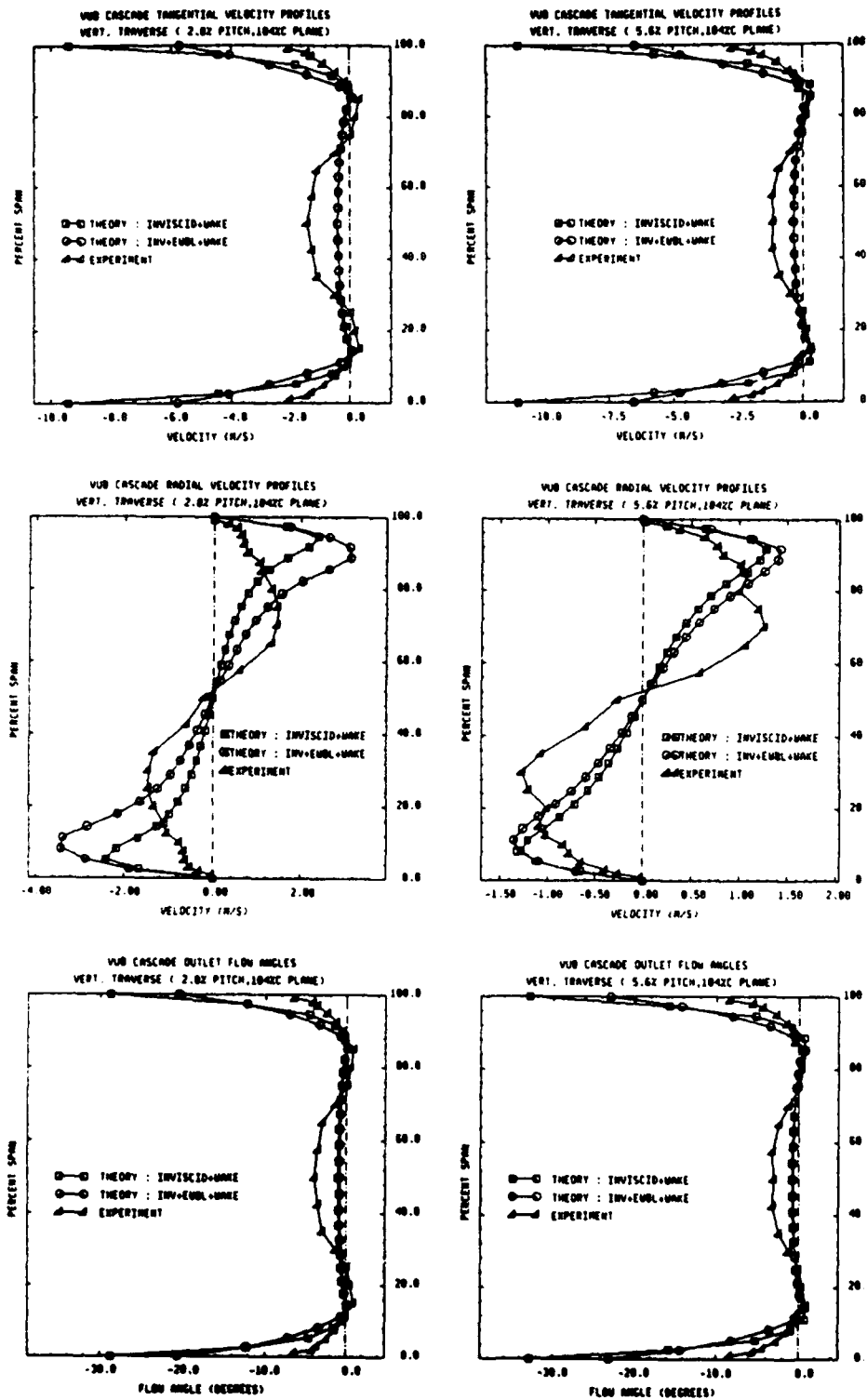


Figure 11.6a : Local spanwise profiles at 2.8% and 5.6% pitch (104% chord plane)

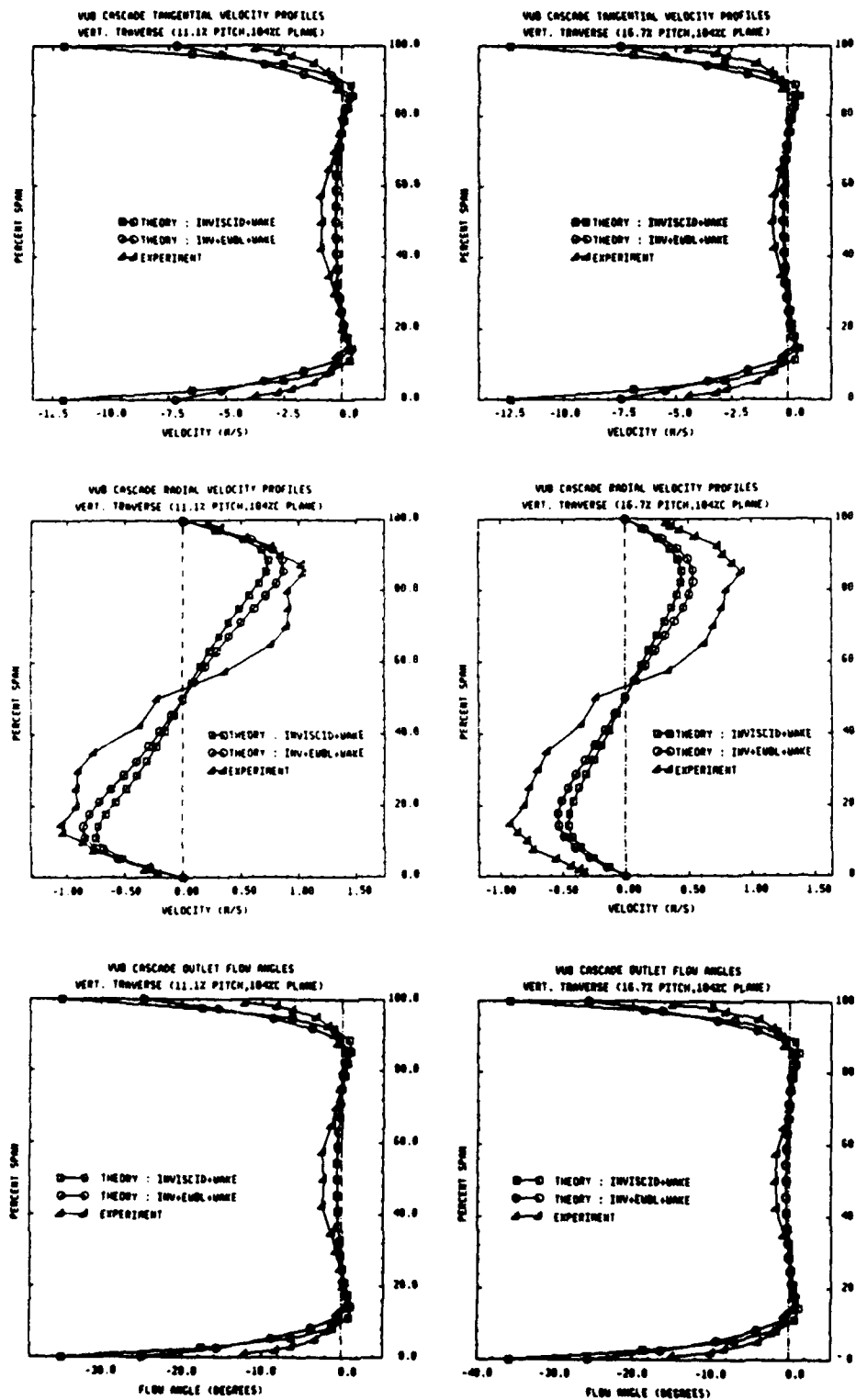


Figure 11.6b : Local spanwise profiles at 11.1% and 16.7% pitch (104% chord plane)

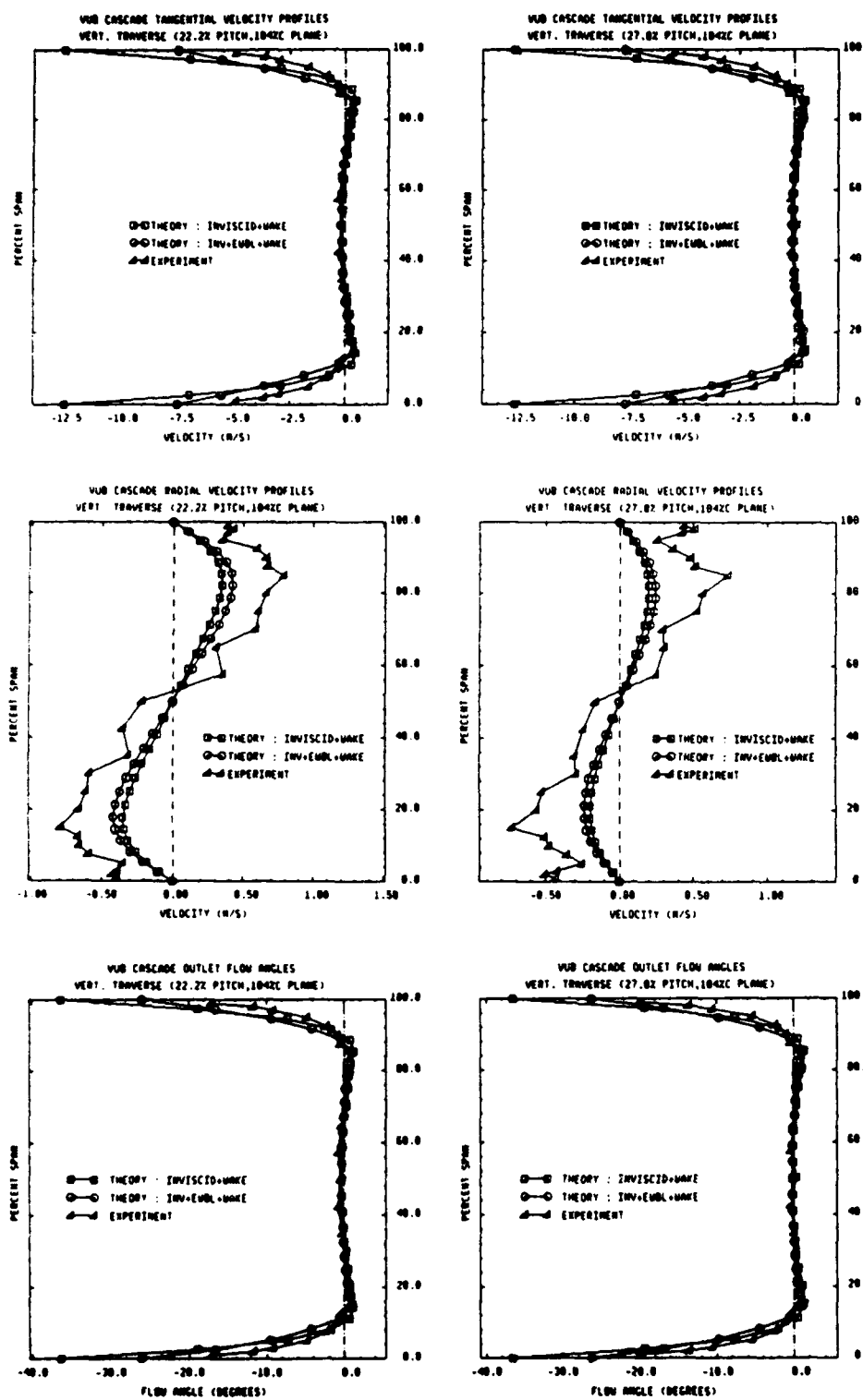


Figure 11.6c : Local spanwise profiles at 22.2% and 27.8% pitch (104% chord plane)

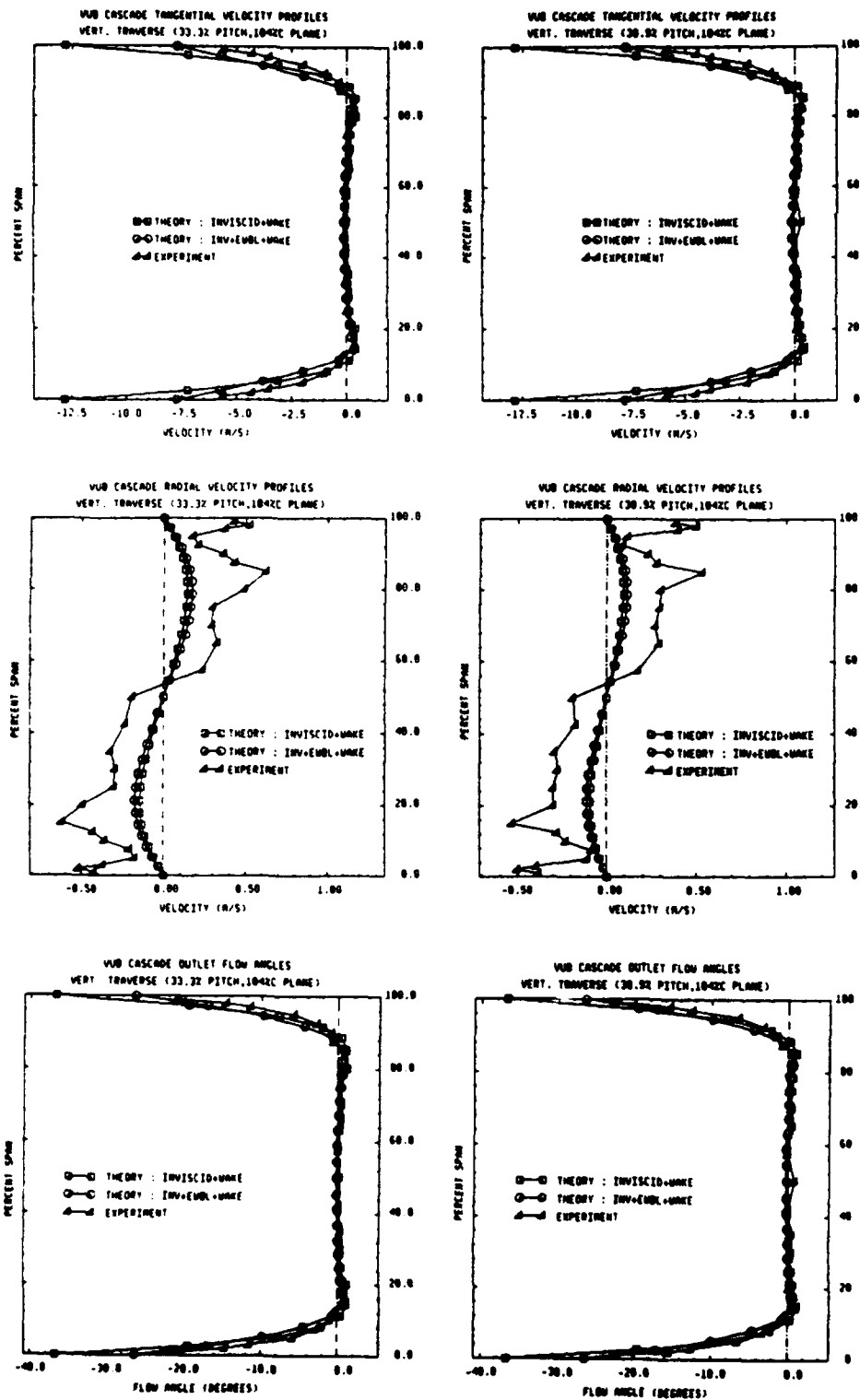


Figure 11.6d : Local spanwise profiles at 33.3% and 38.9% pitch (104% chord plane)

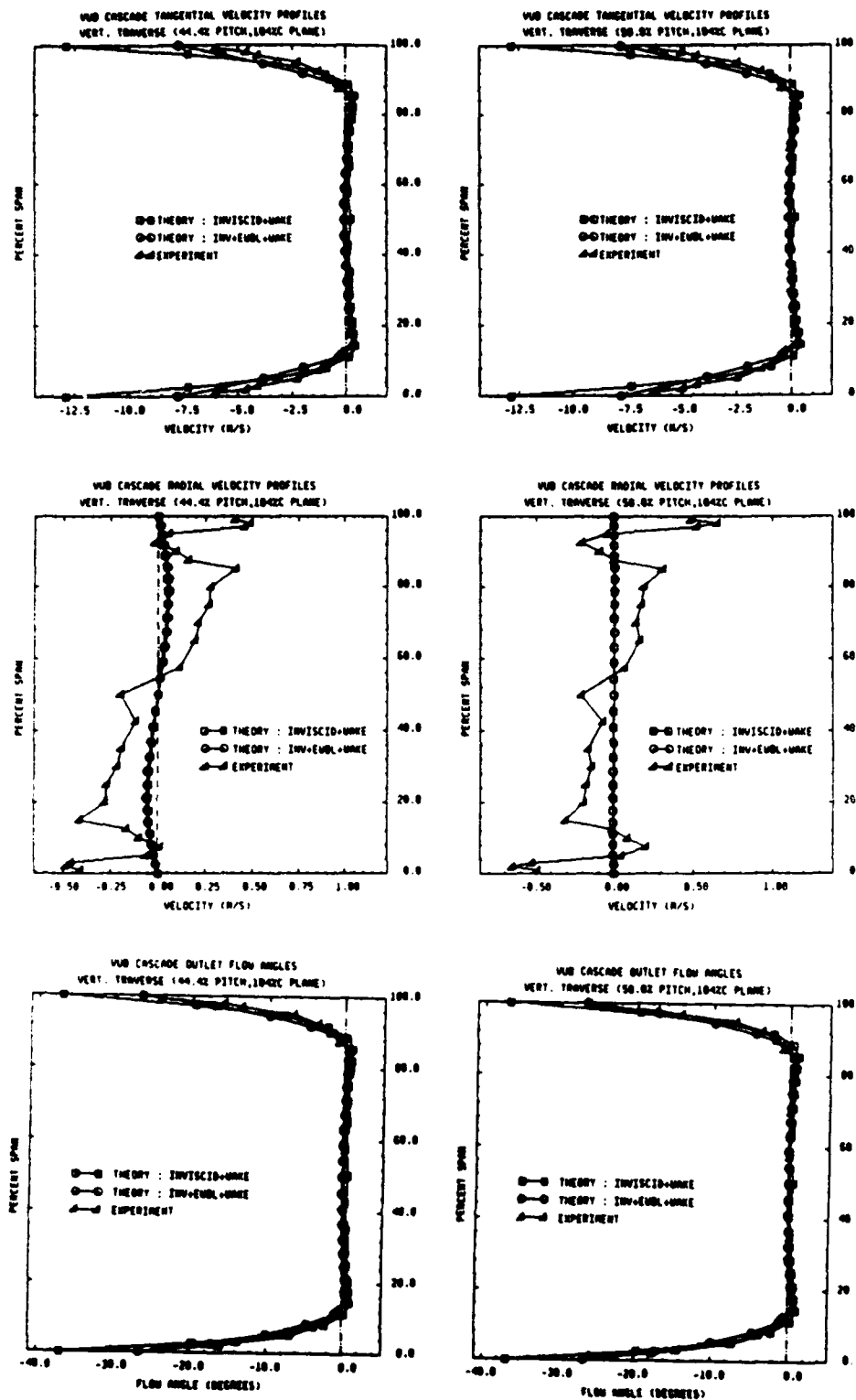


Figure 11.6e : Local spanwise profiles at 44.4% and 50.0% pitch (104% chord plane)

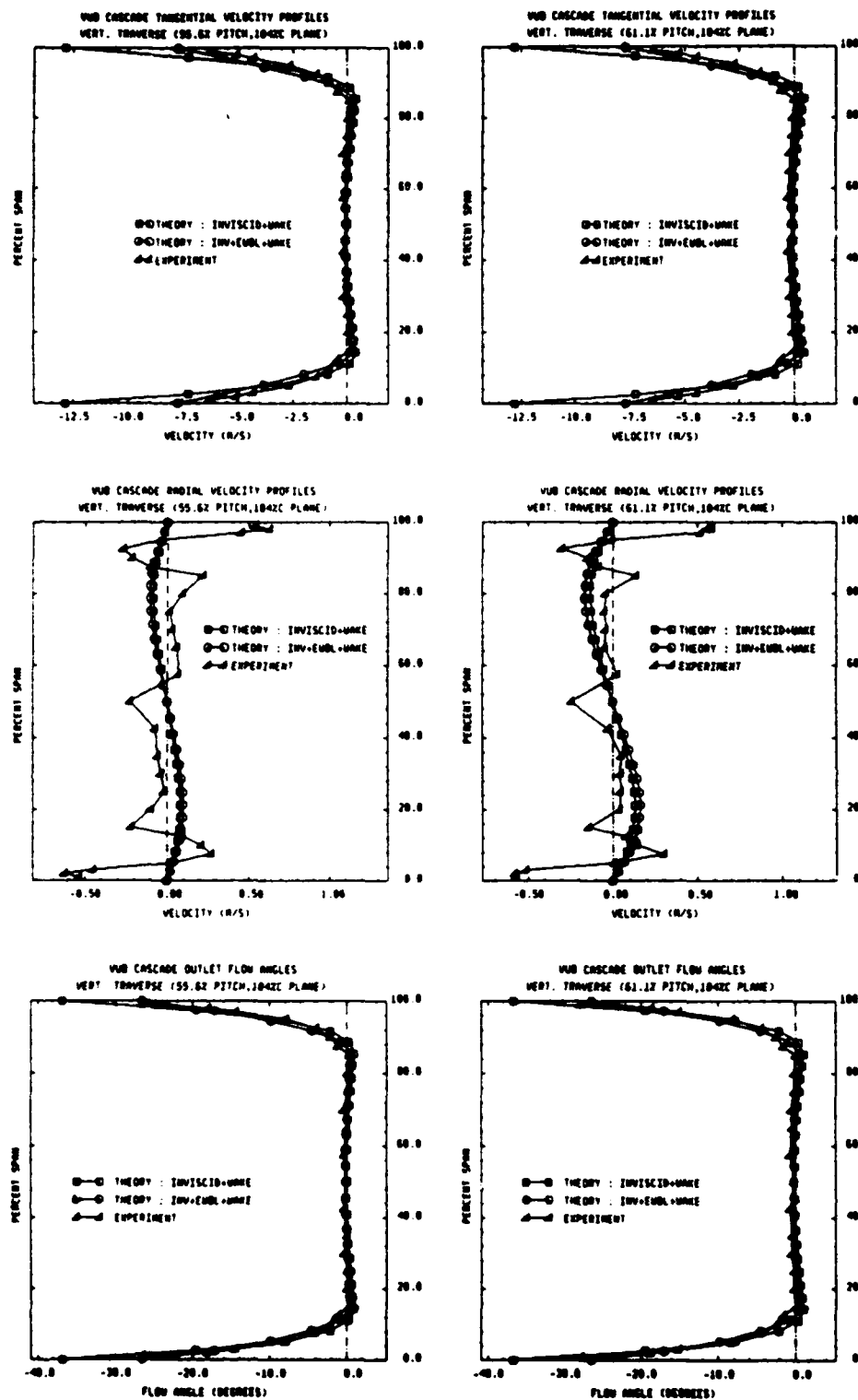


Figure 11.6f: Local spanwise profiles at 55.6% and 61.1% pitch (104% chord plane)

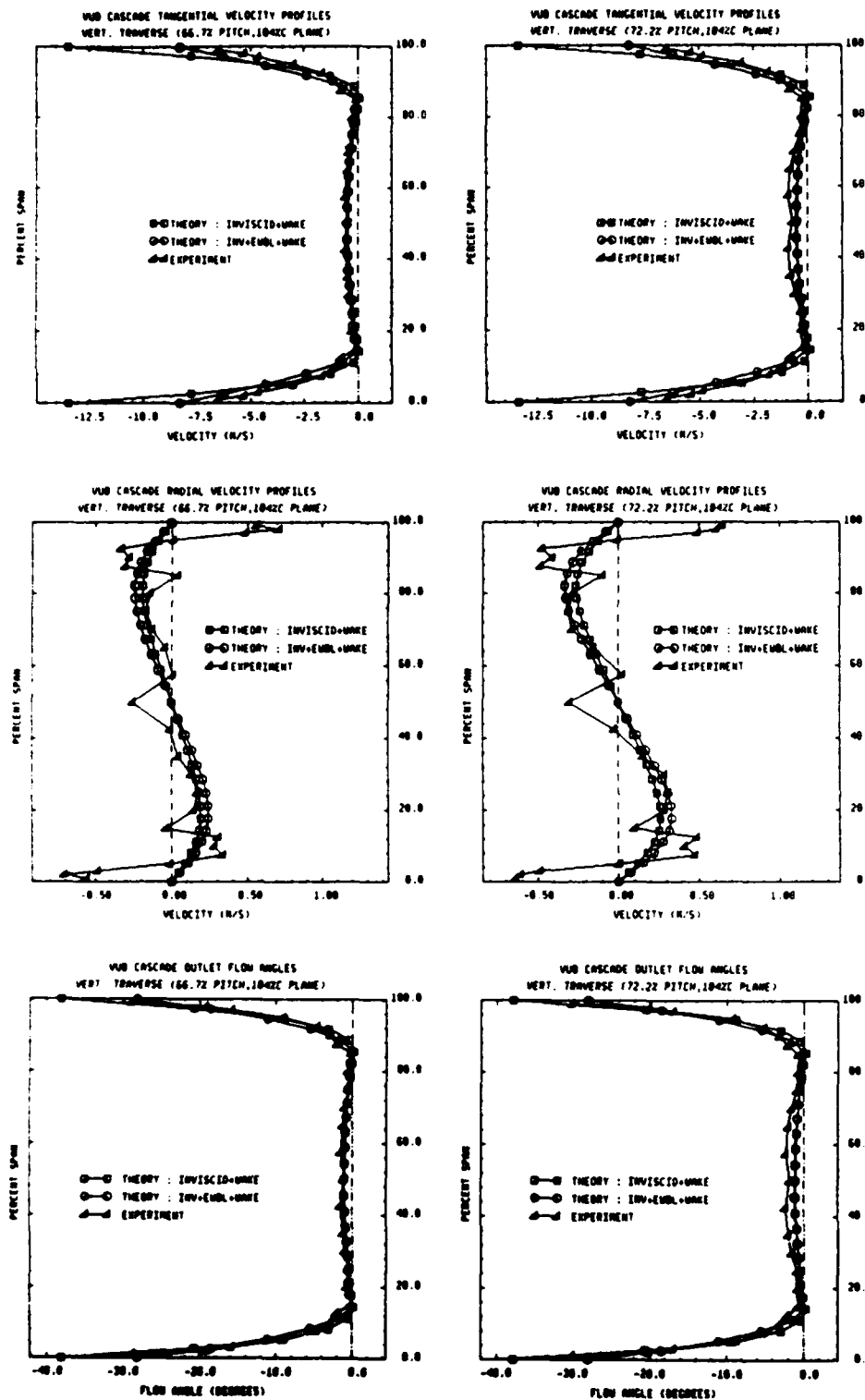


Figure 11.6g : Local spanwise profiles at 66.7% and 72.2% pitch (104% chord plane)

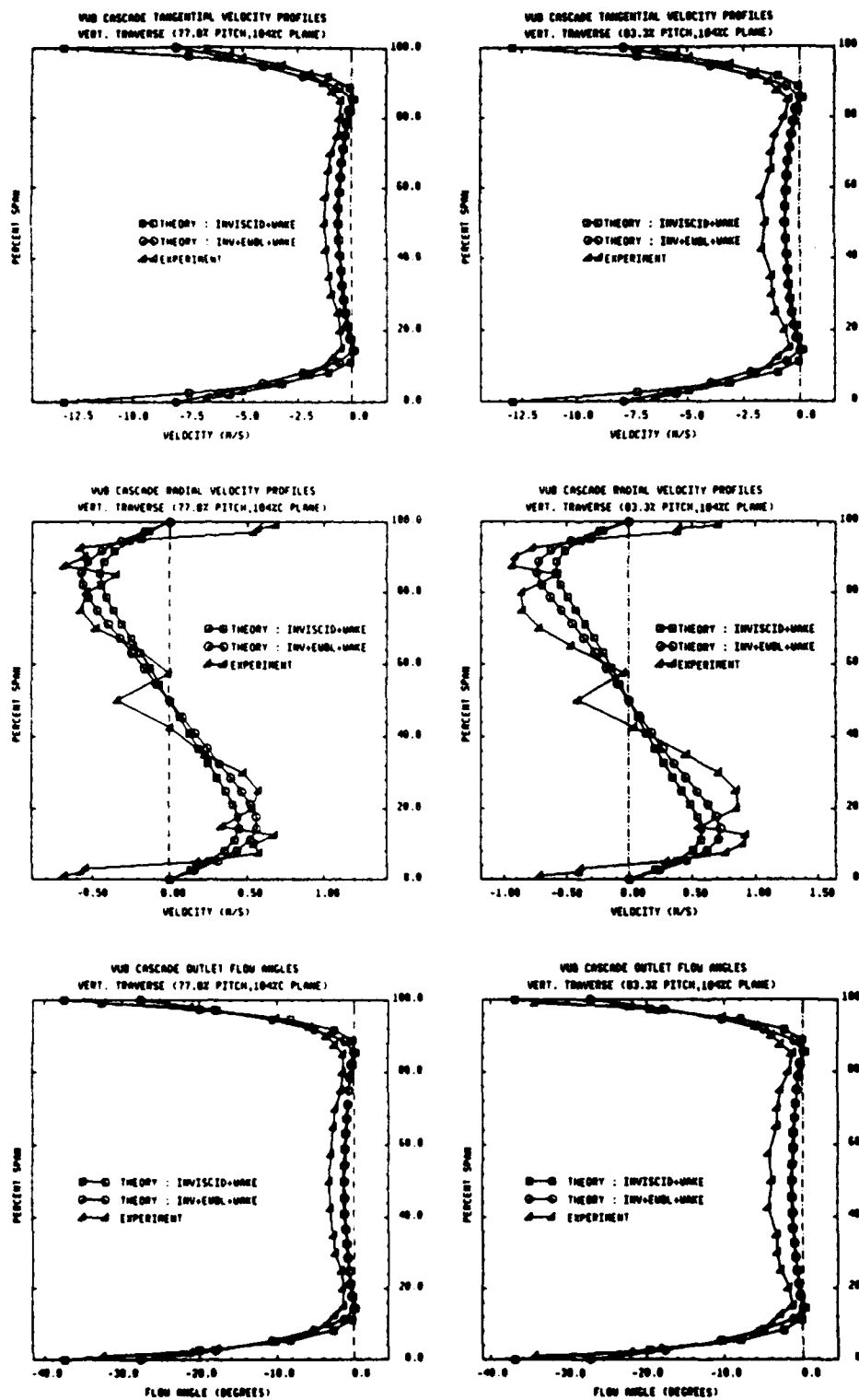


Figure 11.6h : Local spanwise profiles at 77.8% and 83.3% pitch (104% chord plane)

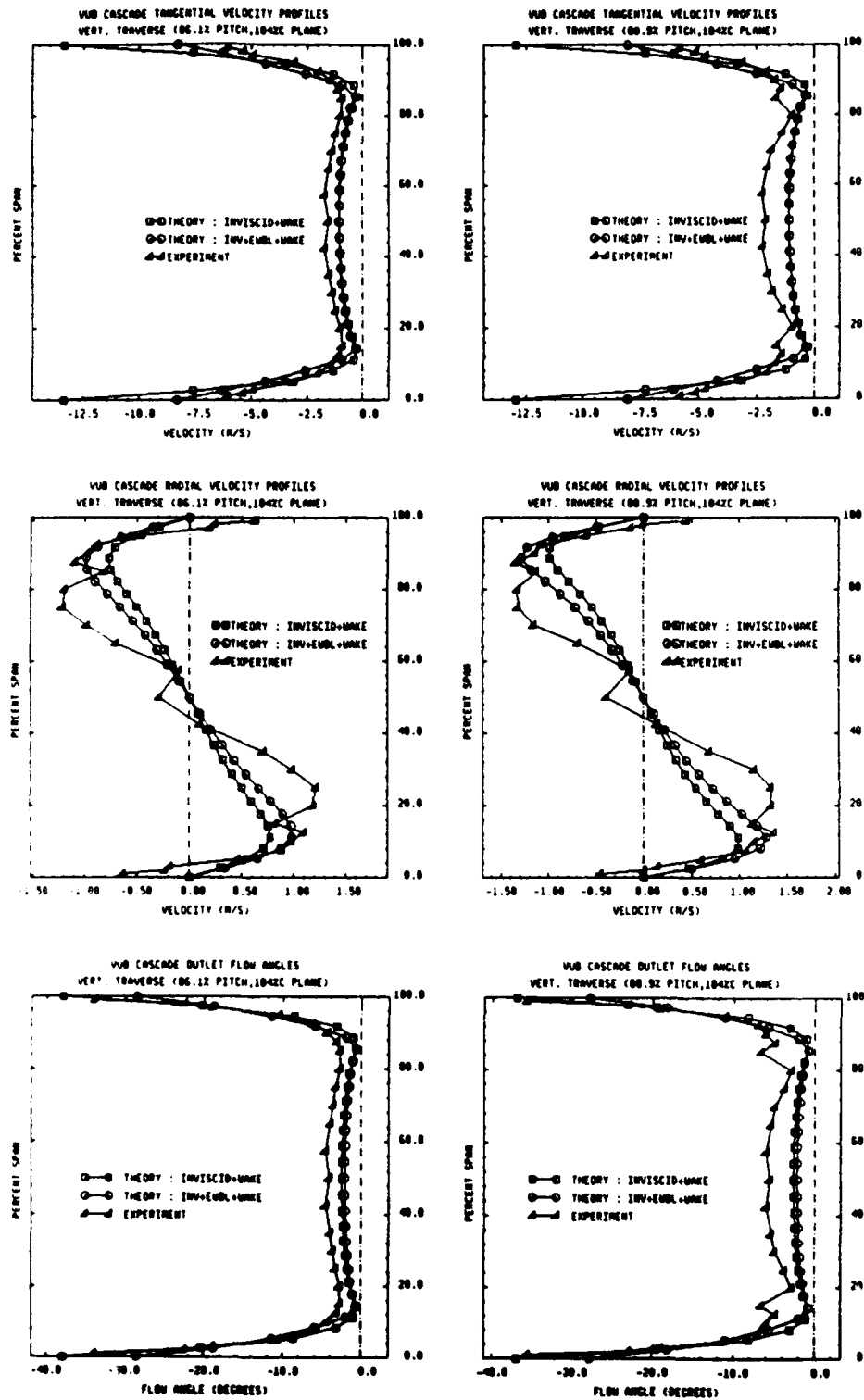


Figure 11.6i : Local spanwise profiles at 86.1% and 88.9% pitch (104% chord plane)

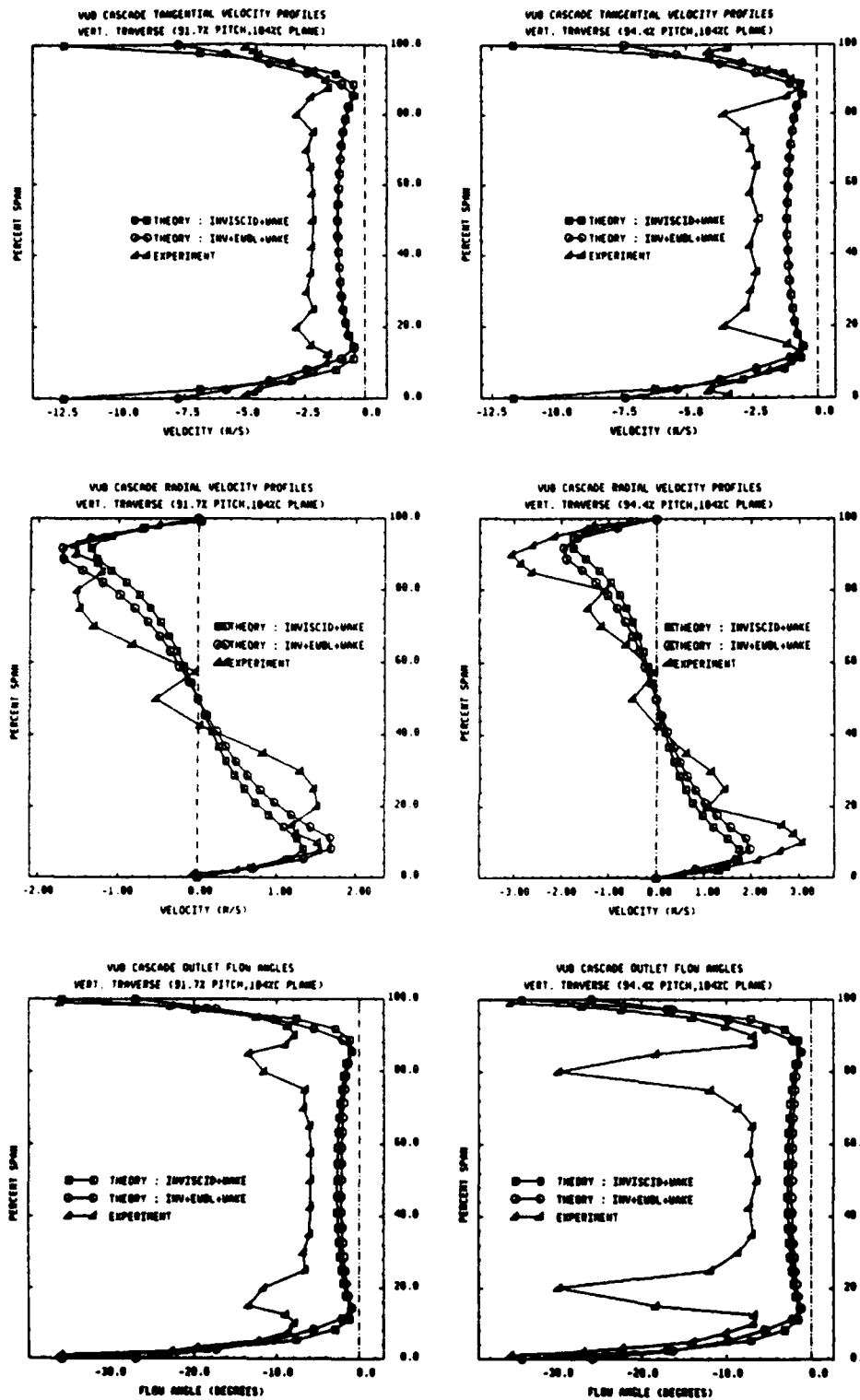


Figure 11.6j: Local spanwise profiles at 91.7% and 94.4% pitch (104% chord plane)

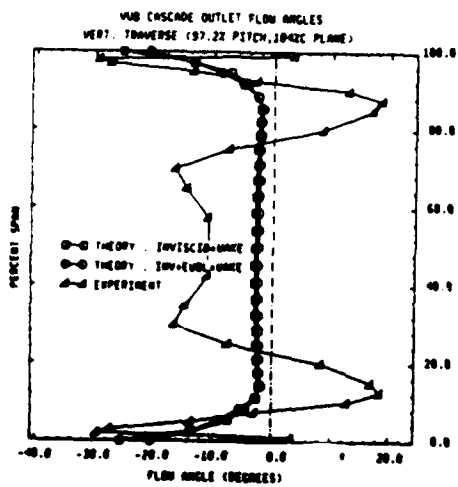
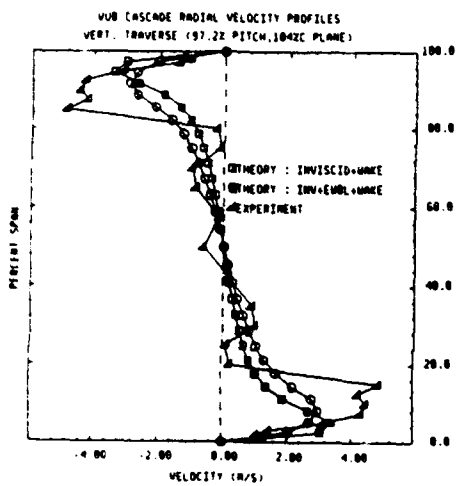
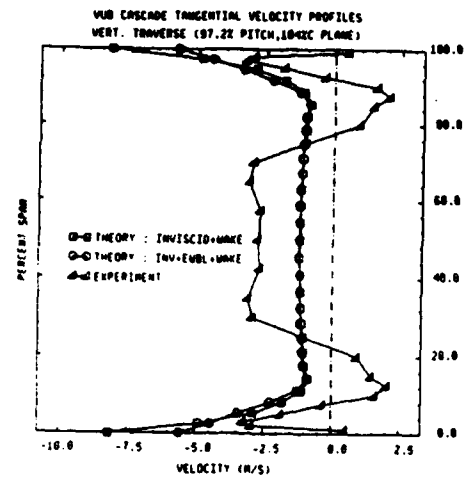


Figure 11.6k : Local spanwise profiles at 97.2% pitch (104% chord plane)

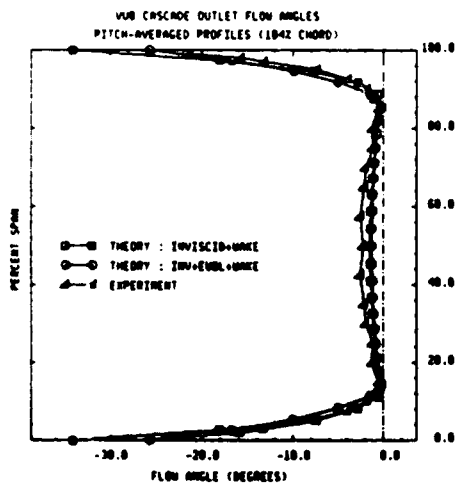
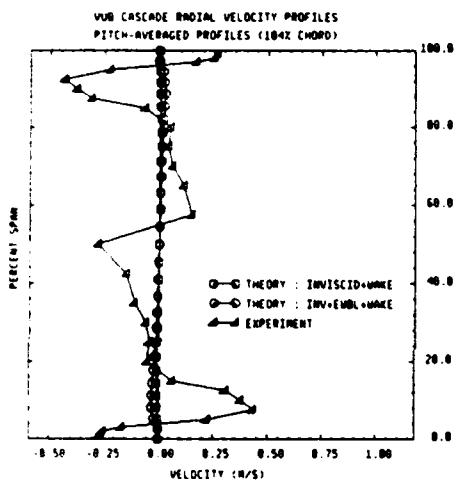
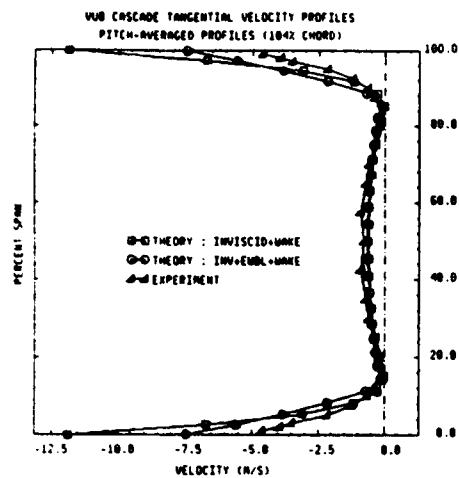


Figure 11.6I : Pitch-averaged spanwise profiles (104% chord plane)

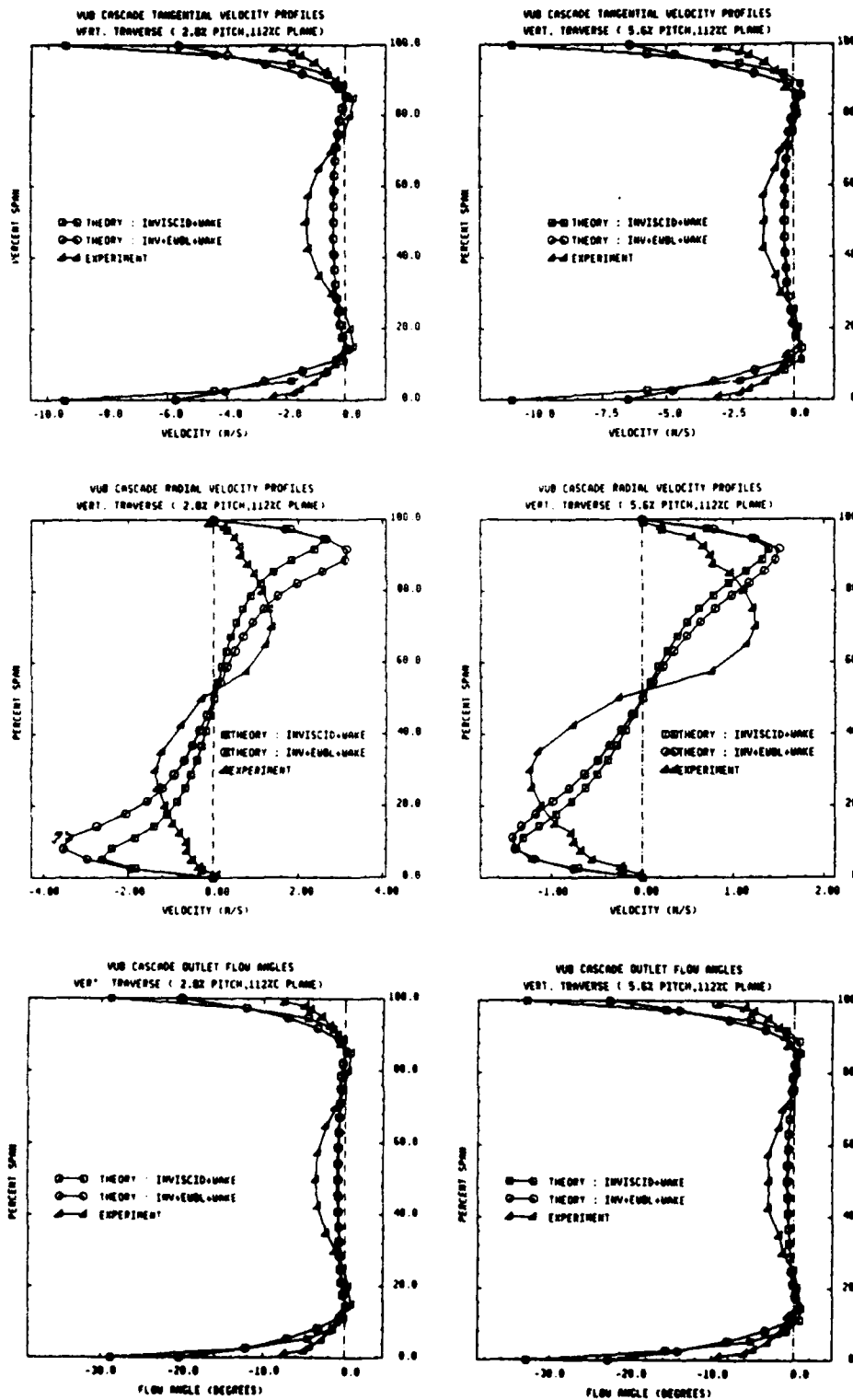


Figure 11.7a : Local spanwise profiles at 2.8% and 5.6% pitch (112% chord plane)

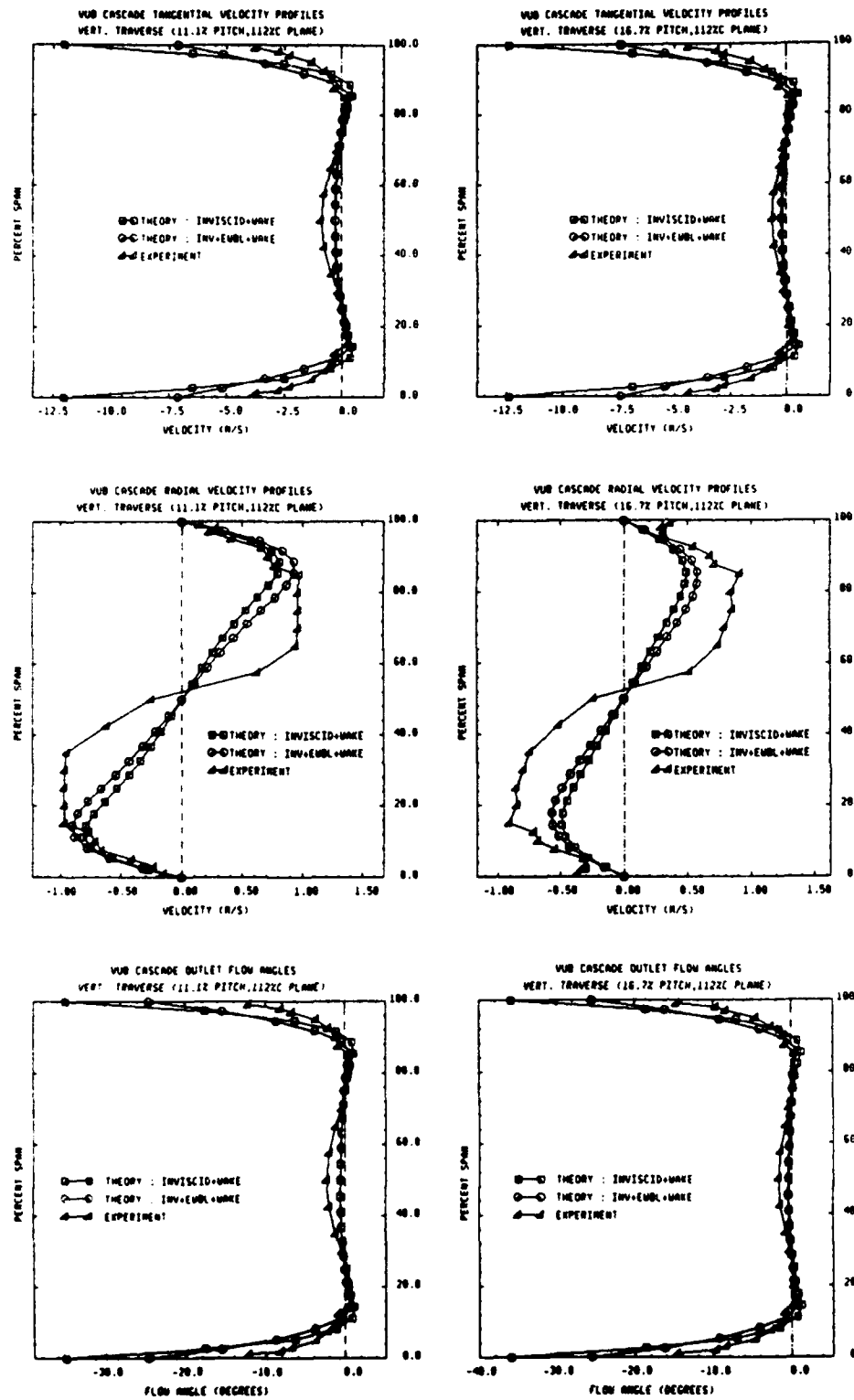


Figure 11.7b : Local spanwise profiles at 11.1% and 16.7% pitch (112% chord plane)

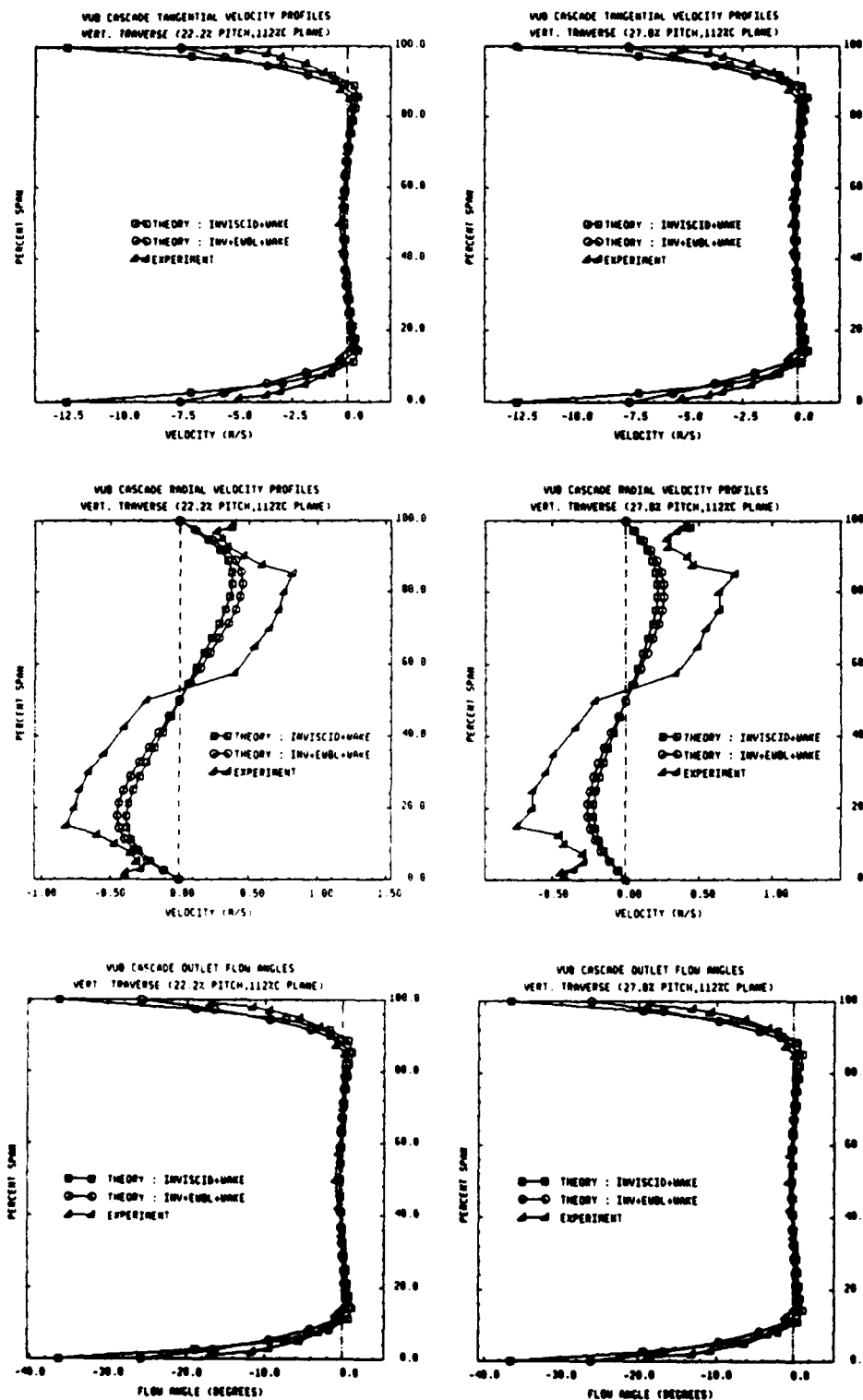


Figure 11.7c : Local spanwise profiles at 22.2% and 27.8% pitch (112% chord plane)

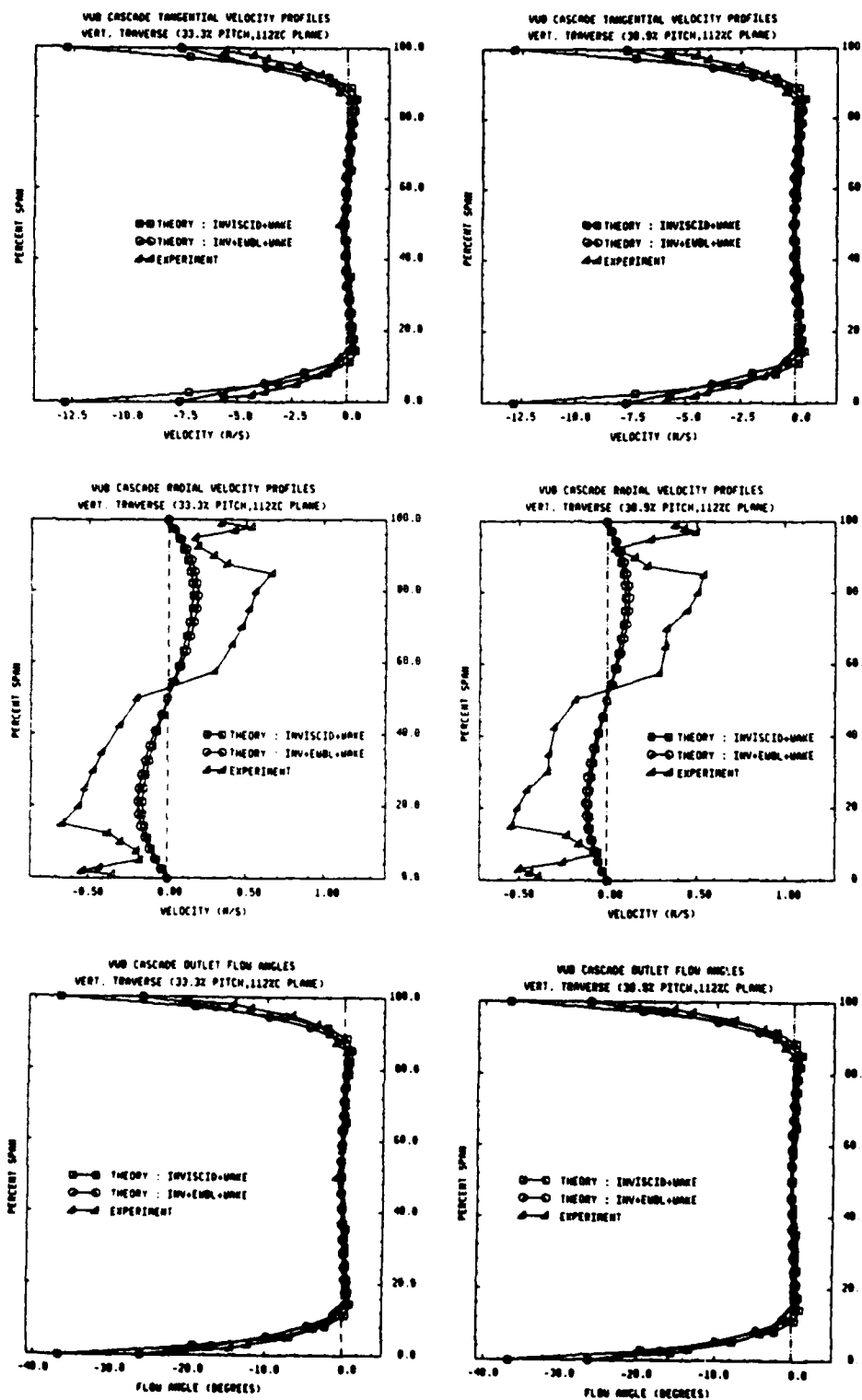


Figure 11.7d : Local spanwise profiles at 33.3% and 38.9% pitch (112% chord plane)

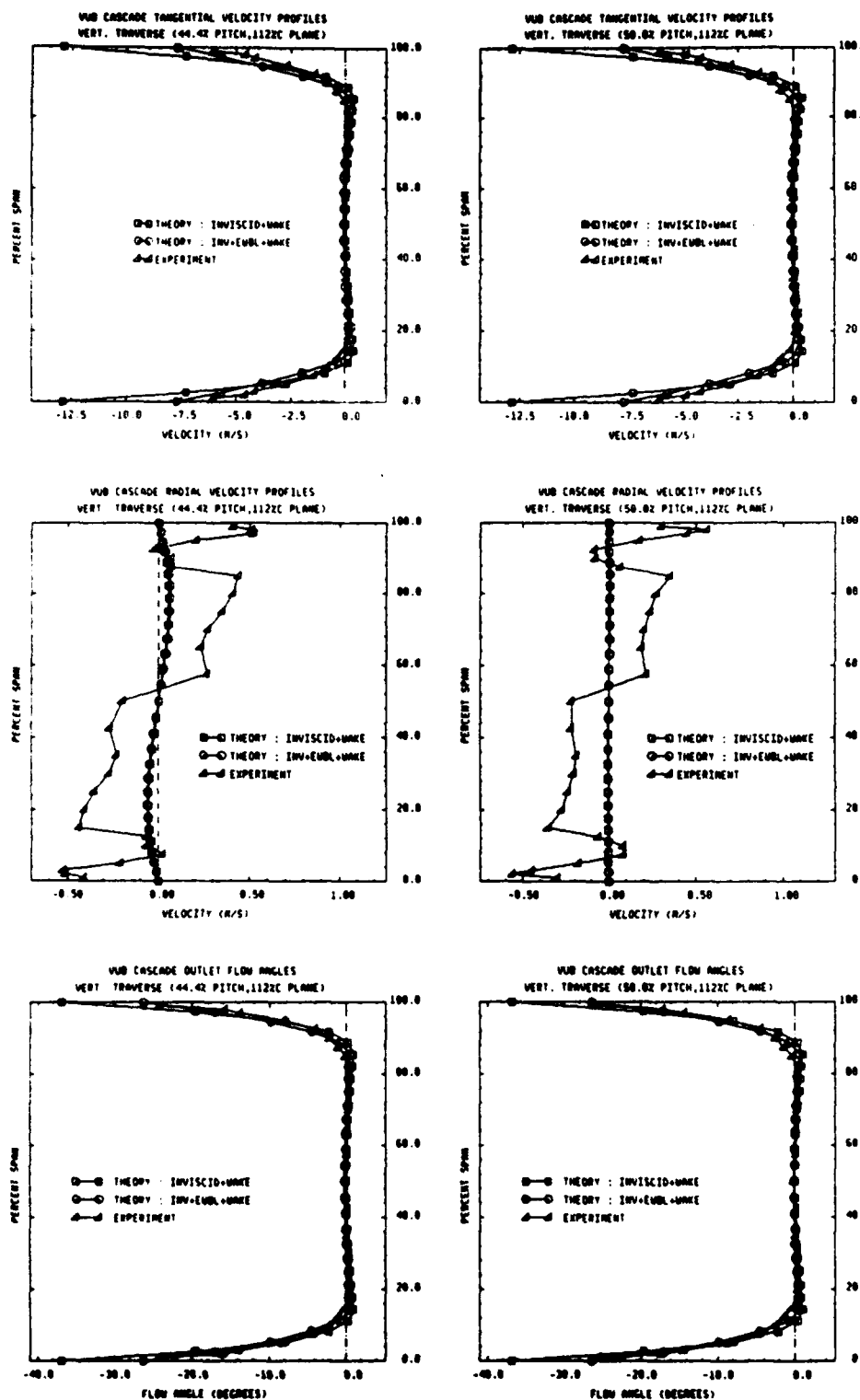


Figure 11.7e : Local spanwise profiles at 44.4% and 50.0% pitch (112% chord plane)

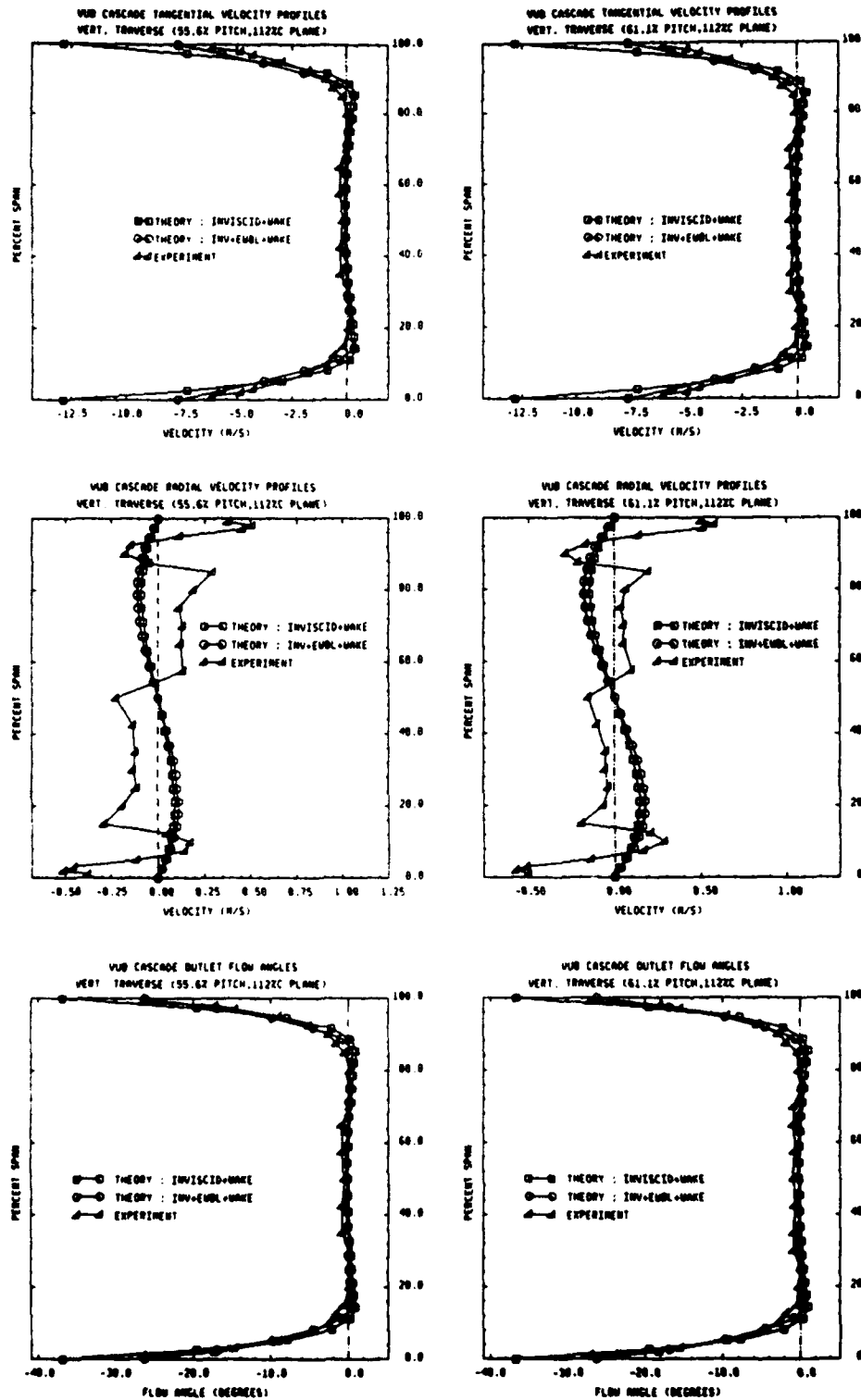


Figure 11.7f: Local spanwise profiles at 55.6% and 61.1% pitch (112% chord plane)

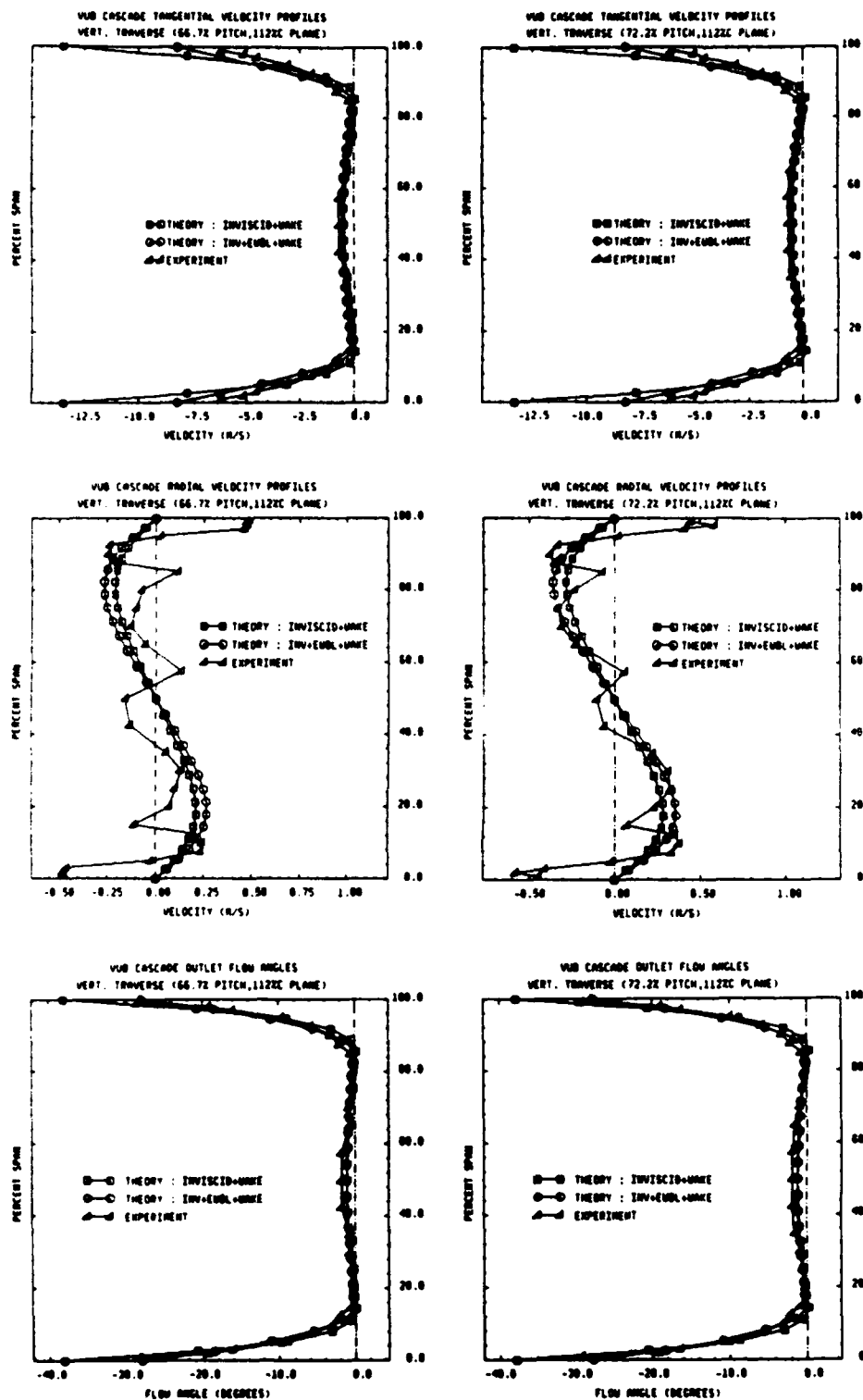


Figure 11.7g : Local spanwise profiles at 66.7% and 72.2% pitch (112% chord plane)

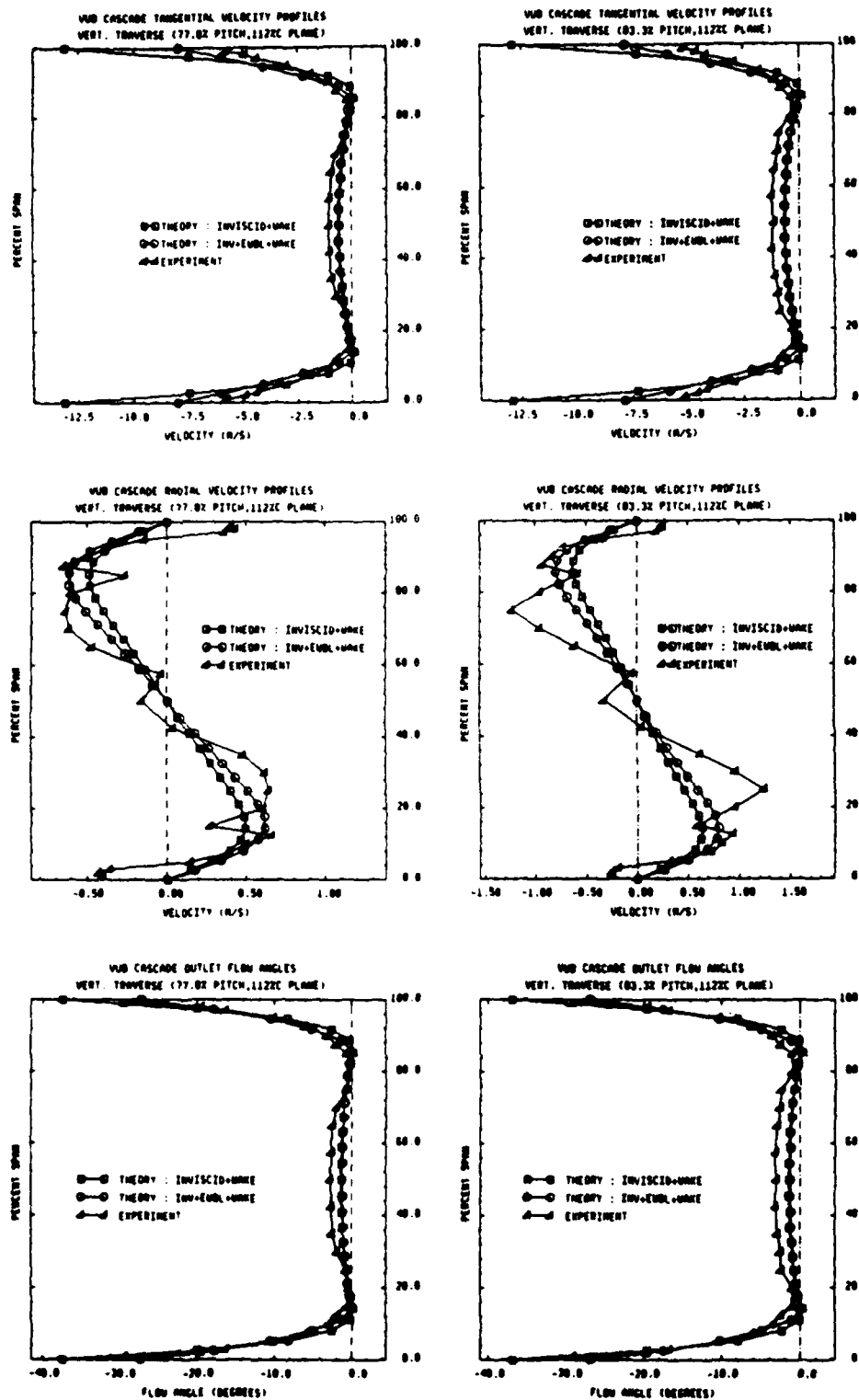


Figure 11.7h : Local spanwise profiles at 77.8% and 83.3% pitch (112% chord plane)

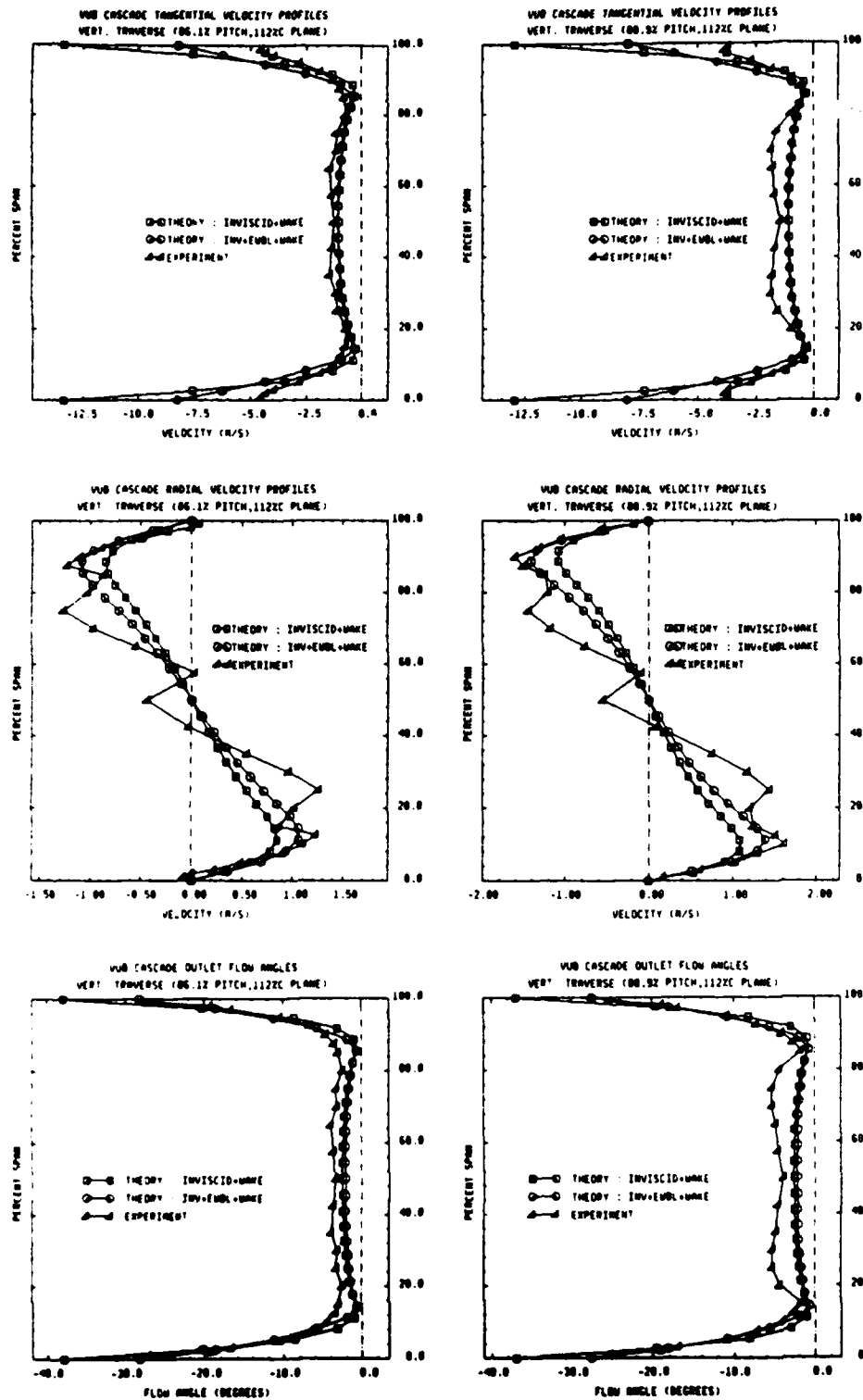


Figure 11.7i: Local spanwise profiles at 86.1% and 88.9% pitch (112% chord plane)

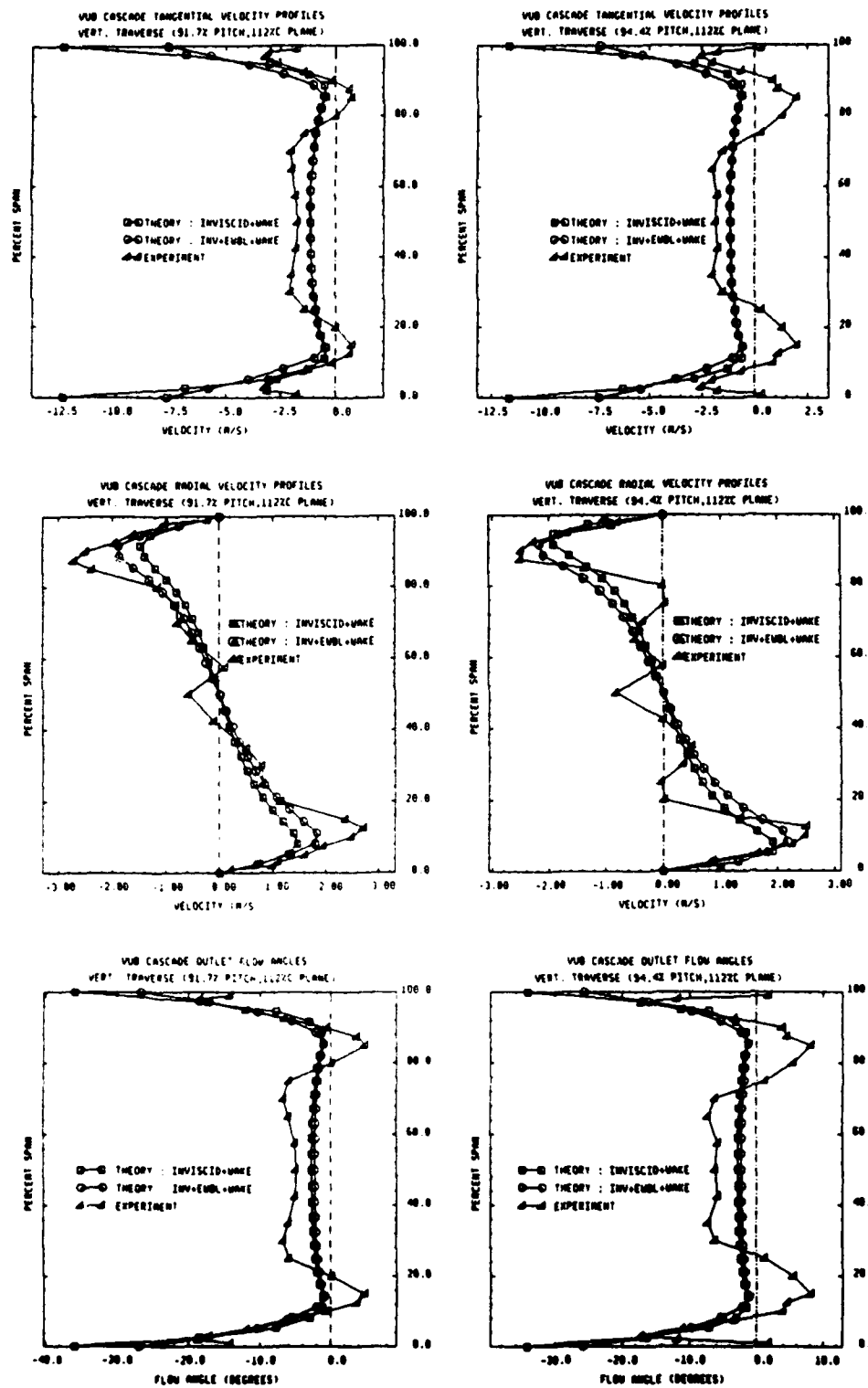


Figure 11.7j: Local spanwise profiles at 91.7% and 94.4% pitch (112% chord plane)

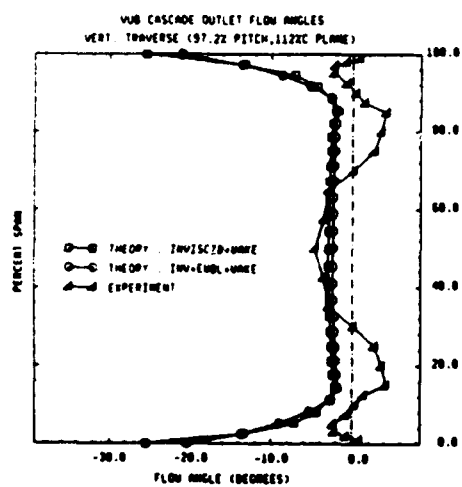
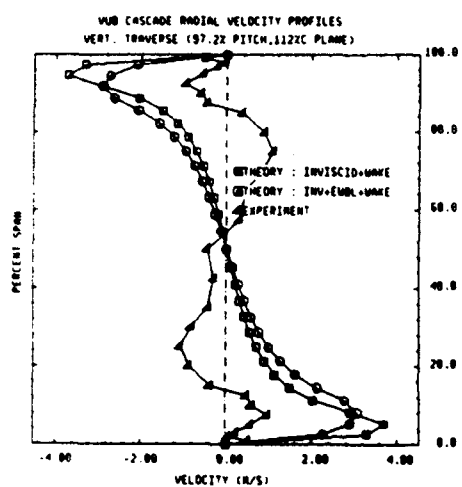
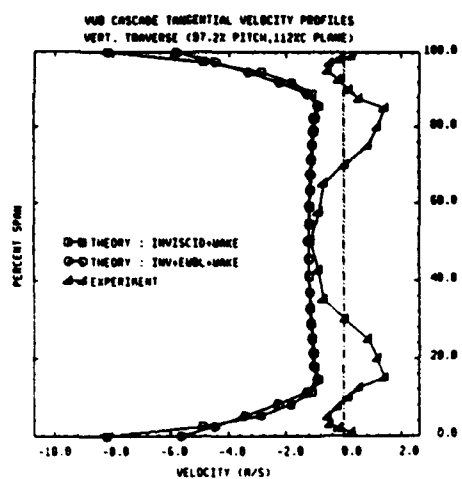


Figure 11.7k : Local spanwise profiles at 97.2% pitch (112% chord plane)

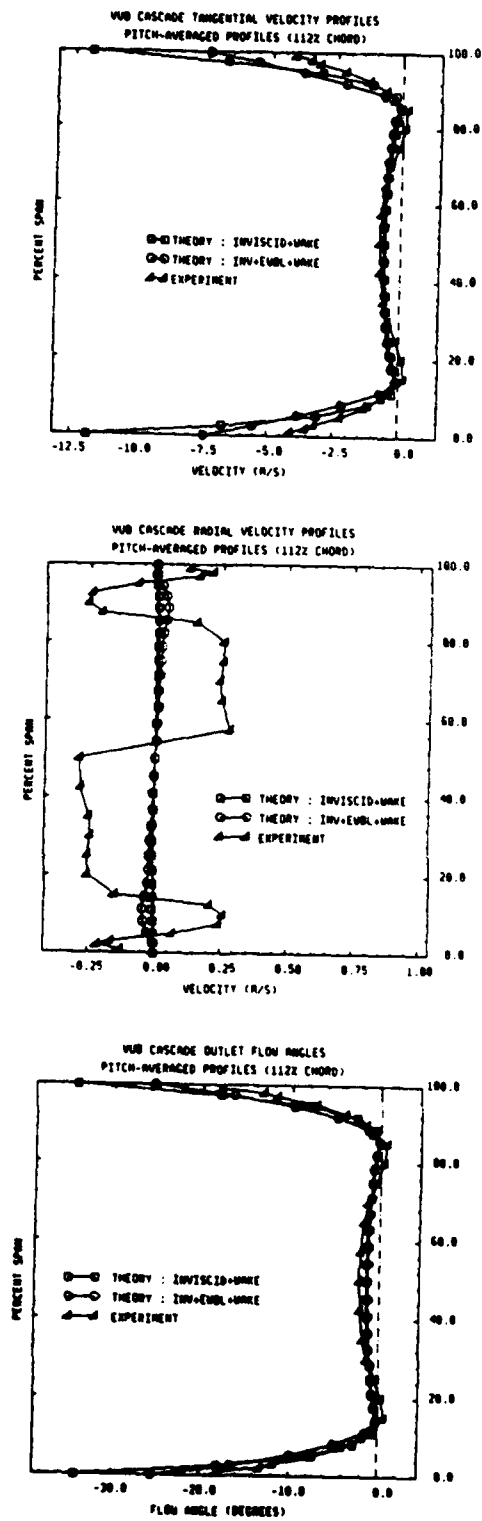


Figure 11.71 : Pitch-averaged spanwise profiles (112% chord plane)

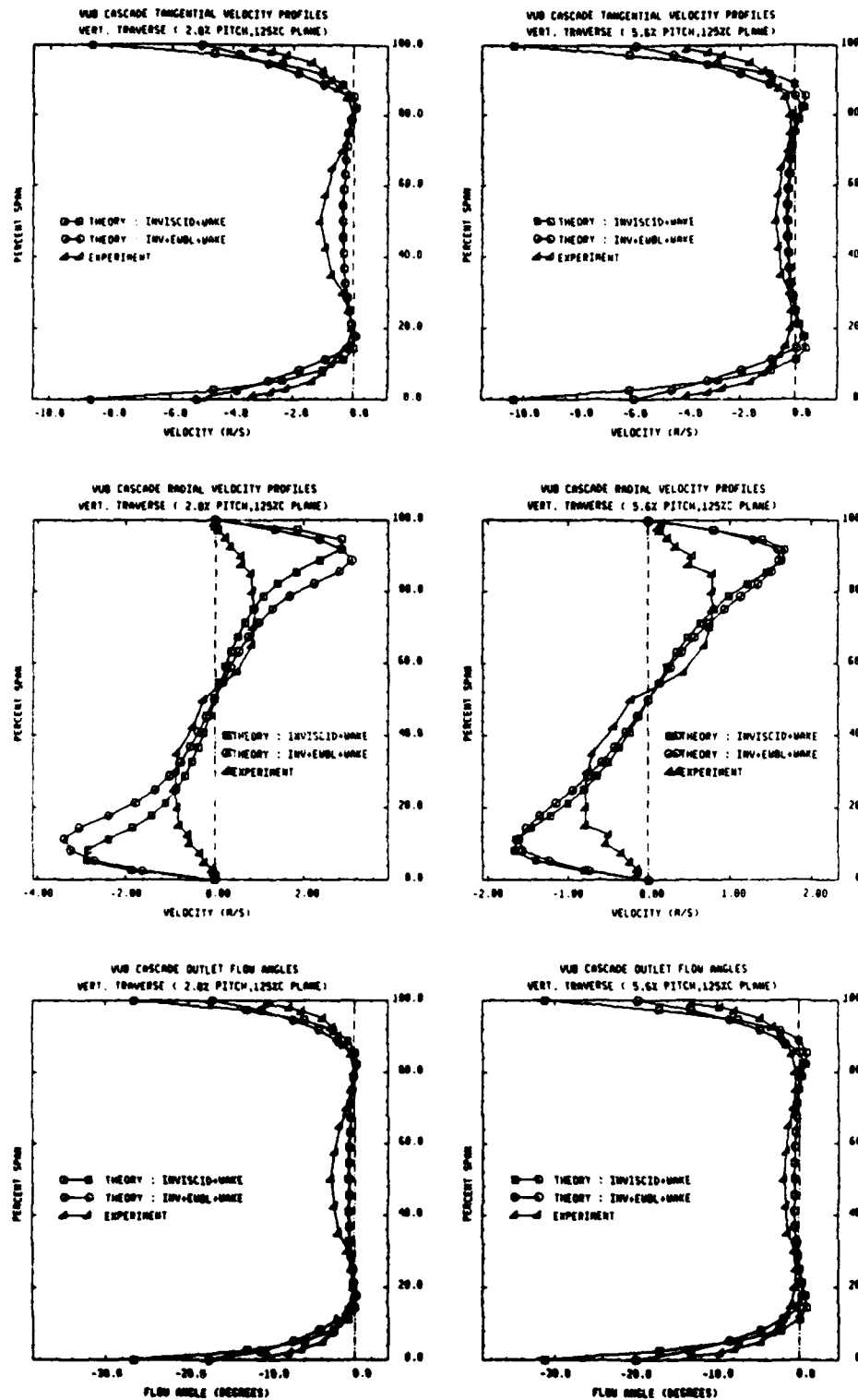


Figure 11.8a : Local spanwise profiles at 2.8% and 5.6% pitch (125% chord plane)

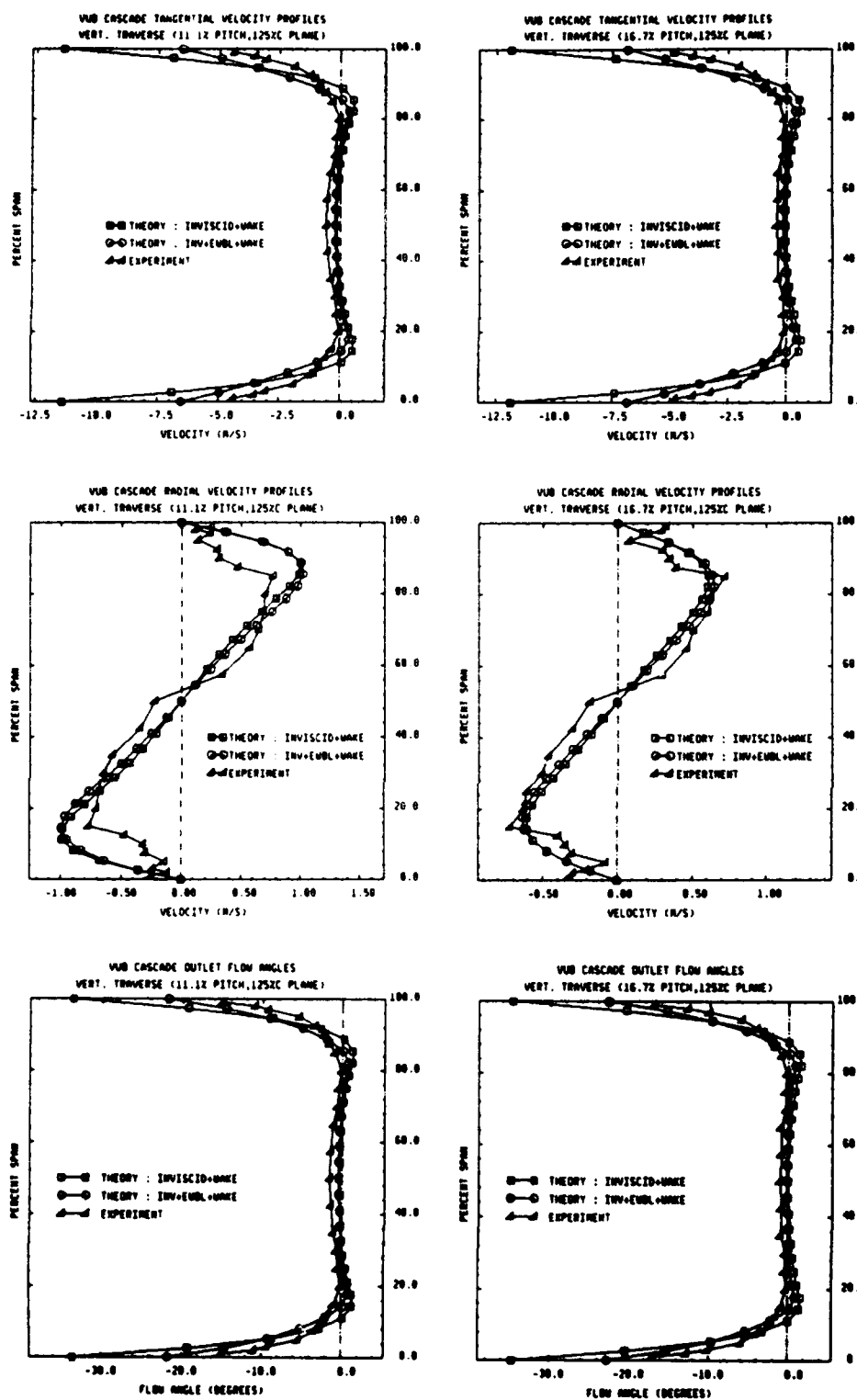


Figure 11.8b : Local spanwise profiles at 11.1% and 16.7% pitch (125% chord plane)

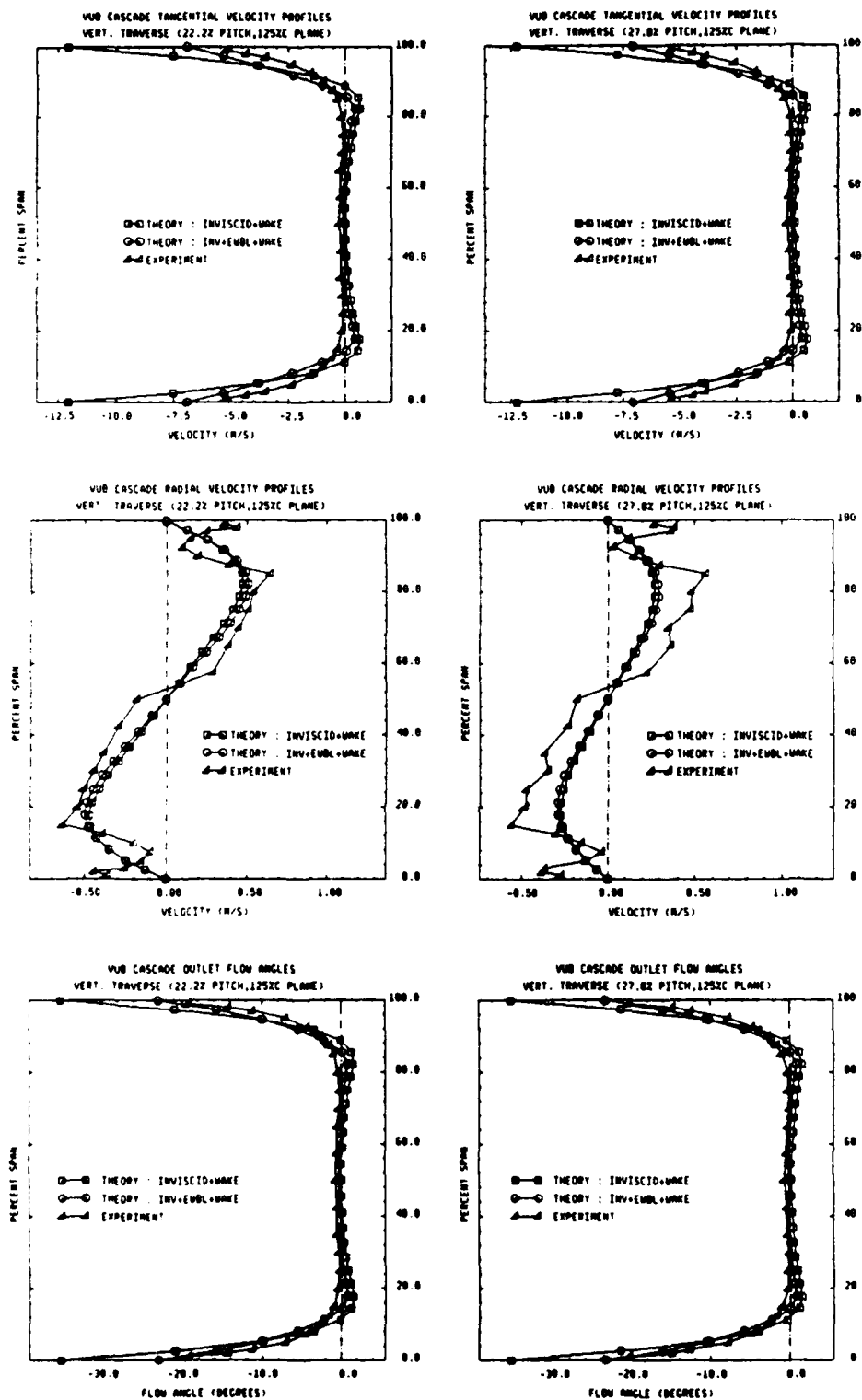


Figure 11.8c : Local spanwise profiles at 22.2% and 27.8% pitch (125% chord plane)

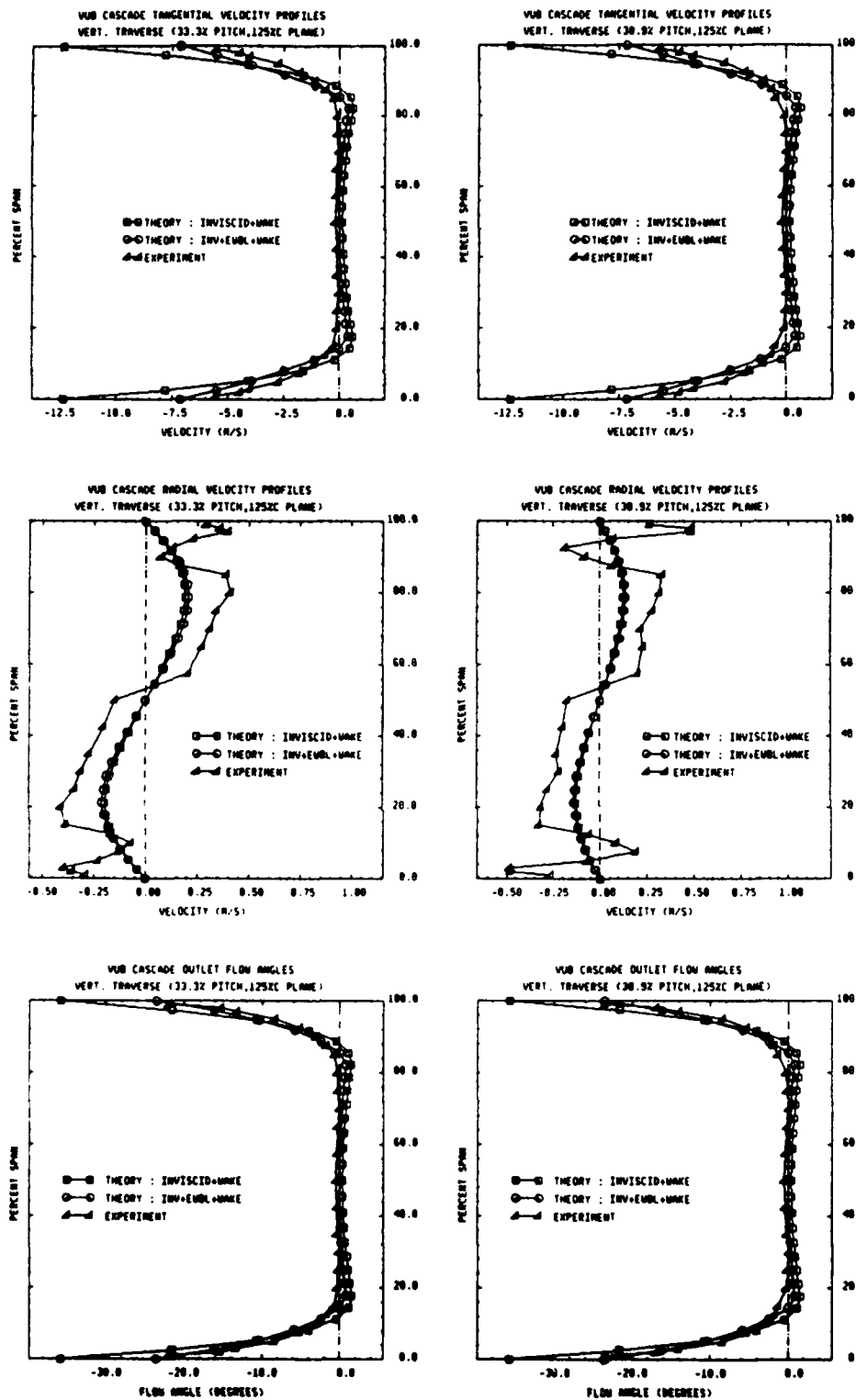


Figure 11.8d : Local spanwise profiles at 33.3% and 38.9% pitch (125% chord plane)

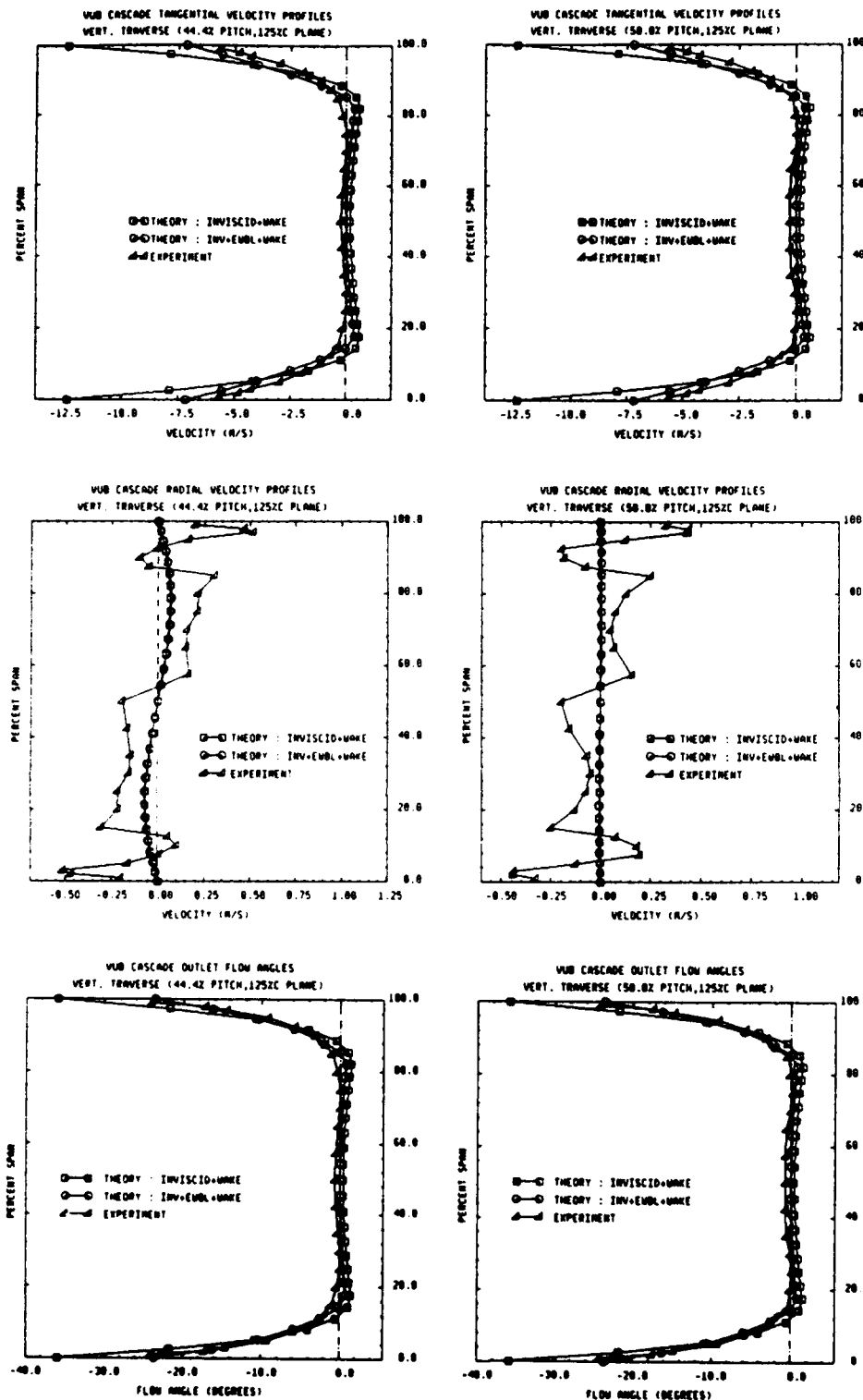


Figure 11.8e : Local spanwise profiles at 44.4% and 50.0% pitch (125% chord plane)

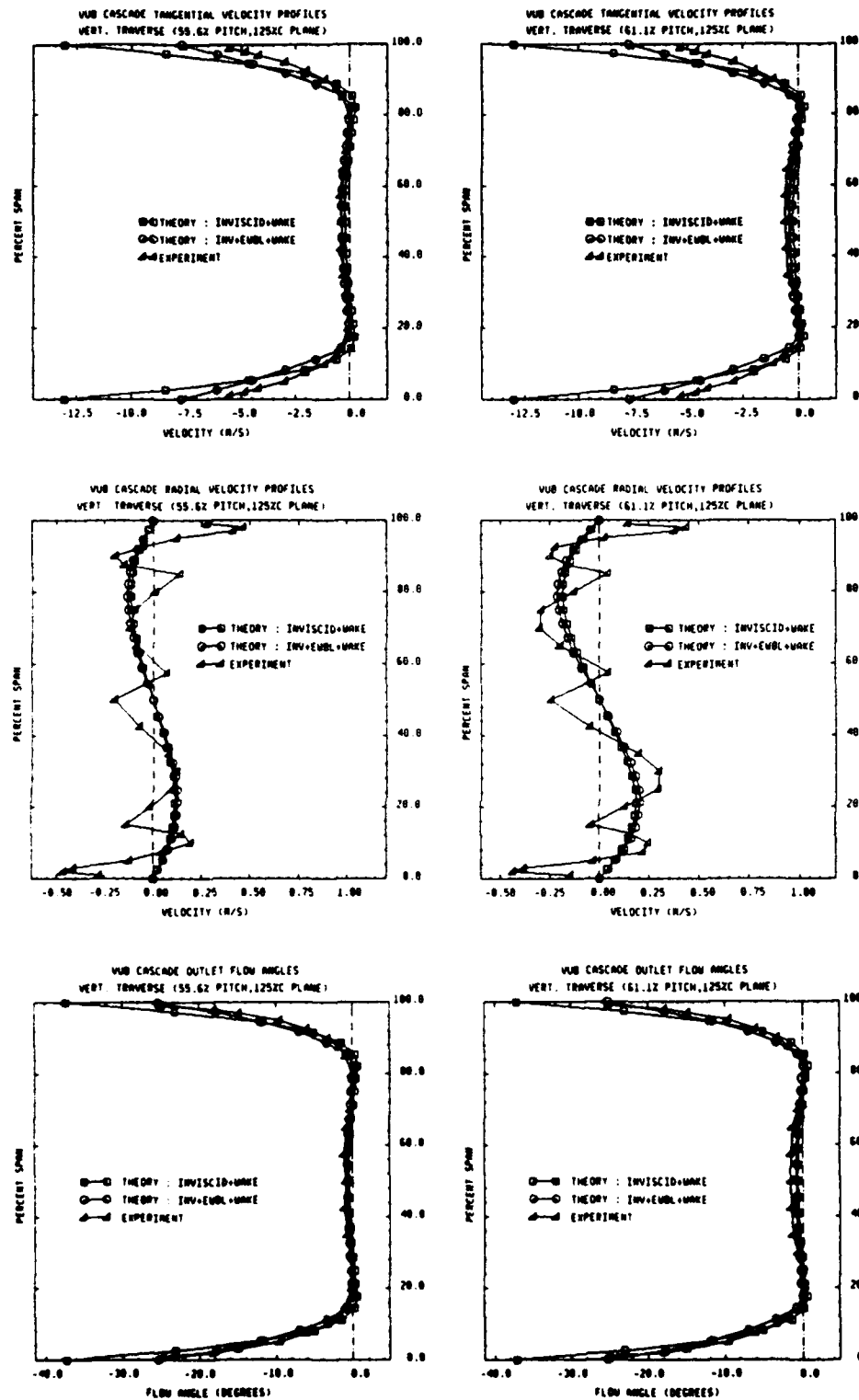


Figure 11.8f: Local spanwise profiles at 55.6% and 61.1% pitch (125% chord plane)

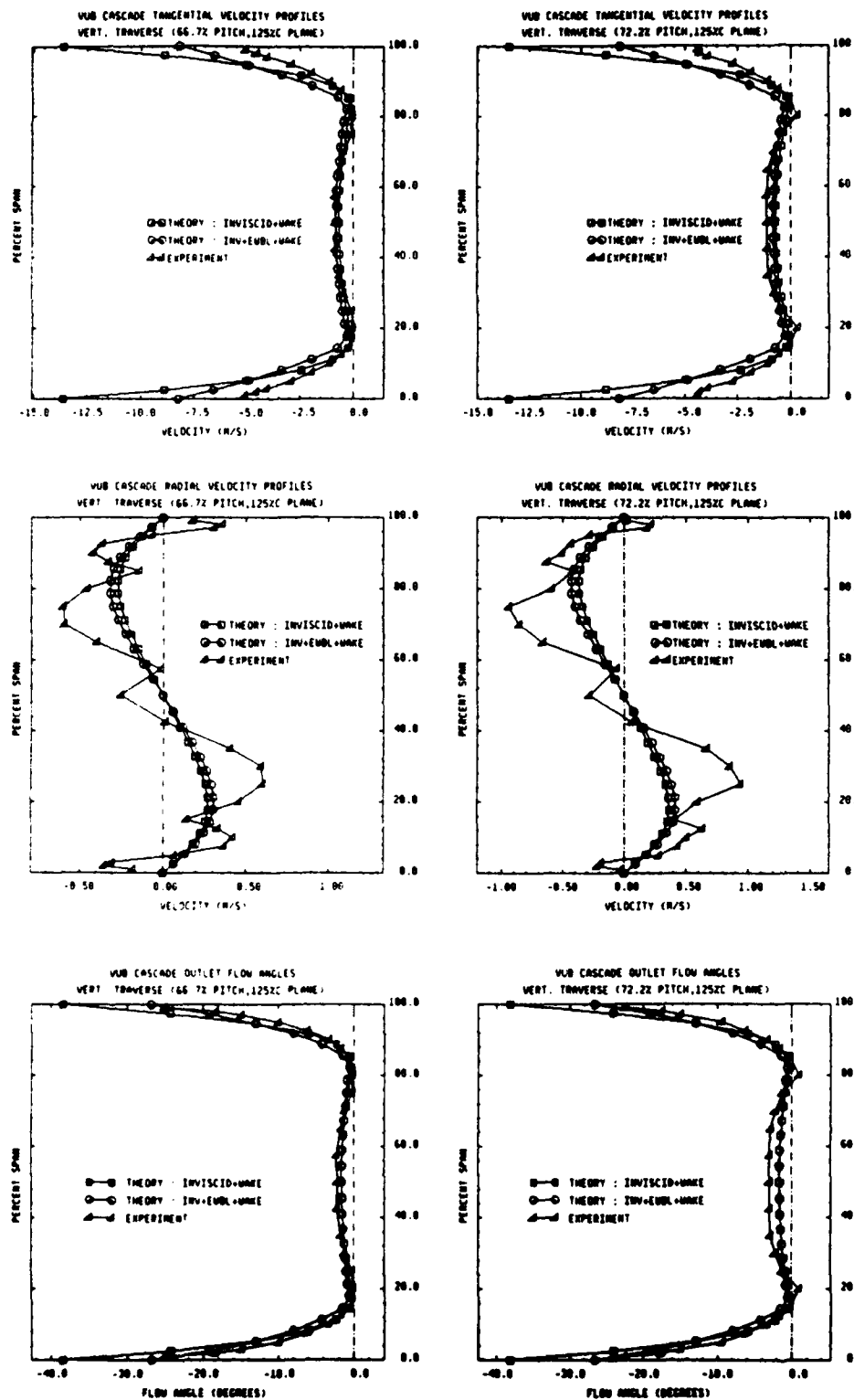


Figure 11.8g : Local spanwise profiles at 66.7% and 72.2% pitch (125% chord plane)

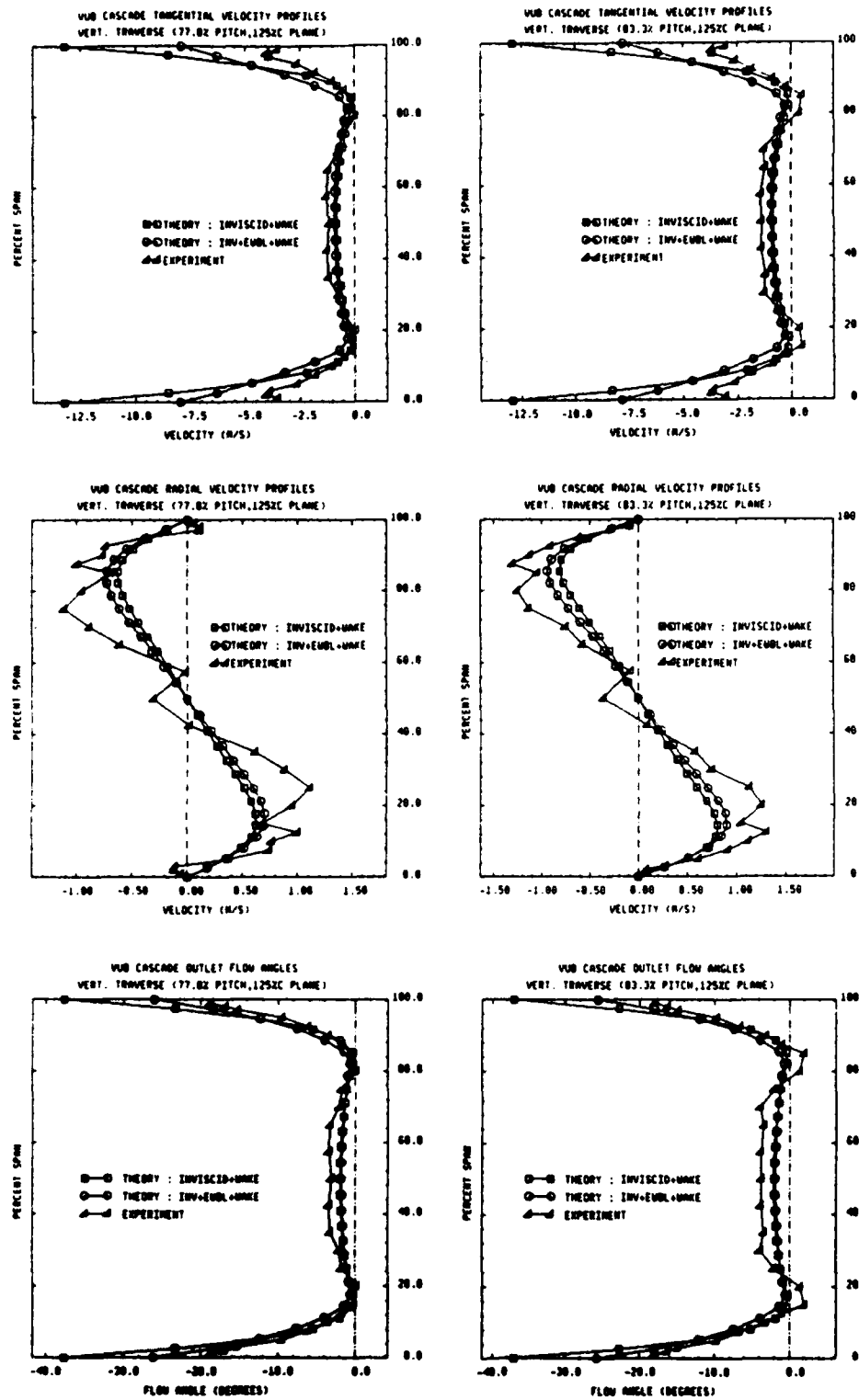


Figure 11.8b : Local spanwise profiles at 77.8% and 83.3% pitch (125% chord plane)

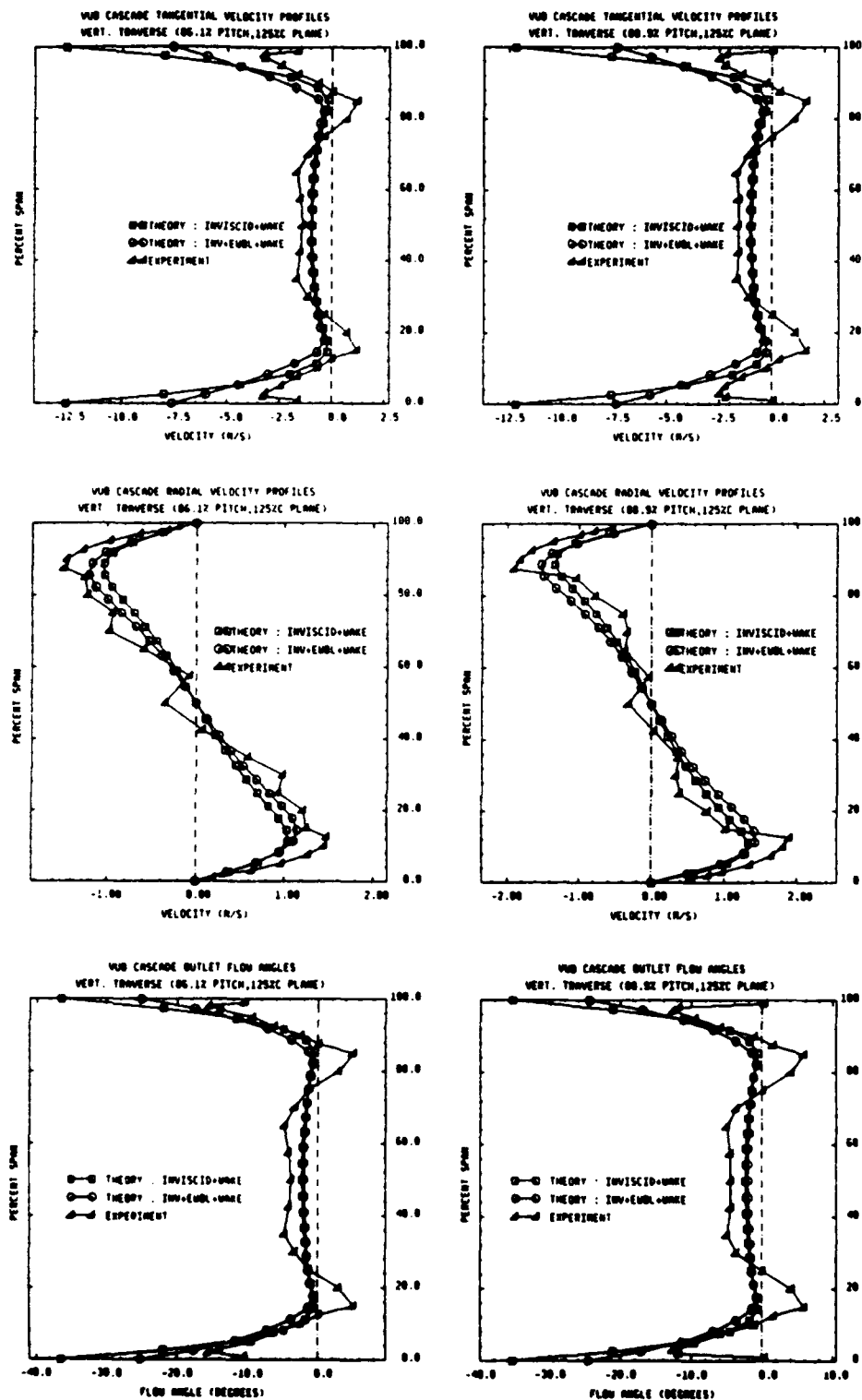


Figure 11.8i : Local spanwise profiles at 86.1% and 88.9% pitch (125% chord plane)

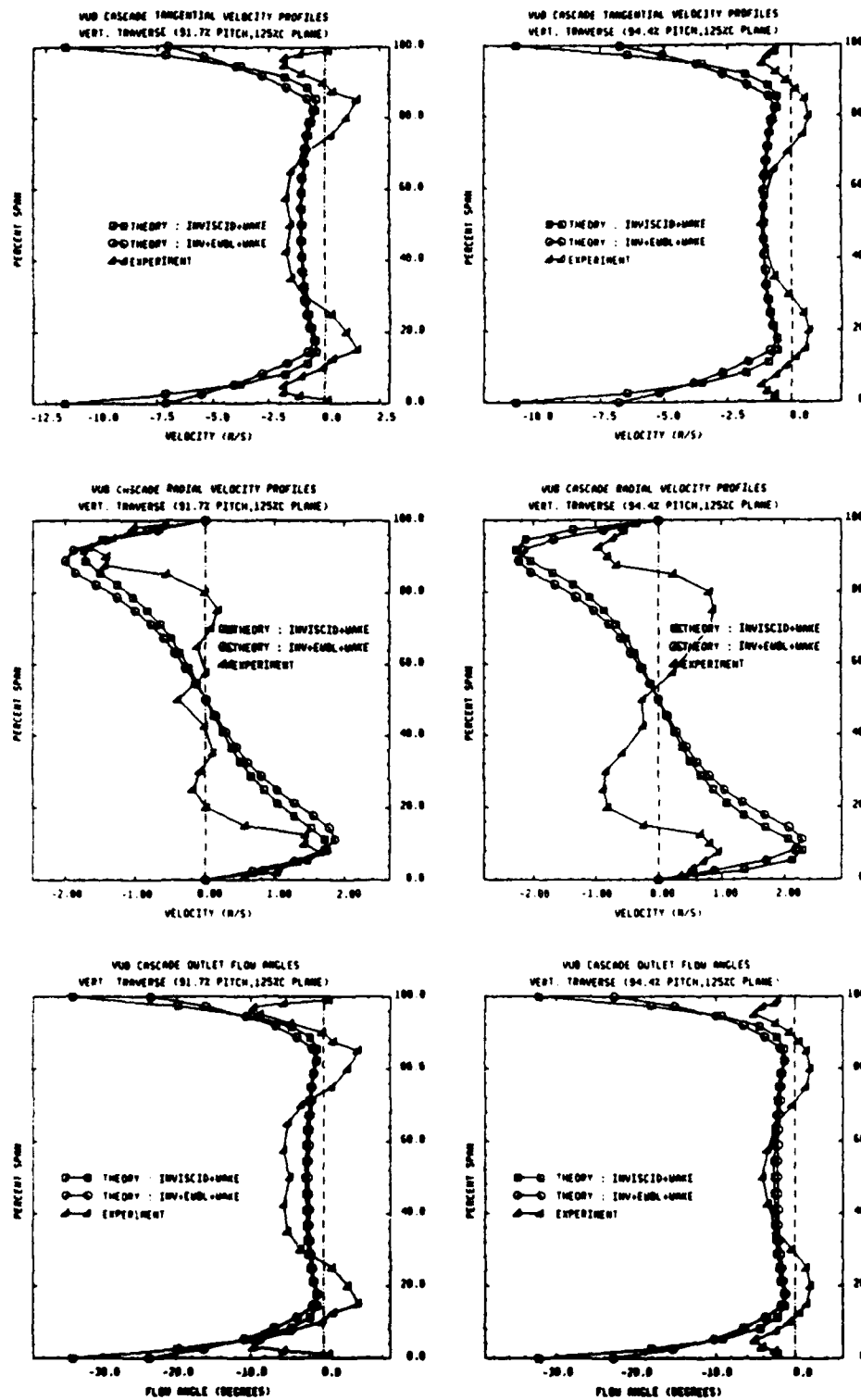


Figure 11.8j : Local spanwise profiles at 91.7% and 94.4% pitch (125% chord plane)

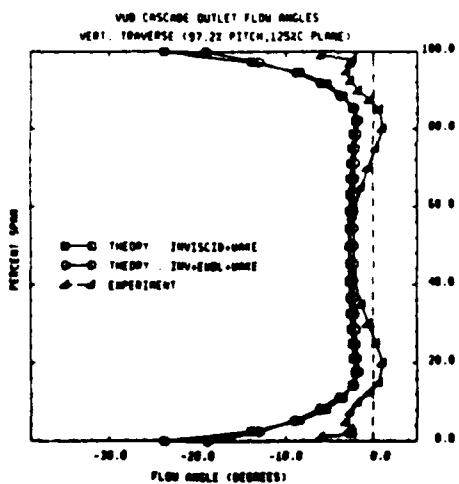
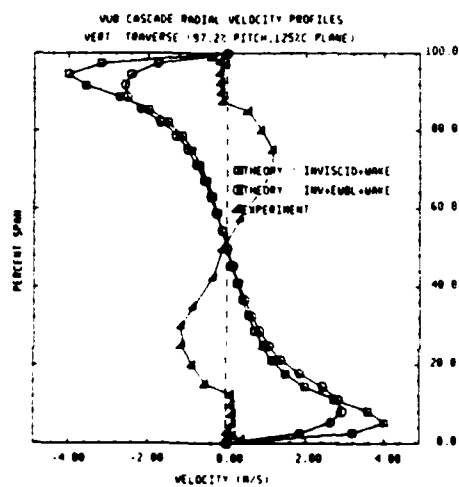
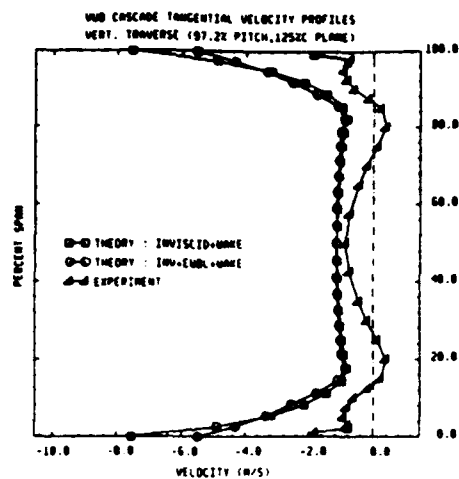


Figure 11.8k : Local spanwise profiles at 97.2% pitch (125% chord plane)

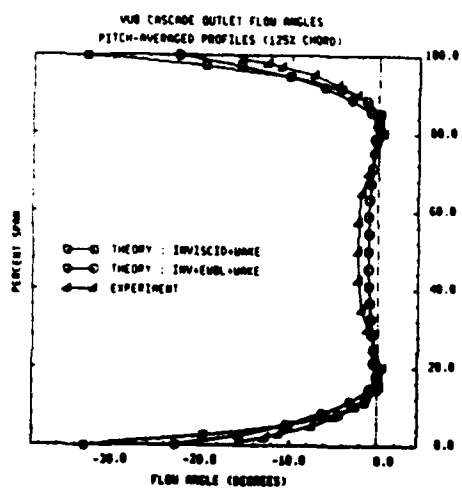
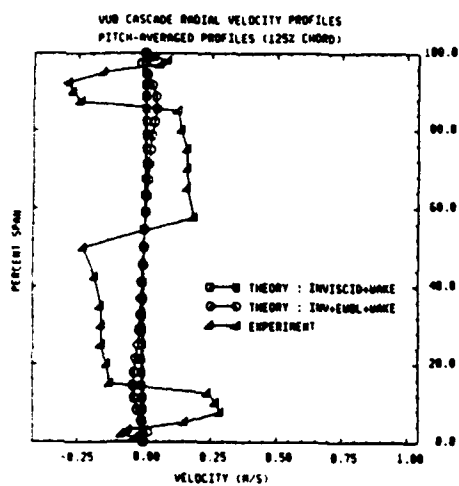
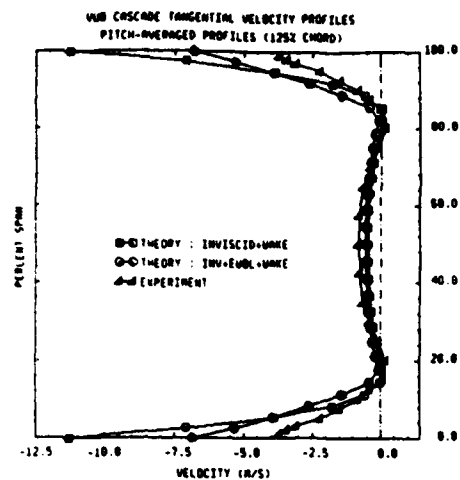


Figure 11.81 : Pitch-averaged spanwise profiles (125% chord plane)

VUB CASCADE (34 degr. deflection)
TOTAL VELOCITY FIELD

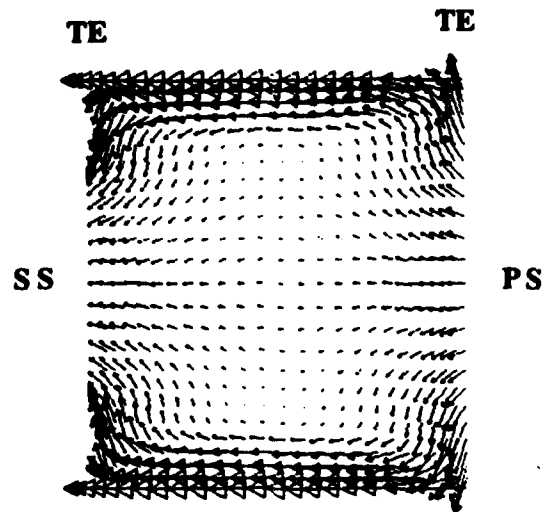


Figure 11.9a : Total velocity field on a transversal S3-plane

VUB CASCADE (34 degr. deflection)
SECONDARY VELOCITY FIELD

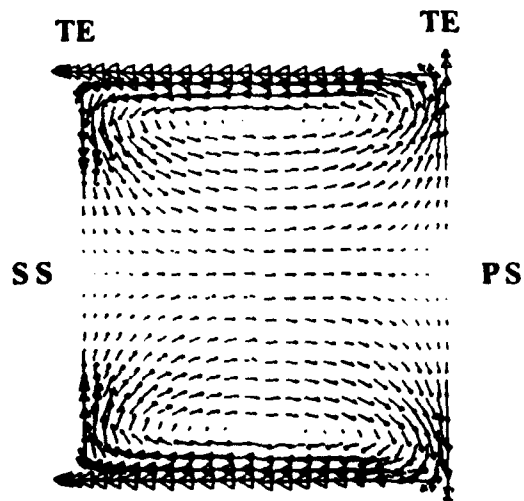


Figure 11.9b : Secondary velocity field on a transversal S3-plane

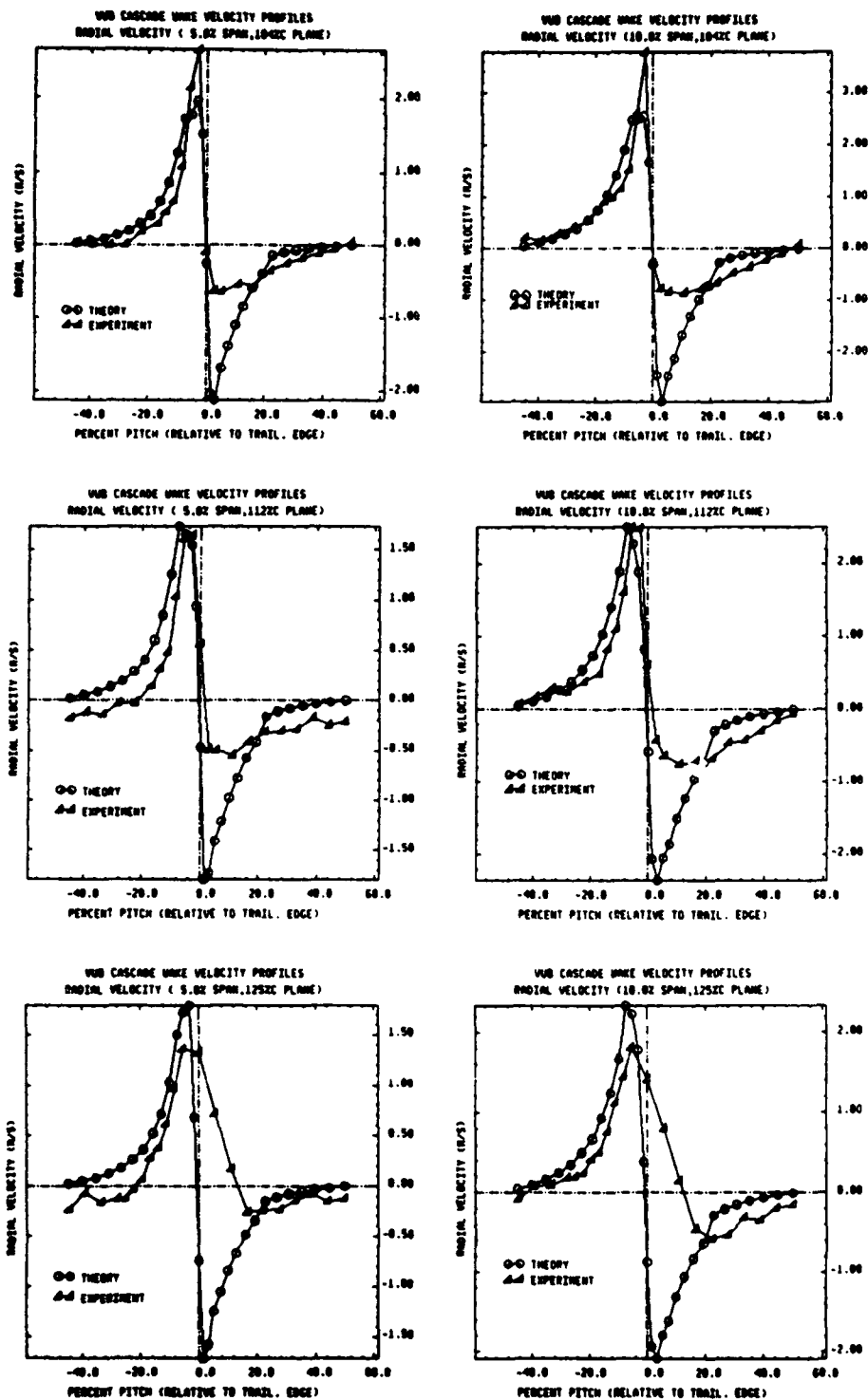


Figure 11.10a : Downstream evolution of radial velocity wake profiles at 5% and 10% span (suction side = left of trailing edge, pressure side = right of trailing edge)

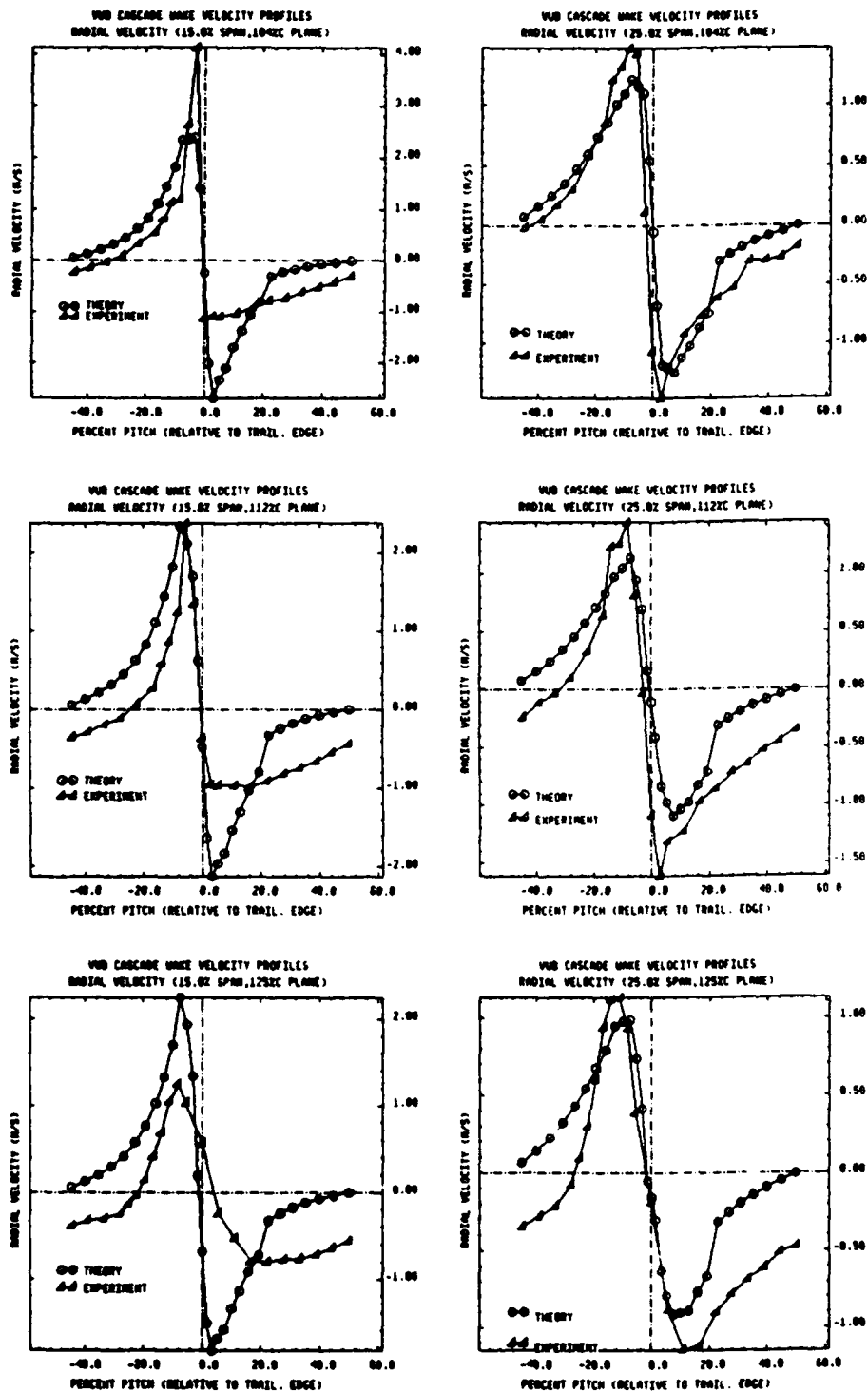


Figure 11.10b : Downstream evolution of radial velocity wake profiles at 15% and 25% span (suction side = left of trailing edge, pressure side = right of trailing edge)

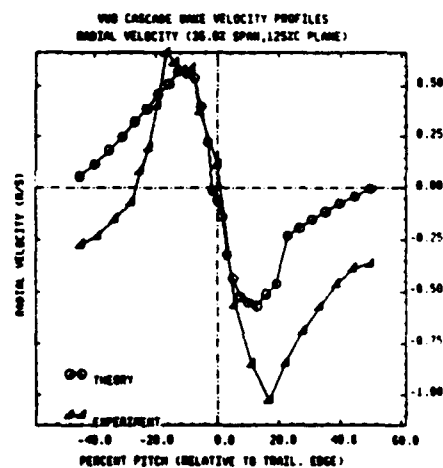
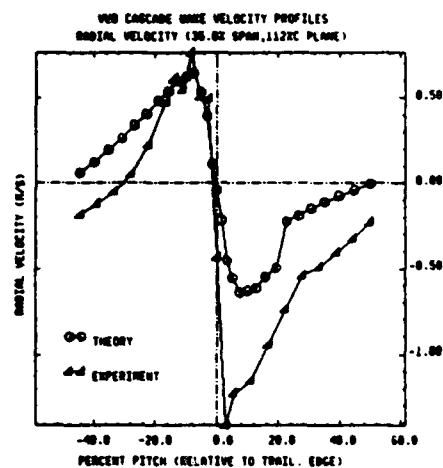
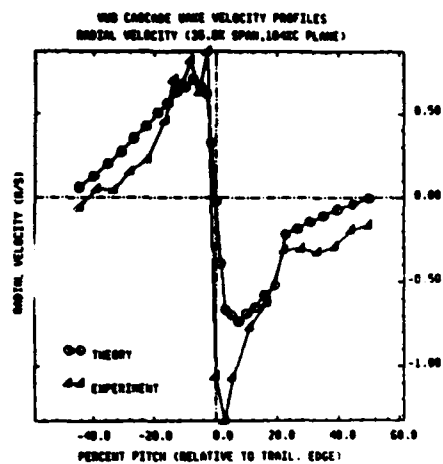


Figure 11.10c : Downstream evolution of radial velocity wake profiles at 35% span
(suction side = left of trailing edge, pressure side = right of trailing edge)

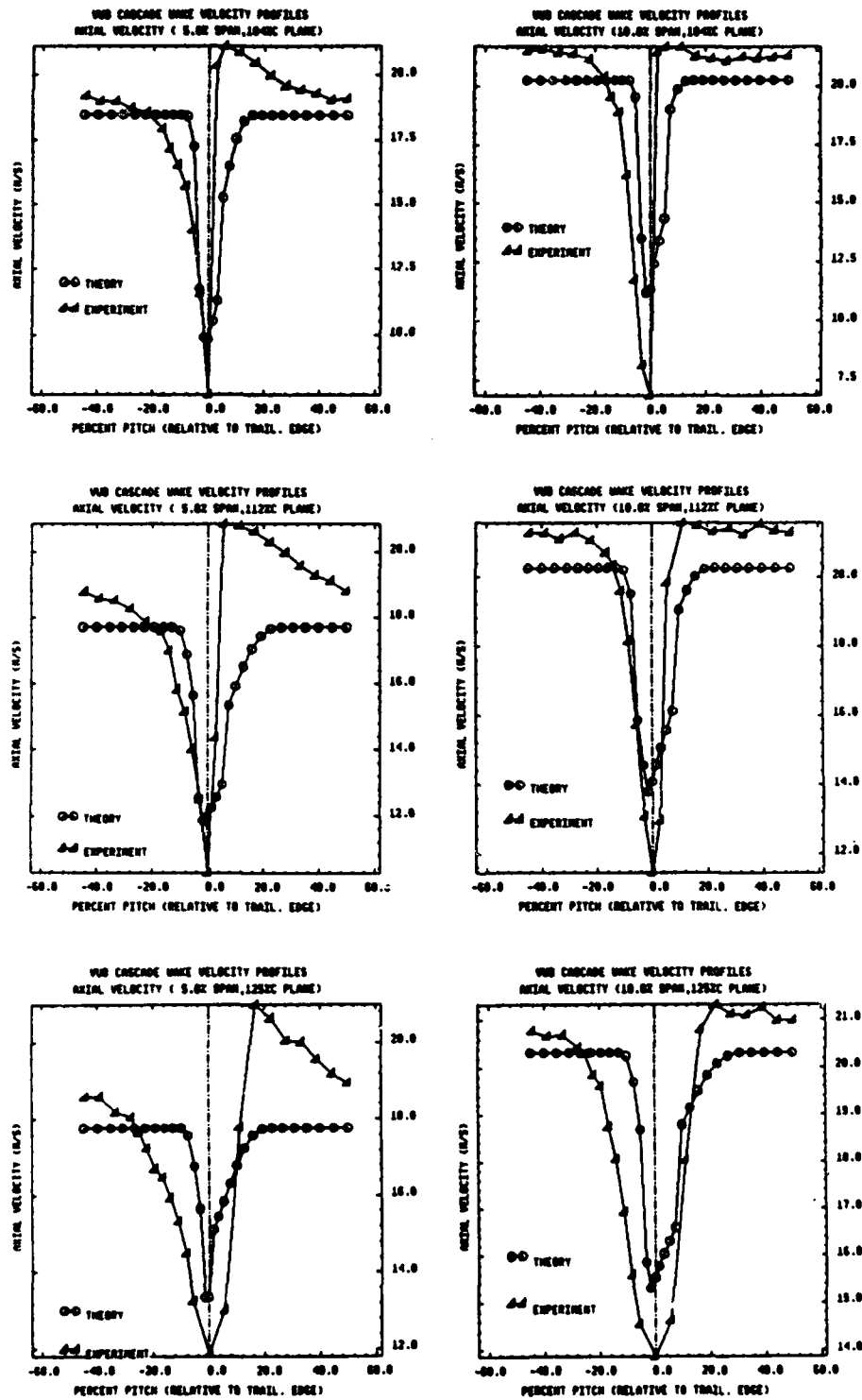


Figure 11.11a: Downstream evolution of axial velocity wake profiles at 5% and 10% span (suction side = left of trailing edge, pressure side = right of trailing edge)

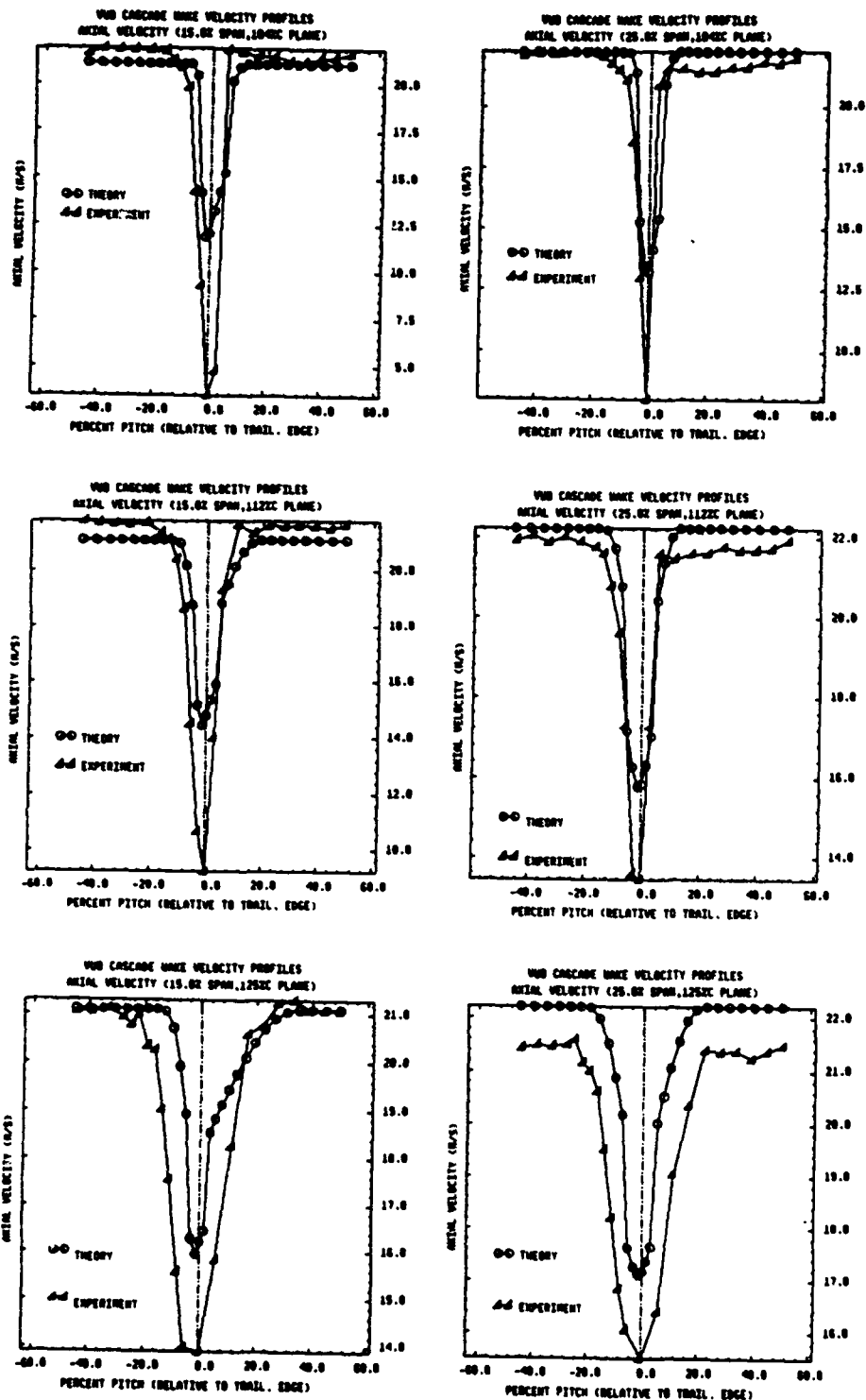


Figure 11.11b: Downstream evolution of axial velocity wake profiles at 15% and 25% span (suction side = left of trailing edge, pressure side = right of trailing edge)

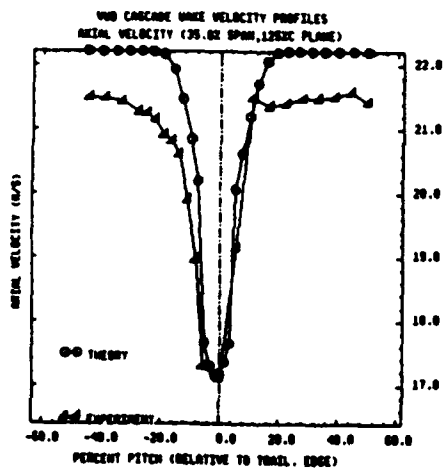
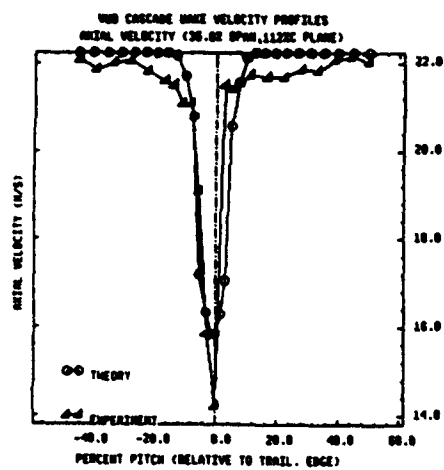
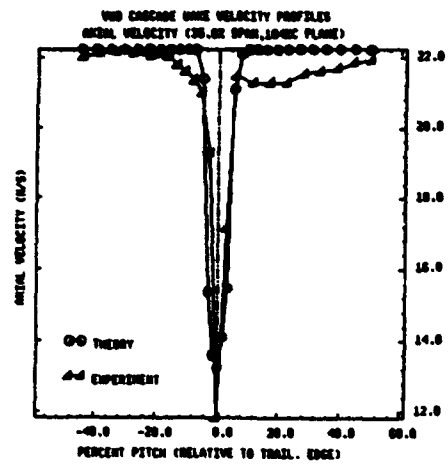


Figure 11.11c : Downstream evolution of axial velocity wake profiles at 35% span
(suction side = left of trailing edge, pressure side = right of trailing edge)

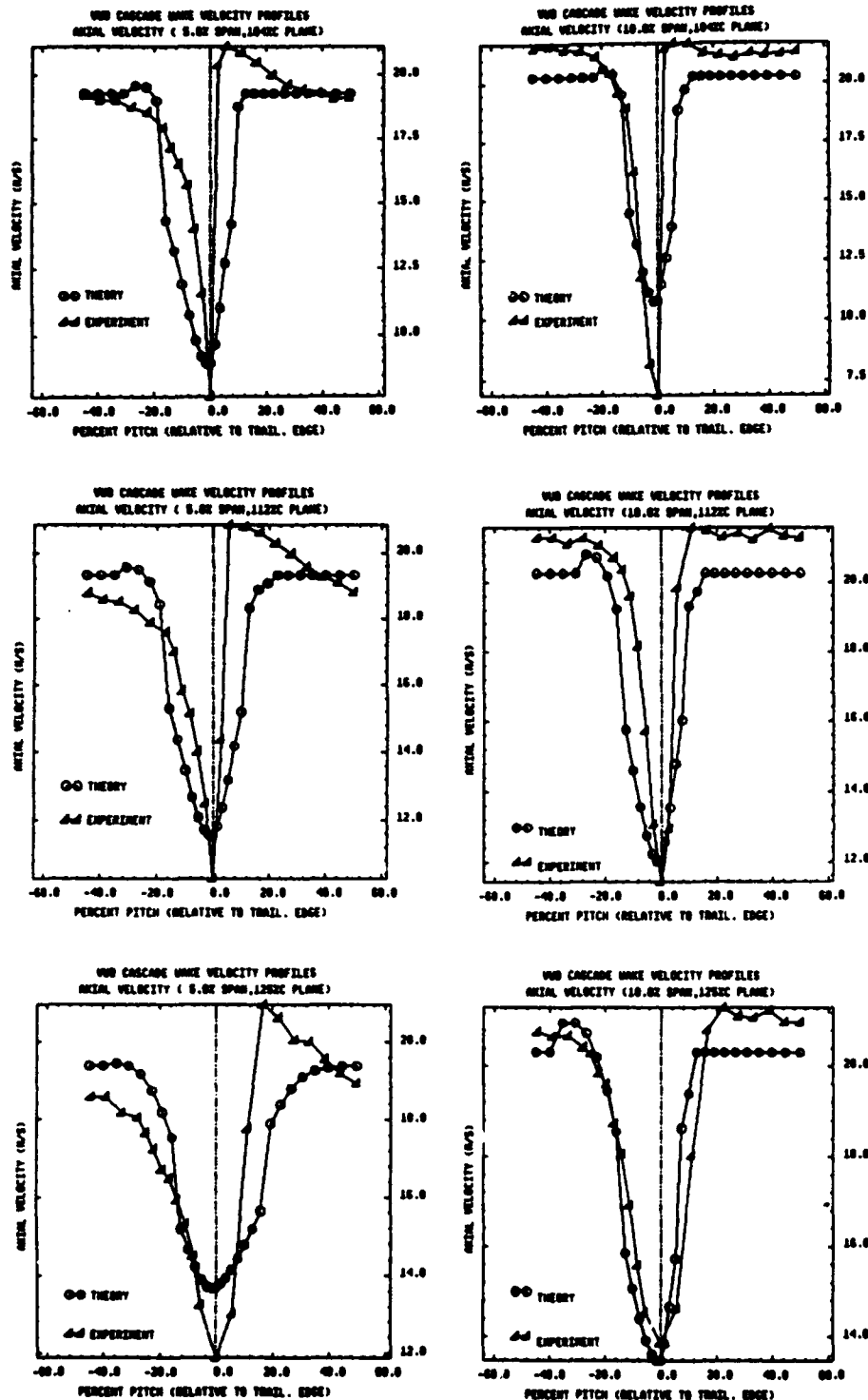


Figure 11.12a : Downstream evolution of axial velocity wake profiles at 5% and 10% span, with increased wake mixing coefficient near the end-walls.
(suction side = left of trailing edge, pressure side = right of trailing edge)

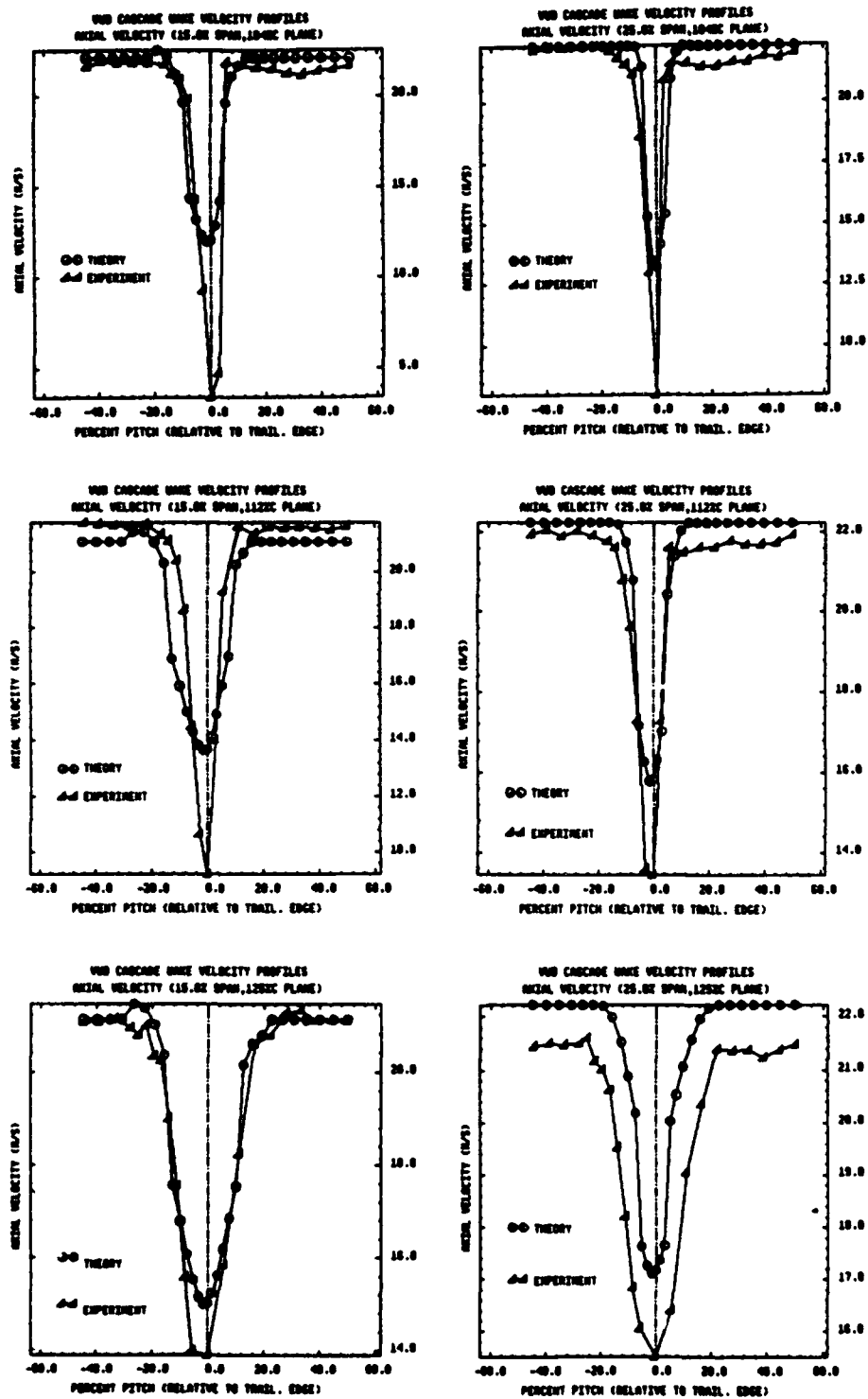


Figure 11.12b: Downstream evolution of axial velocity wake profiles at 15% and 25% span, with increased wake mixing coefficient near the end-walls. (suction side = left of trailing edge, pressure side = right of trailing edge)

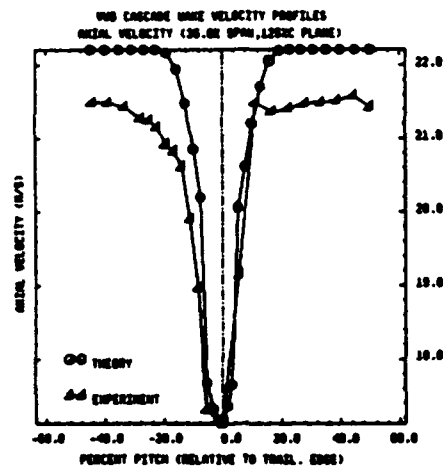
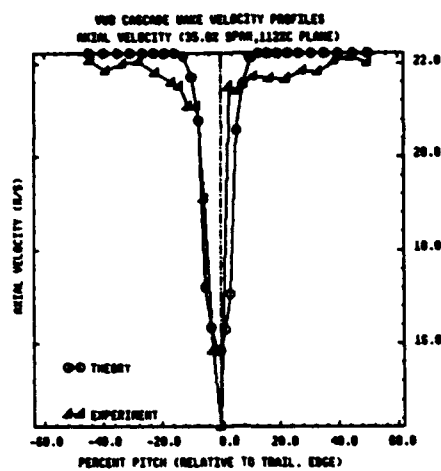
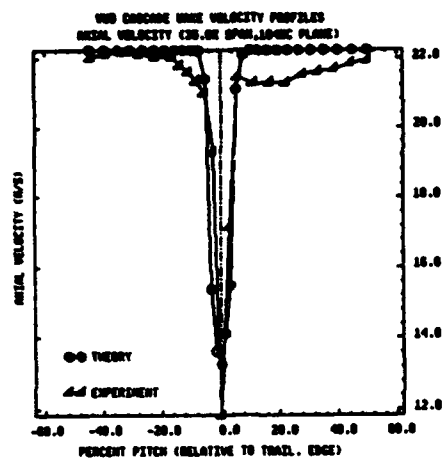


Figure 11.12c : Downstream evolution of axial velocity wake profiles at 35% span, with increased wake mixing coefficient near the end-walls.
(suction side = left of trailing edge, pressure side = right of trailing edge)

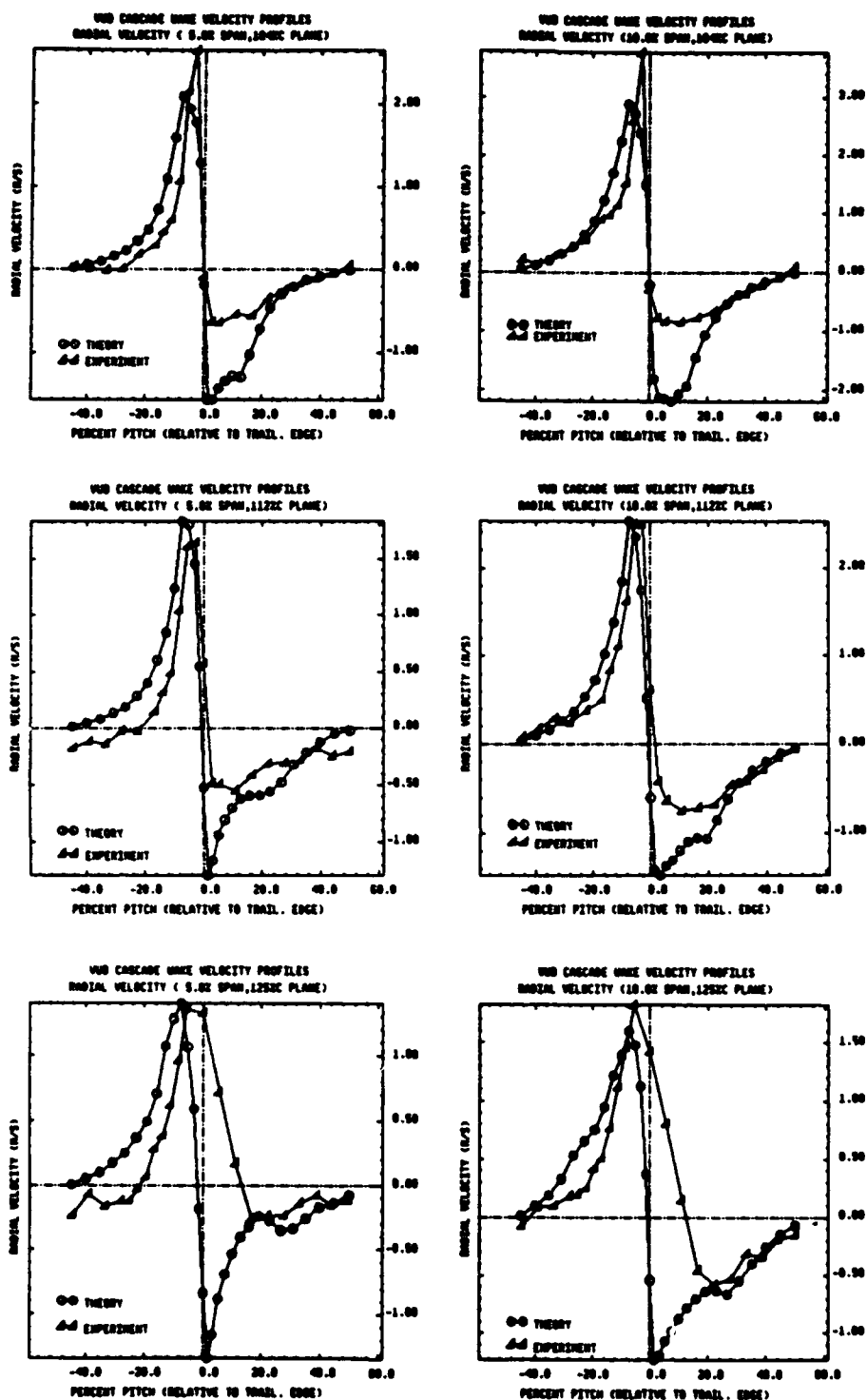


Figure 11.13a : Downstream evolution of radial velocity wake profiles at 5% and 10% span, with increased wake mixing coefficient near the end-walls.
(suction side = left of trailing edge, pressure side = right of trailing edge)

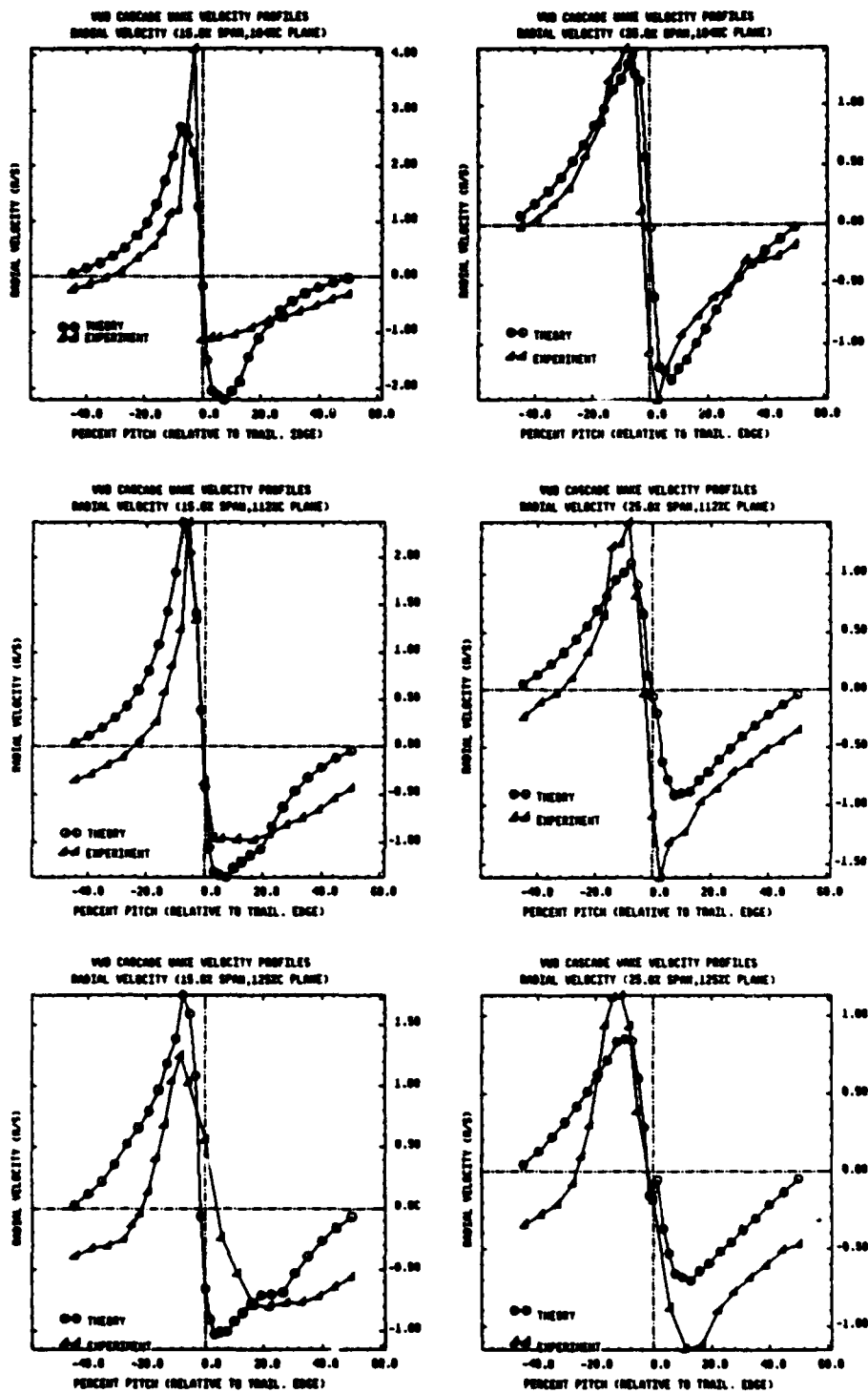


Figure 11.13b : Downstream evolution of radial velocity wake profiles at 15% and 25% span, with increased wake mixing coefficient near the end-walls.
(suction side = left of trailing edge, pressure side = right of trailing edge)

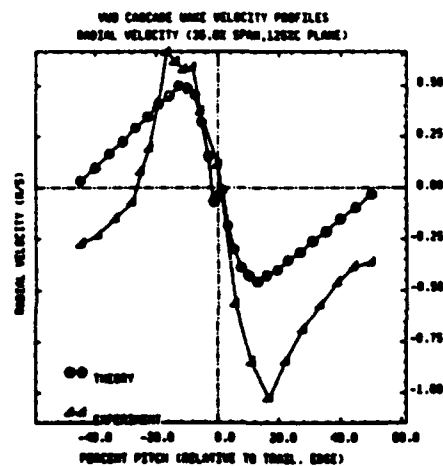
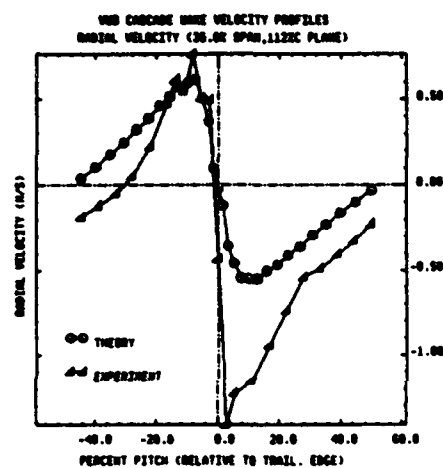
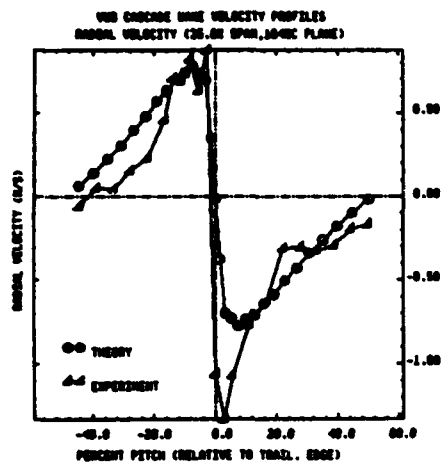


Figure 11.13c : Downstream evolution of radial velocity wake profiles at 35% span, with increased wake mixing coefficient near the end-walls.
(suction side = left of trailing edge, pressure side = right of trailing edge)

REFERENCES

- ADKINS G.G., SMITH L.H., 1982, "Spanwise Mixing in Axial-Flow Turbomachines", *ASME Journal of Engineering for Power*, Vol. 104, January 1982, pp. 97-110.
- DE RUYCK J., 1982, "Computation of End-Wall Boundary Layers in Axial Compressors", PhD Thesis, Dept of Fluid Mechanics, Vrije Universiteit Brussel.
- DE RUYCK J., HIRSCH Ch., 1981, "Investigations of an Axial Compressor End-Wall Boundary Layer Prediction Method", *ASME Journal of Engineering for Power*, Vol. 103, January 1981, pp. 20-33.
- DE RUYCK J., HIRSCH Ch., 1983, "End-Wall Boundary Layers in Multistage Axial Compressors", AGARD Conference Proceedings CP-351 *Viscous Effects in Turbomachines*.
- DE RUYCK J., HIRSCH Ch., 1987, "Radial Mixing in Turbomachines", *VUB-TN-39*, Dept of Fluid Mechanics, Vrije Universiteit Brussel.
- DE RUYCK J., HIRSCH Ch., 1988a, "Radial Mixing in Turbomachines", *VUB-TN-40*, Dept of Fluid Mechanics, Vrije Universiteit Brussel.
- DE RUYCK J., HIRSCH Ch., 1988b, "A Radial Mixing Computation Method", *ASME Paper 88-GT-68*.
- DE RUYCK J., HIRSCH Ch., SEGAERT P., 1989, "Secondary Flows and Radial Mixing Predictions in Axial Compressors", AGARD Conference Proceedings CP-469 *Secondary Flows in Turbomachines*.
- GALLIMORE S.J., CUMPSTY N.A., 1986a, "Spanwise Mixing in Multistage Axial Flow Compressors : Part I - Experimental Investigation", *ASME Journal of Turbomachinery*, Vol. 108, July 1986, pp. 2-9.
- GALLIMORE S.J., 1986b, "Spanwise Mixing in Multistage Axial Flow Compressors : Part II - Throughflow Calculations Including Mixing", *ASME Journal of Turbomachinery*, Vol. 108, July 1986, pp. 10-16.
- HIRSCH Ch., 1988, *Numerical Computation of Internal and External Flows*, Volume 1 - "Fundamentals of Numerical Discretization", John Wiley & Sons, Chichester.
- HIRSCH Ch., DRING R.P., 1987, "Through-Flow Models for Mass and Momentum-Averaged Variables", *ASME Journal of Turbomachinery*, Vol. 109, July 1987, pp. 362-370.
- HIRSCH Ch., WARZEE G., 1976, "A Finite-Element Method for Through Flow Calculations in Turbomachines", *ASME Journal of Fluids Engineering*, Vol. 98, September 1976, pp. 403-421.
- HIRSCH Ch., WARZEE G., 1979, "An Integrated Quasi-3D Finite Element Calculation Program for Turbomachinery Flows", *ASME Journal of Engineering for Power*, Vol. 101, January 1979, pp. 141-148.

HORLOCK J.H., LAKSHMINARAYANA B., 1973, "Secondary Flows : Theory, Experiment, and Application in Turbomachinery Aerodynamics", *Annual Review of Fluid Mechanics*, Volume 5, pp. 247-280.

KANG S., HIRSCH Ch., 1991, "Three Dimensional Flow in a Linear Compressor Cascade at Design Conditions", *ASME Paper 91-GT-114*.

KERREBROCK J.L., 1981, "Flow in Transonic Compressors", *AIAA Journal*, Vol. 19, No. 1, pp. 4-19.

KOTIDIS P.A., 1989, "*Unsteady Radial Transport in a Transonic Compressor Stage*", PhD Thesis, Gas Turbine Laboratory Report #199, Massachusetts Institute of Technology, September 1989.

KOTIDIS P.A., EPSTEIN A.H., 1990, "Unsteady Radial Transport in a Transonic Compressor Stage", *ASME Paper 90-GT-133*

LEYLEK J.H., WISLER D.C., 1990, "Mixing in Axial-Flow Compressors : Conclusions Drawn from 3-D Navier-Stokes Analyses and Experiments", *ASME Paper 90-GT-352*

SALVAGE J.W., 1974, "A Review of the Current Concept of Cascade Secondary Flow Effects", *Technical Note 95*, von Karman Institute, March 1974.

SCHLICHTING H., 1979, *Boundary-Layer Theory* (7th Ed.), McGraw-Hill, New York, pp. 739-743.

SIEVERDING C.H., 1985, "Secondary Flows in Straight and Annular Turbine Cascades". In *Thermodynamics and Fluid Mechanics of Turbomachinery - Volume II* (Eds. A.S. Üçer, P. Stow and Ch. Hirsch), NATO ASI Series E 97B, Martinus Nijhoff Publishers, Dordrecht, pp. 621-663.

VAVRA M.H., 1960, *Aero-Thermodynamics and Flows in Turbomachines*, John Wiley & Sons, New York.

WENNERSTROM A.J., 1990, "A Review of Predictive Efforts for Transport Phenomena in Axial Flow Compressors", to be published.

WISLER D.C., BAUER R.C., OKIISHI T.H., 1987, "Secondary Flow, Turbulent Diffusion and Mixing in Axial-Flow Compressors", *ASME Journal of Turbomachinery*, Vol. 109, October 1987, pp. 455-482.

WU C.H., 1952, "A General Theory of Three-Dimensional Flow in Subsonic and Supersonic Turbomachines of Axial-, Radial-, and Mixed-Flow Types", *NACA TN 2604*.

YIH C.S., 1979, *Fluid Mechanics* (2nd Ed.), West River Press, Ann Arbor.

ZIENKIEWICZ O.C., 1977, *The Finite Element Method* (3rd Ed.), McGraw-Hill, Maidenhead, England.

APPENDIX A

MERIDIONAL COORDINATE SYSTEM

The meridional coordinate system (m,n,u) , illustrated in Figure A.1, is an orthogonal curvilinear coordinate system. The tangential direction u is identical with the circumferential direction θ of the cylindrical coordinate system, while the m and n coordinates form a two-dimensional curvilinear coordinate system on the S2 through-flow plane, which is the (r,z) -plane in cylindrical coordinates. In the present theory, the m coordinate lines are defined by the streamlines of the axisymmetric Quasi-3D flow on the through-flow plane, while the n coordinate lines are orthogonal to these lines in every point.

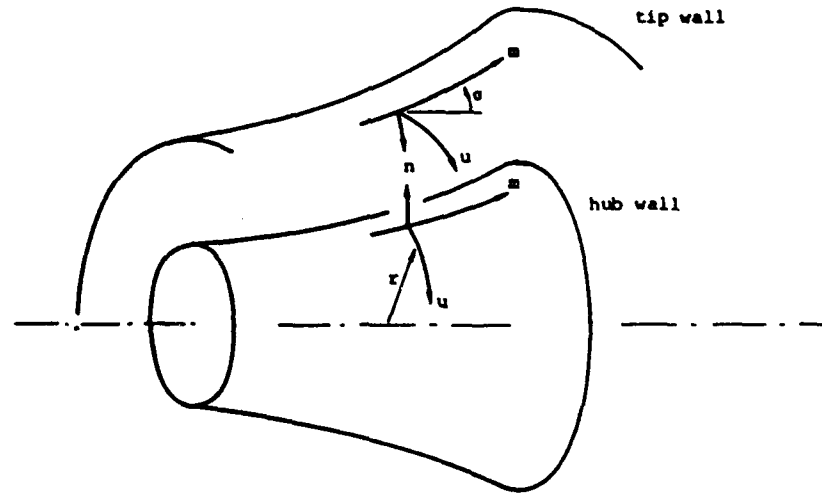


Figure A.1 : Meridional coordinate system

The relation between both coordinate systems is very straightforward, since it is completely defined by the angle σ between the axial direction and the local meridional direction (cf. Figure A.2). Since the meridional direction has been defined as the direction of the axisymmetric streamline in the through-flow plane, this angle is given by :

$$\sigma = \arctan \frac{\bar{W}_{r,Q3D}}{\bar{W}_{z,Q3D}} \quad (A.1)$$

Therefore, the local meridional and normal unit vectors can be expressed as follows :

$$\vec{l}_m = \sin \sigma \vec{l}_r + \cos \sigma \vec{l}_z \quad (A.2a)$$

$$\vec{l}_n = \cos \sigma \vec{l}_r - \sin \sigma \vec{l}_z \quad (A.2b)$$

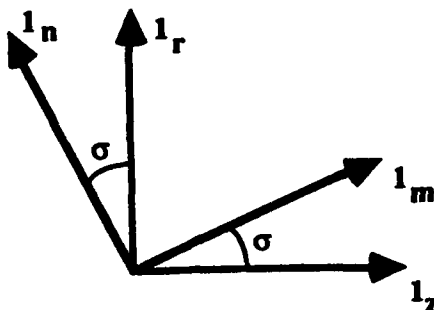


Figure A.2 : Relation between base vectors of cylindrical and meridional coordinate system

The following relations can also be introduced :

$$\sin \sigma = \frac{\partial r}{\partial m} = -\frac{\partial z}{\partial n} \quad (\text{A.3a})$$

$$\cos \sigma = \frac{\partial z}{\partial m} = \frac{\partial r}{\partial n} \quad (\text{A.3b})$$

The convective variation of any quantity along a meridional streamline is expressed by :

$$W_r \frac{\partial}{\partial r} + W_z \frac{\partial}{\partial z} = (W_r \vec{l}_r + W_z \vec{l}_z) \cdot \left(\frac{\partial}{\partial r} \vec{l}_r + \frac{\partial}{\partial z} \vec{l}_z \right) = \vec{W}_m \cdot \vec{\nabla}_m \quad (\text{A.4})$$

where the meridional velocity and meridional gradient are defined as, taking into account that the meridional coordinate lines are streamlines and using equations (A.3a) and (A.3b) :

$$\vec{W}_m = W_r \vec{l}_r + W_z \vec{l}_z = W_m \vec{l}_m \quad \text{meridional velocity} \quad (\text{A.5a})$$

$$\vec{\nabla}_m = \frac{\partial}{\partial r} \vec{l}_r + \frac{\partial}{\partial z} \vec{l}_z = \frac{\partial}{\partial m} \vec{l}_m + \frac{\partial}{\partial n} \vec{l}_n \quad \text{meridional gradient} \quad (\text{A.5b})$$

Combining equations (A.5a) and (A.5b) finally yields

$$\vec{W}_m \cdot \vec{\nabla}_m = W_m \frac{\partial}{\partial m} \quad (\text{A.6})$$

APPENDIX B

CONSTANT BLOCKAGE ASSUMPTION

The purpose of this appendix is to demonstrate that the assumption of constant blockage amounts to an error of second order.

The exact formula for the geometrical pitch-average of the partial derivative of an arbitrary function g with respect to an arbitrary argument z reads (Leibnitz' rule) :

$$\left(\frac{\partial g}{\partial z}\right)_{\text{exact}} = \frac{1}{\theta_s - \theta_p} \frac{\partial}{\partial z} [(\theta_s - \theta_p) \bar{g}] - \frac{1}{\theta_s - \theta_p} \left[g_s \frac{\partial \theta_s}{\partial z} - g_p \frac{\partial \theta_p}{\partial z} \right] \quad (\text{B.1})$$

where the geometrical pitch average is defined as :

$$\bar{A} = \frac{1}{\theta_s - \theta_p} \int_{\theta_p}^{\theta_s} A \, d\theta \quad (\text{B.2})$$

The angular distance $\theta_s - \theta_p$ between suction and pressure side is proportional to the tangential blockage factor b :

$$\theta_s - \theta_p = 2\pi b/N \quad (\text{B.3})$$

Substitution of this identity into equation (B.1) yields the following relation :

$$\left(\frac{\partial g}{\partial z}\right)_{\text{exact}} = \frac{1}{b} \frac{\partial}{\partial z} (b \bar{g}) - \frac{1}{2\pi b/N} \left[g_s \frac{\partial \theta_s}{\partial z} - g_p \frac{\partial \theta_p}{\partial z} \right] \quad (\text{B.4})$$

Assuming constant blockage implies that b is a constant, which in turn implies that (cf. equation (B.3)) :

$$\frac{\partial \theta_s}{\partial z} = \frac{\partial \theta_p}{\partial z} = \overline{\left(\frac{\partial \theta}{\partial z}\right)} \quad (\text{B.5})$$

Hence, the corresponding approximate formula for the geometrical pitch-average of a partial derivative reads :

$$\left(\frac{\partial g}{\partial z}\right)_{\text{approx}} = \frac{\partial \bar{g}}{\partial z} - \frac{1}{2\pi b/N} [g_s - g_p] \overline{\left(\frac{\partial \theta}{\partial z}\right)} \quad (\text{B.6})$$

The error on this approximation can be computed by subtracting equation (B.6) from equation (B.4) :

$$\begin{aligned} \text{Error} &= \left(\frac{\partial \bar{g}}{\partial z} \right)_{\text{exact}} - \left(\frac{\partial \bar{g}}{\partial z} \right)_{\text{approx}} \\ &= \frac{\bar{g}}{b} \frac{\partial b}{\partial z} - \frac{1}{2\pi b/N} \left[g_s \frac{\partial \theta_s}{\partial z} - g_p \frac{\partial \theta_p}{\partial z} \right] + \frac{1}{2\pi b/N} [g_s - g_p] \left(\frac{\partial \theta}{\partial z} \right) \end{aligned} \quad (\text{B.7})$$

Introducing the following relations into equation (B.7) :

$$\frac{\partial \theta_s}{\partial z} = \left(\frac{\partial \theta}{\partial z} \right)'_s + \left(\frac{\partial \theta}{\partial z} \right)'_s \quad (\text{B.8a})$$

$$\frac{\partial \theta_p}{\partial z} = \left(\frac{\partial \theta}{\partial z} \right)'_p + \left(\frac{\partial \theta}{\partial z} \right)'_p \quad (\text{B.8b})$$

yields :

$$\begin{aligned} \text{Error} &= \frac{\bar{g}}{b} \frac{\partial b}{\partial z} - \frac{1}{2\pi b/N} \left[g_s \left(\frac{\partial \theta}{\partial z} \right)'_s - g_p \left(\frac{\partial \theta}{\partial z} \right)'_p \right] \\ &= \frac{\bar{g}}{2\pi b/N} \frac{\partial}{\partial z} [\theta_s - \theta_p] - \frac{1}{2\pi b/N} \left[g_s \left(\frac{\partial \theta}{\partial z} \right)'_s - g_p \left(\frac{\partial \theta}{\partial z} \right)'_p \right] \end{aligned}$$

which can further be transformed, using equations (B.8a) and (B.8b) and introducing the notation $[\]_p$ for the difference between suction and pressure side of an arbitrary quantity :

$$\text{Error} = \frac{\bar{g}}{2\pi b/N} \left[\left(\frac{\partial \theta}{\partial z} \right)'_p \right]_p - \frac{1}{2\pi b/N} \left[g \left(\frac{\partial \theta}{\partial z} \right)'_p \right]_p = \frac{1}{2\pi b/N} \left[(\bar{g} - g) \left(\frac{\partial \theta}{\partial z} \right)'_p \right]_p \quad (\text{B.9})$$

and finally becomes :

$$\text{Error} = \frac{1}{2\pi b/N} \left[g' \left(\frac{\partial \theta}{\partial z} \right)'_p \right]_p \quad (\text{B.10})$$

This equation shows that the error between the exact and the approximate formula amounts to a product of fluctuation quantities and thus can be assumed to be at least one order of magnitude smaller than the averaged quantities.

Hence, the assumption of constant blockage amounts to an error of second order.

APPENDIX C

INVISCID FLOW RELATIONS

C.1 VELOCITY JUMP RELATIONS

C.1.1 TANGENTIAL VELOCITY JUMP

In the inviscid approximation, the velocity vector at the blade surface is tangent to this surface :

$$\vec{W} \cdot \vec{n} = 0 \quad (C.1)$$

where \vec{n} denotes the vector normal to the blade surface.

Substituting the explicit form of the normal vector, equation (3.7), yields the following relation between the geometry of the blade and the velocity vector :

$$W_\theta = \tan \eta W_r + \tan \beta' W_z \quad (C.2)$$

From this, the following formula for the jump in tangential velocity between the pressure and suction side of the blade passage can immediately be derived, assuming constant blockage :

$$[W_\theta]_p^s = \tan \eta [W_r]_p^s + \tan \beta' [W_z]_p^s \quad (C.3)$$

C.1.2 RADIAL VELOCITY JUMP

The jump in radial velocity between the pressure and suction side of the blade passage can be decomposed into its Quasi-3D and S3 contributions :

$$[W_r]_p^s = [W_{r,Q3D}]_p^s + [W_{r,S3}]_p^s \quad (C.4)$$

The contribution $[W_{r,S3}]_p^s$ is computed through a supplementary continuity equation for the S3 flow components, but the Quasi-3D contribution $[W_{r,Q3D}]_p^s$ can be computed directly.

The radial flow angle σ of a Quasi-3D axisymmetric streamsurface is defined through :

$$\tan \sigma = \frac{\bar{W}_{r,Q3D}}{\bar{W}_{z,Q3D}} = \frac{\bar{W}_{r,Q3D}}{\bar{W}_z} \quad (C.5)$$

From this, the following relation for the radial velocity jump $[W_{r,Q3D}]_p^s$ is immediately derived :

$$[W_{r,Q3D}]_p^s = \tan\sigma [W_z]_p^s = \tan\sigma [W_{z,Q3D}]_p^s \quad (C.6)$$

C.2 TANGENTIAL VORTICITY

The pitch-averaged tangential vorticity component is defined as :

$$\bar{\zeta}_{abs,\theta} = \bar{\zeta}_\theta = \left[\vec{\nabla} \times \vec{W} \right]_\theta = \frac{\partial W_r}{\partial z} - \frac{\partial W_z}{\partial r} \quad (C.7)$$

The geometrical pitch-average of an arbitrary quantity A is defined as :

$$\bar{A} = \frac{1}{\theta_s - \theta_p} \int_p^s A \, d\theta = \frac{1}{2\pi b/N} \int_p^s A \, d\theta \quad (C.8)$$

The pitch-average of a partial derivative (with respect to an arbitrary variable z, independent of the integration variable θ) can be written as , using Leibniz' rule :

$$\begin{aligned} \frac{\partial \bar{A}}{\partial z} &= \frac{1}{2\pi b/N} \int_p^s \frac{\partial A}{\partial z} \, d\theta = \frac{1}{b} \frac{\partial}{\partial z} (b \bar{A}) - \frac{1}{2\pi b/N} \left[A_s \frac{\partial \theta_s}{\partial z} - A_p \frac{\partial \theta_p}{\partial z} \right] \\ &= \frac{1}{b} \frac{\partial}{\partial z} (b \bar{A}) - \frac{1}{2\pi b/N} \left[A \frac{\partial \theta}{\partial z} \right]_p^s \end{aligned} \quad (C.9)$$

Applying equation (C.9) to equation (C.7) yields the following relation :

$$\begin{aligned} \bar{\zeta}_{abs,\theta} &= \frac{1}{b} \frac{\partial}{\partial z} (b \bar{W}_r) - \frac{1}{b} \frac{\partial}{\partial r} (b \bar{W}_z) \\ &\quad - \frac{1}{2\pi b/N} \left[\frac{\partial \theta}{\partial z} W_r \right]_p^s + \frac{1}{2\pi b/N} \left[\frac{\partial \theta}{\partial r} W_z \right]_p^s \end{aligned} \quad (C.10)$$

Taking into account that a linear variation is assumed for the radial component of the S3 flow component, and hence $\bar{W}_{r,S3}$ is equal to zero, taking into account that there is no S3 flow component in the z direction, and introducing the defining relations for the blade angles (equation (3.7)) yields :

$$\begin{aligned} \bar{\zeta}_{abs,\theta} &= \frac{1}{b} \frac{\partial}{\partial z} (b \bar{W}_{r,Q3D}) - \frac{1}{b} \frac{\partial}{\partial r} (b \bar{W}_{z,Q3D}) \\ &\quad - \frac{1}{2\pi b/N} [\tan\beta' W_r]_p^s + \frac{1}{2\pi b/N} [\tan\eta W_z]_p^s \end{aligned} \quad (C.11)$$

Finally, assuming constant blockage and introducing the velocity jump relations, the following formula is obtained :

$$\begin{aligned}\bar{\zeta}_{abs,\theta} &= \frac{\partial \bar{W}_{r,Q3D}}{\partial z} - \frac{\partial \bar{W}_{z,Q3D}}{\partial r} \\ &- \frac{1}{bs} \left\{ \tan \beta' [W_{r,S3}]_p^s + (\tan \beta' \tan \sigma - \tan \eta) [W_{z,Q3D}]_p^s \right\}\end{aligned}\quad (C.12)$$

C.3 RADIAL VORTICITY

The pitch-averaged radial vorticity component is defined as :

$$\bar{\zeta}_{abs,r} = \bar{\zeta}_r = \left[\vec{\nabla} \times \vec{W} \right]_r = \frac{1}{r} \frac{\partial W_z}{\partial \theta} - \frac{\partial W_\theta}{\partial z}\quad (C.13)$$

Applying equation (C.9) to equation (C.13) yields the following relation :

$$\bar{\zeta}_{abs,\theta} = -\frac{1}{b} \frac{\partial}{\partial z} (b \bar{W}_\theta) + \frac{1}{2\pi br/N} [W_z]_p^s + \frac{1}{2\pi b/N} \left[\frac{\partial \theta}{\partial z} W_\theta \right]_p^s\quad (C.14)$$

Introducing the defining relations for the blade angles (equation (3.7)) and the velocity jump relations, and assuming constant blockage finally yields :

$$\begin{aligned}\bar{\zeta}_{abs,\theta} &= -\frac{\partial \bar{W}_\theta}{\partial z} + \frac{1}{bs} \left\{ (1 + \tan^2 \beta' + \tan \beta' \tan \eta \tan \sigma) [W_{z,Q3D}]_p^s \right\} \\ &+ \frac{1}{bs} \left\{ (\tan \beta' \tan \eta) [W_{r,S3}]_p^s \right\}\end{aligned}\quad (C.15)$$